DISS. ETH NO. 23327

DEVELOPMENT AND UNDERSTANDING OF RHENIUM-BASED ALKENE METATHESIS CATALYSTS

A thesis submitted to attain the degree of

DOCTOR OF SCIENCES of ETH ZURICH

(Dr. sc. ETH Zurich)

presented by

MAXENCE DANIEL GODEFROY MARIE VALLA

Dipl. MSc., CPE Lyon and Université Claude Bernard Lyon 1- University of Lyon, France

Born on June, 3rd 1988

Citizen of France

accepted on the recommendation of

Prof. Christophe Copéret, examiner

Prof. Peter Chen, co-examiner

Prof. Philippe Sautet, co-examiner

Dr. Pascal Raybaud, co-examiner

2016

"Bien qu'on ait du coeur à l'ouvrage,
L'art est long et le Temps est court."

-Charles Baudelaire.

Acknowledgments

Through my four years at ETH, I am in debt toward a lot of persons. First of all, I would like to acknowledge Prof. Christophe Copéret for the clear guidance through the PhD, for all the projects we completed together and for the exciting research I could do in his laboratories. I would like thank all the collaborators I had the chance to work with: R. Verel, L. Emsley, A. Lesage, P. Sautet, P. Florian, D. Gajan, I. Herman, P. Wolf and so on… Thank you for the inspired research.

I would like to thank the jury of my PhD, Prof. C. Copéret, Prof. P. Chen, Prof. P. Sautet and Dr. P. Raybaud for taking the time for the review of my PhD thesis.

Secondly, I would like to thank my lab mate, Florian, Georges, WC, Victor, Pavel, Margherita, Karen, Tigran, for making the cave a nice place to work even without sunlight. Thanks to the "babyfoot" and kitchen team for making the lunch break the highlight of most of my working days. The "classico" will be missed.
I would like to acknowledge the rest of the group, Dma and Deven for nice ski trip, TC, Emma, Rick, Tsung-Han, Marius, Indre, Daniel, Alexey for un-finishable project.

Cheap David, Angry David, Giuseppe, Martin, Matt and Karol are thanks for introducing me to the lab and for making me feel at home.

Former member of the group are also thanks, Sohei (Don't believe such like thing), Raphael, Kenji, Florent for the first version of the "classico".

I would like to thank my Lyon team (Gael, Laura and Marie) for all the moment that we could spend together when I was in Lyon. Thank you for being there.

I would like to thank my family, especially my mom and my brother who were always there for me.

Finally, I would like to thank Zoé, my partner in life, for having supporting me through all these years. Thank you for all the quality moment we spent together. Thank you for being so understanding with me. Thank you.

Abstract.

Metathesis has become a very appealing reaction in the past decades, both academically and industrially. Of all the classical catalysts, Re_2O_7/Al_2O_3 is the only one that shows good activity at room temperature and that can catalyze the metathesis of functionalized olefin upon activation with Me_4Sn. However, to date this catalyst is poorly understood; the structures of its active sites are unknown and because of this it can only be improved through empirical approaches. Therefore, this PhD thesis has aimed at understanding and developing heterogeneous Re-based metathesis catalysts through Surface Organometallic Chemistry; combining advanced spectroscopic techniques and computational approaches. We used these methods to develop detailed characterization of the support, the supported Re species, and the key metathesis alkylidene and the metallacycle intermediates. Through this work, it was possible to show that the active sites of CH_3ReO_3/Al_2O_3, considered as a model of Re_2O_7/Al_2O_3, correspond to oxo-μ-methylene species, where the Al_{III} defect sites of alumina play an essential role. CH_3ReO_3/Al_2O_3 was also linked to the heterogeneous Me_4Sn activated Re_2O_7/Al_2O_3. Through the understanding of alumina and silica-alumina supports, it was possible to develop the first metathesis active supported Re Oxo alkylidene, thus to further bridging the gap between the well-defined supported catalysts prepared via SOMC and the classical, ill-defined, Re_2O_7/Al_2O_3 catalyst.

Résumé.

La réaction de métathèse est devenue une réaction incontournable ces dernières années tant dans le paysage académique qu'industriel. De tous les catalyseurs hétérogènes connus, Re_2O_7/Al_2O_3 est le seul à avoir montré d'excellentes activités à température ambiante et à être compatible avec des alcènes fonctionnels, quand ce dernier est activé avec du Me_4Sn. Malgré ces bonnes propriétés, ce catalyseur n'est pas compris à l'échelle moléculaire. En effet la structure de son site actif est toujours inconnue et son développement utilise donc une approche purement empirique. Ainsi, cette thèse de doctorat a été dédiée à la caractérisation et au développement de catalyseurs hétérogènes de métathèse à base de rhénium. Pour cela nous utiliserons la chimie organométallique de surface, en combinant des techniques telles que la spectroscopie ou encore la chimie théorique. Un accent particulier est donné a la caractérisation du support utilisé, des espèces de surface ainsi qu'aux intermédiaires clefs de la réaction de métathèse: les alkylidénes et le métallacycles. En utilisant cette approche, il a été possible de montrer que le site actif du catalyseur CH_3ReO_3/Al_2O_3, considéré comme étant un modèle de Re_2O_7/Al_2O_3, est composé d'un oxo-μ-methyléne supporté. Les sites d'attache du complexe Re à la surface d'alumine sont très importants. Ainsi, les sites Al_{III}, souvent considéré comme des défauts de surface, joue un rôle crucial sur l'activité en métathèse. Il a été également possible de lier ce modèle au catalyseur hétérogène, Me_4Sn,Re_2O_7/Al_2O_3. A travers la compréhension des surfaces d'alumine et de silice-alumine, il a été possible de développer le premier rhénium oxo alkylidéne supporté actif en métathèse. Ces travaux permettent de se rapprocher de plus en plus de la compréhension du catalyseur hétérogène, Re_2O_7/Al_2O_3.

Chapter 1: Introduction

1.1 General Introduction.

Metathesis is a key reaction widely used in industry, with applications ranging from petrochemicals to fine chemicals. This reaction is catalysed by metal complexes from groups 6-8 (mainly, Mo, W, Re and Ru), and these catalysts are usually divided in two main categories: homogeneous catalysts, which nowadays are mainly well-defined and used in the fine chemical industry, and the ill-defined heterogeneous catalysts based on supported transition metal oxides of groups 6-7; the latter are used mainly for the production of propene. Supported metal oxide metathesis catalysts are typically prepared by impregnations of metal precursors on metal oxides followed by high temperature calcination step. They are very robust catalysts, containing only a small concentration of active sites, making them difficult to understand at a molecular level; they are thus mainly improved by empirical approaches. For instance, the rhenium based metathesis catalysts are especially interesting because of their high activity at low temperatures, 25-150 °C, in contrast to its Mo and W equivalent, which require much higher activation and operating temperatures. Despite these advantages, Re-based metathesis catalysts have not been widely used in industry because of the difficulties to improve their performance.

In contrast, homogeneous catalysts – based on well-defined metal alkylidenes – have been greatly improved over the past 40 years, thanks to structure – activity relationship and rational designs, and they are now used in several industrial processes.

In the past twenty years, an alternative approach has emerged to understand and improve heterogeneous catalysts, which is based on the development of well-defined supported species through surface organometallic chemistry (SOMC). This approach allows the preparation of supported catalysts with close to 100% of active sites. It relies on the controlled grafting of a tailored molecular precursor on the surface functionalities of an oxide support, typically the hydroxyl groups (OH), and on the detailed characterization of the resulting surface species through multiple spectroscopy techniques combined with computational chemistry.

The PhD thesis is devoted in the understanding and development of Re-based well-defined metathesis catalysts through SOMC. This implies the detailed study of alumina-contained supports and the understanding of the model catalysts, in order to establish links with classical ill-defined systems used in industry.

1.2 Metathesis

Alkene metathesis has gained a tremendous importance in the past 6 decades in both industry and academia. This reaction was discovered by Anderson and Merckling in 1955 at Dupont, where they observed the polymerization via ring opening metathesis of norbornene using lithium aluminium tetraheptyl and titanium tetrachloride.[1,2] In 1964, Banks and Bailey reported the first observation of olefin disproportionation using heterogeneous tungsten and molybdenum supported catalyst.[3] It is in 1967 that the term metathesis was introduced by Calderon and co-workers at Goodyear[4] after their discovery that a homogeneous solution of tungsten tetrachloride would produce 3-hexenes and 2-butenes from 2-pentenes.[2,4] Metathesis catalytic systems are now days typically based on transition-metal elements from the groups 6-8, based on molecular complexes or the corresponding metal oxides.[5,6]

In 1970, Y. Chauvin proposed a mechanism for this reaction, for which he shared the 2005 Nobel Prize of chemistry with R.G. Grubbs and R.R. Schrock.[7-9] The metathesis mechanism involves metal alkylidenes (M=C(R')(R'')) as key intermediates (Scheme 1.1); they react with an olefin via a [2+2] cycloadddition to yield a metallacyclobutane, and the corresponding reverse steps (cycloreversion) lead to the overall exchange of alkylidene fragments between olefins, hence the name metathesis.[5]

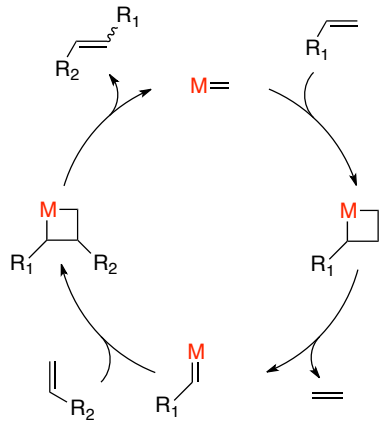

Scheme 1. 1. Chauvin Mechanism of the metathesis of olefins describing the elementary steps in d^0 metal-based catalysts.

The Chauvin mechanism is universally accepted, but requires additional steps associated with coordination and de-coordination of the olefins from the metal sites. For instance, d^6 $RuCl_2(=CHR)\text{-}L_2$ must lose one of its ligands to allow olefin coordination.[10-12] Similarly, tetrahedral d^0 alkylidene complexes need to distort in order to accommodate the incoming olefin. Experimental and computational studies have also evidenced the presence of metallacyclobutanes as key reaction intermediates, which can adopt a trigonal bypyramid (TBP) or square pyramidal (SP) geometry in these ML_5 systems. In d^0 and d^6 systems, the TBP metallacycles are key reaction intermediates, while SP observed only on d^0 systems correspond to a resting state for the catalysts and can lead to possible deactivation processes; both structures can inconvert between each other through a turnstile process (Scheme 1.2).[13-19]

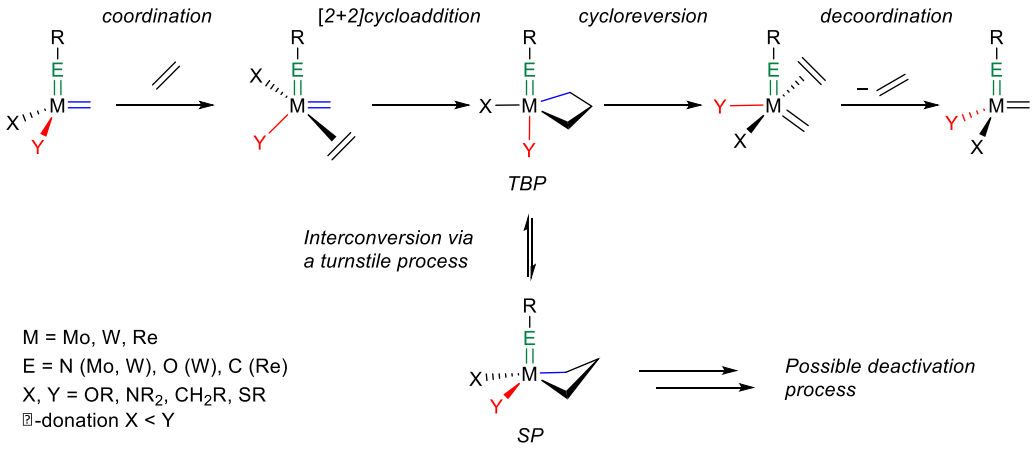

Scheme 1. 2. Elementary steps in d0 alkene metathesis.

Depending on the substrates, five different types of reaction patterns are possible (Scheme 1.3): self- and cross-metathesis (CM) which involves acyclic olefins, ring opening metathesis (ROM) in which cyclic olefins react to yield acyclic products, ring closing metathesis (RCM) which cyclizes dienes, ring opening metathesis polymerization (ROMP) that polymerizes cyclic alkenes, and the Acyclic Diene Metathesis (ADMet).[5]

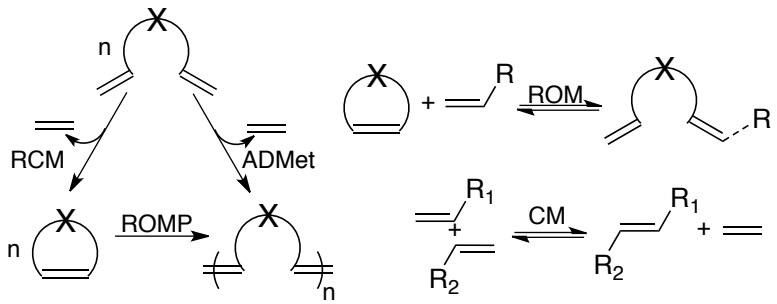

Scheme 1. 3. Classification of olefins metathesis reactions.

1.3 Heterogeneous Metathesis Catalyst

1.3.1 General Considerations

Metathesis catalysts are usually prepared by impregnation of an active metal precursor on a high surface area metal oxide support (100-500 $m^2 \cdot g^{-1}$). This step is followed by a high temperature calcination process (> 500°C) yielding surface sites that can be present as isolated and oligomeric oxo surface species; it may also contain crystalline nanoparticles. The most widely used heterogeneous catalysts are based on MO_x (M = Mo, W and Re) supported on SiO_2, Al_2O_3, and SiO_2-Al_2O_3.[2,6]

1.3.2 W-Metal Based Heterogeneous Catalysts

WO_3/SiO_2 has become a key catalyst in the petrochemical industry in the past decades. It is used in the Lummus OCT process, allowing the production of propylene via the ethenolysis of 2-butenes (cross-metathesis).[6] The reverse process called "Phillips triolefin process" was industrially used by Phillips Petroleum Co. from 1966 to 1972.[6 3]

Supported WO_3/SiO_2 catalysts are usually prepared via impregnation of an aqueous solution of tungsten molecular precursor followed by a drying step and calcination under oxidative conditions at high temperature (calcination).[20] The surface species are present as monomeric isolated di-oxo and mono-oxo tungsten as dominant sites, along with crystalline WO_3 nanoparticle when the maximum dispersion limit is reached.[20-22] The exact structure of the active species and initiation step of these catalysts remains unknown. WO_3 supported on Al_2O_3 has received less attention in the literature compared to WO_3/SiO_2 or the analogous rhenium or molybdenum alumina supported catalysts.[23] WO_3 supported on SiO_2-Al_2O_3 show equal to improved catalytic performances compare to the silica-supported system.[24]

1.3.3 Mo-Metal Based Heterogeneous Catalysts

Alumina-supported molybdenum metathesis catalysts were also reported in 1964.[3] Few years later, in 1968, the Shell Higher Olefin Process (SHOP) was developed based on this catalyst, and it was commercialized in 1977. After 45 years this technology has not lost its significance,[25] and it is still one of the major processes for the production of α–olefins.

Alumina or silica supported molybdenum catalysts are typically prepared by impregnation of a ammonium salt using incipient wetness impregnation followed by

calcination at high temperature (500°C) under oxidative conditions.[26,27] Other methods can be used such as sol-gel or flame spray pyrolysis. [28,29]

MoO_3/SiO_2 is about one order of magnitude less active than its alumina-supported analogue.[5] However, it has been extensively studied because only isolated species are present on the surface of this catalyst; it is thus viewed as a model for olefin metathesis catalysts. The structure of the isolated species are very similar to the one found on the surface of WO_3/SiO_2 according to UV-vis, Raman, XAS and IR spectroscopies. The surface species are mainly isolated mono and di-oxo species. Above the maximum dispersion limit, MoO_3 nanoparticles are formed.[21,30-35] *In-situ* IR studies have lead to the proposal that molybdenum alkylidene can be formed upon contacting cyclopropene with reduced species.[36,37] Similarly, metallacyclobutanes have been proposed to be observed by IR spectroscopy upon adsorption of ethylene on CO treated photo-reduced MoO_3/SiO_2.[36,38] However, the spectroscopic evidences of these metathesis intermediates are only tenuous.

The surface structure of MoO_3/Al_2O_3 is more complicated than its silica supported analogue. Recent extensive spectroscopy[26,30] and DFT calculations have shed lights on the structures of possible surface species.[39,40] At low molybdenum coverage, molybdenum di-oxo isolated species are present on the surface, while several species can be detected at high coverage (> MoO_3 monolayer); they include the di-oxo isolated species along with oligomeric mono oxo species as well as crystalline molybdenum nanoparticles at high Mo loadings. Handzlik and Sautet reported a DFT study underlying the importance of the anchoring sites of the molybdenum species on the alumina surface. They showed that Mo alkylidene are more stable when supported on (110) surface. They also showed that the reactivity of the alkylidene species strongly depends on their geometry and the location on the alumina surface.[41] However, no irrevocable experimental evidences can attest yet on the presence of these types of intermediates.

MoO_3/SiO_2-Al_2O_3 have been claimed to exhibit higher catalytic performances in the metathesis reaction compare to the silica or alumina supported catalysts. While only limited amount of studies are available for this system, it was proposed that strong Brønsted acidity character of aluminosilicate supports enhanced the activity of the molybdenum complex.[27-29,42-44]

1.3.4 Re-Metal Based Heterogeneous Catalysts

In 1967, British Petroleum (BP),[45] developed Re_2O_7/Al_2O_3 as a catalyst for disproportionation of short and long chain olefins. Re_2O_7/Al_2O_3 demonstrates very good activity in olefin metathesis at room temperatures. It is also the only classical heterogeneous catalyst, which is compatible with functionalized olefins, when activated with SnR_4.[2,46-48] However, the small fraction of activate sites in these catalysts makes difficult a detailed understanding and a rational development via structure-reactivity relationship of the system.[49]

1.3.4.1 Surface sites for Re_2O_7/Al_2O_3

Extensive research has been reported on Re_2O_7/Al_2O_3, addressing in particular the structure of the active sites. While there is not yet a clear molecular understanding of the systems, several correlations have been found: Re active sites are formed upon consumption of surface Al_{IV}-OH groups and are associated with monomeric tetrahedral perrhenate (Re^{VII}) surface species; they are formed only with Re loadings above 6%wt of Re_2O_7.[50-52]

The catalytic activity of Re_2O_7/Al_2O_3 depends mainly on three factors:

i) The Re content: no activity was observed for a surface with content of rhenium lower than 6%. Above this value the metathesis activity increases exponentially until 15% of Rhenium content is reached; above that olefin oligomerisation competes with metathesis, which leads to a poor selectivity and the deactivation of the catalysts.[2]

ii) The acidity of the surface: it was shown that the acidic OH on alumina was an important parameter to generate the active sites of the catalyst (Re loading > 6%wt).

iii) High temperature of pre-treatment (calcination): it gives a better redistribution of the surface species and augments the Lewis acidity of the surface and the activity of the catalysts.[52]

Recently, a detailed study (UV-vis, XANES, Raman and IR spectroscopy combined with first principles DFT calculations) has allowed the understanding of the isolated surface species obtained upon activation/calcination (Scheme 1.4). In all cases, the Re surface species is a bis-grafted tetra-coordinate Re(VII) species bound to the alumina surface with two terminal oxo ligands. It was revealed that the initial structure of the active site was a ReO_4^- tetrahedron coordinated to Al_{III} defect sites and Al_{IV} sites of the alumina surface (Scheme 1.4). Similarly, the inactive species is a ReO_4- with a very distorted geometry where two extra oxygens from the surface

coordinate the Re centre. At low Re loading the molecular complex will populate the basic μ_1-Al_{IV} sites leading to an inactive species; above 6% of Re loading the more acidic μ_2 and μ_3-Al_{VI} sites will start to host perrhenate species inducing the formation of the metathesis active species.[53]

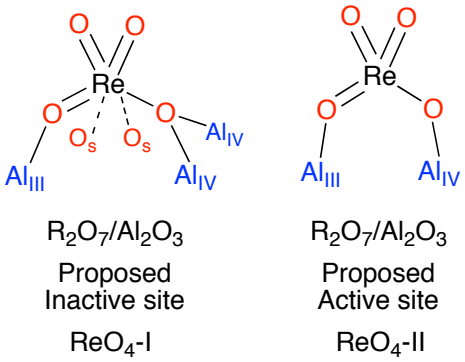

Scheme 1. 4. Proposed inactive and active sites for the heterogeneous catalyst, Re_2O_7/Al_2O_3. O_s designed extra coordination from the surface oxygen.

1.3.4.2 Initiation step for Re_2O_7/Al_2O_3

The Re_2O_7/Al_2O_3 system is active in metathesis without any co-catalysts, and the active species are formed *in situ* by contacting rhenium with the olefins, the only exception being ethylene. Several mechanisms have been proposed over the past decades.[54] The most popular mechanisms describing the formation of the surface active alkylidene species discussed in the literature are: 1) the H-assisted mechanism, 2) the vinylic and 3) allylic C-H activations and 4) the pseudo Wittig mechanism.[5] The H-assisted and vinylic C-H activation can be ruled out because of the absence of formation of 3-methyl-2-pentene in the metathesis of (*Z*)-2-butene.[55] The two most likely mechanisms are shown in Scheme 1.5. The π-allyl mechanism involves the oxidative addition of the propylene C-H bond on a reduced metal centre; this generates a π-allyl species, which is then converted into a metallacyclobutane and carbene species via cycloreversion.[56] However, this route is not consistent with the fact that Re_2O_7/Al_2O_3 is active in the cross-metathesis of (*Z*)-stilbene and ethylene to form styrene since none of these olefins contain allylic protons.[55] The other possibility is the formation of a metallaoxetane, which proceeds for instance by a pseudo-Wittig type mechanism (Scheme 1.5).[54,55] This would lead to the formation of a metallaoxetane intermediate and the release of one molecule of CH_3CHO. However, none of these intermediates/co-products have been observed experimentally. In conclusion, the initiation step remains ambiguous.

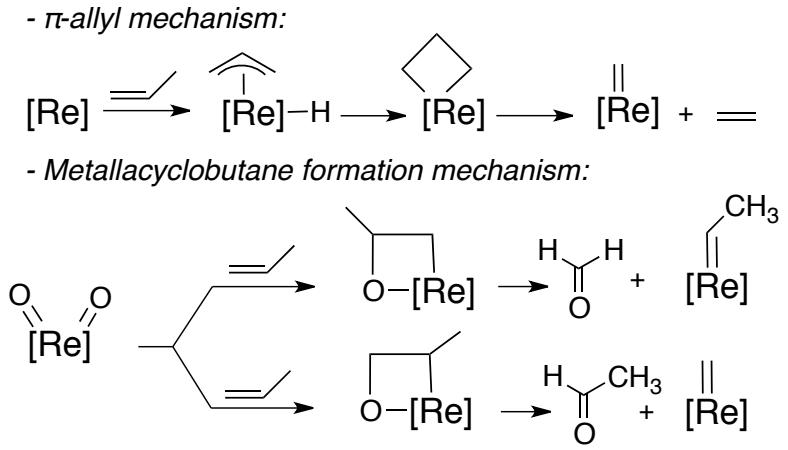

Scheme 1. 5. Initiation step (2 mechanisms) for the system Re_2O_7

The only support for the pseudo-Wittig mechanism arose recently with the work of Chen and co-workers, who have shown that the generation of a molecular Re^{VII} oxo carbene is possible from a Re^{V} diolate using Collision Induced Dissociation (CID) coupled with mass spectroscopy.[57,58] The Re^{V} diolate undergoes a 1,2 shift to generate a Re^{VII} dioxo metallaoxetane. Retrocyclization yields the Re dioxo carbene and aldehydes (Scheme 1.6).[57,58] This experimental finding is a large step forward, and may help to understand these Re-based heterogeneous catalysts. However due to the very low number of active sites (around 2%), the study of the specific initiation step of Re_2O_7/Al_2O_3 remains extremely challenging.

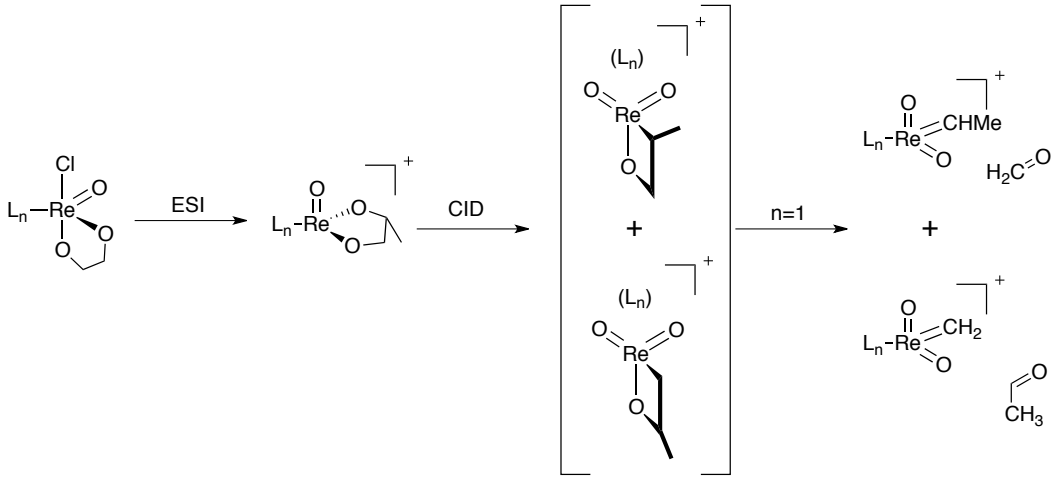

Scheme 1. 6. Mechanism of the formation of the Re(VII) oxo carbene from Re(V) diolate. Figure reproduced form the work of Chen *et al.*.[57,58]

1.3.4.3 Re_2O_7 supported on SiO_2-Al_2O_3

In contrast to WO_3 or MoO_3, Re_2O_7 supported on SiO_2 is completely inactive; this has been associated with the lack of surface acid sites and the impossibility to generate the propagating active species of rhenium.[59] On the other hand, the catalytic

activity of Re_2O_7/Al_2O_3 can be greatly improve for Re loading below 10% when using other mixed oxides such as SiO_2-Al_2O_3 or Al_2O_3-B_2O_3.[52,59-61] Several infrared studies suggest that the Brønsted acidity of aluminosilicates support enhances the catalytic activity of the catalyst by stabilizing the Re centre.[62] Re_2O_7 supported on (SiO_2/Al_2O_3) has however received much less attention than its alumina-supported analogues and little is known on the structures of the surface species. Nevertheless, it was shown, using XPS and TEM, that below 3% of Re loading the surface species were monomeric while, above this value, 3-dimensional Re cluster could be found on the surface of aluminosilicates.[59] The high activity of this catalyst at low Re content has been proposed to arise from the fact that ReO_4^- tetrahedra react with the so-called Brønsted acidic surface "pseudo bridging" silanol. This results in electron-poor Re centres which are believed to be the active sites precursors.[52]

1.4 Metal Oxide Supports: the Case of Al_2O_3 and SiO_2.

The first step toward generation of well-defined supported catalysts using surface organometallic chemistry is to understand the supports in terms of surface functionalities and to control their type and density. Due to extensive studies on both γ-alumina and silica, it is now possible to reach a good level of molecular understanding.

1.4.1 γ-Alumina

γ-alumina is a key component of Re_2O_7/Al_2O_3 and related Re-based catalysts such as CH_3ReO_3/alumina since the corresponding silica-supported analogues are inactive. This alumina is prepared by calcination of Boehmite (an aluminum hydroxide: AlO(OH)) at temperature ranging between 450°C and 750°C. Above this temperature, the thermal treatment leads to a phase transition to δ-alumina, then θ and finally the α phase.[63]

1.4.1.1 Model for γ-alumina

Despite its essential importance in industry, the structure of the γ-alumina is still under debate and unknown at the molecular level. Recently, Krokidis et al. constructed a model of γ-alumina from the simulated topotactic dehydration of boehmite.[64] Their model presented calculated structural parameters similar to the experimental findings, in particular the ratio between tetra- and hexa-coordinated aluminum, the 3D structure and the lattice density. γ-alumina (Figure 1.1) exhibits

three facets: the major (110) surface (74% of the total area), the (100) surface (16% of the area) and the (111) surface (10% of the total area).[63,65]

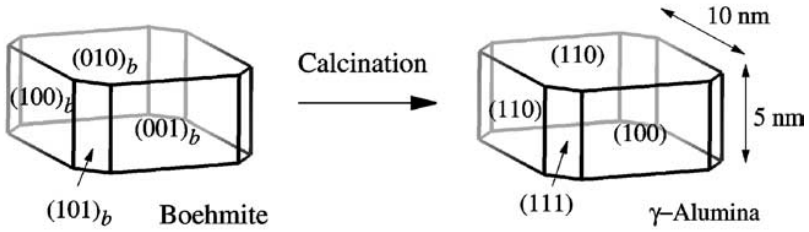

Figure 1. 1. Transformation of boehmite into γ-alumina. Figure reproduced from Digne *et al.* work.[65]

1.4.1.1.1 Dehydrated surface model

The (100) surface exhibits only Al_V atoms (fivefold coordinate, quoted as I, II and III in Figure 1.2) and μ_3-O oxygen atoms (threefold coordinated, quoted as A, B and C), and is not very reactive. The (111) surface presents a particular structure with an alternative stacking of oxygen and aluminum atoms. In contrast, the (110) surface has aluminum atoms with low coordination number and exhibits in particular one Al_{III} (I, threefold coordination) and two Al_{IV} (II and III, in fourfold coordination). In addition, surface oxygen atoms are in twofold (A, B) and threefold (C, D) coordination.[63,65]

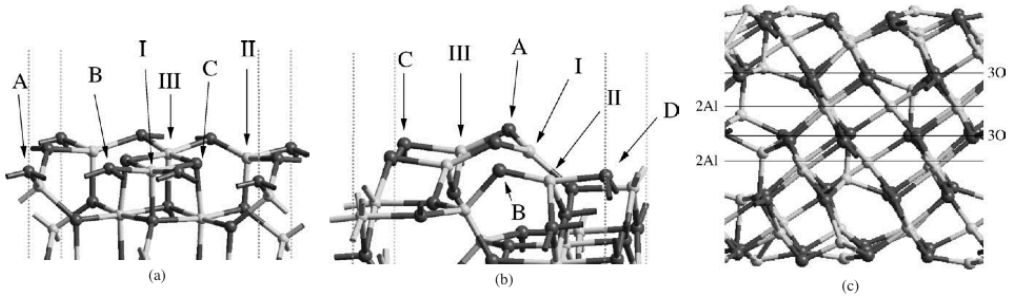

Figure 1. 2. Dehydrated γ-alumina local structure of (a) (100), (b) (110) and (c) (111) surface. Figure reproduced from Digne *et al.* work.[63,65]

The Lewis acidity of the aforementioned aluminum sites is ranked as follows: **Al_{III}** *I*(110) > **Al_V** *I*(100) > **Al_{IV}** *II* (110) > **Al_{IV}** *III* (110) > **Al_V** *II* (100) > **Al_V** *III* (100).

The general trend is the lower the aluminum coordination number, the stronger the Lewis acidity, one exception being the Al_V site of the (100) surface, which is even more acidic than the Al_{IV} sites of the (110) surface.

Knowing that the (110) surface predominates the γ-alumina particle and that this surface exposes the strongest Lewis acid sites, a large number of calculations

focused on this facet. Figure 1.3 describes this unit cell with one aluminum atom in three-fold coordination (the defect site, Al_{III}), two equivalent aluminum sites in four-fold coordination (Al_{IVa} and $Al_{IVa'}$), and an aluminum atom in four-fold coordination that differs from the two other in term Lewis acidity (Al_{IVb}) by its special location on the surface. On this lattice, Al_{III} is the strongest Lewis acid followed by Al_{IVb} and Al_{IVa}.[63,65]

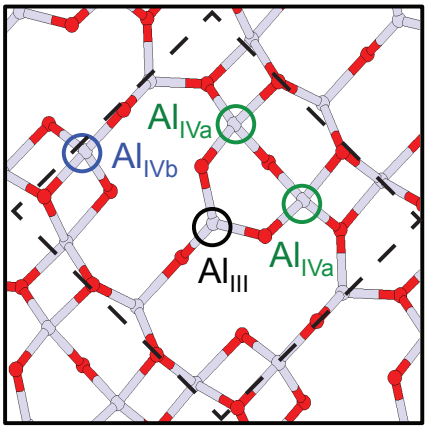

Figure 1. 3. Relaxed structure of the fully dehydrated (110) γ-alumina surface (s0). Only the top layer of the slap is showed here for clarity. The dashed line described the unit cell of the surface.

1.4.1.1.2 Effect of surface hydration

Experimentally, to fully dehydrate the γ-alumina surface, the material would need to be heated at temperature above 1000°C. At this temperature the solid undergoes phase transition form γ to δ- or θ-alumina, and this is always associated with a loss of surface area. In fact, γ-alumina is always hydrated to a significant extent; the water coverage decreases with the temperature of pre-treatment between 400°C and 1000°C.[66,67] Similar observations have been obtained on Evonik Alu-C alumina (Figure 1.4), which is a mixture of γ- and δ-alumina. This alumina is often chosen because of its similar properties combined with a higher thermal stability and better transparencies for IR studies.[68]

Thermal treatment also affects the Lewis acidity of the support and results in the formation of defect sites at temperatures above 400°C. These defect sites have been identified as Al_{III} surface sites; they react/interact with various probe molecules (H_2, CH_4 and N_2) and exhibit a maximum surface density at 700°C (Figure 1.5 for CH_4). It is also noteworthy that H_2 reacts with more defect sites than CH_4, which is likely related to the higher reactivity (acidity) of hydrogen.[69]

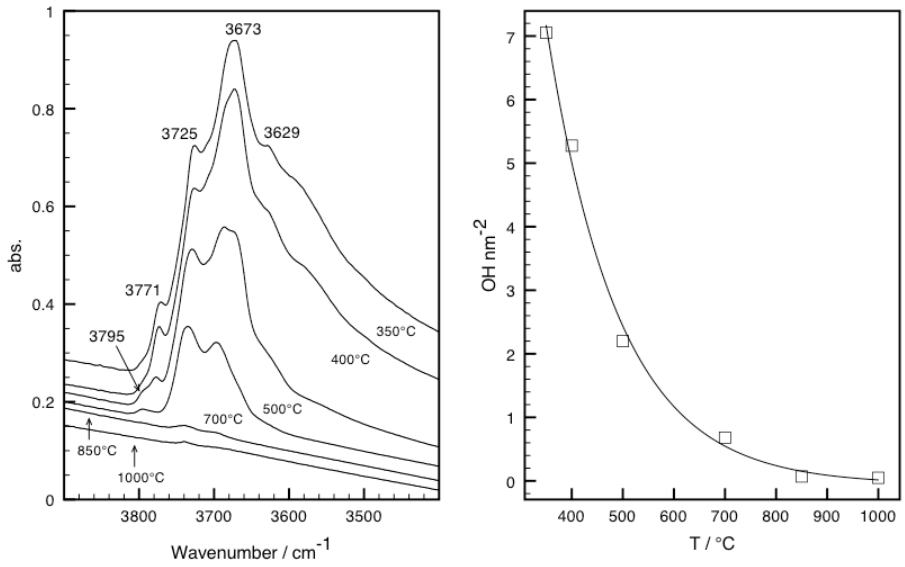

Figure 1. 4. Left figure: IR spectra of the OH-region of Evonik AluC alumina treated at different temperature, right figure: Integration of the OH group from the IR spectra vs the temperature of pre-treatment.

In 2012, Grabrienko and co-workers have studied the reactivity of alumina toward propylene.[70] Using solid-state NMR techniques, they have shown that propoxy and π-allyl surface complexes are formed; the former via protonation of the olefin and the latter via C-H bond activation of propylene on Al,O sites.

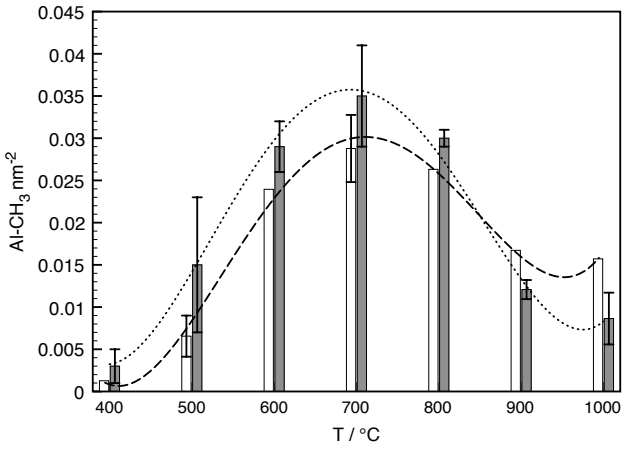

Figure 1. 5. Density of Al-CH_3 sites in SBa-200 (empty bars) and Evonik AluC alumina (full bar) as a function of temperature pre-treatment.

When one molecule of water is added per unit cell on the computed surface of the γ-alumina model, the most stable surface is associated with a molecule of water dissociated on Al_{III} sites (and neighbours oxygen). Surprisingly and in contrast with the acidity trend of the Al surface site, the second most stable surface has a free Al_{III} defect site. The OH is bridging the two Al_{IVa} aluminium atoms of the unit cell, and

increases the basicity of the adjacent O atoms, without significantly affecting the Lewis acidity of Al_{III}. This leads to the formation of Al,O Frustrated Lewis Pairs (FLP),[67] which can activate the C-H bond of methane

This degree of hydration (1 water per unit cell, corresponding to 3 OH nm^{-2} and about a temperature of dehydroxylation of 500°C, Figure 1.4) is important as it has free surface defect sites.[67] When hydration is increased to two molecules of water per unit cell, corresponding to a OH coverage of 6 $OH.nm^{-2}$ and a temperature of dehydration of 400°C, the 110 facet of alumina re-organizes and the Al_{III} sites become tetracoordinated inducing the lost of its strong Lewis acidity.[67]

1.4.2 Amorphous Silica.

Similarly to alumina, the density of surface functional group (-OH) of silica nanoparticles can be tuned by a thermal treatment under vacuum (Figure 1.6.a). Silica remains stable (no loss of surface area) up to thermal treatment of 700°, keeping its high surface area (100-1000 $m^2.g^{-1}$).[71]

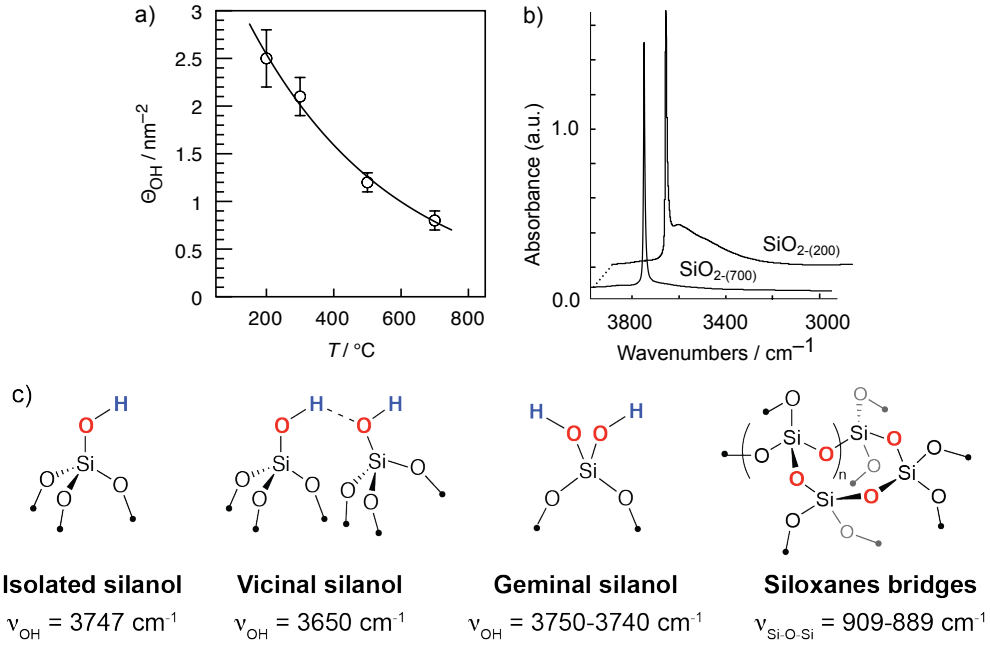

Figure 1. 6. a) Silica OH coverage in function of the temperature of dehydroxylation, b) IR spectrum of SiO2 dehydroxylated at 700°C and 200°C, zoomed in the OH regions, c) Types of silanols and siloxanes bridges with the corresponding vibrations (in wavenumbers, cm^{-1}). Adapted from Rascon *et al.*[68].

Figure 1.6.b shows the difference between silica partially dehydroxylated at 700°C ($SiO_{2\text{-}(700)}$) and 200°C ($SiO_{2\text{-}(200)}$) under high vacuum (10^{-5} mBar). The termination of $SiO_{2\text{-}(200)}$ expose several types of silanols: isolated, vicinal and germinal (Figure 1.6.c) while the surface of $SiO_{2\text{-}(700)}$ displays mostly isolated silanol with a

concentration of 0.8 $OH.nm^{-2}$. Thus, it is possible to use $SiO_{2-(700)}$ as a source of isolated silanols, which allow the generation of well-defined mono-grafted (mono-siloxy) surface species. A higher proportion of bis-grafted species will be obtained when using silica partially dehydroxylated at lower temperature. This approach has been successful for the immobilization of a wide range of organometallic complexes.[72] For example the grafting of $Ta(=CHtBu)(CH_2tBu)_3$ on silica dehydroxylated at 700°C leads to a mono-grafted (mono-siloxy) well-defined species (Scheme 1.7a) while the grafting of the same molecular precursor leads to the formation bis-grafted (bis-siloxy) Ta surface species. (Scheme 1.7b).[73]

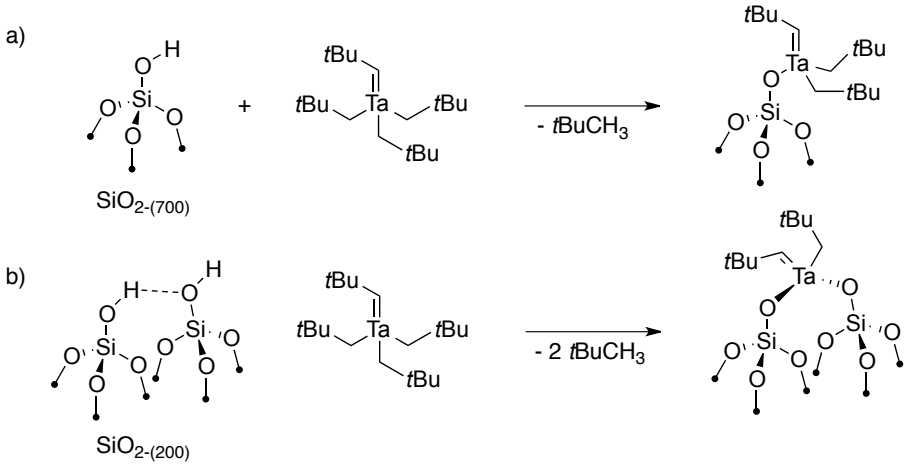

Scheme 1. 7. Grafting of $Ta(=CHtBu)(CH_2tBu)_3$ on silica dehydroxylated at 700°C (a) and 200°C (b).

1.5 Well-defined heterogeneous metathesis catalyst.

1.5.1 Well-Defined Silica Supported Metathesis Catalyst.

The first well-defined alkylidene surface complexes active in metathesis was ((≡SiO)Re(CtBu)(=CHtBu)(CH_2tBu) (Scheme 1.8).[74,75] It was also the first heterogeneous metathesis catalyst which was fully characterized at the molecular level, allowing the observation of the alkylidene ligand using solid-sate NMR spectroscopy (peak at 246 ppm in carbon-13 NMR).[74] It showed unprecedented activity in alkene metathesis by comparison to both its homogeneous and heterogeneous analogues, which showed that heterogeneous catalysts do not intrinsically display lower activity.

From this first well-defined silica-supported alkene metathesis catalyst, a large number of well-defined supported catalysts have been developed, and they can be divided in two distinct families, shown in Scheme 1.8:

a) the well-defined Mo, W and Re alkylidene species – containing ancillary alkylidyne, oxo or imido ligands, for which initiation starts via cross-metathesis with the existing bulky alkylidene ligand[16,18,74-88]

b) the well-defined supported metal (Mo and W) complexes that form an alkylidene under reaction conditions, typically via α-H abstraction of two alkyl ligands.[76,84,89,90]

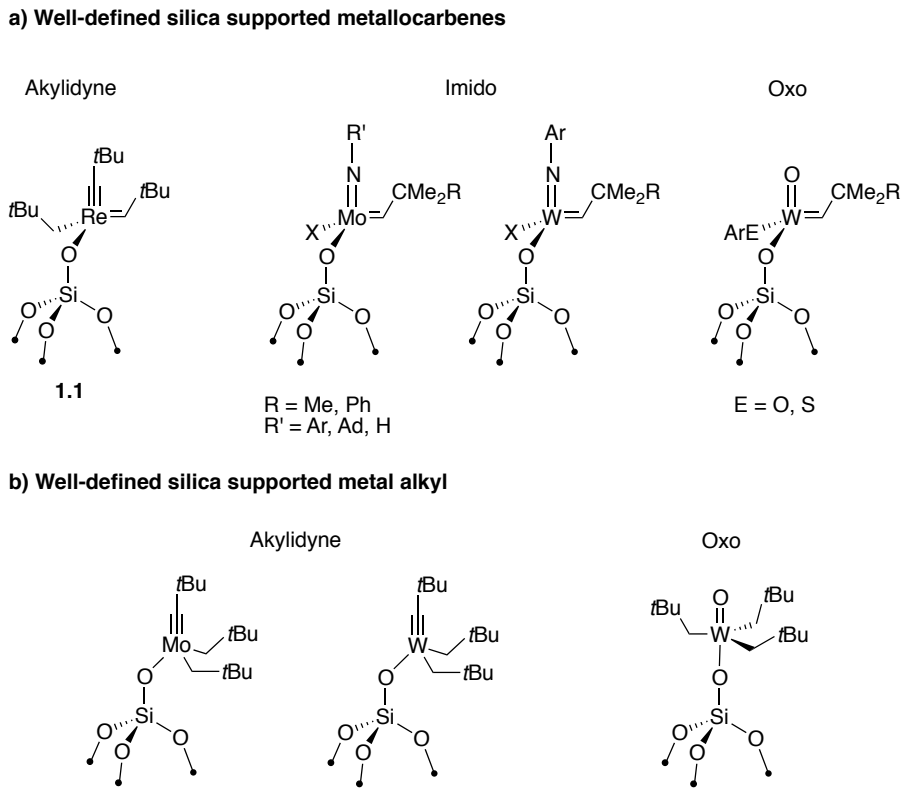

Scheme 1. 8. Well-defined alkene metathesis catalyst.

In this introduction we will focus on the first family of catalysts.

The well-defined silica-supported Re complex, ((≡SiO)Re(CtBu)(=CHtBu)(CH_2tBu), displays much higher metathesis activity than its molecular analogues $(X)_2$Re(CtBu)(=CHtBu) (X = CH_2tBu or OR).[74]

Computational studies have revealed that the high reactivity of this complex and the corresponding Mo and W analogues result from the dissymmetry at the metal center that decreases the energy barrier for coordination/de-coordination of the olefin and destabilizes the metallacyclobutane intermediates (Scheme 1.2).[15,91] In 2008, Blanc and co-worker reported the first observation of reaction intermediates for a well-defined heterogeneous alkene metathesis catalyst, (≡SiO-W(≡NAr)(=CH*t*Bu)(2,5-$Me_2NC_4H_2$)).[16] By simply contacting this supported compound with an excess of ethylene with respect to tungsten, it was possible to experimentally observe the key

metathesis intermediates, namely the methylidene and the metallacyclobutanes. The solid-state NMR spectra, in particular the 2D HETCOR, allowed distinguishing the NMR signatures of the two different metallacyclobutanes with TBP and SP geometries (Scheme 1.2 and Figure 1.7).

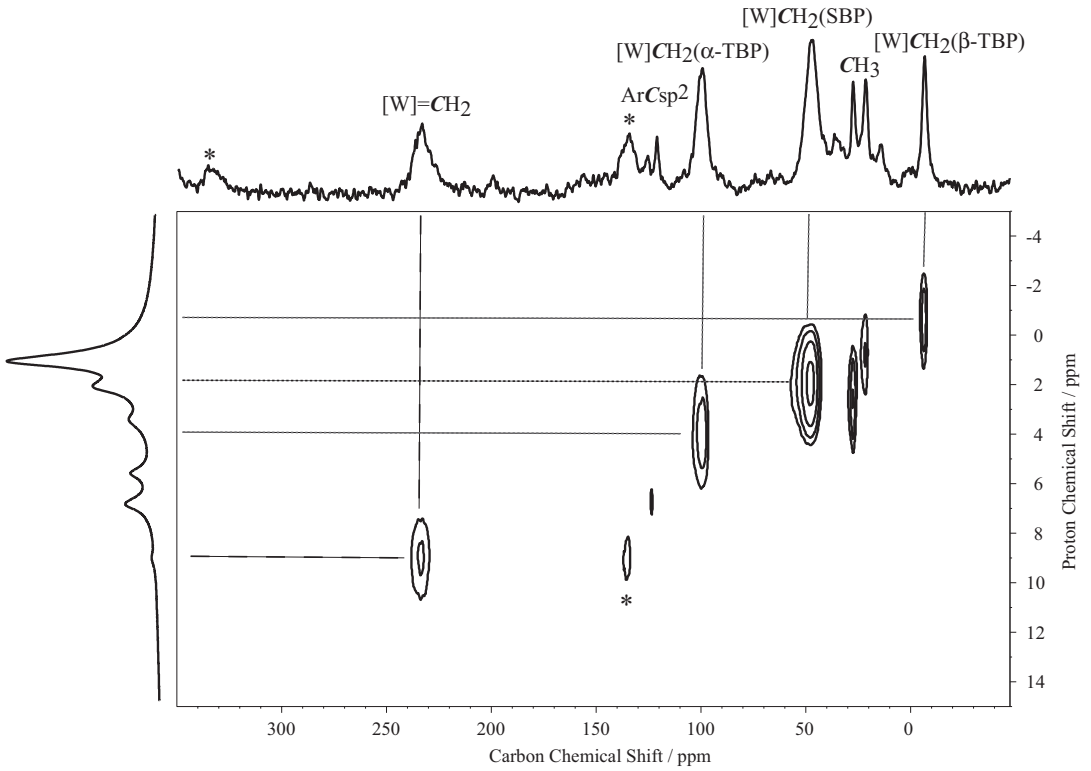

Figure 1. 7. 2D ^{1}H-^{13}C HETCOR solid state NMR of (≡SiO-W(≡NAr)(=CH*t*Bu)(2,5-$Me_2NC_4H_2$)) contacted with ^{13}C labelled ethylene. Reproduced from ref. [16].

More recently, homogeneous oxo alkylidene W molecular complex W(O)(=CH*t*Bu)$(OHMT)_2$ were described,[92] and were used to prepare the corresponding silica-supported system, (≡SiO)W(O)(=CH*t*Bu)(OHMT).[85] The supported complex was fully characterized using NMR techniques and its catalytic performances were studied. In *cis*-4-nonene metathesis, (≡SiO)W(O)(=CH*t*Bu)(OHMT) has a high turnover frequency at 3 min (TOF_{3min}) of 280 min^{-1}. It is among the most active well-defined heterogeneous metathesis catalysts, with activity far greater than its homogeneous precursor (3 min^{-1}). This large difference in activity has been proposed to arise from the presence of two very large aryloxy ligands in W(O)(=CH*t*Bu)$(OHMT)_2$ vs. only one in the silica-supported species; the surface siloxy ligand being a rather small ligand.[85] Using the bulkier (≡SiO)W(O)(=CH*t*Bu)(OdAdPO), TOF_{3min} of 356 min^{-1} and higher TON can be reached in the self metathesis of *cis*-4-nonene.[86] Worthy of note

(≡SiO)W(O)(=CH*t*Bu)(OAr) catalysts are active in ethyl oleate metathesis, in contrast to the classical WO_3/SiO_2 catalyst. The large difference of reactivity observed with WO_3/SiO_2 is probably related to the fact that high reaction temperatures are necessary to form a small amount of active sites.

1.5.2 Alumina Supported Metathesis Catalyst Prepared by Surface Organometallic Chemistry

Due to the more complex population of surface functionalities on the dehydrated alumina surface, less study of well-defined metathesis catalysts have been reported. Most of the research efforts has been conducted on CH_3ReO_3/Al_2O_3 and related systems (e.g. SiO_2-Al_2O_3),[93] which have been used as models for Re_2O_7/Al_2O_3.[94-98] It was shown that grafting CH_3ReO_3 on alumina yields two different kinds of surface species: the major one, inactive, is generated by the coordination of two oxo ligands on Al surface sites (oxo species), and the minor one, highly active, is generated by the C-H bond activation of the methyl ligand on Al,O sites (μ-methylene species), similarly to methane (see **Chapter 3** for further details). The initial – resting – state are now well understood, but it is not clear how the alkylidene is formed (if it is) or what are the metathesis reaction intermediates.

1.6 Strategy and Outline.

Re_2O_7/Al_2O_3 has unique properties in the reaction of metathesis. It is, for instance, the only catalyst that can be operated at low temperature (25-150°C) and it is active towards functionalized olefins upon activation with Me_4Sn. Despite its unprecedented catalytic performances, the structure, the initiation step and the overall mechanism are still a matter of debates in the literature. Therefore, this thesis is devoted to the understanding and the development of Re-based metathesis catalysts and to the study of two key supports, alumina and silica-alumina. The characterization of the surface sites of selected supported Re-based metathesis catalyst is inevitable, as most intermediates for this reaction have not yet been observed. Therefore, by the use of surface organometallic chemistry, the structure of the active sites and the intermediate of these catalysts will be addressed and linked to the ill-defined industrial catalysts. Through this thesis, we will use Surface Organometallic Chemistry, which combined experimental and theory methods, with a particular focus on using advanced solid-state NMR spectroscopy, including surface enhanced dynamic nuclear polarization NMR spectroscopy.[99] This approach will allow us to

understand the structure of surface sites at the molecular level and to propose rational approaches to improve supported metathesis catalysts.

First, it was shown that alumina alone is able to trigger unusual reactions, ranging from coordination of N_2 to the activation of the C-H bond of methane. The reactivity of this support toward olefins in particular propylene and the formation of alkoxide/π-allyl surface species still need to be understood. These questions will be raised in **Chap. 2**.

Second, it has been shown that CH_3ReO_3/Al_2O_3, a model catalyst of Re_2O_7/Al_2O_3, still suffers from a lack of understanding at the molecular level. Indeed, none of key metathesis intermediates – alkylidene or metallacyclobutanes – have been observed so far in contrast to their well-defined silica supported analogues. Therefore, several major questions remain to be answered: (i) how does the resting state, namely the μ-methylene, participate in the metathesis reaction, (ii) what are the intermediates and (iii) how does alumina and its surface sites influence the structure and the reactivity of the corresponding supported rhenium complexes. **Chap. 3** will be devoted to answering these questions using a combined experimental and computational approach.

Furthermore, in view of the similarities in reactivity between CH_3ReO_3/Al_2O_3 and Me_4Sn activated Re_2O_7/Al_2O_3, **Chap. 4** will try to decipher a possible relation between the two systems.

It was shown that aluminosilicates are excellent supports for rhenium-based metathesis catalysts. However, there is no clear molecular understanding of the role of silica-alumina in activating these catalysts. **Chap. 5** will thus investigate the structure of silica-alumina supports, and **Chap. 6** will concentrate on generating better-defined silica-alumina supports through a molecular approach and on obtaining well-defined Re oxo alkylidene in order to evaluate their metathesis activity.

This thesis will end with general conclusions and perspectives in **chap. 7**.

1.7 References.

(1) Anderson, A. W.; Merckling, N. G.; Polymeric bicyclo-(2, 2, 1)-2-heptene. U.S. Patent 2721189 (A): 1955.

(2) Lwin, S.; Wachs, I. E. *ACS Catal.* **2014**, *4*, 2505.

(3) Banks, R. L.; Bailey, G. C. *Ind. Eng. Chem. Prod. Rd.* **1964**, *3*, 170.

(4) Calderon, N.; Chen, H. Y.; Scott, K. W. *Tetrahedron Lett*. **1967**, *8*, 3327.

(5) Ivin, K. J.; Mol, J. C. *Olefin Metathesis and Metathesis Polymerization*, 1997.

(6) Mol, J. C. *J. Mol. Catal. A* **2004**, *213*, 39.

(7) Grubbs, R. H. *Angew. Chem. Int. Ed.* **2006**, *45*, 3760.

(8) Schrock, R. R. *Angew. Chem. Int. Ed.* **2006**, *45*, 3748.

(9) Chauvin, Y. *Angew. Chem. Int. Ed.* **2006**, *45*, 3740.

(10) Weskamp, T.; Kohl, F. J.; Hieringer, W.; Gleich, D.; Herrmann, W. A. *Angew. Chem. Int. Ed.* **1999**, *38*, 2416.

(11) Torker, S.; Merki, D.; Chen, P. *J. Am. Chem. Soc.* **2008**, *130*, 4808.

(12) Jović, M.; Torker, S.; Chen, P. *Organometallics* **2011**, *30*, 3971.

(13) Feldman, J.; Davis, W. M.; Schrock, R. R. *Organometallics* **1989**, *8*, 2266.

(14) Feldman, J.; Davis, W. M.; Thomas, J. K.; Schrock, R. R. *Organometallics* **1990**, *9*, 2535.

(15) Solans-Monfort, X.; Clot, E.; Copéret, C.; Eisenstein, O. *J. Am. Chem. Soc.* **2005**, *127*, 14015.

(16) Blanc, F.; Berthoud, R.; Copéret, C.; Lesage, A.; Emsley, L.; Singh, R.; Kreickmann, T.; Schrock, R. R. *Proc. Nat. Acad. Sci. U.S.A.* **2008**, *105*, 12123.

(17) Solans-Monfort, X.; Copéret, C.; Eisenstein, O. *Organometallics* **2012**, *31*, 6812.

(18) Mougel, V.; Copéret, C. *Chem. Sci.* **2014**, *5*, 2475.

(19) Mougel, V.; Santiago, C. B.; Zhizhko, P. A.; Bess, E. N.; Varga, J.; Frater, G.; Sigman, M. S.; Copéret, C. *J. Am. Chem. Soc.* **2015**, *137*, 6699.

(20) Ross-Medgaarden, E. I.; Wachs, I. E. *J. Phys. Chem. C* **2007**, *111*, 15089.

(21) Lee, E. L.; Wachs, I. E. *J. Phys. Chem. C* **2007**, *111*, 14410.

(22) Lee, E. L.; Wachs, I. E. *J. Phys. Chem. C* **2008**, *112*, 6487.

(23) Thomas, R.; Moulijn, J. A. *J. Mol. Catal.* **1982**, *15*, 157.

(24) Liu, N.; Ding, S.; Cui, Y.; Xue, N.; Peng, L.; Guo, X.; Ding, W. *Chem. Eng. Res. Des.* **2013**, *91*, 573.

(25) Keim, W. *Angew. Chem. Int. Ed.* **2013**, *52*, 12492.

(26) Tian, H.; Roberts, C. A.; Wachs, I. E. *J. Phys. Chem. C* **2010**, *114*, 14110.

(27) Debecker, D. P.; Stoyanova, M.; Rodemerck, U.; Gaigneaux, E. M. *J. Mol. Catal. A* **2011**, *340*, 65.

(28) Debecker, D. P.; Bouchmella, K.; Poleunis, C.; Eloy, P.; Bertrand, P.; Gaigneaux, E. M.; Mutin, P. H. *Chem. Mat.* **2009**, *21*, 2817.

(29) Debecker, D. P.; Schimmoeller, B.; Stoyanova, M.; Poleunis, C.; Bertrand, P.; Rodemerck, U.; Gaigneaux, E. M. *J. Catal.* **2011**, *277*, 154.

(30) Radhakrishnan, R.; Reed, C.; Oyama, S. T.; Seman, M.; Kondo, J. N.; Domen, K.; Ohminami, Y.; Asakura, K. *J. Phys.Chem. B* **2001**, *105*, 8519.

(31) Ohler, N.; Bell, A. T. *J. Phys.Chem. B* **2006**, *110*, 2700.

(32) Chempath, S.; Zhang, Y.; Bell, A. T. *J. Phys. Chem. C* **2007**, *111*, 1291.

(33) Thielemann, J. P.; Ressler, T.; Walter, A.; Tzolova-Müller, G.; Hess, C. *Appl. Catal. A* **2011**, *399*, 28.

(34) Handzlik, J.; Ogonowski, J. *J. Phys. Chem. C* **2012**, *116*, 5571.

(35) Amakawa, K.; Sun, L.; Guo, C.; Hävecker, M.; Kube, P.; Wachs, I. E.; Lwin, S.; Frenkel, A. I.; Patlolla, A.; Hermann, K.; Schlögl, R.; Trunschke, A. *Angew. Chem. Int. Ed.* **2013**, *52*, 13553.

(36) Vikulov, K. A.; Elev, I. V.; Shelimov, B. N.; Kazansky, V. B. *Catal. Lett.* **1989**, *2*, 121.

(37) Kazansky, V. B.; Shelimov, B. N.; Vikulov, K. A. In *Studies in Surface Science and Catalysis*; L. Guczi, F. S., P, T., Eds.; Elsevier: 1993; Vol. Volume 75, p 515.

(38) Vikulov, K. A.; Shelimov, B. N.; Kazansky, V. B.; Mol, J. C. *J. Mol. Catal.* **1994**, *90*, 61.

(39) Handzlik, J.; Sautet, P. *J. Phys. Chem. C* **2008**, *112*, 14456.

(40) Handzlik, J.; Sautet, P. *J. Phys. Chem. C* **2010**, *114*, 19406.

(41) Handzlik, J.; Sautet, P. *J. Catal.* **2008**, *256*, 1.

(42) Aritani, H.; Fukuda, O.; Miyaji, A.; Hasegawa, S. *Appl. Surf. Sci.* **2001**, *180*, 261.

(43) Li, X.; Zhang, W.; Liu, S.; Han, X.; Xu, L.; Bao, X. *J. Mol. Catal. A* **2006**, *250*, 94.

(44) Debecker, D. P.; Stoyanova, M.; Colbeau-Justin, F.; Rodemerck, U.; Boissière, C.; Gaigneaux, E. M.; Sanchez, C. *Angew. Chem. Int. Ed.* **2012**, *51*, 2129.

(45) British Petroleum Corporation. Disproportionation catalyst. U.S. Patent US 3485889 A, **1967**.

(46) Fridman, R. A.; Nosakova, S. M.; Liberov, L. G.; Bashkirov, A. N. *B. Acad. Sci. U.S.S.R. Ch.* **1977**, *26*, 614.

(47) Mol, J. C. *J. Mol. Catal.* **1982**, *15*, 35.

(48) Valla, M.; Conley, M. P.; Copéret, C. *Catal. Sci. Technol.* **2015**, *5*, 1438.

(49) Chauvin, Y.; Commereuc, D. *J. Chem. Soc., Chem. Commun.* **1992**, 462.

(50) Turek, A. M.; Wachs, I. E.; DeCanio, E. *J. Phys. Chem.* **1992**, *96*, 5000.

(51) Vuurman, M. A.; Stufkens, D. J.; Oskam, A.; Wachs, I. E. *J. Mol. Catal.* **1992**, *76*, 263.

(52) Schekler-Nahama, F.; Clause, O.; Commereuc, D.; Saussey, J. *Appl. Catal. A* **1998**, *167*, 247.

(53) Lwin, S.; Keturakis, C.; Handzlik, J.; Sautet, P.; Li, Y.; Frenkel, A. I.; Wachs, I. E. *ACS Catal.* **2015**, *5*, 1432.

(54) Danilyuk, A. F.; Kuznetsov, V. L.; Shmachkov, V. A.; Kochubey, D. I.; Chuvilin, A. L.; Yermakov, Y. I. *J. Mol. Catal.* **1988**, *46*, 209.

(55) Salameh, A.; Copéret, C.; Basset, J.-M.; Böhm, V. P. W.; Röper, M. *Adv. Synth. Catal.* **2007**, *349*, 238.

(56) Adam, G. J. A.; Davies, S. G.; Ford, K. A.; Ephritikhine, M.; Todd, P. F.; Green, M. L. H. *J. Mol. Catal.* **1980**, *8*, 15.

(57) Chen, X. Y.; Zhang, X. Y.; Chen, P. *Angew. Chem. Int. Ed.* **2003**, *42*, 3798.

(58) Zhang, X.; Chen, X.; Chen, P. *Organometallics* **2004**, *23*, 3437.

(59) Mol, J. C. *Catal. Today* **1999**, *51*, 289.

(60) Tarasov, A. L.; Shelimov, B. N.; Kazansky, V. B.; Mol, J. C. *J. Mol. Catal. A* **1997**, *115*, 219.

(61) Xiaoding, X.; Mol, J. C. *J. Chem. Soc., Chem. Commun.* **1985**, 631.

(62) Xiaoding, X.; Boelhouwer, C.; Vonk, D.; Benecke, J. I.; Mol, J. C. *J. Mol. Catal.* **1986**, *36*, 47.

(63) Digne, M.; Sautet, P.; Raybaud, P.; Euzen, P.; Toulhoat, H. *J. Catal.* **2002**, *211*, 1.

(64) Krokidis, X.; Raybaud, P.; Gobichon, A. E.; Rebours, B.; Euzen, P.; Toulhoat, H. *J. Phys. Chem. B* **2001**, *105*, 5121.

(65) Digne, M.; Sautet, P.; Raybaud, P.; Euzen, P.; Toulhoat, H. *J. Catal.* **2004**, *226*, 54.

(66) Wischert, R.; Copéret, C.; Delbecq, F.; Sautet, P. *Angew. Chem. Int. Ed.* **2011**, *50*, 3202.

(67) Wischert, R.; Laurent, P.; Copéret, C.; Delbecq, F.; Sautet, P. *J. Am. Chem. Soc.* **2012**, *134*, 14430.

(68) Rascon, F.; Wischert, R.; Coperet, C. *Chem. Sci.* **2011**, *2*, 1449.

(69) Joubert, J.; Salameh, A.; Krakoviack, V.; Delbecq, F.; Sautet, P.; Copéret, C.; Basset, J. M. *J. Phys.Chem. B* **2006**, *110*, 23944.

(70) Gabrienko, A. A.; Arzumanov, S. S.; Toktarev, A. V.; Stepanov, A. G. *J. Phys. Chem. C* **2012**, *116*, 21430.

(71) Conley, M. P.; Rossini, A. J.; Comas-Vives, A.; Valla, M.; Casano, G.; Ouari, O.; Tordo, P.; Lesage, A.; Emsley, L.; Copéret, C. *Phys. Chem. Chem. Phys.* **2014**, *16*, 17822.

(72) Copéret, C.; Comas-Vives, A.; Conley, M. P.; Estes, D.; Ninez-Zarur, F.; Fedorov, A.; Mougel, V.; Nagae, H.; Zhizhko, P. *Chem. Rev.* **2015**, DOI:10.1021/acs.chemrev.5b00373.

(73) Lefort, L.; Chabanas, M.; Maury, O.; Meunier, D.; Copéret, C.; Thivolle-Cazat, J.; Basset, J.-M. *J. Organomet. Chem.* **2000**, *593–594*, 96.

(74) Chabanas, M.; Baudouin, A.; Copéret, C.; Basset, J.-M. *J. Am. Chem. Soc.* **2001**, *123*, 2062.

(75) Chabanas, M.; Copéret, C.; Basset, J.-M. *Chem. –Eur. J.* **2003**, *9*, 971.

(76) Blanc, F.; Chabanas, M.; Copéret, C.; Fenet, B.; Herdweck, E. *J. Organomet. Chem.* **2005**, *690*, 5014.

(77) Rhers, B.; Quadrelli, E. A.; Baudouin, A.; Taoufik, M.; Copéret, C.; Lefebvre, F.; Basset, J.-M.; Fenet, B.; Sinha, A.; Schrock, R. R. *J. Organomet. Chem.* **2006**, *691*, 5448.

(78) Rhers, B.; Salameh, A.; Baudouin, A.; Quadrelli, E. A.; Taoufik, M.; Copéret, C.; Lefebvre, F.; Basset, J.-M.; Solans-Monfort, X.; Eisenstein, O.; Lukens, W. W.; Lopez, L. P. H.; Sinha, A.; Schrock, R. R. *Organometallics* **2006**, *25*, 3554.

(79) Blanc, F.; Thivolle-Cazat, J.; Basset, J.-M.; Copéret, C.; Hock, A. S.; Tonzetich, Z. J.; Schrock, R. R. *J. Am. Chem. Soc.* **2007**, *129*, 1044.

(80) Blanc, F.; Berthoud, R.; Salameh, A.; Basset, J.-M.; Copéret, C.; Singh, R.; Schrock, R. R. *J. Am. Chem. Soc.* **2007**, *129*, 8434.

(81) Blanc, F.; Rendon, N.; Berthoud, R.; Basset, J.-M.; Copéret, C.; Tonzetich, Z. J.; Schrock, R. R. *Dalton Trans.* **2008**, 3156.

(82) Rendón, N.; Berthoud, R.; Blanc, F.; Gajan, D.; Maishal, T.; Basset, J.-M.; Copéret, C.; Lesage, A.; Emsley, L.; Marinescu, S. C.; Singh, R.; Schrock, R. R. *Chem. –Eur. J.* **2009**, *15*, 5083.

(83) Gajan, D.; Rendon, N.; Wampler, K. M.; Jean-Marie, B.; Copéret, C.; Lesage, A.; Emsley, L.; Schrock, R. R. *Dalton Trans.* **2010**, *39*, 8547.

(84) Mazoyer, E.; Merle, N.; Mallmann, A. d.; Basset, J.-M.; Berrier, E.; Delevoye, L.; Paul, J.-F.; Nicholas, C. P.; Gauvin, R. M.; Taoufik, M. *Chem. Commun.* **2010**, *46*, 8944.

(85) Conley, M. P.; Mougel, V.; Peryshkov, D. V.; Forrest, W. P.; Gajan, D.; Lesage, A.; Emsley, L.; Copéret, C.; Schrock, R. R. *J. Am. Chem. Soc.* **2013**, *135*, 19068.

(86) Conley, M. P.; Forrest, W. P.; Mougel, V.; Copéret, C.; Schrock, R. R. *Angew. Chem. Int. Ed.* **2014**, *126*, 14445.

(87) Mougel, V.; Pucino, M.; Copéret, C. *Organometallics* **2015**, *34*, 551.

(88) Valla, M.; Stadler, D.; Mougel, V.; Copéret, C. *Angew. Chem. Int. Ed.* **2015**, DOI:10.1002/anie.201509390.

(89) Le Roux, E.; Taoufik, M.; Copéret, C.; de Mallmann, A.; Thivolle-Cazat, J.; Basset, J. M.; Maunders, B. M.; Sunley, G. J. *Angew. Chem. Int. Ed.* **2005**, *44*, 6755.

(90) Popoff, N.; Macqueron, B.; Sayhoun, W.; Espinas, J.; Pelletier, J.; Boyron, O.; Boisson, C.; Merle, N.; Szeto, K. C.; Gauvin, R. M.; De Mallmann, A.; Taoufik, M. *European Journal of Inorganic Chemistry* **2014**, *2014*, 888.

(91) Solans-Monfort, X.; Clot, E.; Copéret, C.; Eisenstein, O. *Organometallics* **2005**, *24*, 1586.

(92) Peryshkov, D. V.; Schrock, R. R. *Organometallics* **2012**, *31*, 7278.

(93) Moses, A. W.; Raab, C.; Nelson, R. C.; Leifeste, H. D.; Ramsahye, N. A.; Chattopadhyay, S.; Eckert, J.; Chmelka, B. F.; Scott, S. L. *J. Am. Chem. Soc.* **2007**, *129*, 8912.

(94) Herrmann, W. A.; Wagner, W.; Flessner, U.; Volkhardt, U.; Komber, H. *Angew. Chem. Int. Ed.* **1991**, *103*, 1704.

(95) Rost, A. M. J.; Schneider, H.; Zoller, J. P.; Herrmann, W. A.; Kuhn, F. E. *J. Organomet. Chem.* **2005**, *690*, 4712.

(96) Salameh, A.; Joubert, J.; Baudouin, A.; Lukens, W.; Delbecq, F.; Sautet, P.; Basset, J. M.; Copéret, C. *Angew. Chem. Int. Ed.* **2007**, *46*, 3870.

(97) Salameh, A.; Baudouin, A.; Basset, J. M.; Copéret, C. *Angew. Chem. Int. Ed.* **2008**, *47*, 2117.

(98) Salameh, A.; Baudouin, A.; Soulivong, D.; Boehm, V.; Roeper, M.; Basset, J.-M.; Copéret, C. *J. Catal.* **2008**, *253*, 180.

(99) Lesage, A.; Lelli, M.; Gajan, D.; Caporini, M. A.; Vitzthum, V.; Miéville, P.; Alauzun, J.; Roussey, A.; Thieuleux, C.; Mehdi, A.; Bodenhausen, G.; Copéret, C.; Emsley, L. *J. Am. Chem. Soc.* **2010**, *132*, 15459.

Chapter 2: Probing the Reactivity of the Alumina Surface with dimethyl ether and ethylene.

2.1 Individual Contributions.

For the part with dimethylether on Al_2O_3 (Section **2.2**, **2.3** and **2.5**): reprinted with permission from:Comas-Vives, A.[†], Valla, M[†], Copéret, C and Sautet, P, *ACS Cent. Sci.*, **2015**, 1, 313.

[†]: Theses authors contributed equally to the work.

Copyright 2015 American Chemical society.

All experimental experiments were carried out by M. Valla and all the calculations were carried out by A. Comas-Vives. All authors contributed to the scientific discussion and the manuscript.

For the part on ethylene (section **2.4**), both experiments and calculations where carried out by M. Valla.

2.2 Introduction.

It is known that pure metal oxides such as alumina can catalyze a broad range of reactions. For example, they are known to be catalytically active in olefin isomerization,[1-3] alcohol dehydration yielding ether or olefins,[4,5] or alkane hydrogenation/isomerization[6,7]. As discussed in **chapter 1**, alumina can in fact activate the C-H bond of methane, dissociate H_2 or coordinate N_2.[8-10] Alumina also reacts with propene to generate surface alkoxide and allyl species,[11], but also with CH_3F yielding olefins.[12] In view of the importance of alumina in Re-based olefin metathesis catalysts and the aforementioned reactivity, this chapter will examine the reaction of alumina towards dimethylether used as a probe molecular (Section **2.3**) and ethylene (Section **2.4**).

2.3 Cooperativity Between Al-sites Promotes H-Transfer and Carbon-Carbon Bond Formation Upon Dimethylether Activation on Al_2O_3.

Forming carbon-carbon bonds from C_1 oxygenated species, which are able to form surface alkoxy species, has been a longstanding scientific and industrial challenge.[13-25] An industrial breakthrough stem from the discovery of the methanol to olefin (MTO) process in the 70's, which allowed the catalytic conversion by zeolites of methanol to olefins such as ethylene and propylene (Scheme 2.1). This process constitutes an alternative route to light alkenes not relying on crude oil / coal. Several industrial plants are being opened, in particular in Asia, in view of the increasing demand in alkene feedstocks.[26]

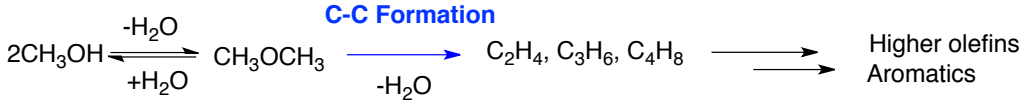

Scheme 2. 1. Methanol to Olefin process catalyzed by zeolites.

The mechanism of this process has been subject of intense debates and investigations both in industry and academia.[27-39] Initially, direct pathways from methanol to olefin were suggested (Scheme 2.2b-e), but in the 90's Dahl and Kolboe proposed an indirect pathway that proceeds via a hydrocarbon pool.[40-42] A dual operating cycle, one for alkenes (Scheme 2.2a left) and another one for aromatics (Scheme 2.2a right) forms the currently accepted mechanism operating under industrial MTO conditions. Carbenium species have been proposed as the active species of the hydrocarbon pool cycle, and a complete catalytic cycle combining theory and experiment was proposed for the HZSM-5 zeolite.[29,43]

Nevertheless, the question related to the site and mechanism of formation of the first olefins and aromatics, requiring carbon-carbon bond forming processes from methanol/dimethylether, has remained a matter of debate. More than 20 mechanisms have been proposed for this step,[14] involving intermediates such as methane–formaldehyde,[18] oxonium ylide, [22] carbenoid or alkoxy species (Scheme 2.2b-e), some proposals also include the presence of adventitious organic compounds such as aromatics.

Extensive attention was devoted to the oxonium ylide mechanism (Scheme 2.2c), which by an intramolecular Steven's rearrangement would produce

methylethylether, which could then form ethene by β-hydride elimination. This mechanism and parent ones were discarded because of the need of formation of highly unstable oxonium ylide species.[17,44]

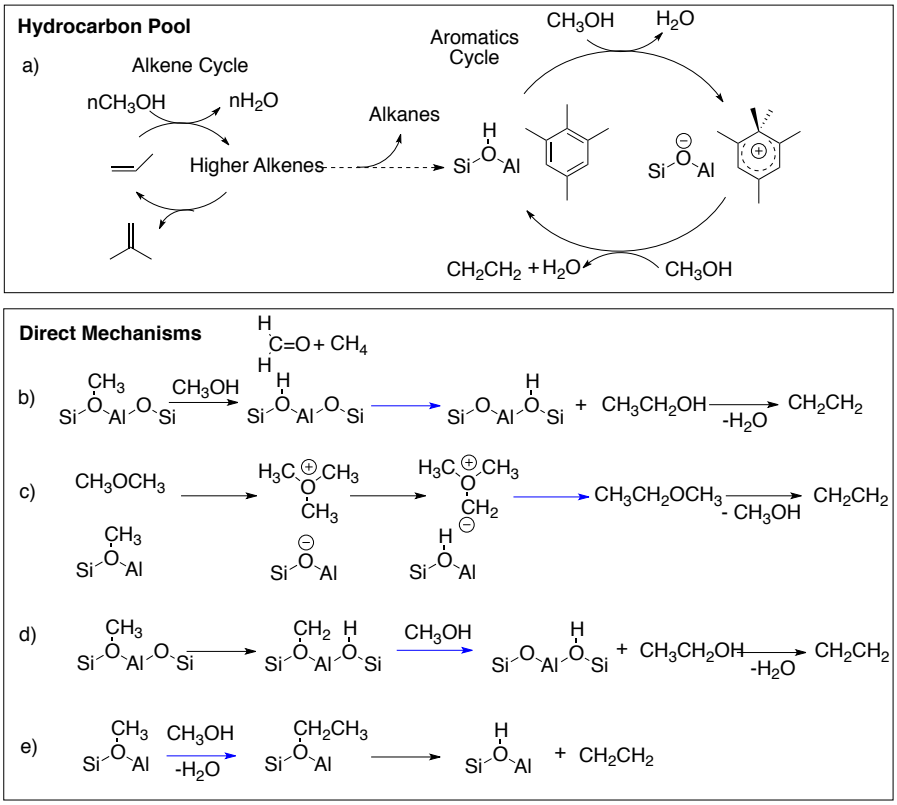

Scheme 2. 2. A selection out of the more than 20 proposed mechanisms for the carbon-carbon bond formation step is shown: a) hydrocarbon pool, b) methane-formaldehyde route, c) oxonium-ylide, d) carbine-carbenoid mechanisms, e) alkoxy mechanism.

Other direct C-C bond formation routes, via methane-formaldehyde (Scheme 2.2b) or carbenoid species (Scheme 2.2d) were found unfavorable on the basis of an extensive *ab initio* study.[20] It is worth noting that all the zeolites active in the MTO process contain Al sites. This element provides acidic sites that play a significant role in the zeolite catalytic activity, and they could participate to the initial carbon-carbon bond formation step. Moreover, there is always a debate whether or not extraframework aluminum, which has been proposed to be alumina, could be responsible for side-reactions in zeolite catalysis.[45,46] Hence, one important aspect that has not been considered is the participation of multiple Al centers, possibly belonging to alumina, in the promotion of carbon-carbon bonds in the MTO process. Indeed, γ-Al_2O_3 and δ-Al_2O_3 contains on their 110 facet[8] highly reactive tri-coordinated Al_{III} and four-coordinated Al_{IVb} sites, which are able to activate the C-H bond of methane at

low temperatures (< 150 °C)[8,9] and to convert CH_3F into branched olefinic products, isobutene and 2-methylbutene at relatively mild temperature, ca. 200 °C, showing that the key carbon-carbon formation step occurs on alumina surfaces via the growth of surface alkoxy chains.[12] In such process, adsorbed water play a key role to facilitate the activation of hydrocarbons, through the formation of basic O sites and the stabilization of the otherwise unstable 110 facet.[10]

Here we show that alumina converts dimethylether (DME) at 300 °C into methane along with smaller amounts of higher olefin products, such as ethene, propene, butenes and pentenes, analogously to what is observed in the MTO process. In addition, combined IR and solid-state NMR show that this process is accompanied by the formation of methoxy and formate surface species besides methane and other hydrocarbons detected in the gas phase. *Ab initio* simulations point to a key step involving a hydride transfer between a methoxy aluminum surface species and an activated DME, adsorbed on adjacent Al sites. This process involves a transition state structure with oxonium($AlO=CH_2^+$)/methane adduct, which evolves either to the formation of methane and adsorbed formate species or olefins through a carbon-carbon bond forming process, consistent with experimental observation. This indicates that two Al sites can play in concert to generate $AlO=CH_2^+$ species as key transient species, able to active C-H bonds and to promote a C-C bond formation step.

2.3.1 Experimental Results: Dimethylether Contacted with Al_2O_3.

First, the reaction of DME (0.05 mmol) with alumina (Evonik aluC, 130 $m^2.g^{-1}$ or SBA, 200 $m^2.g^{-1}$) partially dehydroxylated at 700°C was monitored by gas chromatography as a function of temperature (Table 2.1a and Table A.2.1). Starting at 300°C, methane evolved (0.029 mmol as sole gaseous product) corresponding to 2.7 CH_4 molecules per nm^2.

Note that above 300°C the dimethyl ether undergoes a homolytic cleavage of the CH_3OCH_3 bond triggered by the surface leaving two radicals in the gas phase which can react with the alumina surface. For this reason, the system will not be studied above 300 °C. Treatment of the solids under high vacuum (10^{-5} mBar) at 100 °C led to desorption of ethene, propene, butenes and pentenes as major products along with traces of hexenes according to GC and GC/MS (Table 2.1b). In contrast, no DME conversion was observed under the same reaction conditions in the absence of

alumina, indicating that alumina is critical to promote the formation of these hydrocarbon products from DME.

Table 1 a) Composition of the gas phase during the reaction of dimethylether with AluC dehydroxylated at 700 °C. (Similar Data are found for γ-Al_2O_3 (SBA), Table A.2.1)

Al_2O_3 with dimethylether	Composition of the gas phase	
Temperature	CH_3OCH_3	CH_4
Room temperature	100 %	0 %
100 °C	100 %	0%
200 ° C	100 %	0 %
300 °C	42 %	58 %[a]

b) Desorption of the surface (molecules/nm^2)

Hydrocarbon removed from the surface	Molecules per nm^2
Ethylene	$3.1x10^{-2}$
Propylene	$1.6x10^{-2}$
Z-2-butene	$0.3x10^{-2}$
E-2-butene	$0.7x10^{-2}$
Isobutene	$0.2x10^{-2}$
Pentene	$1.0x10^{-2}$

To further understand the reaction, an *in-situ* IR study was carried out. Figure 2.1a-d shows a series of IR spectra taken at different stages of the reaction (Full IR spectrum are available in Figure A.2.1 in the appendix). Addition of DME at room temperature to Al_2O_3 (40 mBar, 4.6 molecules of DME per nm^2) led to the decrease of the intensity of the alumina OH bands at 3840 and 3600 cm^{-1} (Figure 2.1a-b). It also showed the presence of CH_3 and CH_2 groups, C-O bond as well as few Csp_2-H species (tentatively attributed from the presence of a peak at 3040 cm^{-1}). At 200°C two new peaks in the region of hydroxyl appeared (3570 cm^{-1} and 3675 cm^{-1}) and the C-O band (1157 cm^{-1}) disappeared, consistent with the cleavage of that bond (Figure 2.1c). At 300°C, the intensity of the ν(C-H) vibration decreased while the intensity of the OH band increased (Figure 2.1d). This was accompanied by the formation of methane in the gas phase and the appearance of two new peaks of strong intensity at 1578 cm^{-1} and 1321 cm^{-1}, tentatively assigned, respectively, to the vibration of the C=O double bond and C-O bond of surface formate species (the same study is available for the pure γ-Al_2O_3 Figure A.2.2).[47] In fact, adsorption of methylformate on Al_2O_3 leads to the appearance of the same bands, but also an additional band at 1683 associated with the carbonyl of physisorbed methyl formate (see Figure A.2.3 in the appendix).

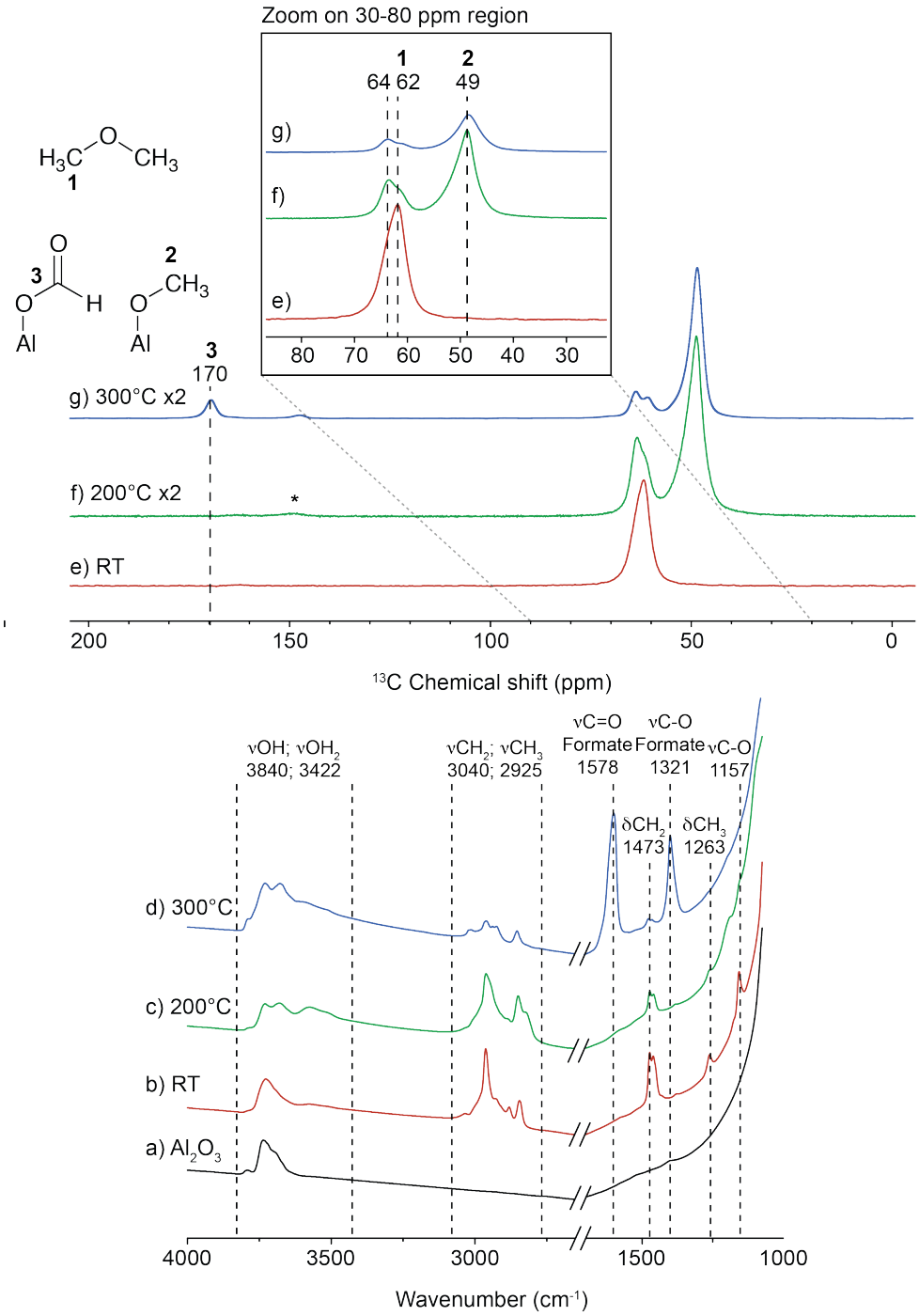

Figure 2. 1. On the bottom: *in-situ* FT-IR Transmission spectra of (a) Al_2O_3 dehydroxylated at 700°C, then reacted with dimethyl ether at room temperature (b), at 200°C (c) and 300°C (d). All the spectra were recorded with the gas phase condensed at -190°C. in-situ IR was used to determine the main changes of the surface species upon heating. We evidenced the activation of the C-O bond of DME as well as the formation of new surface species including formate. The same IR study can be found in Figure A.2.2 for pure γ-Al_2O_3. On the top: ^{1}H-^{13}C CPMAS NMR, 400 MHz NMR spectrometer, spinning rate of 10 kHz. Spectrum of Al_2O_3 reacted with 2-^{13}C-$(CH_3)_2O$ (e) at room temperature, number of scans was set to 5k; (f) at 200°C, number of scans was set to 100k; and (g) at 300°C, number of scans was set to 50k. The recycling delay was set to 1 sec of all the spectra. The radio frequency field for ^{1}H excitation was set to 100 kHz.

Overall, these IR data suggest that carbon-carbon forming and carbon-oxygen cleavage reactions took place on the Al_2O_3 surfaces upon reaction with DME, while methane and formate species are formed.

The reaction was also monitored by solid-state NMR using ^{13}C di-labeled DME. The insets e-g of Figure 2.1 show the ^{13}C Cross Polarization Magic Angle spinning NMR (CP-MAS) spectra obtained on $Al_2O_{3-(700)}$ after reaction with DME at three different temperatures: 25 °C, 200°C and 300°C. At low temperature, only one peak was observed at 62 ppm (Figure 2.1e), which is assigned to adsorbed DME. At higher temperatures, the intensity of the peak at 62 ppm decreased, while a new peak progressively appeared at 49 ppm, reaching a maximum of intensity at 200 °C (Figure 2.1f). This peak is assigned to surface methoxy species. In addition, a shoulder appeared at higher field for the peak at 64 ppm, which could be assigned to the adsorption of DME molecule on different Al sites. At 300°C, these three signals are easily distinguishable (Figure 2.1g), and a new peak appears at 169 ppm, consistent with adsorbed formate species with methyl groups at 49 ppm overlapping with the methanol peak.

Adsorption of methyl formate on γ-$Al_2O_{3-(700)}$ leads to the same NMR signal consistent with its attribution to formate surface species (see Figure A.2.4 in the appendix) as previously discussed from the IR data. These assignments were confirmed by recording 2-Dimensional solid-state NMR: the ^{1}H-^{13}C HETCOR (Heteronuclear Correlation) of the Al_2O_3 sample reacted with 2-^{13}C-$(CH_3)_2O$ at 200°C and 300 °C (see Figure A.2.5 in the appendix) showed correlation of the carbon peak at 169 ppm with a proton at 9.2 ppm consistent with the proton of a formate species. The correlation with the OCH_3 group suggests that the formate species are in close proximity to methoxy species. No direct detection of hydrocarbons could be observed, suggesting that they are present in small amounts or remain adsorbed as minor alkoxy surface species.

2.3.2 Calculation Study on the First C-C Bond Formation When Dimethylether is Contacted with Al_2O_3.

The formation of methane, higher hydrocarbons, methoxy and formate species was investigated by means of DFT periodic calculations. We used the 110 termination of γ-Al_2O_3 because it is the most abundant one for γ-Al_2O_3 (75%) and δ-Al_2O_3 (one of

the component of our sample AluC) particles. In addition, this surface when completely dehydrated contains the most reactive sites (strong Lewis acid sites, see Figure A.2.6).[48-50] Considering first the fully dehydrated alumina surface model (**s0** surface) the adsorption (coordination) of CH_3OCH_3 on the most acidic Al_{III} forms the species **0-III** with an internal energy gain of 131 kJ.mol^{-1}. This adsorbed species can further react through the activation of either the C-H or the C-O bonds of CH_3OCH_3. The C-O activation route with the transfer of the methoxy on the bare alumina surface is associated with a high-energy barrier equal to 179 kJ.mol^{-1} and is endothermic by 16 kJ.mol^{-1}. On the more realistic monohydrated surfaces, the initial C-O activation step is lowered by more than 50 kJ.mol^{-1} (vide infra). The alternative C-H bond activation pathway presents overall higher energy barriers and would also lead to the formation of unlikely Al-alkyl intermediates in the presence of proton sources (Figure A.2.7 and Scheme A.2.1). Therefore only the results for the C-O activation pathway will be discussed thereafter. In a previous study, we did an extensive analysis of the possible adsorption sites of water on the 110 termination of the γ-Al_2O_3 surface. Depending on the initial adsorption site of water in the unit cell, corresponding to an OH coverage equal to 3.0 OH/nm^2, analogous energy profiles can be obtained for the ethylene formation route (Figure A.2.8). Here, we will discuss ethylene formation from the most stable and probable **s1a** surface, in which one OH group coordinates to Al_{III} and one proton is bonded to the O_{2a} center, since the minima and the transition-states of the corresponding energy profile present the lowest energies of all the different surfaces evaluated with water initially adsorbed. From the **s1a** surface, the coordination of dimethylether to the Al_{IVb} center yields a binding energy equal to 118 kJ.mol^{-1} (**s1a-IVb** species in Figure 2.2a). In this case, the coordinated OH eases the CH_3 migration of the dimethylether to produce the **CO-1** intermediate, via a barrier of 127 kJ.mol^{-1} (hence significantly lower than for the non-water asssisted process) and a reaction step endoenergetic by 31 kJ.mol^{-1}. The results here presented show that water assist the dimethylether/methanol conversion as already proposed for acidic zeolites.[51,52]

Overall, the participation of (Frustated) Lewis acid-base pairs,[53] involving the acidic Al_{III} and Al_{IVb} centers and the basic oxygen atoms of both dimethylether molecule and the OH group coordinated to such centers act in a synergistic way providing a low energy pathway for the activation of dimethylether through the

energy favorable C-O bond cleavage. After this step, the participation of two Al acid sites allows the previously transferred methyl group to abstract a hydride from the remaining methoxy group coordinated to Al_{IVb}, generating methane and a Al–O=CH_2 species with the O bound to Al_{IVb} (**CO-2a** species in Figure 2.2).

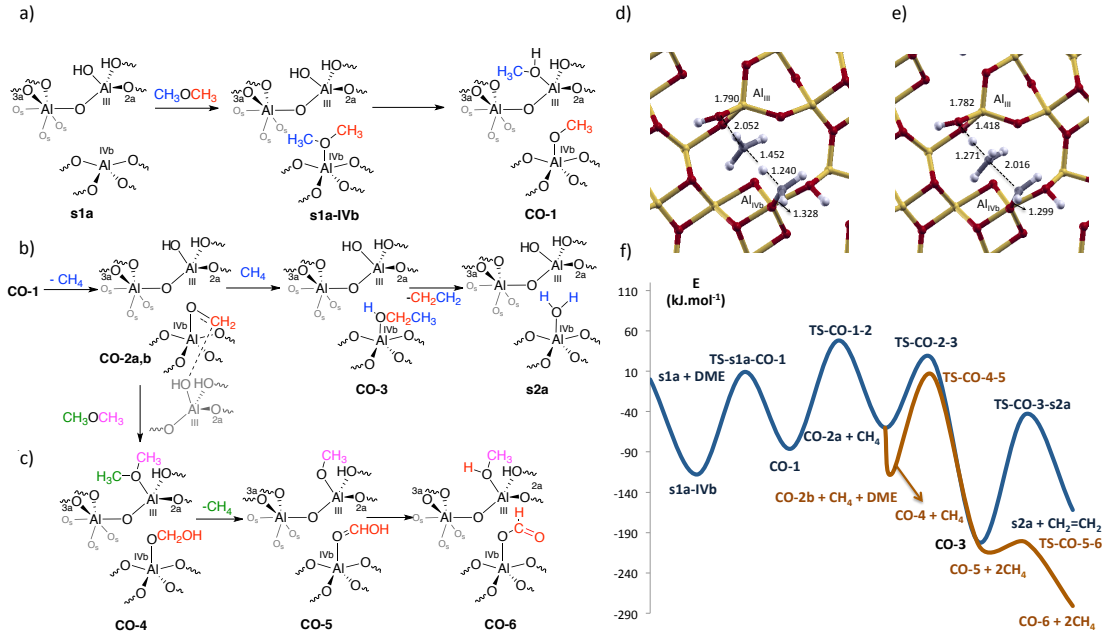

Figure 2. 2. a) C-OCH_3 activation process assisted by an OH group of the CH_3OCH_3 molecule on γ-Al_2O_3. b) Formation of methane and oxonium, carbon-carbon bond formation step (from CO-1 to CO-3) and subsequent ethylene formation along with s2a surface c) Formate route from the CO-2 species. d) Transition state structures corresponding to the formation of methane and oxonium (TS-CO-1-2) and e) carbon-carbon bond formation steps (TS-CO-2-3). f) Electronic energy profiles (in kJ.mol^{-1}) for the ethylene and formate formation. The energies are referred to two CH_3OCH_3 and the γ-Al_2O_3 surface. For the ethylene route (dark blue) the second DME molecule is not depicted since it does not participate in the reaction. The formate route is depicted in brown.

In **CO2a** the –O=CH_2 species is not interacting with the OH group of Al_{III} while it is in **CO2b**. In the corresponding transition-state (Figure 2.2d), a Al-O=CH_2^+ oxonium group is being formed along with methane. The former group is characterized by a C=O distance equal to 1.328 Å at the transition-state while the newly formed C-H bond has a distance equal to 1.452 Å and the one being broken equal to 1.240 Å (see Figure 2.2d). This step has an energy barrier equal to 134 kJ.mol^{-1} in a process endothermic by 26 kJ.mol^{-1} when reaching **CO2a**. CH_4 can be released or subsequently undergo a C-H bond activation by the Al-O=CH_2^+ oxonium group leading to the formation of ethanol coordinated to Al_{IVb} (**CO-3** in Figure 2.2b). This carbon-carbon bond forming step is exoenergetic by 146 kJ.mol^{-1} and has an energy barrier of 86 kJ.mol^{-1}. The corresponding transition-state for the carbon-carbon

bond formation step is shown as inset in Figure 2.2e, in which the incoming carbon-carbon bond has a distance at the transition-state equal to 2.016 Å. Due to the structural similarity between **TS-CO-12** and **TS-CO-23** structures (corresponding to Figures 2.2d and e, respectively), there is also the possibitly that from the **TS-CO-12** structure a slight rotation of the methane molecule could lead directly to the **TS-CO-23** structure. Finally, the formation of ethene (from the dehydration of the ethanol group in **CO-3** giving the hydrated termination **s2a** of the alumina surface in Figure 2.2b) has an energy barrier equal to 159 kJ.mol^{-1} in a process endothermic by 40 kJ.mol^{-1}. The formed water remains adsorbed on the Al_{IVb} center. Alcohol dehydration on γ-Al_2O_3 has been addressed previously both experimentally and using DFT calculations on both 110 and 100 terminations.[4,54-59] While the 100 facet is more active than the 110 one towards alcohol dehydration, both facets can allow this reaction, and the 110 facet exposes unsaturated Al_{III} and Al_{IVb} sites, which are significantly more reactive towards C-H activation and able to allow for the carbon-carbon bond formation from CH_3F to yield isobutene formation, in contrast to the Al sites present in the 100 surface. From the **CO-2** intermediate, in the advent where the formed methane departs, an alternative route can lead to the formation of the formate species. The OH group present in Al_{III} can interact with the Al-O=CH_2^+ group in the Al_{IVb} via an interaction favorable by 57 kJ.mol^{-1} (**CO-2b**) Subsequently, the OH group can decoordinate from the Al_{III} site and a new dimethylether molecule can coordinate to this Al center in a practically isoenergetic reaction (**CO-4** from Figure 2.2c). In a subsequent step a hydrogen is transferred from the CH_2 group of the Al_{IVb}-OCH_2-OH species to the dimethylether molecule coordinated to Al_{III} in a process similar to that from **CO-1** to **CO-2a**. This step releases methane, while a O=CHOH group remains bonded a Al_{IVb} and a OCH_3 group to Al_{III} (**CO-5** species in Figure 2.2c). This step is exoenergetic (– 95 kJ.mol^{-1}) and associated with an energy barrier equal to 115 kJ.mol^{-1}. Finally, the proton of the OH group can be transferred from the Al_{IVb}-OCHOH species to the Al_{III}-OCH_3 species via a very low energy barrier equal to 4 kJ.mol^{-1} in a process exoergic by 76 kJ.mol^{-1}. Overall, the formation of formate and methanol adsorbed on the surface (**CO-6** species in Figure 2.2c) and two methane molecules is globally exoenergetic by 281 kJ.mol^{-1} with respect to initial reactants (Al_2O_3 and two dimethylether molecules), in agreement with the experimental observations. This route competes with ethylene formation in view of its similar

energy barrier and more favorable thermodynamics. The whole energy profile for the formation of the ethylene from one dimethylether molecule is shown in Figure 2.2f. In this energy profile, the energy barriers present values equal to 127-143 kJ.mol^{-1}, except the elimination step which produces ethylene, which is slightly higher: 159 kJ.mol^{-1}. All these barriers are accessible at 300 °C. From the partially hydrated alumina surface **s1a** and DME, the formation of ethylene and of the more hydrated alumina **s2a** surface is exothermic by 162 kJ.mol^{-1}. From this **s2a** surface**,** the water adsorbed on the Al_{IVb} site can be exchanged by an incoming dimethylether molecule regenerating the **s1a-IVb** species in an step endothermic by 44 kJ.mol^{-1} The formate route is very favored thermodynamically, being exothermic by more than 281 kJ.mol^{-1} with respect to initial reactants, in agreement with the experimental observation of formate on the γ-Al_2O_3 surface. The formate route is kinetically favored without considering entropic contributions, since at the branching point in the energy profile, the barrier is lower by 28 kJ.mol^{-1}.

Overall, the formation of ethylene and water from dimethyl ether is endergonic by 20 kJ.mol^{-1} while when including entropic contributions the reaction is exergonic by 85 kJ.mol^{-1}. In Gibbs free energy (Figure A.2.9), the formate route is slightly more demanding than the ethylene route by 16 kJ.mol^{-1}. The energy barriers for both ethylene and formate routes are higher due to the stabilization of the gas phase species. By including the entropic terms the formation of ethylene and the **s2a** surface is exergonic by 146 kJ.mol^{-1} while the formate route leading to **CO-6** and 2 CH_4 molecules is exergonic by 209 kJ.mol^{-1} (104 kJ.mol^{-1} per DME molecule).

2.4 Reactivity of Al_2O_3 towards ethylene.

It was previously shown that γ-alumina activated the C-H bond activation of CH_4 on the surface Al_{III} sites, the so-called defect site of alumina.[8-10,60] Gabrienko and co-workers have shown that alumina can also activate the C-H bond of propene to form π-allyl surface complexes along with surface propoxy species.[11] In view of the difference of reactivity between ethylene and propene towards Re_2O_7/Al_2O_3, this section is devoted to the investigation of the reactivity of alumina towards using a combined use of IR/NMR spectroscopy and DFT calculations.

2.4.1 *Experimental Results: Reaction Between Ethylene and Al_2O_3 Dehydroxylated at 700°C.*

Previous studies have shown that the highest concentration of alumina defect sites (Al_{III}) is reached at a dehydroxylation temperature of 700 °C for γ-alumina, $Al_2O_{3\text{-}700}$. Therefore, $Al_2O_{3\text{-}700}$ was contacted with ethylene ($7.7x10^{-3}$ mmol.m^{-2}), and the gas phase was analyzed over time. After 6 h at 25 °C, ethylene was the only gaseous product detected by gas chromatography. The reaction was also monitored by infrared spectroscopy (Figure 2.3), which revealed the presence of surface C-H containing species as evidenced by the appearance of bands corresponding to ν(Csp^3-H) (3000 to 2800 cm^{-1}) and ν(Csp^2-H) (3000 and 3100 cm^{-1}). Figure 2.3 shows that all the C-H bands increase in intensity, which is consistent with the increase of more hydrocarbyl surface species with time. Concerning the OH region, after 6 hours of reaction a broad band at 3600 cm^{-1} can also be observed; it can be assigned to OH groups in interaction with surface species or displacement and redistribution of water on the alumina surface.

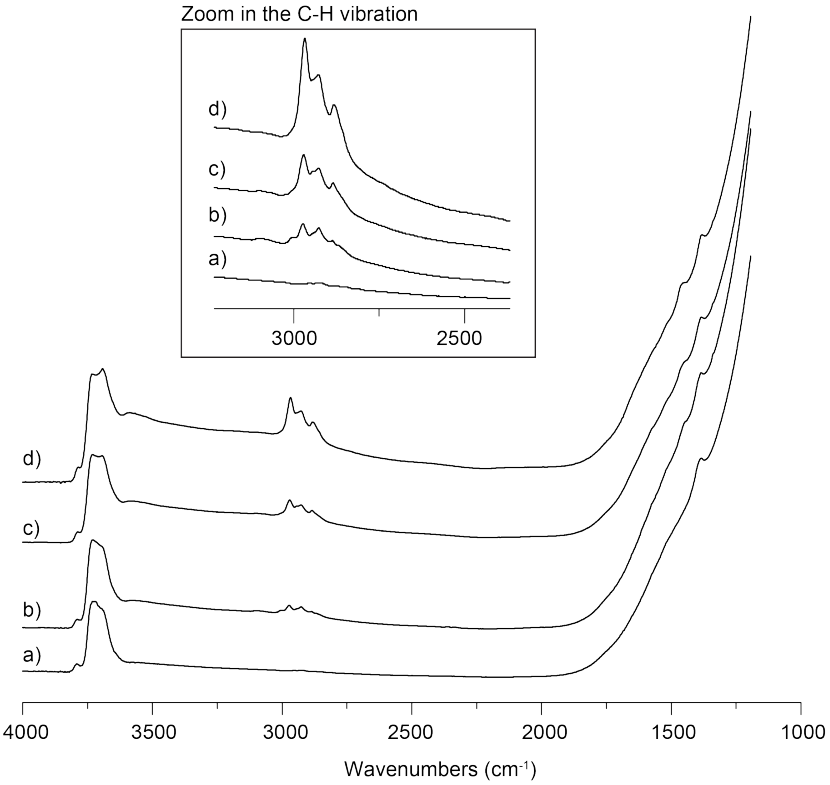

Figure 2. 3. In-situ FT-IR. a) pure alumina, b) 1 hour, c) 3 hours and d) 6 hours reaction of ethylene contacted with alumina at room temperature.

In order to identify the surface species, the solid was further treated under high vacuum treatment (10^{-5} mbar) at 25°C, contacted with degassed water at the same

temperature, and the gas phase was the analyzed by GC-MS. It showed the presence of ethene, butenes ((*Z*)-but-2-ene, but-1-ene and (*E*)-but-1-ene) and traces of hexenes (hex-1-ene and (*E*)-3-methylpent-2-ene) as shown in Table 2.1. These data show that oligomers are formed during the contact of ethylene with alumina at 25 °C.

Table 2. 1. Ratio of olefins produce on the alumina surface with ethane and the amount of desorbed molecules per surface unit.

Olefins	Ratio (in %)	Desorbed molecule per nm^2 of Al_2O_3
ethene	36%	22×10^{-3}
(*E*)-but-2-ene	24%	7.3×10^{-3}
but-1-ene	3%	1.0×10^{-3}
(*Z*)-but-1-ene	37%	12×10^{-3}
hex-1-ene	<1%	-[a]
(*E*)-3-methylpent-2-ene	<1%	-[a]

[a]: the number of molecules could not be calculated for these olefins due to a too low amount.

The most abundant compound is ethylene, which likely arises from strongly adsorbed ethylene or the hydrolysis of Al-(vinyl) surface species, generated by the C-H bond activation of ethylene on Al,O sites, similarly to what was observed with methane.[10] Higher hydrocarbons are also detected, in particular butenes and even hexenes, which result from the oligomerization of ethylene. It is however not clear whether these compounds are the result of Brønsted acid catalysis or the insertion of ethylene in surface Al-R species. The total amount of ethylene (0.022 molecule.nm^{-2}) and higher hydrocarbons (0.020 molecule.nm^2) correspond to 0.042 per nm^2, which is close to the amount of defect sites as evaluated by reaction with methane on $Al_2O_{3\text{-}700}$ at 150 °C (0.035 Al-CH_3.nm^{-2}).[10]

To further understand the reaction of ethylene and alumina, and the nature of the associated surface species, two types of NMR experiments were performed: an *ex-situ* experiment, consisting of contacting alumina with ^{13}C labeled ethylene, followed by evacuation of the gas phase under high vacuum (10^{-5} mBar) prior to recording an NMR spectrum, and an *in-situ* experiment, where the ^{13}C labeled ethylene and the alumina are sealed into a glass insert for NMR measurements. The carbon-13 solid-state cross polarization magic angle spinning (CP-MAS) NMR spectrum of the *ex-situ* experiment shows 5 major peaks at 13, 20, 31, 136 and 146 ppm. The peaks between 13 and 31 ppm can be assigned to the alkyl fragments of ethylene oligomers, which is consistent with what was observed upon titration of the surface species and the IR data. The two major peaks at 146 and 136 ppm are consistent with sp^2 carbons, which

can be tentatively assigned to vinyl surface species or strongly absorbed ethylene at the surface of alumina.[11] The carbon-13 solid-state CP-MAS NMR spectrum of the *in-situ* experiment (Figure 2.4) show a broad feature at 20-60 ppm, and two intense peaks at 138 and 162 ppm, consistent with downfield shifted sp^2 carbons. While the former was already observed previously, the latter appears in the presence of ethylene in the gas phase ; it can therefore be tentatively assigned to a π–olefin complex.[11] No peak associated with surface ethoxide (expected at 70-50 ppm) can be observed, in sharp contrast with what has been observed upon reaction of propene with alumina.[11]

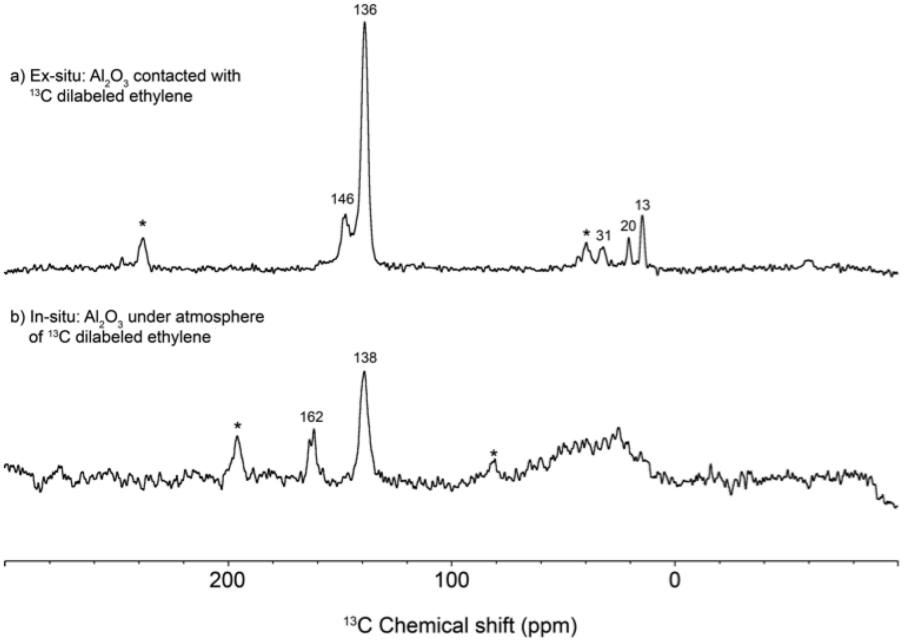

Figure 2. 4. ^{13}C CPMAS NMR. a) *Ex-situ* experiment of Al_2O_3 (700°C) contacted with ^{13}C-dilabeled ethylene for one hour and then removed under vacuum, 60k scans, 400 MHz. b) *In-situ* experiment of Al_2O_3 (700°C) sealed under pressure of ^{13}C-dilabeled in an glass insert, 60k scans, 700 MHz.

2.4.2 Modeling the Reaction of Ethylene with Dehydroxylated Alumina by DFT.

In order to gain further insights about the possible surface species formed upon contacting ethylene and alumina, this reaction was studied by periodic DFT calculations using the fully dehydrated (**s0**) and partially dehydrated alumina surface (3 $OH.nm^{-2}$; **s1**).[10] Concerning the position of the OH on the s1 surface, not all the possibilities were investigated. The position were taken according to the previous work of R. Wischert.[10]

2.4.2.1 Coordination of Ethylene on Alumina Surface.

First, the coordination of gas phase ethylene on the various aluminum sites of **s0** and **s1** surfaces was investigated. The **s1c** surface was used (see part **2.3**) because it

has been shown to display the strongly Lewis acidic Al_{III} sites. Ethylene coordinated on Al sites were located only on Al_{III} sites for **s0** and **s1** surfaces (Figure 2.5). In addition, no transition state could be located for the formation of this π-complex. Two types of coordination mode could be found, where ethylene lies parallel or perpendicular to the Al,O bond (Figure 2.5 a)/b) and c)/d)).

The adsorption energy was found exoenergetic for **s0** surface with E_{ads} = –60 and –71 kJ.mol^{-1} for the parallel and perpendicular configurations, respectively (Table 2.2). The presence of water (**s1**) increase drastically the adsorption energies to E_{ads} = + 48 or + 61 kJ.mol^{-1} for the parallel and perpendicular configurations probably because of a strong interaction between the ethylene and the OH moiety bridging the Al_{IVa} sites. All the species have similar structures with aluminum-carbon bond comprised between 2.57 and 2.43 Å.

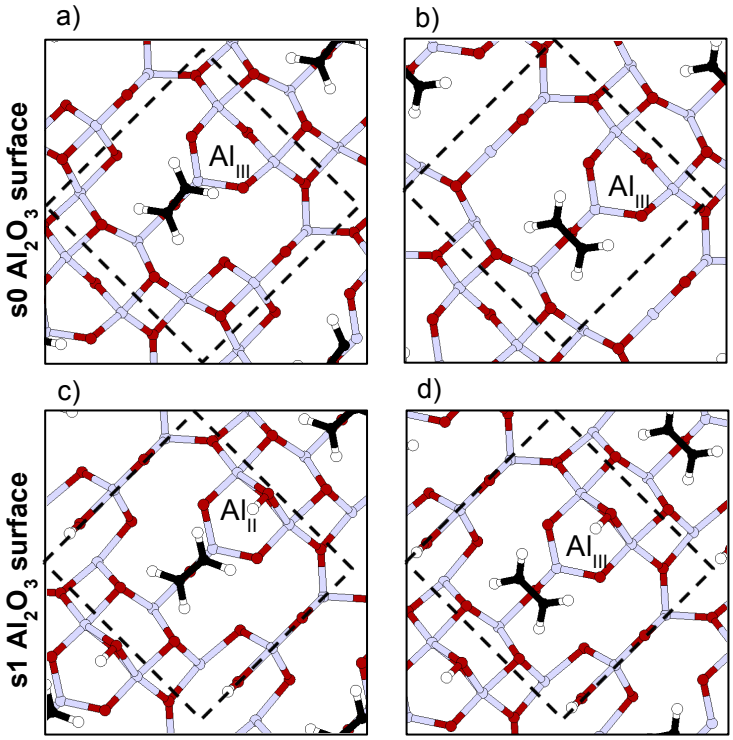

Figure 2. 5. Structure of ethylene molecule coordinated on different Al sites on the fully dehydrated alumina surface (**s0**) and on the hydrated surface (**s1**). The bottom two layers of the slab have been omitted for clarity. The surface unit cell is indicated by a dashed line. Al (grey), O (red), C (black), H (white) balls.

The NMR signatures of the chemisorbed C_2H_4 were calculated using the CASTEP code (Table 2.2).[61,62] The calculated values for the isotropic chemical shift are 144 and 169 ppm when ethylene is coordinated parallel to AlIII,O bond on the **s0** surafce. Considering rotation around the axis of the Al-ethylene centroid axis would

lead to an average chemical shift of 155 pm, close to the calculated ones for the other structures (*ca*. 155 ppm). All the calculated values are clearly shifted downfield by ca. 33 ppm with respect to free ethylene (122 ppm).

Table 2. 2. Adsorption energies of the coordination of ethylene on Al_{III} sites and their calculated NMR signature.

	Aluminum sites	Surface hydration	E_{ads} (Al-C_2H_4 complex) (kJ.mol^{-1})[a]	Al-C (Å) distances	^{13}C Chemical shift (ppm)
a	Al_{III}	**s0**	–60	2.51/2.43	169/144
b	Al_{III}	**s0**	–71	2.46	155/155
c	Al_{III}	**s1**	+ 48	2.57	152/154
d	Al_{III}	**s1**	+ 61	2.49	151/154

2.4.2.2 C-H bond Activation of Ethylene on Al_2O_3.

The C-H bond activation of ethylene on the Al_{III}, Al_{IVa} and Al_{IVb} sites of the **s0** surface generating the corresponding Al-vinyl species was investigated. The calculated adsorption energies are -75, +4 and -27 kJ.mol^{-1}, respectively (Figure 2.6 and Table 2.3). Similarly to what was found for the activation of methane,[10] the most stable species corresponds to the C-H bond activated ethylene bound to Al_{III} followed by Al_{IVb} and Al_{IVa}. On **s1** surfaces (where we used **s1a** and **s1c** to prove various sites), the C-H bond activation of ethylene remains favorable on Al_{III} (– 73 kJ.mol^{-1}), but becomes endoenergetic on Al_{IVa} (+14 kJ.mol^{-1}) and Al_{IVb} (+16 kJ.mol^{-1}) (Figure 2.6 and Table 2.3). The associated vinyl-Al_{III} surface species show Al-C distances of 1.95 Å for both **s0** and **s1** surface. The Al-C distance slightly increases for Al_{IVb} (1.95 Å for **s0** and 1.97 Å for **s1**), while it decreases for Al_{IVa} (2.07 Å for **s0** and 1.97 Å for **s1**).

The energy barriers for the C-H bond activation were calculated on all the sites on the **s0** surface; they are very similar for the three aluminum sites and equal to 91, 103 and 89 kJ.mol^{-1} for Al_{III}, Al_{IVa} and Al_{IVb} respectively (Table 2.3). On **s1** surface, the energy barrier was evaluated only for the Al_{III} site and found to be decreased to only 64 kJ.mol^{-1}.

The ^{13}C chemical shifts for these Al-vinyl species were also calculated; they vary between 180 to 155 ppm and 179 to 135 ppm for the α- and β-carbons, respectively (Table 2.3). In the case of Al_{III} site, the carbon bounded to the aluminum

site has a chemical shift of 180 ppm on the fully dehydrated **s0** surface whereas it is only 155 ppm when the surface is hydrated (**s1**) and it thus shifted with respect to ethylene by 48 to 33 ppm, respectively. The β-carbon has a calculated chemical shift of 142 and 135 ppm on the **s0** and **s1** surface, respectively.

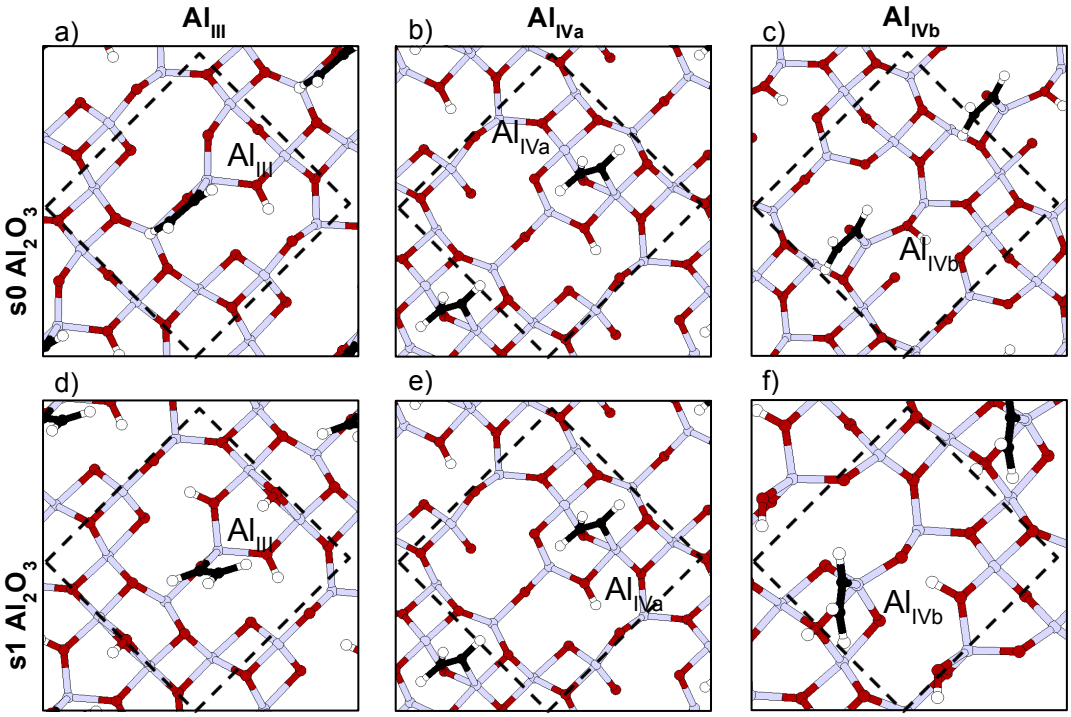

Figure 2. 6. Structure of ethylene molecule C-H activated on different Al sites on the fully dehydrated alumina surface (**s0**) and on the hydrated surface (**s1**). The bottom two layers of the slab have been omitted for clarity. The surface unit cell is indicated by a dashed line. Al (grey), O (red), C (black), H (white) balls.

Table 2. 3. Adsorption energies of the ethylene – surface aluminum complex, their C-H activation energy barriers (in kJ.mol^{-1}) and the corresponding ^{13}C NMR chemical shifts.

Entry	Aluminum sites	Surface hydration	E_{ads} (Al-C_2H_4 complex)[a] (kJ.mol-1)	Energy barrier E_b (kJ.mol^{-1})	^{13}C chemical shift α/β C_2H_4(ppm)	Distance Al-C (Å)
a	Al_{III}	**s0**	–75	+91	180/142	1.95
b	Al_{IVa}	**s0**	+4	+103	172/179	2.07
c	Al_{IVb}	**s0**	–27	+89	165/145	1.95
d	Al_{III}	**s1**	–73 (–255)	+64	155/135	1.95
e	Al_{IVa}	**s1**	+43 (–179)	-[b]	-[c]	1.99
f	Al_{IVb}	**s1**	+16 (–206)	-[b]	-[c]	1.97

[a]: Co-adsorption energy indicated in parentheses for the hydrated surface. [b]: Transition state energy were not calculated due to positive adsorption energies. [c]: No NMR calculation were done due to high adsorption energies.

2.4.3 Conclusion.

The results of the calculations suggest that on a completely dehydrated alumina surface, the C-H bond activation of ethylene can occur on all the 3 different

surface aluminum sites, but it would only lead to a stable Al-vinyl species on Al_{III} sites, especially when the surface is partially hydrated. Worthy of note, calculations also show that ethylene is strongly adsorbed on Al_{III}, making a π-complex, which can be as stable as the vinyl species. Based on energy, one would expect that it is possible to observed both vinyl and π-ethylene complex when ethylene is present in the gas phase, while only the vinyl species could be detected when ethylene was removed since adsorption/desorption is not associated with an activated process, while C-H bond activation is. Both species are associated with specific NMR signatures. The calculated chemical shifts of the π-ethylene complex would be expected to be shifted downfield by 10-60 ppm, and the vinyl complex by 20-30 ppm, on the realistic **s1** surface, compare to gas phase ethylene (122 ppm) The peak at 162 ppm, which disappears when ethylene is not in the gas phase (Figure 2.4a), can be assigned to the π-olefin complex on Al_{III}. For the peaks observed at 146 and 136 ppm, both observable in the absence of ethylene in the gas phase and the latter also in the presence of ethylene, one can propose that they can be attributed to the α- and β-carbon of the Al-vinyl complex (Scheme 2.3).

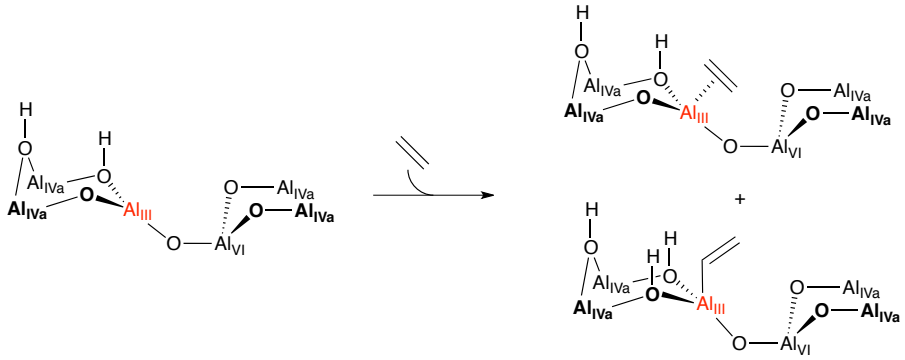

Scheme 2. 3. Proposed product of the reaction of ethylene on Alumina dehydrated at 700°C.

2.5 Conclusion.

Overall, we have seen that dehydrated alumina surfaces are highly reactive; they can activate DME at low temperature yielding methane and higher olefins at 300 °C, similarly to what is observed in the methanol-to-olefin (MTO) process occurring on acidic zeolites. This reaction generates methoxy and formate surface species according to IR and NMR spectroscopies. It was shown that they occur via the formation of oxonium ion as a key reaction intermediate. This is possible through the cooperation between two adjacent aluminum sites of Al_2O_3, which can readily help H–transfer and C-C bond forming reaction processes.

We have also shown in this chapter that ethylene also react with Al_2O_3. *In-situ* and *ex-situ* NMR experiments coupled with DFT calculation indicate that ethylene can strongly bind to Al_{III} sites, but also undergo C-H bond activation across Al_{III},O sites, similarly to methane. While further evidence is clearly needed to confirm this assignment, it is clear that the corresponding surface alkoxy (ethoxy) species is not formed, in sharp contrast with what has been observed with propene. These data demonstrate that alumina is not an innocent support and that detailed investigations are required to understand its surface chemistry and its reactivity once modified by Re.

2.6 Experimental part.

2.6.1 Experimental Considerations.

The alumina samples were a boehmite-derived pure γ-Al_2O_3 with a specific surface area of 230 $m^2.g^{-1}$ provided by Sasol (SBa-200) and a pyrogenic Al_2O_3 with a surface area of *approx.* 130 $m^2.g^{-1}$ (Evonik/Degussa Alu C), composed of γ and δ-phase. NMR spectroscopy was done using a 400 or 700 MHz Bruker NMR spectrometer. 4 mm probe were used. The radio frequency field was always kept at 80 kHz for 1H.

2.6.1.1 Study of the reaction of dimethylether and alumina.

A pellet of Al_2O_3 (AluC or SBa 200) was pressed and loaded in a reactor equipped with CaF_2 windows on the head allowing the measure of *in situ* infrared spectra. The pellet was calcined at 500°C under static air for 12 hours and treated under vacuum for 16 h at 700°C. Dry dimethyl ether, stored over 3A molecular sieves, was added to the reactor (40 mBar, 4.6 molecules per nm^2) contained alumina, and the reaction mixture was treated at different temperatures (25°C, 200°C and 300°C during 12 hours). At each step, IR spectra were recorded, and the gas phase was analyzed. For the removal of the surface hydrocarbons, the pellet was evacuated at 100°C under high vacuum, the gas phase was condensed in a liquid nitrogen trap. The gas phase was then concentrated and analyzed by GC (equipped with a HP-Plot Q column). For the description of Al_2O_3 we use a model with nonspinel sites occupied, based on the simulated dehydration of boehmite. The γ-Al_2O_3 model has three type of Al centers: one tri-coordinated (Al_{III}) and two tetra-coordinated (Al_{IVa} and Al_{IVb}), whose Lewis acidity follows in decreasing order $Al_{III} > Al_{IVb} > Al_{IVa}$.

2.6.1.2 Study of the reaction of ethylene and alumina.

2.6.1.2.1 *Ex-situ* reaction of ethylene and alumina.

Al_2O_3 (160 mg) dehydroxylated at 700°C was loaded in a reactor of known volume (300 mL). Di-labelled ethylene (0.4 mmol) was added to the powder. The gas phase was analyzed by GC after 1 h of reaction, then the gas phase was evacuated by high vacuum (10-5 mBar) for 30 min. The resulting powder was either analyzed by ^{13}C CPMAS solid-state NMR spectroscopy or contacted with degassed water in order to desorbed the surface oligomers.

2.6.1.2.2 *In-situ* reaction of ethylene and alumina.

Al_2O_3 (30 mg) dehydroxylated at 700°C was loaded into a glass insert fitting into a 4 mm solid-state NMR rotor. ^{13}C di-labelled ethylene ($2.6\ 10^{-3}$ mmol of ethylene) was added into the glass insert. The glass insert was flame-sealed, and inserted into the 4 mm rotor for solid-state NMR measurements.

2.6.2 Calculations Methods.

DFT calculations in periodic boundary conditions are carried out in the Perdew-Wang (PW91) implementation of the generalized gradient approximation (GGA) for the correlation and exchange energy functional, using the VASP code (version 5.2). The projected augmented wave (PAW) method was adopted for describing electron-ion interactions. The climbing nudge elastic band method (CI-NEB) was used to determine transition-states. The (110) surface of γ- (or δ-) Al_2O_3 is based on a previous established model, being described by a 8.07 x 8.40 Å unit cells and 8-layers (unit formula $Al_{32}O_{48}$). The inner-slab distance is *ca*. 24 Å. The Brilloun zone integration is performed with a 3 x 3 x 1 *k*-point grid generated by the Monkhorst-Pack algorithm. In order to reproduce the properties of extended surfaces, the bottom two-layers were kept fixed during the calculation at bulk coordinates, while the top layers were allowed to relax. For some calculations we took the dehydrated unit cell of γ-Al_2O_3 since the experimental OH density for the γ-Al_2O_3 surface pretreated at 700 °C under high vacuum during 12 h is equal to 0.7 OH/nm^2. We included the effect of having one additional water on the unit cell for the finally proposed mechanism (corresponding to an OH coverage equal to 3.0 OH/nm^2). No Van der Waals nor dipole corrections were taken into account.

2.7 Reference.

(1) Corado, A.; Kiss, A.; Knözinger, H.; Müller, H. D. *J. Catal.* **1975**, *37*, 68.

(2) Guisnet, M.; Lemberton, J. L.; Perot, G.; Maurel, R. *J. Catal.* **1977**, *48*, 166.

(3) Lombardo, E. A.; Conner Jr, W. C.; Madon, R. J.; Hall, W. K.; Kharlamov, V. V.; Minachev, K. M. *J. Catal.* **1978**, *53*, 135.

(4) Kwak, J. H.; Rousseau, R.; Mei, D.; Peden, C. H. F.; Szanyi, J. *ChemCatChem* **2011**, *3*, 1557.

(5) Larmier, K.; Chizallet, C.; Cadran, N.; Maury, S.; Abboud, J.; Lamic-Humblot, A.-F.; Marceau, E.; Lauron-Pernot, H. *ACS Catal.* **2015**, *5*, 4423.

(6) Woodman, J. F.; Taylor, H. S. *J. Am. Chem. Soc.* **1940**, *62*, 1393.

(7) Harrison, D. L.; Nicholls, D.; Steiner, H. *J. Catal.* **1967**, *7*, 359.

(8) Wischert, R.; Coperet, C.; Delbecq, F.; Sautet, P. *Chem. Commun.* **2011**, *47*, 4890.

(9) Wischert, R.; Copéret, C.; Delbecq, F.; Sautet, P. *Angew. Chem. Int. Ed.* **2011**, *50*, 3202.

(10) Wischert, R.; Laurent, P.; Copéret, C.; Delbecq, F.; Sautet, P. *J. Am. Chem. Soc.* **2012**, *134*, 14430.

(11) Gabrienko, A. A.; Arzumanov, S. S.; Toktarev, A. V.; Stepanov, A. G. *J. Phys. Chem. C* **2012**, *116*, 21430.

(12) Comas-Vives, A.; Schwarzwälder, M.; Copéret, C.; Sautet, P. *J. Phys. Chem. C* **2015**, *119*, 7156.

(13) Lunsford, J. H. *Angew. Chem. Int. Ed.* **1995**, *107*, 1059.

(14) Lunsford, J. H. *Angew. Chem. Int. Ed.* **1995**, *34*, 970.

(15) Crabtree, R. H. *Chem. Rev.* **1995**, *95*, 987.

(16) Lunsford, J. H. *Catal. Today* **2000**, *63*, 165.

(17) Labinger, J. A.; Bercaw, J. E. *Nature* **2002**, *417*, 507.

(18) Woertink, J. S.; Smeets, P. J.; Groothaert, M. H.; Vance, M. A.; Sels, B. F.; Schoonheydt, R. A.; Solomon, E. I. *Proc. Nat. Acad. Sci. U.S.A.* **2009**, *106*, 18908.

(19) Crabtree, R. H. *Chem. Rev.* **2010**, *110*, 575.

(20) Coperet, C. *Chem. Rev.* **2010**, *110*, 656.

(21) Schwarz, H. *Angew. Chem. Int. Ed.* **2011**, *123*, 10276.

(22) Schwarz, H. *Angew. Chem. Int. Ed.* **2011**, *50*, 10096.

(23) Hazari, N.; Iglesia, E.; Labinger, J. A.; Simonetti, D. A. *Acc. Chem. Res.* **2012**, *45*, 653.

(24) Kwapien, K.; Paier, J.; Sauer, J.; Geske, M.; Zavyalova, U.; Horn, R.; Schwach, P.; Trunschke, A.; Schlögl, R. *Angew. Chem. Int. Ed.* **2014**, *126*, 8919.

(25) Tsai, M.-L.; Hadt, R. G.; Vanelderen, P.; Sels, B. F.; Schoonheydt, R. A.; Solomon, E. I. *J. Am. Chem. Soc.* **2014**, *136*, 3522.

(26) Tian, P.; Wei, Y.; Ye, M.; Liu, Z. *ACS Catal.* **2015**, *5*, 1922.

(27) Haw, J. F.; Song, W.; Marcus, D. M.; Nicholas, J. B. *Acc. Chem. Res.* **2003**, *36*, 317.

(28) Marcus, D. M.; McLachlan, K. A.; Wildman, M. A.; Ehresmann, J. O.; Kletnieks, P. W.; Haw, J. F. *Angew. Chem. Int. Ed.* **2006**, *45*, 3133.

(29) McCann, D. M.; Lesthaeghe, D.; Kletnieks, P. W.; Guenther, D. R.; Hayman, M. J.; Van Speybroeck, V.; Waroquier, M.; Haw, J. F. *Angew. Chem. Int. Ed.* **2008**, *47*, 5179.

(30) Van Speybroeck, V.; De Wispelaere, K.; Van der Mynsbrugge, J.; Vandichel, M.; Hemelsoet, K.; Waroquier, M. *Chem. Soc. Rev.* **2014**, *43*, 7326.

(31) Blaszkowski, S. R.; van Santen, R. A. *J. Am. Chem. Soc.* **1997**, *119*, 5020.

(32) Tajima, N.; Tsuneda, T.; Toyama, F.; Hirao, K. *J. Am. Chem. Soc.* **1998**, *120*, 8222.

(33) Li, J.; Wei, Z.; Chen, Y.; Jing, B.; He, Y.; Dong, M.; Jiao, H.; Li, X.; Qin, Z.; Wang, J.; Fan, W. *J. Catal.* **2014**, *317*, 277.

(34) Lesthaeghe, D.; Van Speybroeck, V.; Marin, G. B.; Waroquier, M. *Angew. Chem. Int. Ed.* **2006**, *45*, 1714.

(35) Sun, X.; Mueller, S.; Liu, Y.; Shi, H.; Haller, G. L.; Sanchez-Sanchez, M.; van Veen, A. C.; Lercher, J. A. *J. Catal.* **2014**, *317*, 185.

(36) Olah, G. A.; Doggweiler, H.; Felberg, J. D.; Frohlich, S.; Grdina, M. J.; Karpeles, R.; Keumi, T.; Inaba, S.-i.; Ip, W. M.; Lammertsma, K.; Salem, G.; Tabor, D. *J. Am. Chem. Soc.* **1984**, *106*, 2143.

(37) Hemelsoet, K.; Van der Mynsbrugge, J.; De Wispelaere, K.; Waroquier, M.; Van Speybroeck, V. *ChemPhysChem* **2013**, *14*, 1526.

(38) Olsbye, U.; Svelle, S.; Bjørgen, M.; Beato, P.; Janssens, T. V. W.; Joensen, F.; Bordiga, S.; Lillerud, K. P. *Angew. Chem. Int. Ed.* **2012**, *124*, 5910.

(39) Olsbye, U.; Svelle, S.; Bjørgen, M.; Beato, P.; Janssens, T. V. W.; Joensen, F.; Bordiga, S.; Lillerud, K. P. *Angew. Chem. Int. Ed.* **2012**, *51*, 5810.

(40) Dahl, I. M.; Kolboe, S. *J. Catal.* **1994**, *149*, 458.

(41) Dahl, I.; Kolboe, S. *Catal. Lett.* **1993**, *20*, 329.

(42) Dahl, I. M.; Kolboe, S. *J. Catal.* **1996**, *161*, 304.

(43) Lesthaeghe, D.; Van der Mynsbrugge, J.; Vandichel, M.; Waroquier, M.; Van Speybroeck, V. *ChemCatChem* **2011**, *3*, 208.

(44) Lesthaeghe, D.; Van Speybroeck, V.; Marin, G. B.; Waroquier, M. *Chem. Phys. Lett.* **2006**, *417*, 309.

(45) Silaghi, M.-C.; Chizallet, C.; Raybaud, P. *Micropor. Mesopor. Mater.* **2014**, *191*, 82.

(46) Corma, A.; Martinez, A.; Martinez, C. *Appl. Catal. A* **1996**, *134*, 169.

(47) Rataboul, F.; Baudouin, A.; Thieuleux, C.; Veyre, L.; Copéret, C.; Thivolle-Cazat, J.; Basset, J.-M.; Lesage, A.; Emsley, L. *J. Am. Chem. Soc.* **2004**, *126*, 12541.

(48) Krokidis, X.; Raybaud, P.; Gobichon, A. E.; Rebours, B.; Euzen, P.; Toulhoat, H. *J. Phys. Chem. B* **2001**, *105*, 5121.

(49) Digne, M.; Sautet, P.; Raybaud, P.; Euzen, P.; Toulhoat, H. *J. Catal.* **2002**, *211*, 1.

(50) Digne, M.; Sautet, P.; Raybaud, P.; Euzen, P.; Toulhoat, H. *J. Catal.* **2004**, *226*, 54.

(51) Jones, A. J.; Iglesia, E. *Angew. Chem. Int. Ed.* **2014**, *53*, 12177.

(52) Blaszkowski, S. R.; van Santen, R. A. *J. Phys.Chem. B* **1997**, *101*, 2292.

(53) Stephan, D. W.; Erker, G. *Angew. Chem. Int. Ed.* **2010**, *49*, 46.

(54) Roy, S.; Mpourmpakis, G.; Hong, D.-Y.; Vlachos, D. G.; Bhan, A.; Gorte, R. J. *ACS Catal.* **2012**, *2*, 1846.

(55) Kang, M.; DeWilde, J. F.; Bhan, A. *ACS Catal.* **2015**, *5*, 602.

(56) Phung, T. K.; Lagazzo, A.; Rivero Crespo, M. Á.; Sánchez Escribano, V.; Busca, G. *J. Catal.* **2014**, *311*, 102.

(57) Christiansen, M. A.; Mpourmpakis, G.; Vlachos, D. G. *ACS Catal*. **2013**, *3*, 1965.

(58) Jenness, G. R.; Christiansen, M. A.; Caratzoulas, S.; Vlachos, D. G.; Gorte, R. J. *J. Phys. Chem. C* **2014**, *118*, 12899.

(59) Christiansen, M. A.; Mpourmpakis, G.; Vlachos, D. G. *J. Catal*. **2015**, *323*, 121.

(60) Joubert, J.; Salameh, A.; Krakoviack, V.; Delbecq, F.; Sautet, P.; Copéret, C.; Basset, J. M. *J. Phys.Chem. B* **2006**, *110*, 23944.

(61) Perdew, J. P.; Burke, K.; Ernzerhof, M. *Phys. Rev. Lett*. **1996**, *77*, 3865.

(62) Perdew, J. P.; Burke, K.; Ernzerhof, M. *Phys. Rev. Lett*. **1997**, *78*, 1396.

Chapter 3: The Role of Tri-Coordinate Al-sites in CH_3ReO_3/Al_2O_3 Olefin Metathesis Catalysts.

3.1 Individual Contribution:

Adapted from: "Valla, M.; Wischert, R.; Comas-Vives, A.; Conley, M.; Verel, R.; Copéret, C.; Sautet, P.; *J. Am. Chem. Soc.,* **2016**, 138, 6774-6785". Copyright American Chemical Company.

All experiments and analyses were planned and done by M. Valla with the help of M. Conley and R. Verel. All calculations except the PDOS calculations were done by M. Valla with the help of R. Wischert. PDOS calculations were done by A. Comas-Vives. All authors contributed to the manuscript.

3.2 Introduction

Olefin metathesis is an important reaction for the synthesis of feedstock and fine chemicals.[1-4] Subtle tuning of the ligand environment in homogeneous organometallic complexes results in exquisite selectivities and activities in olefin metathesis using Group VI[5-7] or Ru[8,9] catalysts. The rational design of these catalysts[10] that led to these properties is due to the deep understanding of the key mechanistic steps in the Chauvin catalytic cycle,[1,2,11-13] shown in Scheme 3.1a. The salient features of this mechanism are olefin coordination to a metal alkylidene, [2+2] cycloaddition to form a TBP metallacyclobutane, turnstile isomerization to form the resting state SP metallacyclobutane in the case of d^0 metals,[14-20] cycloreversion from the TBP metallacycle, and olefin decoordination to reform the metal alkylidene and free olefin. Industrial olefin metathesis catalysts contain metal oxide (MO_x) precursors of Mo, W, or Re dispersed onto oxide supports.[1,3,4,11-13,21-24] The structures of active sites and reaction intermediates in heterogeneous metathesis catalysts are difficult to determine because only a typically a fraction of the metals sites are catalytically active.[2,3,25,26] The industrial metathesis catalysts are prepared by incipient wetness impregnation of SiO_2 or Al_3O_3 with a MO_x precursor followed by high temperature calcination. This step forms isolated metal oxo species in high-oxidation states, which forms active

species under the reaction conditions, presumably alkylidene and metallacyclobutane intermediates.[11-13] The low quantity of active sites prohibits structure-activity optimization of these catalysts, and may also explain why many industrial heterogeneous catalyst operate at > 200 °C and are incompatible with functional groups.

The reaction of organometallic alkylidene complexes with partially dehydroxylated oxide supports forms well-defined heterogeneous catalysts that are active at room temperature and compatible with functionalized olefins. [27-31] This method, referred to as Surface Organometallic Chemistry,[26,32]yields catalysts with high concentrations of active sites,[27-29,31] which can be characterized by spectroscopic techniques.[19,26,31,33-40] The structural characterization of the alkylidene active site allows quantitative assessment of ligand environment on heterogeneous metathesis catalyst activity;[17,19,20] an approach that is similar to optimization of homogeneous catalysts.

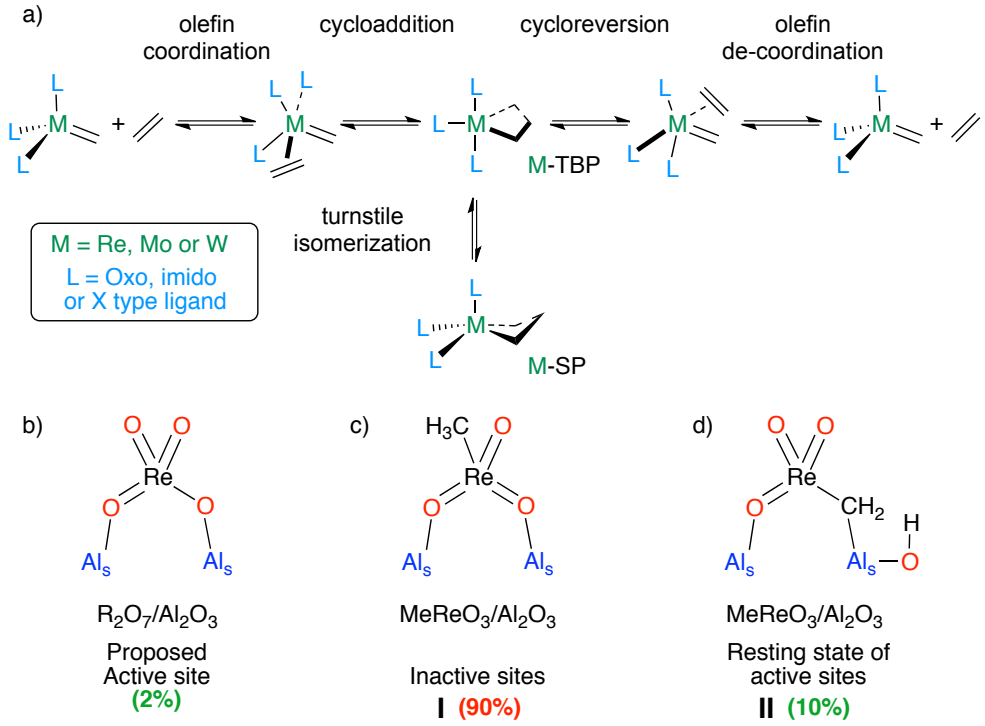

Scheme 3. 1. a) General mechanism of metathesis with alkylidene complexes, b) Proposed active sites of Re_2O_7/Al_2O_3, c) Inactive sites and d) Resting state of the active sites of CH_3ReO_3/Al_2O_3.

Re_2O_7/Al_2O_3 is a unique industrial heterogeneous catalyst because it operates at low temperature (25-80°C),[11,12,28,41,42] and is compatible with functionalized substrates when activated with Me_4Sn.[43,44] The structure of the active site is unknown, though the Lewis acidic sites in Al_2O_3 appear to play a key role in metathesis activity

(Scheme 3.1b).[12,45] Detailed spectroscopic studies on Re_2O_7/Al_2O_3 showed that tetrahedral ReO_4^- coordinated to a pair of Al_{III} and Al_{IV} atoms on the alumina surface are active site precursors. Inactive species are associated with ReO_4^- bound to two Al_{IV} and one Al_{III} atoms in a very distorted geometry where extra oxygen from the surface coordinates to the Re center.[12,45] CH_3ReO_3 supported on alumina and Me_4Sn-activated Re_2O_7/Al_2O_3 have similar reactivity patterns.[28,46-52] The major species (90%) in CH_3ReO_3/Al_2O_3 contains two Re-oxos in CH_3ReO_3 coordinated to Al Lewis acid sites (**I**, Scheme 3.1c), and is inactive in metathesis.[53] The minor species (ca. 10%) in CH_3ReO_3/Al_2O_3 is the μ^2-methylene **II**, which is formed by the activation of a C-H bond in CH_3ReO_3 across an Al–O site (Scheme 3.1d).[30,54] Labeling and spectroscopic studies showed that **II** is a reservoir of active sites for metathesis.[28] However, neither alkylidenes nor metallacycle metathesis intermediates have been observed in CH_3ReO_3/Al_2O_3. In view of the accepted alkene metathesis mechanism and the characterization of **II**, several questions remain: (i) how does **II** participate in alkene metathesis? (ii) what are the reaction intermediates for this catalyst, and are they observable? and (iii) how do the various Al surface sites and their hydration affect the formation and the reactivity of the Re-sites?

This chapter establishes connections between **II** (the resting state) and the accepted Chauvin metathesis cycle by combination of experiment and theory. Solid-state NMR measurements of CH_3ReO_3/Al_2O_3 in the presence of ^{13}C-dilabelled ethylene results in the formation of metallacycle metathesis intermediates. DFT calculations of CH_3ReO_3/Al_2O_3 on model Al_2O_3 surfaces[41,53,55] provided structures and energetics of five possible μ^2-methylene sites as a function of the aluminum site. These results showed the critical role of Al_{III} defect sites in accessing metathesis active Re-sites, and is consistent with the increase of propylene metathesis activity in CH_3ReO_3/Al_2O_3 as surface hydration decreases observed experimentally. As surface hydration decreases the quantity of Al_{III} "defect" sites increases.

3.3 Experimental study

3.3.1 Effect of Al_2O_3 activation temperature on the quantity of active sites.

The activity of CH_3ReO_3/Al_2O_3[28] in propene metathesis, and the number of active sites in these catalyst, were determined as a function of the activation temperature of alumina. As the temperature of activation increases the density of

surface –OH groups decreases; this behavior is coupled with the generation of highly reactive (defect) Lewis acidic Al-sites.[30,54,56] We prepared CH_3ReO_3/Al_2O_3 on alumina activated at T = 200, 300, 500, 600, 700, 800, and 1000°C to form $CH_3ReO_3/Al_2O_{3\text{-}T}$. For clarity, in the discussions below, CH_3ReO_3/Al_2O_3 and $*CH_3ReO_3/Al_2O_3$ refer to natural abundance and ^{13}C-enriched CH_3ReO_3, respectively. In all cases, contacting CH_3ReO_3/Al_2O_3 with 450 equiv. of propene per Re at 25 °C results in the formation of ethylene and 2-butenes, indicating that all CH_3ReO_3/Al_2O_3 catalysts are active in olefin metathesis. $CH_3ReO_3/Al_2O_{3\text{-}500}$ reaches 10% of propene conversion in less than 50 min. Catalysts prepared on alumina activated above 500 °C display similar catalytic activities (Figure A.3.1). In contrast, catalysts prepared on alumina activated below 500°C show significantly lower activities. For instance, 80 min is needed for $CH_3ReO_3/Al_2O_{3\text{-}300}$ to reach 10 % conversion, while 220 min are necessary for $CH_3ReO_3/Al_2O_{3\text{-}200}$ under these conditions.

The quantity of active sites in these catalysts was evaluated by the reaction of ^{13}C-di-labelled ethylene (0.5 equiv per Re) with CH_3ReO_3/Al_2O_3.[49] The amount of ^{12}C incorporated into gas phase ethylene corresponds to the number of active sites. A plot of the amount of ^{12}C-label detected in the gas phase after 30 min and 16 h of reaction time is given in Figure 3.1. After 30 min of reaction more than 8% of the Re-sites are active for catalysts prepared on Al_2O_3 activated at or above 500 °C.

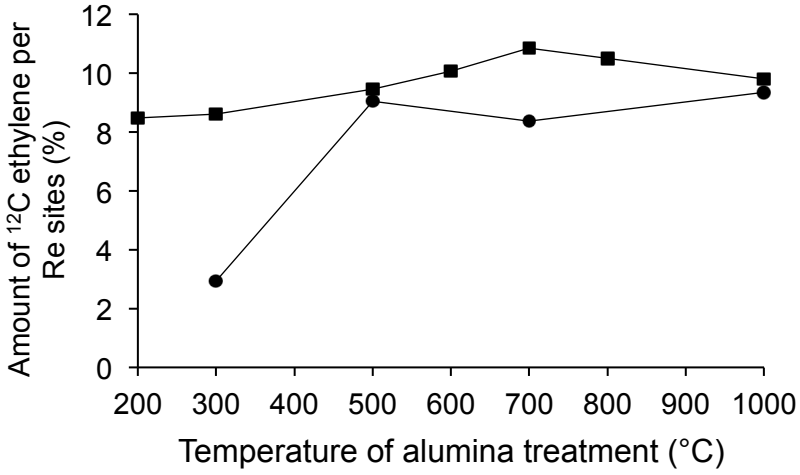

Figure 3. 1. Quantification the amount of ^{12}C-ethylene after 30 min reaction of CH_3ReO_3/Al_2O_3 and ^{13}C-ethylene (●); quantification after 16 h reaction time(■).

In contrast, $CH_3ReO_3/Al_2O_{3\text{-}300}$ contains only 3 % active sites according to the titration. These results parallel the activity of CH_3ReO_3/Al_2O_3 in the metathesis of propene discussed above, and suggest that the activity of the catalyst depends on the

level of hydroxylation of the alumina support.[45,57,58] However, titration of active sites carried out after 16 h reaction times showed that all catalysts have roughly the same number of active sites, suggesting a distribution of sites in CH_3ReO_3/Al_2O_3.

3.3.2 Detection of reaction intermediates.

The ^{13}C Cross-Polarization Magic Angle-Spinning (CPMAS) spectrum of $*CH_3ReO_3/Al_2O_{3-(500)}$ contains one signal at 66 ppm with a width at half-maximum ($\nu_{1/2}$) of 2600 Hz and one signal at 30 ppm ($\nu_{1/2}$ = 4000 Hz), assigned to the μ-methylene species **II** and the inactive oxo-species **I**, respectively (Figure 3.2). The ^{13}C CPMAS spectrum of $*CH_3ReO_3/Al_2O_{3-(500)}$ after contact with natural abundance propene or ethylene (450 equiv per Re) contains the μ-methylene, though with much lower intensity (Figure A.3.2), indicating that not all μ-methylene sites participate in the metathesis reaction. The ^{13}C CPMAS spectrum of $CH_3ReO_3/Al_2O_{3-(500)}$ after contact with ^{13}C-di-labelled ethylene, and removal of the gas phase, also contains the μ-methylene signal at 66 ppm, though with a narrower linewidth ($\nu_{1/2}$ = 1800 Hz) for the μ-methylene species than $*CH_3ReO_3/Al_2O_3$ (Figure A.3.3). These results further support the presence of a distribution of Re-sites in CH_3ReO_3/Al_2O_3, some of them being more reactive than others.

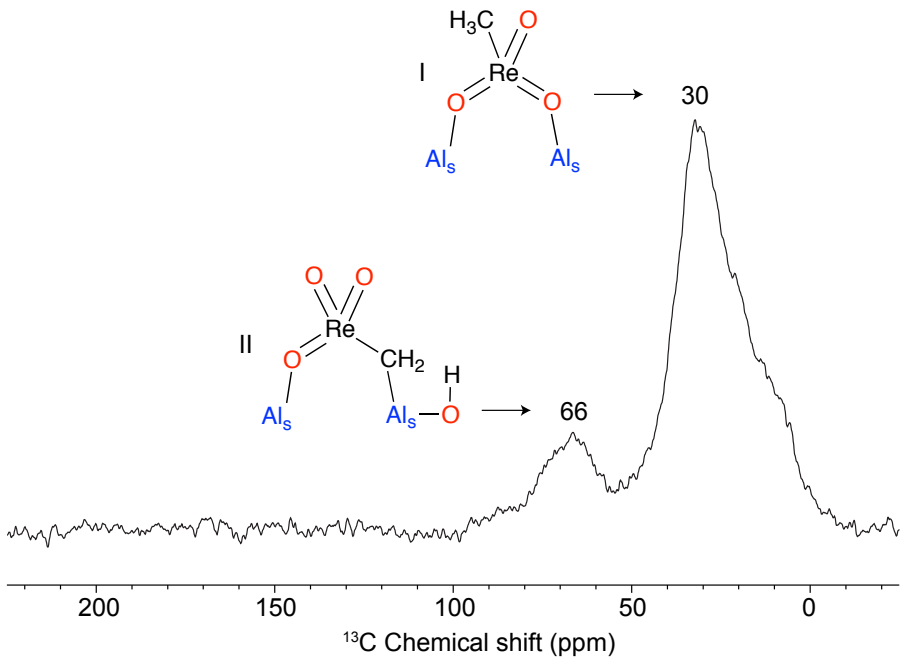

Figure 3. 2. ^1H-^{13}C CPMAS NMR, 700 MHz, $*CH_3ReO_3/Al_2O_{3-(500°C)}$, 5k scans, 10 kHz, the recycling delay was set to 1s and the cross polarization contact time was set to 600 μsec.

NMR signals of Re-alkylidenes (expected between 200 and 300 ppm),[59] or of the metallacycles (two peaks for TBP geometry at *approx.* 0/100 ppm vs. two peaks

for SBP at *approx*. 20-50 ppm) were not observed for all $*CH_3ReO_3/Al_2O_3$. In the absence of olefins, metallacycle intermediates can decompose to alkylidenes, or in this case to the μ-methylene species **II**. The ^{13}C-CPMAS spectrum of $CH_3ReO_3/Al_2O_{3\text{-}500}$ in the presence of ^{13}C di-labelled ethylene (0.5 equiv per Re) using a glass insert contains signals at 19, 36, 43, 66, and 120 ppm (Figure 3.3). Signals typical for alkylidenes were not detected (Figure A.3.4). The signal at 66 ppm ($\nu_{1/2}$ = 1900 Hz) corresponds to the μ-methylene species **II** having low reactivity towards olefins. The peaks at 120 ppm ($\nu_{1/2}$ = 510 Hz) and 19 ppm ($\nu_{1/2}$ = 520 Hz) are characteristic for the α- and β-carbons of a metallacycle in TBP geometry (Figure 3.3),[14,15,17,19,60] and those at 43 ($\nu_{1/2}$ = 440 Hz) and 36 ppm ($\nu_{1/2}$ = 1200 Hz) for the α– and β-carbons of a metallacycle in SP geometry.[17,19] The blank experiment of Al_2O_3 dehydroxylated at 700°C contacted with ^{13}C labeled ethylene exhibits peaks assigned for coordinated, C-H activated and oligomerized ethylene (Figure A.3.5). These peaks cannot be found in the present NMR spectra (Figure 3.2-3) excluding any of the observed peaks above to the reaction of ethylene with Al surface sites alone. The assignments of the TBP- and SP-metallacycles are further supported by a two-dimensional ^1H-^{13}C heteronuclear correlation (HETCOR) spectrum in Figure 3.3.

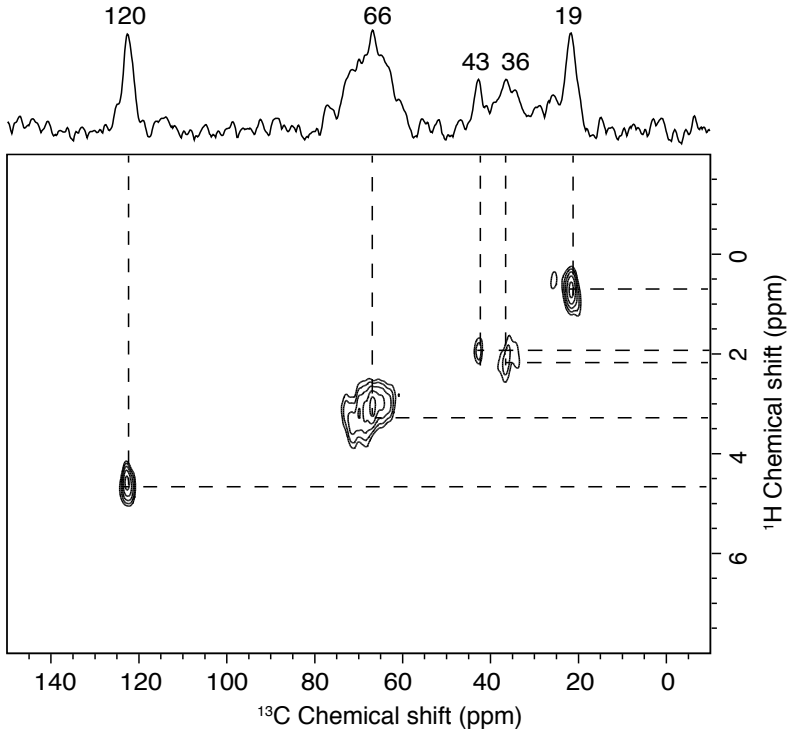

Figure 3. 3. ^1H-^{13}C HETCOR NMR spectrum of $CH_3ReO_3/Al_2O_{3\text{-}500}$ in the presence of 0.5 equiv ^{13}C di-labelled ethylene/Re sealed in a glass insert at 9 kHz spinning speed. DUMBO[61,62] decoupling was applied, the contact time was set to 250 μsec and the recycle delay was set to 1 sec.

The cross-peaks between proton and carbon resonances (H/C) at (19/0.4) and (120/4.2) are consistent with their assignment as the α- and β- (carbon/proton) of the TBP metallacyclobutane. In addition, the cross-peaks at (43/1.8) and (36/2.0) support their assignment to the SP metallacycle. The narrow linewidths of the peaks corresponding to the TBP- and SP metallacycles indicate a narrow site distribution, in contrast to the much broader μ-methylene signal. The absence of alkylidene signals suggest that they are either difficult to observe or less stable than the corresponding μ-methylene.

3.4 Calculation studies of CH_3ReO_3 adsorbed on dehydrated Al_2O_3

The experimental results discussed above (exchange experiments) show that μ-methylene species **II** are active site precursors. **II** is present as a distribution of sites from active site titrations and solid state NMR studies. In order to obtain a more detailed understanding of the Re-sites in CH_3ReO_3/Al_2O_3 we investigated the structure, spectroscopic signatures and reactivity of μ-methylene sites in CH_3ReO_3/Al_2O_3 using computational modelling. The structure and stability of the inactive Re-oxo bound **I** was previously reported.[53]

A typical γ-alumina particle contains 110 (74%), 100 (16%) and 111 (10%) facets.[63-65] The model of the fully dehydroxylated 110 facet (s0) contains one type of tri-coordinate aluminum (Al_{III}) and two types of four-coordinate aluminum sites (Al_{IVa} and Al_{IVb}) per unit cell (Figure 3.4a). Al_{III} is defined as a defect site because of its low surface density on hydroxylated surfaces; this site is generally occupied by hydroxyl.[59-60] The stability of a surface Re site can be defined by its adsorption energy (E_{ads}) on s0, as follows:

$$E_{ads} = E(\mathbf{s0} + CH_3ReO_3) - E(CH_3ReO_3) - E(\mathbf{s0}), \qquad (1)$$

where $E(\mathbf{s0} + CH_3ReO_3)$, $E(CH_3ReO_3)$ and $E(\mathbf{s0})$ correspond to the electronic energies of CH_3ReO_3 adsorbed on the surface, CH_3ReO_3, and the dehydroxylated alumina surface (**s0**).

3.4.1 Stability of Re-oxo species on the fully dehydrated alumina surface.

The adsorption of CH_3ReO_3 on Al_{III} and Al_{IVa} centers through one oxo ligand (**0-III** and **0-IVa**) is exoenergetic by –144 and –56 kJ mol^{-1}, respectively. A similar

structure was not obtained on Al_{IVb} because it directly evolved into a structure where two Re=O groups are coordinated to the surface (vide infra, **0-IVa,IVb**). Bis-grafted Re-oxo species are referred to as **0-A,B** to indicate to which Al centers (A and B) the oxo groups of CH_3ReO_3 are bound (Figure 3.4b-c). The most stable species, associated with an adsorption energy of –224 kJ mol^{-1} is **0-III,IVb**, which also contains one oxygen atom from the alumina surface coordinated to Re. **0-IVa,IVb** has an adsorption energy of –202 kJ mol^{-1} and also contains an additional surface oxygen atom coordinated to Re, while the adsorption energy of **0-IVa,IVa** is only –72 kJ mol^{-1}.

3.4.2 Stability of the μ-methylene species on the fully dehydrated alumina surface.

CH_3ReO_3 adsorbs on two Al-sites of the fully dehydrated (**s0)** 110 facet to form μ-methylene surface species and a proton on an adjacent O atom (Figure 3.4a).[53] Five μ-methylene adsorbates can form, which differ in the surface aluminum atoms bound to the μ-CH_2 and oxo ligands. The models for the μ-methylene surface species are referred to as **1**-A,B to indicate that the μ-CH_2 ligand sits on A and the oxo on B (Figure 3.4b). The stability of a surface Re site can be defined by its adsorption energy (E_{ads}) as follows:

$$E_{ads} = E(\mathbf{si} + CH_3ReO_3) - E(CH_3ReO_3) - E(\mathbf{si}) \quad (2)$$

where $E(CH_3ReO_3)$ and E(**si**) correspond to the electronic energies of CH_3ReO_3 and the alumina surface at degree of hydration of **s0**, **s1** or **s2**. The structures and adsorption energies of these species are summarized in Table 3.1 and Figure 3.4.

CH_3ReO_3 preferentially adsorbs to Al_{III} and Al_{IVb} sites with high E_{ads} of –233 kJ mol^{-1} and –211 kJ mol^{-1} for **1–III,IVb** and **1–IVb,III**, respectively. CH_3ReO_3 forms less stable surface complexes with sites not involving Al_{III}. E_{ads} for **1–IVa,IVb, 1–IVb,IVa, 1–IVa,IVa** are –96 kJ mol^{-1}, –129 kJ mol^{-1} and –90 kJ mol^{-1}, respectively. In **1–III,IVb**, **1–IVb,III**, and **1–IVa,IVa**, the Re center adopts a pseudo tetrahedral geometry with Re-C bond length of 2.00–2.01 Å. In these three structures, two oxo ligands are pointing away from the surface with Re-O bond lengths of *ca*. 1.71 Å, and one oxo ligand is coordinated to an adjacent aluminum and is elongated to *ca*. 1.78 Å. The Re centers in **1–IVa,IVb** and **1– IVb,IVa** are pseudo-octahedral due to the presence of two additional dative interactions from surface oxygen atoms.

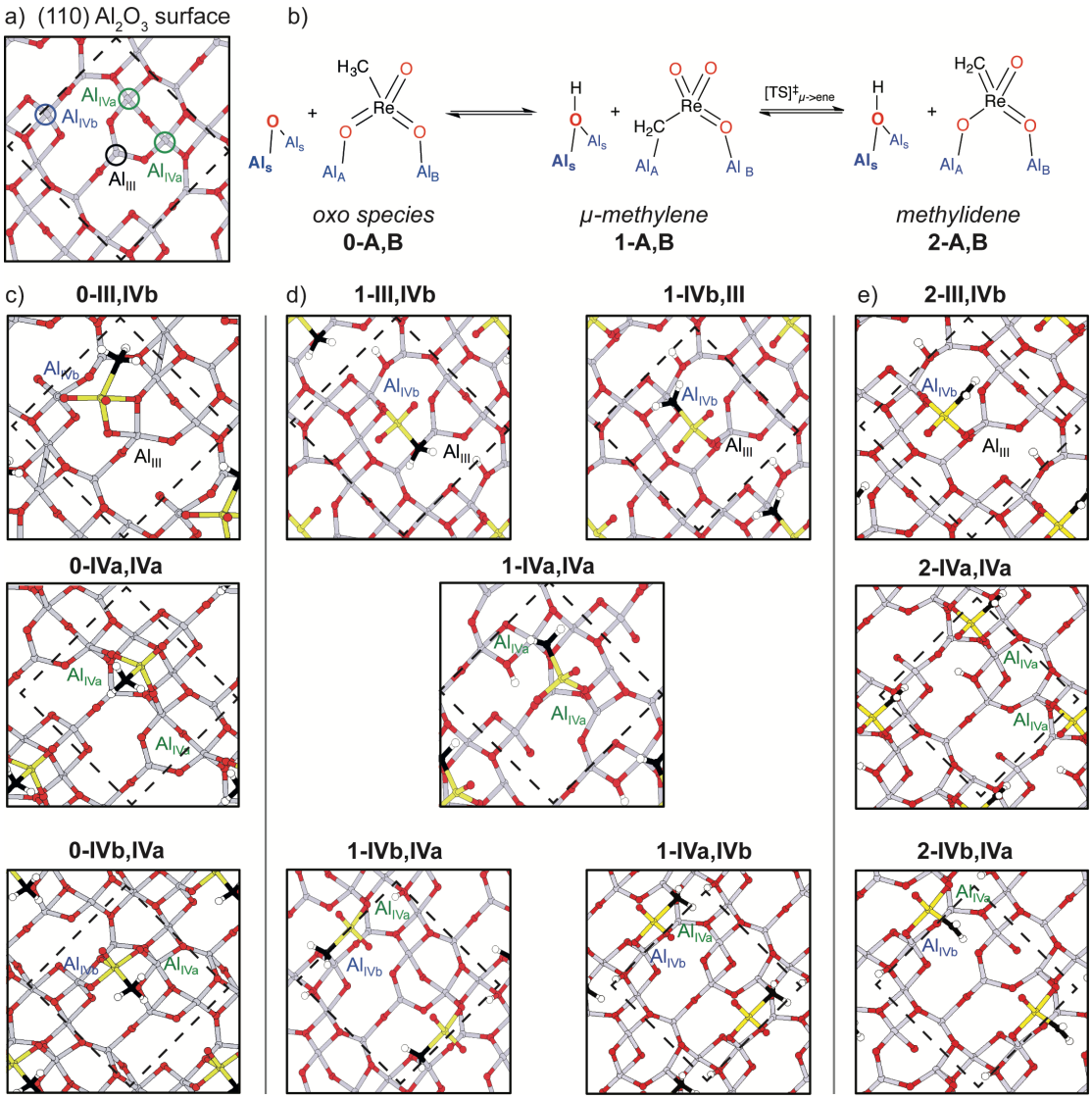

Figure 3. 4. a) Fully dehydroxylated γ-Al_2O_3 (110) surface; b) Interconversion of the oxo species (**0-A,B**) to the μ-methylene species (**1-A,B**) followed by its interconversion into the corresponding alkylidene (**2-A,B**); c) Optimized structures of the oxo-species (**0-A,B**) on different Al site pairs of the fully dehydrated γ-Al_2O_3 (110) surface (s0); d) optimized structures of the μ-methylenes species (**1-A,B**) where A and B correspond to Al sites bound to CH_2 and oxo, respectively; e) Optimized structures of the alkylidene species (**2-A,B**) (s0). Only the two top layers of the periodical slab of the alumina are shown for clarity. The surface unit cell is indicated by a black dashed line. Al (Grey), O (red), Re (yellow), C (black), H (white) balls.

To summarize, the stability (E_{ads}) of the oxo and m-methylene species decreases as follows: **1-III,IVb** (–233) > **0-III,IVb** (–224) > **1-IVb,III** (–211) > **0-IVa,IVb** (–202) >> **0-III** (–144) > **1-IVb,IVa** (–129) > **1-IVa,IVb** (–96) > **1-IVa,IVa** (–90) > **0-IVa,IVa** (–72) > **0-IVa** (–56). While the μs-methylene species **1-III,IVb** is the overall most stable structure, from a thermodynamic point of view a mixture of oxo and methylene species should be present, due to the small energy differences between them and the presence of adsorbed water on various Al sites in the initial

support. Not surprisingly, mono-bound species (such as **0-III**) are much less stable than structures in which CH_3ReO_3 interacts with the surface through two or more bonds.

Table 3. 1. Adsorption sites, symmetry at Re (G.), adsorption energies (E_{ads}) for the oxo species (0-A,B), the μ-methylene species (1-A,B) and the Re methylidene species (2-A,B) on the fully dehydrated γ-Al_2O_3 (110) surface (s0). Transition state energies $[TS]^{\ddagger}$ and activation energies $E^{\ddagger}$ for their interconversion (0-A,B to 1-A,B and 1-A,B to 2-A,B) are also given. All energies are in kJ mol^{-1}.

0-A,B	E_{ads}	**1-A,B**	G.[a]	E_{ads}[c]	$[TS]^{\ddagger}$	$E^{\ddagger}$
IVa,IVb	–202	-[a]	-[a]	-[a]	-[a]	-[a]
III,IVb	–224	III,IVb	T	–233 (-31)	–59	143
III	–144	IVb,III	T	–211 (-67)	–77	67
IVa	–56	-[a]	-[a]	-[a]	-[a]	-[a]
IVa,IVa	–72	IVa,IVa	T	–90 (-34)	–11	45
IVa	-56	IVb,IVa	O	–129 (-73)	-[a]	-[a]
IVa,IVb	–202	IVa,IVb	O	–96 (+ 106)	-[a]	-[a]

2-A,B	G.[a]	E_{ads} (ΔE)[d]	$[TS]^{\ddagger}_{\mu\rightarrow ene}$	$E^{\ddagger}_{\mu\rightarrow ene}$
-[a]	-[a]	-[a]	-[a]	-[a]
III,IVb	T	–269 (–36)	–33	+200
III,IVb	T	–269 (–58)	–162	+49
-[a]	-[a]	-[a]	-[a]	-[a]
IVa,IVa	T	–127 (–37)	+5	+95
IVb,IVa	O	–151 (–22)	-[a]	-[a]
IVb,IVa	O	–151 (–55)	+17	+113

[a]: Structures not calculated, [b]: Symmetry of the surface Re species. T and O indicates pseudo-tetrahedral or octahedral coordination of Re, respectively. [c]: The energy in parentheses (ΔE) corresponds to the difference in stability of the the μ-methylene and the oxo species: $\Delta E = E_{ads}(\mu\text{-}CH_2) - E_{ads}(oxo)$.[d]: The energy in parentheses (ΔE) corresponds to the difference in stability of the methylidene and the μ-methylene species: $\Delta E = E_{ads}(methylidene) - E_{ads}(\mu\text{-}CH_2)$. [e] no transition state could be located.

3.4.3 Formation of the μ-methylene on the fully dehydrated alumina surface.

Below we refer to $[TS]^{\ddagger}$, as the energy of the transition state structure, and $E^{\ddagger}$, as the energy barrier with respect to the preceding intermediate. These energies are defined as follows:

$$[TS]^{\ddagger} = E(\mathbf{si} + CH_3ReO_3 + C_2H_4)^{\ddagger} - E(CH_3ReO_3) - E(\mathbf{si}) - E(C_2H_4) \quad (2)$$

$$E^{\ddagger} = [TS]^{\ddagger} - E_{intermediate}\ (\mathbf{si} + CH_3ReO_3 + C_2H_4) \quad (3)$$

where **si** is the surface containing **i** dissociated water molecules per unit cell. For the interconversion between μ-methylene and the corresponding methylidene, ethylene was not considered in the transition state calculations.

Table 3.1 summarizes the reaction energies associated with the formation of the m-methylene species **1** with respect to separated reactants and possible oxo-bound initial states (**0**). Transition states were calculated, starting from oxo-bound species **0** since the coordination of the oxo ligand is likely barrierless (for transition state structures, see Figure S8). For the formation of the most stable surface species **1–III,IVb,** starting from **0-IVa,IVb**, a transition state was located at an energy $[TS]^{\ddagger}$ = –59 kJ mol^{-1} below separated reactants (CH_3ReO_3 and Al_2O_3). While the energy gain from **0-IVa,IVb** is 31 kJ mol^{-1}, the energy barrier is rather high, $E^{\ddagger}$ = 143 kJ mol^{-1}. For **1–IVb,III**, a transition state was located starting from **0-III** at $[TS]^{\ddagger}$ = –77 kJ mol^{-1} in a process associated with a reaction energy of –67 kJ mol^{-1} and an energy barrier of $E^{\ddagger}$ = +67 kJ mol^{-1}. The formation of **1-IVa,IVa** from **0-IVa** is associated with a reaction energy of –34 kJ mol^{-1} and an energy barrier of $E^{\ddagger}$ = 45 kJ mol^{-1}. The formation of **1-IVa,IVb** and **1-IVb,IVa** was not investigated since they are much less stable than **0-IVa,IVb.** Overall, **1-IVb,III** and **1-IVa,IVa** are kinetically accessible, while other species, including the very stable **1-III,IV**, are much less likely on the **s0** surface. This computational data shows that mixtures of **0** and **1** species will be formed on the alumina surface, consistent with experiment.

3.4.4 Stability and structures of alkylidene on fully dehydrated alumina.

Alkylidene intermediates are expected in metathesis catalysts. The structures of alkylidenes **2-A,B** are shown in Figure 3.4. The interconversion of **1-A,B** to **2-A,B** conserved the geometry at Re; **2-III,IVb** and **2-IVa,IVa** are tetrahedral and **2-IVb,IVb** is octahedral. **2-A,B** have short Re-C bond distances (1.87 – 1.88 Å), significantly shorter than the Re-C distances in **1-A,B** (see Tables A.3.1 and A.2.2 for more detailed bond distances). In all cases, the alkylidene species are slightly more stable than the corresponding μ-methylene (Table 3.1). **2–III,IVb** (E_{ads} = –269 kJ mol^{-1}) is 36 kJ mol^{-1} more stable than **1-III,IVb** and 58 kJ mol^{-1} more stable than **1-IVb,III**. Similarly, **2-IVa,IVa** (E_{ads} = –127 kJ mol^{-1})is 37 kJ mol^{-1} more stable than **1-IVa,IVa**. Octahedral **2-IVb,IVa** (E_{ads} = –151 kJ mol^{-1}) is 22 kJ mol^{-1} more stable than **2-IVb,IVa** and 55 kJ mol^{-1} more stable than **2-IVa,IVb**.

3.4.5 *Interconversion between μ-methylene and alkylidene species on dehydrated Al_2O_3.*

Forming the methylidene involves the de-coordination of the methylene ligand, rotation, and coordination of an additional Re=O unit to the surface. The energy barrier for interconversion depends on the Al-sites. The transition state structures are given in Figure 3.5. The energy barrier for the formation of **2-III,IVb** is 200 kJ mol^{-1} above **1-III,IVb** (Table 3.1), suggesting that these sites probably do not interconvert at room temperature. In contrast, the energy barrier to form **2-III,IVb** from **1-IVb,III** is only 49 kJ mol^{-1}. The weaker Lewis acidity of Al_{IVb} compared to the Al_{III} site probably allows easier decoordination of the μ-methylene hence the lower barrier to form **2-III,IVb**. **1-IVa,IVa** and **1-IVa,IVb** from **2-IVa,IVa** and **2-IVb,IVa** with energy barrier of 95 and 113 kJ mol^{-1}, respectively. In addition, **2-IVa,IVa** and **2-IVb,IVa** are less stable than **2-III,IVb**, suggesting that these sites may not play an important role in metathesis. We were unable to locate the transition state for the formation of **2-IVb,IVa** from **1-IVb,IVa**.

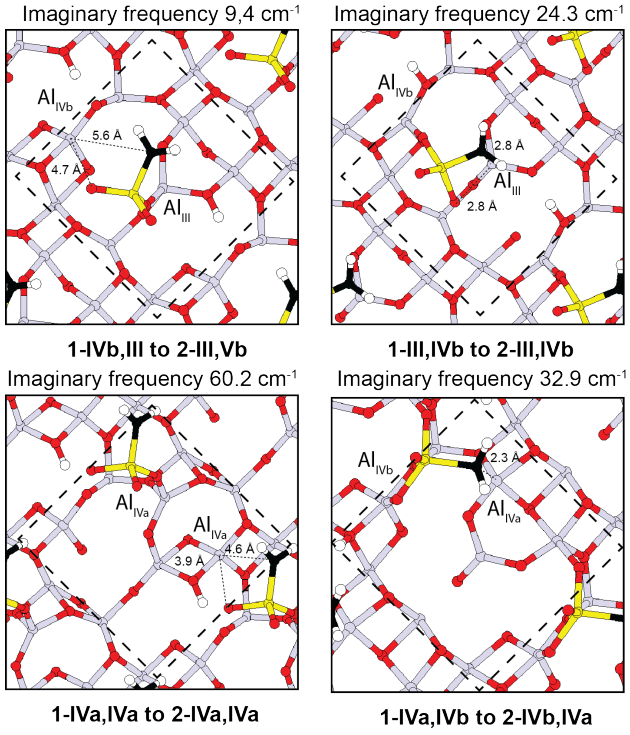

Figure 3. 5. Structure of the transition state and imaginary frequency of the interconversion reaction from the μmethylene to the alkylidene on the dehydrated (110) facet of γ-Al_2O_3. The bottom two layers of the slab have been omitted for clarity. The surface unit cell is indicated by a dashed black line. Al (yellow), O (red), Re (grey), C (black), H (white) balls. Distances are indicated (in Å).

3.4.6 Reactivity of the alkylidene species with ethylene.

[2+2]-cycloaddition of **2-A,B** and ethylene forms the TBP– or SP–metallacyclobutanes, **3-TBP-A,B** and **3-SP-A,B** shown in Scheme 3.2 and Figure 3.6a (Figure A.3.6 for structural details). **3-TBP-A,B** contains two Re=O axial ligands; one pointing away from the surface (d(Re-O) = 1.75 Å) and one bound to an Al of the surface with a longer Re-O bond (1.80 – 1.85 Å, Tables A.3.3-5). The basal plane contains one oxygen ligand bound to the surface and the two carbons of the metallacyclobutane. The TBP metallacycle has a Re-C-C-C dihedral angle close to 0° and a characteristic short Re-β-carbon bond distance (2.38 Å).[14,18,66] In contrast, the SP metallacyclobutanes are puckered with a dihedral angle of 25° and display a long Re-β-carbon bond.[17,19,67] On all sites, the formation of metallacyclobutanes **3** is exoenergetic relative to the alkylidene **2**.

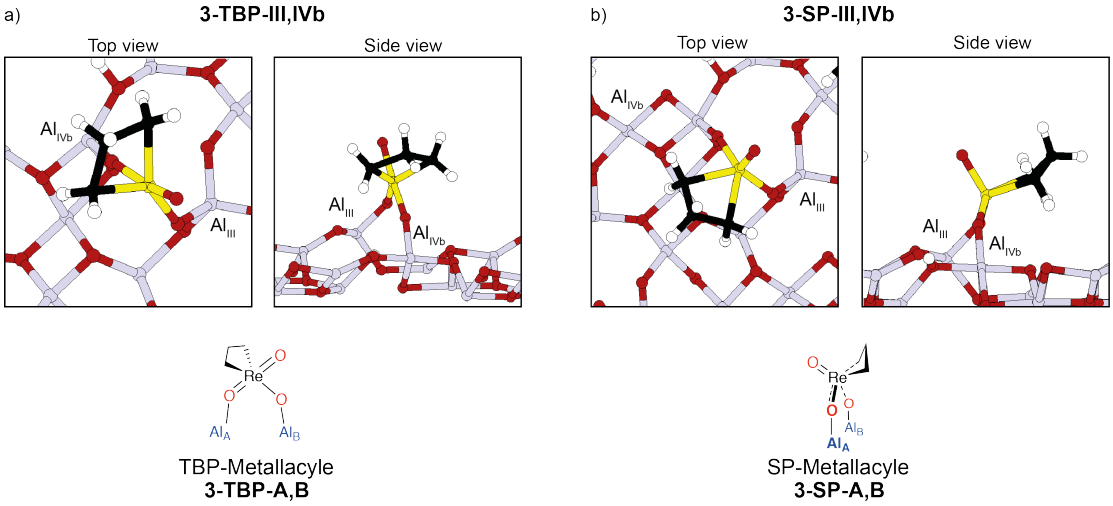

Scheme 3. 2. Optimized structures and schematic representation of surface metallacycles from the alkylidene 2-III,IVb in a) TBP (3-TBP-III,IVb) and b) SP geometry (3-SP-III,IVb). Only the two top layers of the periodical slab is shown for clarity. Al (grey), O (red), Re (yellow), C (black), H (white) balls.

When both the SP and TBP isomers were located, the SP isomer is more stable (Figure 3.6 and Table 3.2), and formally corresponds to a resting state in the metathesis catalytic cycles.[66] In contrast, the barrier to form **3-SP-A,B** from **2-A,B** and ethylene ($E^{\ddagger}_{2+2\text{-}SP}$) is always much higher than for the formation of **3-TBP-A,B** ($E^{\ddagger}_{2+2\text{-}TBP}$). However, **3-TBP-A,B** can interconvert with **3-SP-A,B** by a turnstile mechanism. Cycloreversion from **3-TBP** or **3-SP** will form **2** and ethylene, which closes the metathesis cycle. Cycloreversion has the same $[TS]^{\ddagger}$ as cycloaddition from microreversibility considerations. The energy barrier to do the cycloreversion of **3-SP**

is high (>100 kj mol^{-1}), and sites that favour formation of **3-SP** through turnstile isomerization will have low activity.

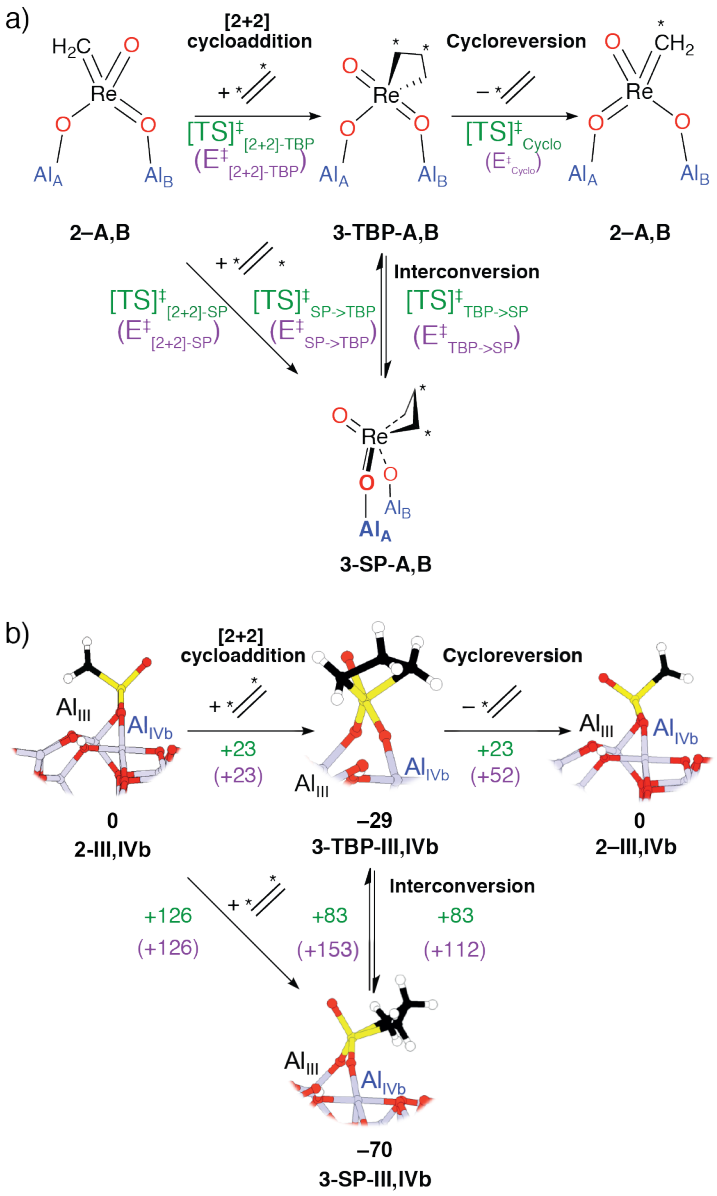

Figure 3. 6. a) Schematic representation of the metathesis pathway of CH_3ReO_3/Al_2O_3 and ethylene for all sites with the corresponding nomenclature for naming the transition states and corresponding energy barriers. b) Structures of the metathesis intermediates starting from **2-III,IVb** on s0, the most favorable site for metathesis. Transition state energies are in green and activation energies of the corresponding elementary steps are in purple. Transition state structures are available Figure A.3.7. Values are in kJ mol^{-1}.

For example, the reaction of **2-III,IVb** and ethylene to form **3-TBP-III,IVb** is favorable (ΔE = –29 kJ.mol^{-1}) and the associated transition state energy is $[TS]^{\ddagger}_{[2+2]\text{-TBP}} = E^{\ddagger} = +23$ kJ.mol^{-1}. The transition state energy to form **3-SP-III,IVb** from **2-III,IVb** and ethylene is $[TS]^{\ddagger}_{[2+2]\text{--SP}} = E^{\ddagger} = +126$ kJ.mol^{-1}, and thus significantly higher than for the formation of **3-TBP-III,IVb** (Table 3.2 and Figure 3.6). **3-TBP-**

III,IVb interconverts with **3-SP-III,IVb** with $E^{\ddagger}_{TBP \rightarrow SP}$ =+112 kJ.mol^{-1}. However, cycloreversion of **3-TBP-III,IVb** has an energy barrier of $E^{\ddagger}_{cyclo}$ = +52 kJ.mol^{-1}. Since the barrier for cycloreversion is lower than TBP-SP interconversion, **2-III,IVb** sites will be particularly active in metathesis.

Table 3. 2. Energies of transition state structures and reaction intermediates with the corresponding energy barriers for elementary steps for ethylene metathesis on **2** adsorbed on the fully dehydrated γ-Al_2O_3 (110) surface (**s0**) (kJ mol-1).

A,B	**2-A,B**	**3-TBP-A,B**	**3-SP-A,B**	$[TS]^{\ddagger}_{[2+2]\text{-TBP}}$
III/IVb	0	–29	–70	+ 23
IVa/IVa	0	–37	–70	+ 40
IVb/IVa	0	–a	–59	– a
	$[TS]^{\ddagger}_{[2+2]\text{-SP}}$	$[TS]^{\ddagger}_{TBP \rightarrow SP}$	$E^{\ddagger}_{TBP\text{-}SP}$	$E^{\ddagger}_{cyclo}$	$E^{\ddagger}_{SP\text{-}TBP}$
III/IVb	+ 126	+ 83	+ 112	+ 52	+ 153
IVa/IVa	+ 121	+ 48	+ 85	+ 77	+ 118
IVb/IVa	+ 177	– a	– a	– a	– a

[a]: the structure or the transition state energies could not be located.

2-IVa,IVa and ethylene form **3-TBP-IVa,IVa** with $[TS]^{\ddagger}_{[2+2]\text{- TBP}} = E^{\ddagger}$ = +40 kJ.mol^{-1} (Figure 3.7). TBP-SP interconversion is slightly higher ($E^{\ddagger}_{TBP \rightarrow SP}$ =+85 kJ.mol^{-1}) than cycloreversion ($E^{\ddagger}_{cyclo}$ =+77 kJ.mol^{-1}). As a result, the formation of the more stable SP metallacycle competes with metathesis on **2-IVa,IVA** sites; as a result it is less reactive than **2-III,IVb** (Table 3.2).

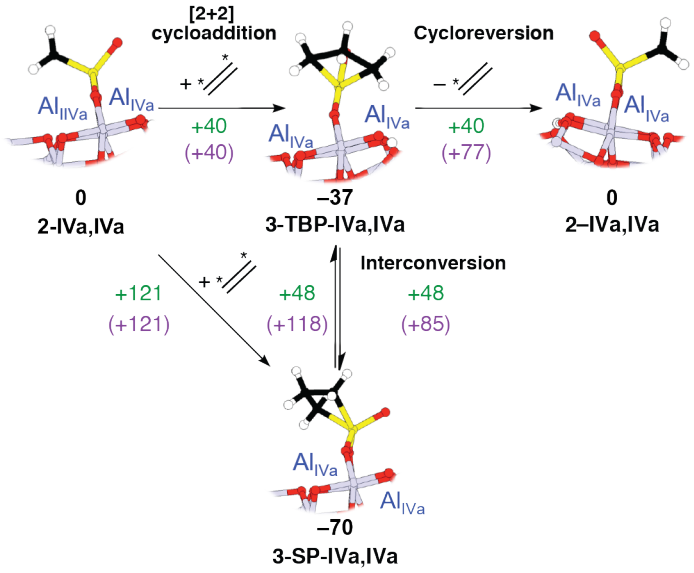

Figure 3. 7. Calculated structures, transition state energies and barrier energies of the intermediates of CH_3ReO_3/Al_2O_3 in the metathesis of ethylene starting from **2-IVa,IVa** on s0. Transition state energies are in green and activation energies are in purple. Values are in kJ mol^{-1}

For the octahedral **2-IVb,IVa** reaction with ethylene yields a 7-coordinate metallacycle **3-IVb,IVa** ($\Delta E = -59$ kJ.mol^{-1}) through a very high transition state energy $(TS]^{\ddagger}_{[2+2]} = +177$ kJ.mol^{-1}), indicating that this site is unreactive in metathesis (Table 3.2 and Figure 3.8).

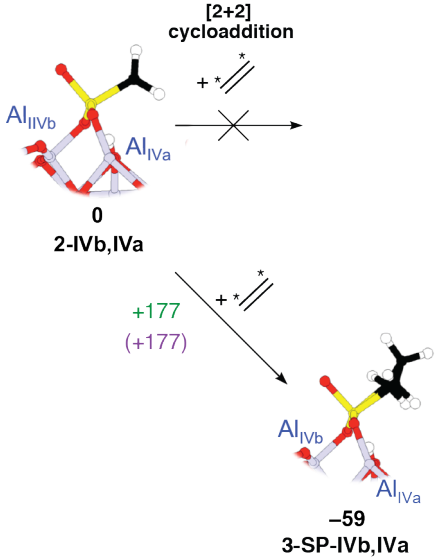

Figure 3. 8. Calculated structures, transition state energies and barrier energies of the intermediates of CH_3ReO_3/Al_2O_3 in the metathesis of ethylene starting from **2-IVb,IVa** on s0. Transition state energies are in green and activation energies are in purple. Values are in kJ mol^{-1}

3.5 Effect of partial hydration of the surface on CH_3ReO_3/Al_2O_3

Complete dehydration of γ-alumina is not possible without phase transition to θ/α phases.[30] We investigated the effect of one (**s1**) or two (**s2**) water molecules per unit cell (corresponding to 3 and 6 OH nm^{-2}) on the stability, structure and reactivity of **1**. In order to have a common reference to the **s0** surface discussed above, Re is attached to the same Al sites and the proton resulting from the C-H bond activation of the methyl group resides on the same oxygen atom.

*3.5.1 Structure, relative energies and interconversion of **0**, **1** and **2** on **s1** and **s2** surfaces.*

The stability of the mono-grafted and bis-grafted Re-oxo species on **III**, **III,IVb** and **IVa,IVb** was evaluated on **s1** (Table 3.3). The adsorption energy for **0-III** is –116 kJ mol^{-1}, slightly lower than on **s0**. **0-III,IVb** and **0-IVa,IVb** have adsorption energies of –184 and –91 kJ mol^{-1}, respectively. The conversion of **0-IVa,IVb** to **1-III,IVb** species has an activation energy of 116 kJ mol^{-1}, whereas the conversion of **0-III** to **1-IVb,III** has a very low activation energy of only 21 kJ mol^{-1}.

The formation of **1-IVb,III** from **0-III** is therefore easier than the formation of **1-III,IVb** from **0-IVa,IVb**, on both **s0** and **s1** surfaces

The adsorption energy of CH_3ReO_3 on alumina to form **1–III,IVb** changes from –233 kJ.mol^{-1} on **s0** to –203 kJ.mol^{-1} on **s1** and –104 kJ.mol^{-1} on **s2**, respectively (Table 3.3, for the structures see Figures A.3.8-12). This result indicates that the μ-methylenes are less stable when the surface is partially hydroxylated. The Re-C bonds are elongated by surface hydration from 2.00 Å on **s0** to 2.02 Å on **s1** and 2.11 Å on **s2** (Table A.3.1). A similar trend is observed for the oxo ligand coordinated to the surface (1.79 Å on **s0**, 1.78 A on **s1**, and 1.84 Å on **s2**), but not for the rhenium – oxo pointing away from the surface (1.72 Å for all the three degrees of hydration). The observed variations in bond distances are associated with an increased coordination number at Re, going from 4 (pseudo-tetrahedral) on both **s0** and **s1** to 5 (distorted trigonal bipyramidal) on **s2**. **1-IVb,III** experiences a similar trend in adsorption energies going from –211 kJ mol^{-1} on **s0** to –140 kJ mol^{-1} and –97 kJ mol^{-1} on **s1** and **s2**, respectively. The coordination numbers at Re follows a similar trend as found for **1–III,IVb**. The adsorption energy for **1-IVa,IVa** is –90 kJ mol^{-1} on **s0** and only –14 kJ mol^{-1} on **s1**, leading to similar pseudo-tetrahedral structures. No reasonable low energy structure was found for that site on **s2**, due to profound changes of the alumina surface at this level of hydration.[30,54]

The adsorption energy of **1-IVb,IVa** increases from –129 kJ mol^{-1} on **s0** to –109 kJ mol^{-1} on **s1**. However, it strongly decreases on **s2** (E_{ads} = –168 kJ mol^{-1}). **1-IVa,IVb,** follows a similar trend with stronger adsorption on **s2** (-140 kJ mol^{-1}) than on **s1** (–66 kJ mol^{-1}) and **s0** (–96 kJ mol^{-1}). In both cases, the pseudo-octahedral geometry of Re is not affected by hydration, and the increase in adsorption energy upon hydration for these hexacoordinated Re sites is probably associated with the increase basicity of surface oxygen atoms coordinated to Re upon adsorption of H_2O.[30,54]

Hydration also decreases the stability of **2-III,IVb** with E_{ads} = –269 kJ mol^{-1} on **s0**, to –193 on **s1**, and –136 kJ mol^{-1} on **s2** (Table 3.3). **1-III,IVb** is more stable than **2-III,IVb** on **s1** and **s2** by 10 kJ mol^{-1} and 32 kJ mol^{-1}, respectively. However, **2-III,IVb** is more stable than the **1-III,IVb** on **s0**, indicating that hydration destabilizes **2** more than **1**. On the other sites, hydration leads to similar trends for the relative stability of **1** and **2**. Note that upon hydration, the surface becomes more flexible, and

thus the coordination number of the Re center becomes higher.[54] Indeed, on **s0** and **s1** surfaces, **2-III,IVb** is 4-coordinate whereas on **s2** surface the complex becomes 5-coordinate.

Table 3. 3. Adsorption sites, symmetry at Re (G.), and adsorption energies (E_{ads}) for the oxo-species (**0-A,B**), μ-methylene species (**1-A,B**) and methylidene species (**2-A,B**) on partially hydrated γ-Al_2O_3 (110) surfaces (**s1** and **s2**) and transition state energies and barriers for the their interconversion. All energies are in kJ mol^{-1} (Figures A.3.8-12 for the structures).

si	0-A,B	G.[a]	E_{ads} (ΔE)[b]	1,A,B	G.[a]	E_{ads} (ΔE)[c]	$[TS]^{\ddagger}$	$E^{\ddagger}$
s1	IVa,IVb	P	-91 (-202)	-[d]	-[d]	-[d]	-[d]	-[d]
s1	III,IVb	P	-184 (-224)	III,IVb	T	-203 (-112)	+25	116
s1	III,-	P	116 (–144)	IVb,III	T	–140 (–24)	95	21
si	**1-A,B**	G.[a]	E_{ads}[b]	**2-A,B**	G.[a]	E_{ads}[c] (ΔE)	$[TS]^{\ddagger}_{\mu\rightarrow ene}$	$E^{\ddagger}_{\mu\rightarrow ene}$
s1	III,IVb	T	–203 (–233)	III,IVb	T	–193 (**+**10)	–4	+199
s2	III,IVb	P	–104	III,IVb	P	–136 (–32)	**+**52	+156
s1	IVb,III	T	–140 (211)	III,IVb	T	–193 (–53)	–126	+14
s2	IVb,III	P	–97	III,IVb	P	–136 (–39)	–77	+20
s1	IVa,IVa	T	–14 (–90)	IVa,IVa	T	–51 (–37)	+52	+66
s2	-[d]	-[d]	-[d]	IVa,IVa	-[d]	-[d]	-[d]	-[d]
s1	IVb,IVa	O	–109 (–129)	IVb,IVa	O	–121 (–12)	-[d]	-[d]
s2	IVb,IVa	O	–168	IVb,IVa	O	–139 (+47)	-[d]	-[d]
s1	IVa,IVb	O	–66 (–96)	IVb,IVa	O	–121 (–55)	-[d]	-[d]
s2	IVa,IVb	O	–140	IVb,IVa	O	–139 (+19)	-[d]	-[d]

[a] Symmetry of the surface Re species: T = pseudo tetrahedral, P = pentacoordinated and O = pseudo octahedral. [b] The numbers in parentheses are the adsorption energies of 0-A,B on s0. [c] The energy in parentheses (ΔE) corresponds to the difference in stability of the Re-oxo and the μ-methylene species: $\Delta E = E_{ads}(\mu\text{-}CH_2) - E_{ads}$(Re-oxo). $E^{\ddagger}$ corresponds to the activation energy from the Re-oxo to the corresponding transition-state structure. [d] The numbers in parenthesis are the adsorption energies of 1-A,B on s0. [e] The energy in parentheses (ΔE) corresponds to the difference in stability of the alkylidene and the μ-methylene species: $\Delta E = E_{ads}$(alk) – $E_{ads}(\mu\text{-}CH_2)$. [f]: No transition state could be located.

The interconversion of **1-III,IVb** to **2-III,IVb** is associated with high-energy barriers (> 150 kJ mol^{-1}) on all surfaces, and is unlikely to generate the alkylidene active species (Structure of the transition state are available Figure A.3.13). In contrast, the interconversion of **1-IVb,III** to **2-III,IVb** becomes nearly barrierless upon hydration (14 kJ mol^{-1} for **s1** and 20 kJ mol^{-1} for **s2** vs. 49 kJ mol^{-1} for **s0**). **2–IVa,IVa** has also a lower interconversion barrier (66 kJ mol^{-1} for **s1** vs 95 kJ mol^{-1} for **s0**). The TS from either **1-IVb,IVa** or **1-IVa,IVb** to form **2-IVb,IVa** could not be located. Although the calculations show that the methylidene (**2**) should be more stable than μ-methylene (**1**) species, except for **III,IVb** on **s1**, while only μ-methylene species are observed experimentally. This discrepancy could arise from the idealized

structures of our models compared to the real surface structures. In addition, the alkylidenes have also rather large chemical shift anisotropies (vide infra) and undergo dynamic exchange on the surface, which could prevent detection of these sites using solid-state NMR.[67] However, the computational data shows that co-adsorbtion of water and CH_3ReO_3 decreases the stability of tetrahedral Re sites, both in their μ-methylene and alkylidene forms, and decreases the energy differences between the two, suggesting that adsorbed water may play a critical role in determining the energy difference between the various species.

*3.5.2 Reactivity of **2**, formation and structure of metallacycle **3** on **s1** surface.*

The **s1** surface has an OH density (3 $OH.nm^{-2}$) close to the experimental surface for dehydroxylation temperature above 500°C. The structures of the metallacycles on **s1** are very similar to those on **s0** (Figure A.3.14 and Tables A.3.6-7).

Overall, the metathesis pathway and the structures of the reaction intermediates are not greatly affected by hydration. Compared to the **s0** surface, formation of the SP-metallacyclobutanes is more difficult upon hydration of the surface, while formation of the TBP metallacyclobutane is almost barrierless on the **s1** surface.

Table 3. 4. Energies of transition state structures and reaction intermediates with the corresponding energy barriers for elementary steps for ethylene metathesis on **2** adsorbed on the partially hydrated γ-Al_2O_3 (110) surface (**s0**) (kJ mol-1).

A,B	**2-A,B**	**3-TBP-A,B**	**3-SP-A,B**		$[TS]^{‡}_{[2+2]\text{-TBP}}$
III/IVb	0	–34	–78		+ 12
IVa/IVa	0	–-19	–63		+ 45
	$[TS]^{‡}_{[2+2]\text{-SP}}$	$[TS]^{‡}_{TBP\rightarrow SP}$	$E^{‡}_{TBP\text{ -}SP}$	$E^{‡}_{cyclo}$	$E^{‡}_{SP\text{ -}TBP}$
III/IVb	+ 172	+ 81	+ 115	+ 46	+ 159
IVa/IVa	+ 171	+ 58	+ 77	+ 64	+ 121

[a]: the structure or the transition state energies could not be located.

Cycloaddition, TBP to SP isomerization, and cycloreversion, follow similar trends as on the **s0** surface. On **s1**, the reaction of **2-III,IVb** with ethylene to form **3-TBP-III,IVb** is exoenergetic by 34 kJ mol^{-1} and associated with a barrier of +12 kJ mol^{-1}. The TBP to SP interconversion process has a higher barrier than cycloreversion, independent of hydration level. As on the **s0** surface, this site is highly active for metathesis. Also similar to what was calculated for the **s0** surface, **2-**

IVa,IVa competitively forms the SP metallacycle by a turnstile process from the TBP isomer, indicating this site is less active than **2-III,IVb**.

For example, on **s1**, the formation of SP- and TBP-metallacycles **3-TBP-III,IVb** or **2-SP-III,IVb)** from the alkylidene (**2–III,IVb**), and ethene is exoenergetic by 34 kJ.mol^{-1} and 78 kJ.mol^{-1}, respectively. Similar to the **s0** surface, the direct formation of **3-SP-III,IVb** from **2–III,IVb** has a high energy TS (+171 kJ.mol^{-1}) compared to **3-TBP-III,IVb**, which has a barrier of only +12 kJ.mol^{-1} (Figure 3.9).

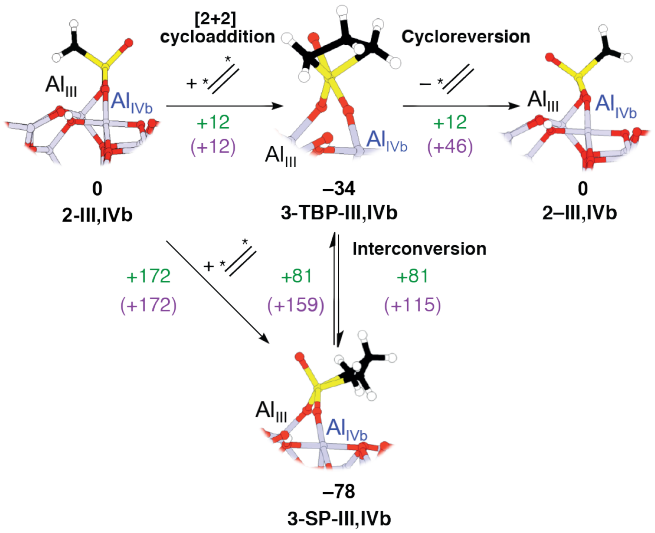

Figure 3. 9. Calculated structures (including transition states) and activation energies of the intermediates of CH_3ReO_3/Al_2O_3 in the metathesis of ethylene starting from **2-III,IVb** on s1. Transition state energies are in green and activation energies are in purple. Transition states structures are available Figure A.3.15. Values are in kJ mol^{-1}

The formation of both TBP and SP-metallacyclobutanes is still exoenergetic for Al_{IVa}/Al_{IVa} alumina sites on **s1** surfaces with relative energy with respect to separated reactants of (ethene + alkylidene) of –19 kJ.mol^{-1} and –63 kJ.mol^{-1} for **3-TBP-IVa,IVa** and **3-SP-IVa,IVa**, respectively (Figure 3.10). The direct formation the SP complex is still associated with an energy barrier of +171 kJ.mol^{-1} whereas the formation of TBP metallacyclobutane has a barrier of 45 kJ.mol^{-1}, hardly affected by the hydration of the surface (Figure 3.10). The metallacycles have very similar structural characteristics on the **s1** and **s0** surfaces: **3-TBP-IVa,IVa** has a flat metallacycle (W(Re-C-C-C) = ca. 0°) with a short Re-b-carbon bond distance of 2.42 Å, while the **3-SP-IVa,IVa** is puckered (W(Re-C-C-C) = 25°) with a long Re-b-carbon bond distance of 2.83 Å and an axial oxo ligand. On Al_{IVa} and Al_{IVa} alumina sites, the barrier for inverconversion from **3-TBP-IVa,IVa** to **3-SP-IVa,IVa** is associated with an energy of 58 kJ.mol^{-1}, only 13 kJ.mol^{-1} higher in energy than

cycloreversion (45 kJ.mol^{-1}), making such sites prompt towards the formation of the more stable SP-metallacycle and thus making this site a reservoir of less active species.

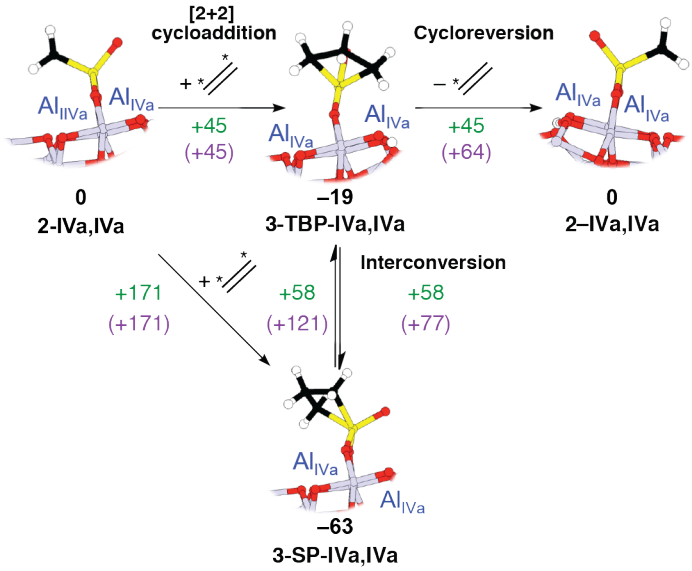

Figure 3. 10. Calculated structures (including transition states) and activation energies of the intermediates of CH_3ReO_3/Al_2O_3 in the metathesis of ethylene starting from **2-IVa,IVa** on **s1**. Transition state energies are in green and activation energies are in purple. Values are in kJ mol^{-1}.

3.6 NMR signatures and Projected Density of State (PDOS) study.

3.6.1 NMR signatures of surface sites and reaction intermediates.

The chemical shift anisotropy (CSA) tensor provides information about the electronic environment at a nucleus, in our case carbon.[29,68] The CSA, in the Herzfeld-Berger convention, is described by the isotropic chemical shift (δ_{iso}, eq 4), the span (Ω, eq 5) and the skew (κ, eq 6), which can be derived from the principal tensor components δ_{11}, δ_{22}, and δ_{33}[69]:

$$\delta_{iso} = (\delta_{11} + \delta_{22} + \delta_{33})/3 \qquad (4)$$

$$\Omega = (\delta_{11} - \delta_{33}) \qquad (5)$$

$$\kappa = 3(\delta_{22} - \delta_{iso})/\Omega \; ; -1 \leq \kappa \leq +1 \qquad (6)$$

δ_{iso} corresponds to the average of δ_{11}, δ_{22}, and δ_{33}, the Ω and κ describe the magnitude of the CSA and the axial symmetry of the tensor, respectively.

The ^{13}C CSA for **1-A,B** and **2-A,B** were calculated, and the results are summarized in Table 3.5-6. For **1-A,B**, the calculated δ_{iso} of the μ-methylene carbon ranges from 54 ppm to 100 ppm, significantly downfield from CH_3ReO_3 (calculated chemical shift of 11 ppm).[70] Octahedral **1–IVa,IVb** and **1– IVb,IVa** have δ_{iso} of 54 and 57 ppm with a Ω of *ca*. 100 ppm. Tetrahedral Re-μ-methylene species have δ_{iso} of 82 and 100 ppm with large span values of 128 – 190 ppm. Sites containing Al_{III} have larger span than those containing only Al_{IV}. The NMR parameters of **2-A,B** do not depend on the Al-site: the isotropic chemical shifts are between 201 and 232 ppm with large Ω of 400-456 ppm (Table 3.5-6), which is typical for metal alkylidenes.[7] Though the alkylidene and μ-methylene have very different NMR signatures, the relatively large span and the distribution of sites expected for the alkylidene suggests that they will be more difficult to observe in CH_3ReO_3/Al_2O_3 under standard solid-state NMR conditions (CP-MAS of 10 kHz), especially considering their relative low amount.[29]

Table 3. 5. Calculated ^{13}C NMR chemical shift parameters in ppm (δ_{iso}, Ω and κ) of **1-A,B** and **2-A,B** found on the **s0** Al_2O_3 surface.

A,B	**1-A,B**			**2-A,B**		
	δ_{iso}	Ω	k	δ_{iso}	Ω	k
III,IVb	82	141	0.7	210	405	0.7
IVb,III	100	190	0.8	210	405	0.7
IVa,IVa	88	128	0.8	201	400	0.7
IVb,IVa	57	108	0.4	204	423	0.8
IVa,IVb	54	99	0.7	204	423	0.8

[a] The structure could not be located.

The calculated NMR properties of **1** and **2** on **s1** and **s2** are qualitatively similar to those calculated on the **s0** surface (Table 3.6). For **1–III,IVb**, the structural changes caused by hydration of the surface are accompanied by a decrease of the calculated chemical shift from 82 ppm for **s0** to 77 ppm for **s1** to 69 ppm and **s2**. The span also decreases as hydration increases. In contrast, the chemical shift of **1–IVb,III** stay relatively constant upon hydration. However, the span is particularly high on this site and tends to the span of an alkylidene ligand (Table 3.5 and 3.6). Experimentally a broad peak centered at 66 ppm was assigned to the **1-A,B** species. We therefore obtain a reasonable fit between experiment and calculated chemical shift

as they are comprised between 54 and 111 ppm with most of them at *approx*. 50-80 ppm.

Table 3. 6. Calculated ^{13}C NMR chemical shift parameters in ppm (δ_{iso}, Ω and κ) of the different μ-methylene and methylidene found stable on the **s0**, **s1** and **s2** Al_2O_3 surfaces.

A,B-sites	**1-A,B**			**2-A,B**		
	δ_{iso}	Ω	k	δ_{iso}	Ω	k
III,IVb-s1	77	121	0.7	228	446	0.7
III,IVb-s2	69	72	0.7	211	414	0.8
IVb,III-s1	82	214	0.8	228	446	0.7
IVb,III-s2	111	192	0.9	211	414	0.8
IVa,IVa-s1	87	170	0.8	216	427	0.7
IVb,IVa-s1	69	119	0.7	232	456	0.7
IVb,IVa-s2	68	122	0.7	222	431	0.7
IVa,IVb-s1	69	136	0.7	232	456	0.7
IVa,IVb-s2	93	140	0.7	222	431	0.7

The NMR signatures of **3** for **s0** surface were calculated and are summarized in Table 3.7. The NMR parameters do not vary greatly between Al sites and surface hydration, but are characteristic of the geometry of the metallacycle. The isotropic chemical shift of the α-carbon in **3-TBP** is 105 ppm with spans ranging between 168 and 175 ppm. The calculated isotropic shift for the β-carbon in **3-TBP** is 16 ppm with a span of 84 – 90 ppm. Experimentally, we found 120 ppm for α-carbon of **3-TBP** and 19 ppm for the β-carbon of **3-TBP** which is in agreement with calculations. For **3-SP,** the isotropic chemical shifts of the α- and β-carbons range from 29 – 67 ppm, where we found experimentally 43/36 ppm.

Table 3. 7. Calculated ^{13}C NMR chemical shift parameters in ppm (δ_{iso}, Ω and κ) of 3 on s0 surface.

		3-TBP-A,B			**3-SP-A,B**		
Sites A,B	C	δ_{iso}	Ω	k	δ_{iso}	Ω	k
III,IVb	α	105	168	0.2	56	65	0.2
	β	16	84	0.6	35	15	0.3
IVa,IVa	α	105	175	0.3	42	43	0.4
	β	16	90	0.6	29	25	0.8
IVb,IVa	α	-[a]	- a	- a	67	87	0.2
	β	- a	- a	- a	39	14	0.6

[a]:TBP metallacyclobutane could not be located on Al_{IVb},Al_{IVa}.

The span of the β-carbons in **3-SP** are larger than those for the α-carbons. These data indicate that the NMR properties of the TBP and SP isomers are different, and distinguishable by NMR spectroscopy, as found experimentally for isoelectronic Mo and W complexes.[17,19,67] Surface hydration has almost no effects on the chemical shift anisotropy tensor of the metallacyclobutane **3-SP** and **3-TBP** (Table 3.8).

Table 3. 8. Calculated ^{13}C NMR chemical shift parameters in ppm (δ_{iso}, Ω and κ) of **3** on **s1** surface.

		3-TBP-A,B			**3-SP-A,B**		
Sites A,B	C	δ_{iso}	Ω	κ	δ_{iso}	Ω	κ
III,IVb	α	104	126	0.5	57	54	0.5
	β	18	53	0.9	27	30	0.7
IVa,IVa	α	106	170	0.5	49	43	0.5
	β	18	87	0.6	32	18	0.8
IVb,IVa	α	-[a]	-[a]	-[a]	64	60	0.4
	β	-[a]	-[a]	-[a]	40	15	0.9

[a]: TBP metallacyclobutane could not be located on Al_{IVb},Al_{IVa}.

3.6.2 Relationship between NMR signature and reactivity.

The most active metathesis site (**1-IVb,III**) displays a very specific NMR signature, in particular a larger calculated span than on other sites. We therefore analyzed the projected density of state (PDOS) on the s and p orbitals of the C atom in **1-III,IVb**, **1-IVb,III**, and **2-III,IVb** (Table 3.9) and compared it with CH_3ReO_3 and its enolic form $CH_2Re(OH)O_2$. The HOMO is essentially composed of the *p* orbitals perpendicular to the CH_2 plane for the molecular Re complex (Figures A.3.16-18). In CH_3ReO_3/Al_2O_3 a similar pattern of peaks arises, but these peaks are shifted. By comparing the HOMO energy of the grafted fragments in **1-IVb,III** and **1-III,IVb** with the corresponding alkylidenes (**2-III,IVb**), we can define the alkylidene character of the μ-methylene species; the closer the energies the higher the alkylidene character. The energy of the HOMO (with main character p on C) in the PDOS for the **1-IVb,III**, **1-III,IVb** and **2-III,IVb** is reported as a function of surface hydration in Table 3.9. The compilation of the PDOS for all the previously described μ-methylene and alkylidene species on all the Al sites can be found in the ESI (Figures A.3.19-34).

Table 3. 9. Position of the HOMO in the PDOS graph for the alkylidene and the μ-methylene formed on Al_{III} and Al_{IVb} sites on the **s0**, **s1** and **s2** surfaces.

Species	p orbital Position in PDOS graph (in eV)[a]
s0 surface	
2-III,IVb	-5.64
1-IVb,III	-6.72
1-III,IVb	-6.87 (minor) and -7.19
s1 surface	
2-III,IVb	-5.61
1-IVb,III	-6.26 and -6.58
1-III,IVb	-6.58 (minor) and -7.23
s2 surface	
2-III,IVb	-5.02
1-IVb,III	-5.73
1-III,IVb	-6.70 and -7.02

[a]: To allow a comparison between the surfaces, the vacuum potential (plane-average electrostatic potential of an electron in the z-direction) of the unit cell far from the surface for every adsorbate-surface system was used as reference value.

On the **s0** surface, the energy of the HOMO p orbital in **2-,III,IVb** is –5.64 eV (Table 3.9). The HOMO of p-character in **1-IVb,III** is closer in energy to **2-III,IVb** than the corresponding orbital in **I-III,IVb**. This suggests that the **1-IVb,III** species has a higher alkylidene character than the **1-III,IVb** species. As the surface becomes hydrated the HOMO in **2-III,IVb** shifts to higher energies. A similar shift to higher energies is also experienced by the HOMOs of **1-IVb,III** and **1-III,IVb**. The HOMO in **1-IVb,III** on the **s2** surface is at -5.73 eV, significantly closer in energy to **2-III,IVb** (-5.02 eV) than **1-III,IVb** (-6.70 eV). Overall, **1-IVb,III** has more alkylidene character than **1-III,IVb**, in particular on the **s1** and **s2** surfaces

3.7 Discussion.

Activation of alumina above 500 °C (≤ 4 $OH.nm^{-2}$) is an essential step to obtain active CH_3ReO_3/Al_2O_3 metathesis catalysts. Titration of active sites with ^{13}C-dilabelled ethylene and NMR spectroscopy of CH_3ReO_3/Al_2O_3 indicated a distribution of Re sites in these catalysts. Although no alkylidene species could be observed, metallacycle intermediates were detected by solid-state NMR spectroscopy in the presence of ^{13}C enriched ethylene.

DFT calculations showed that bis-Re-oxo (**0-A,B**) and m-methylene (**1-A,B**) species are accessible. **1-A,B** forms by the activation of a C-H bond in $MeReO_3$

across a surface Al,O bond. In **1-A,B**, aluminum A coordinates to the m-methylene and B to a Re=O; a proton is present on a nearby O atom. **1-III,IVb** is the thermodynamically preferred m-methylene species for all the hydroxylation levels studied (**s0**, **s1** and **s2** surfaces). While **1-IVb,III** is slightly less stable (by 22 to 63 kJ mol^{-1} for **s0** and **s1** resp.), it is the kinetically preferred m-methylene (obtained through pathways with lower activation energies). Considering the experimental conditions and the non-uniform hydroxylation state of alumina, a mixture of di-oxo grafted and m-methylene species on the various Al sites is expected to be formed.

A first question to answer is the origin of the low activity of CH_3ReO_3 on alumina pretreated at a temperature of only 300 °C. Indeed, at this temperature the Al_{III} defect sites of Al_2O_3 are occupied by water molecules and are not accessible to bind N_2 or activate H_2 or CH_4. The reason for the activity of CH_3ReO_3 supported on alumina activated at 300 °C can be understood by looking at the co-adsorption energy (E_{coads}) of CH_3ReO_3 and i water molecules per unit cell, taking the **s0** surface as common reference (eq. 7). It allows comparing the stability of isomers and to check whether adsorption of water is less or more favorable than that of CH_3ReO_3:

$$E_{coads} = E(\mathbf{si} + CH_3ReO_3) - E(CH_3ReO_3) - \mathbf{i} * E(H_2O) - E(\mathbf{s0}) \quad (7)$$

Where **si** defines the surface with i the number of H_2O molecules.

We also define the co-adsorption energy of water on the surface of alumina (eq. 8):

$$E_{coads} = E(\mathbf{si}) - \mathbf{i} * E(H_2O) \quad (8)$$

The calculated energies of co-adsorption of CH_3ReO_3 and water on the alumina sites (E_{coads}) are reported in Table 3.10.[54] The E_{coads} of CH_3ReO_3 and H_2O is stronger than the adsorption of only water. Thermodynamically, this result suggests that, if the most Lewis acidic sites are occupied by adsorbed water, CH_3ReO_3 should be able to displace H_2O to generate the μ-methylene sites (Table 3.10). At 300 °C the Al_{III} defect sites of Al_2O_3, which bind N_2 or activate H_2 or CH_4, are occupied by water molecules.[30,54]

Table 3. 10. Co-adsorption energy of **1-III,IVb**, **1-IVb,III** and water as a function of OH coverage on alumina surface.

Water Coverage OH.nm^{-2}	E_{coads} **1-III,IVb** (kJ mol-1)	E_{coads} **1-IVb,III** (kJ mol-1)	E_{coads} **H_2O** (kJ mol-1)
0	–233	–211	0
3	–373	–318	–226
6	–503	–496	–406

However, CH_3ReO_3/Al_2O_3 does have measurable metathesis activity when supported on alumina activated at 300 °C. The displacement of adsorbed water by CH_3ReO_3 is consistent with the E_{coads} in Table 8 and experimental observations. For example, the μ-methylene species **II** is observed by NMR spectroscopy on alumina dehydroxylated at 300 °C (Figure 3.11).

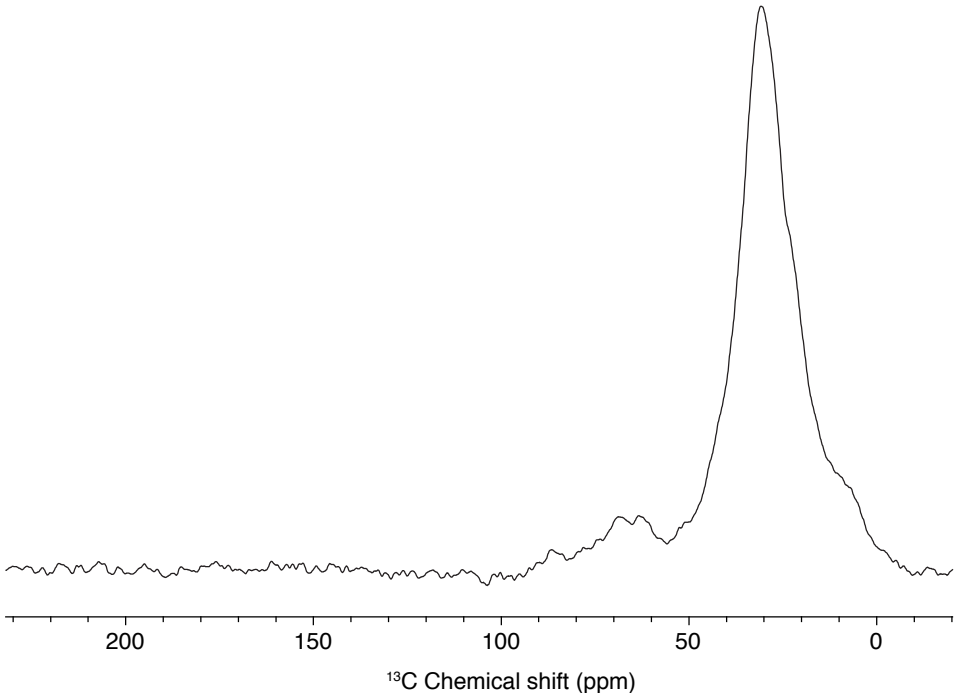

Figure 3. 11. ^1H-^{13}C CPMAS (700 MHz) of CH_3ReO_3 supported on Al_2O_3 dehydroxylated at 300°C. The number of scans was set to 5k and the recycling delay was set to 1 sec. The contact time was set to 500 μsec.

This is also consistent with the observation of broad OH bands upon adsorption of CH_3ReO_3 by IR spectroscopy, suggesting restructuring of surface OH upon adsorption of CH_3ReO_3 on Al_2O_3. [28,49]

A second question concerns the presence of different μ-methylene sites and their different activity in metathesis. The isomerisation of the m-methylene **1-III,IVb** into the methylidene **2-III,IVb** is associated with a very high energy barrier (200 kJ

mol^{-1} for **s0**, 199 kJ mol^{-1} for **s1** and 156 kJ mol^{-1} for **s2**), indicating that metathesis is unlikely at this site. **1-IVb,IVa** and **1-IVa,IVb** are calculated to be unreactive because of very high energy barriers for [2+2] cycloaddition. These results are consistent with the experimental observation that some m-methylene species do not react with ethylene. Of the other possible combinations, 1-IVa,IVa can kinetically form active species. Although the adsorption of CH_3ReO_3 on two adjacent Al_{IVa} sites is not associated with particularly high adsorption energies (–90 kJ mol^{-1} on s0, -51 kJ mol^{-1} on s1), Al_{IVa} sites are typically free of adsorbed H_2O at low OH coverage. However, on these sites, the TBP metallacycle easily interconvert into the more stable and less reactive SP isomer, which will lead to less active sites.

The third question is the optimal structure for the active sites for metathesis. **1-IVb,III** is only slightly less thermodynamically stable than **1-III,IVb**. However, interconversion of **1-IVb,III** into **2-III,IVb** has a low barrier. Subsequent [2+2] cycloaddition of **2-III,IVb** and ethylene to form the TBP-metallacyclobutane, and the cycloreversion have low barriers on this site. Equally important, the TBP to SP interconversion, a source of resting-state SP metallacycles, has a higher barrier than cycloreversion, making that site particularly active for metathesis.

The computational data suggests that the TBP and SP metallacycles observed by NMR spectroscopy are associated with **1-IVb,III** and **1-IVa,IVa** sites, respectively. The computational data also indicates that the "defect" sites in alumina (Al_{III}) are key to generate highly active sites. From the computed catalytic reactions the metathesis activity of the different m-methylene sites will follow this order: **1-IVb,III** > **1-IVa,IVa** >> **1-III,IVb**, **1-IVb,IVa**, **1-IVa,IVb**.

A characteristic feature of each m-methylene site is the calculated span value of the m-CH_2. The largest span values were computed for the most active site **1-IVb,III**. Further comparison of the PDOS of active **1-IVb,III**, inactive **1-III,IVb**, and alkylidene **2-III,IVb** showed that **1-IVb,III** has methylidene character and is therefore more prompt to generate the active sites. Taken together, the data presented here shows that the combination of Al_{III} and Al_{IVb} sites are essential for metathesis activity, and that adsorbed water assists the formation of active sites.

Finally, the fourth question concerns the optimal treatment of the alumina support. The presence of *one* adsorbed water molecule per unit cell (**s1**, 3 $OH.nm^{-2}$) leads to both easier formation of **1-IVb,III**.and easier [2+2]-cycloreversion, compared

to the fully dehydroxylated **s0** surface. Additional water molecules (**s2** surface) destabilize **1-A,B** and generate penta-coordinated Re surface species, consistent with the decrease in catalyst performance with alumina dehydroxylated at lower temperature (< 500 °C, > 6 $OH.nm^{-2}$) and the finding of an optimal activity at intermediate coverage.

3.8 Conclusion.

The resting state leading to the most active catalytic intermediate in the CH_3ReO_3/Al_2O_3 alkene metathesis catalyst is **1-IVb,III**. This m-methylene species contains a tetra-coordinate Re-oxo center bound to the alumina surface through two bonds; one between Al_{IVb} and C, and another between an Al_{III} site and an oxo ligand. The analysis of the projected density of state (PDOS) shows that the m-methylene species on **1-IVb,III** already has a stronger methylidene character than other sites. **1-IVb,III** is optimal because it can readily interconvert into the corresponding methylidene isomer, which is the catalytically active species forming with ethene the metallacyclobutane through a very low barrier (23 kJ mol^{-1}). In addition, this site allows fast cycloreversion, rather than interconversion into the more stable SP isomer. Other less active m-methylene species can also be formed, hence explaining the distribution of site strength on the catalyst and the presence of unreacted m-methylene after reaction. This study also explains the role of pre-activation temperature on metathesis activity. As the temperature increases the density of OH groups decreases, freeing Al_{III} sites to interact with CH_3ReO_3 instead of water. The presence of some adsorbed water (<3 OH nm^{-2}) increases the flexibility of the surface, resulting in a decrease of the activation barrier for the formation of methylidene and TBP metallacyclobutane intermediates. The presence of too much adsorbed water (>6 OH nm^{-2}) is enough to destabilize the formation of m-methylene species. The existence of an optimal pretreatment temperature for the alumina support used in the preparation of the CH_3ReO_3/Al_2O_3 catalyst, and the need for Lewis acidic Al_{III} sites parallels what was found for Re_2O_7/Al_2O_3. Overall, this is strong evidence for the essential role of Al_{III} "defect" sites in industrial Re-based metathesis catalysts.

3.9 Experimental part.

3.9.1 General procedure.

All gases were purified by passing over 4 Å molecular sieves and Ru-3/11 BASF copper catalyst prior to use. Gas chromatography measurements were performed on an Agilent Technologies 7890A GC system equipped with a flame ionization detector and a KCl/Al_2O_3 on fused silica column (50 m x 0.32 mm). Liquid state NMR spectra were performed on 200, 250, or 300 MHz Bruker spectrometers. Solid state NMR was performed on a 700 MHz Bruker spectrometer equipped with a 4 mm double resonance probe head. The ^1H radio frequency field was set to 100 kHz for cross polarization (CP-MAS) and heteronuclear correlation (HETCOR) spectroscopy. A 1 sec recycle delay was used. HETCOR was recorded with heteronuclear decoupling spinal 64 at the same RF field and homonuclear ^1H DUMBO decoupling was used. The states-TPPI procedure was applied to achieve quadrature detection in the indirect dimension. Acetonitrile was purchased from Sigma-Aldrich and purified by distillation over CaH_2. Re_2O_7 was purchased from Strem and used as received. Tributylmethyltin and trifluoroacetic anhydride were purchased from Sigma-Aldrich and distilled prior to use. ^{13}C labeled ethylene was purchased from Cortecnet and stored over 4 Å molecular sieves and Ru-3/11 BASF copper catalyst prior to use. Alu C was obtained from Evonik and agglomerated to large particles by suspending in distilled water, drying at 100 °C and sieving (grain size 250-400 μm) for easier handling. Sieved Al_2O_3 was calcined under a flow of synthetic air for 12 hours at 500°C (ramp of 4 °C.min^{-1}). The atmosphere was removed under vacuum (10^{-5} mBar) while the reactor was still hot and the alumina was stored in an Ar glove box.

3.9.2 Syntheses and reactions with CH_3ReO_3/Al_2O_3.

3.9.2.1 Synthesis of methyltrioxorhenium (CH_3ReO_3).

This synthesis was inspired from a procedure found in the literature.[71] A solution of Re_2O_7(2.5 g, 5.16 mmol, 1 equiv.) in 40 mL of acetonitrile was treated with trifluoroacetic anhydride (1.08 g, 5.16 mmol) at room temperature. After few minutes, tributylmethyltin (3.14 g, 10.3 mmol, 2 equiv) was added, and the reaction mixture was stirred for 3 h at room temperature. Acetonitrile was then carefully removed at 0°C, and the resulting oil was distilled under high vacuum (10^{-5} mBar).

The resulting powder was then sublimed yielding to a colorless compound (yield of 47%). ^{1}H liquid state NMR (200MHz), C_6D_6, δ (ppm): 1.13 (s).

3.9.2.2 Synthesis of ^{13}C Tributylmethyltin.

To a solution of magnesium turnings (0.16 g, 6.7mmol, 1.21 equiv) were added dropwise a solution of ^{13}C-labeled iodomethane (0.79 g, 5.5 mmol, 1.1 equiv). The reaction was left at room temperature until the partial disappearance of solids (about 1 h). Tributyltinchloride (1.6 g, 5 mmol, 1 equiv) was then added via syringe. After stirring the reaction mixture for 1 h, the resulting mixture was quenched with HCl (0.1 M) and the organic phase was extracted 3 times with 30 mL of diethyl ether. After drying over $MgSO_4$, all the volatile were removed, and the resulting oil was distilled (244°C at 80 mBar) yielding to a colourless oil. ^{1}H liquid state NMR (200MHz), C_6D_6, δ (ppm): –0.23 and 0.23 (Sn-$^{13}C\mathbf{H_3}$, 3H, double triplet), 0.94 (Sn-CH_2-CH_2-C$\mathbf{H_3}$, 14H, t), 1.35 (Sn-CH_2-C$\mathbf{H_2}$-CH_3, 6H, m) and 1,52 (Sn-C$\mathbf{H_2}$-CH_2-CH_3, 6H, m).

3.9.2.3 Synthesis of ^{13}C labelled methyltrioxorhenium ($^{*}CH_3ReO_3$).

This synthesis was inspired from a procedure found in the literature.[71] A solution of Re_2O_7(0.87 g, 1.8 mmol, 1 equiv) in 40 mL of acetonitrile was treated with trifluoroacetic anhydride (0.37 g, 1.8 mmol) at room temperature. After few minutes, the ^{13}C labeled tributylmethyltin (1.1 g, 3.6 mmol, 2 equiv) was added, and the mixture was stirred for 3 h at room temperature. Acetonitrile was then carefully removed at 0 °C, and the resulting mixture (oil) was distilled under high vacuum. The resulting powder was then sublimed yielding to a colorless compound (yield= 47%). ^{1}H liquid state NMR (200MHz), C_6D_6, δ (ppm): 1.0 and 1.7 (Sn-$^{13}CH_3$, 3H, s). The proton NMR gave to major peak due two the ^{13}Carbon-Proton coupling.

3.9.2.4 Acitvation of Al_2O_3 at temperatures below 500°C.

500 mg of the calcined support was rehydrated (with de-gassed ultra pure water) for 1h at room temperature and treated under high vacuum at the desired temperature (200 to 400 °C) for 16 hours with a 4 °C.min^{-1} ramp.

3.9.2.5 Preparation of the CH_3ReO_3 or $*CH_3ReO_3$ supported on Al_2O_3 dehydrated at X °C. CH_3ReO_3/Al_2O_{3-X}.

In a 350 mL reactor equipped with breakable seal, 500 mg of γ -Al_2O_3 was treated under vacuum (10^{-5} mBar) at the desired temperature (from 200 to 1000°C) for 16 h (ramp of 4 °C.min^{-1}).[28] 50 mg of CH_3ReO_3 or ^{13}C- CH_3ReO_3 was sublimed and the solid mixture slowly stirred. After 3 h of reaction, the excess molecular complex was removed by reverse sublimation at room temperature under high vacuum (10^{-5} mBar) for 30 min yielding a dark powder. Elemental analysis for CH_3ReO_3/Al_2O_{3-X}: X = 200 °C Re = 6.44 wt%; X = 500 °C Re = 5.63 wt%; X = 700 °C Re = 6.37 wt% and X = 900 °C Re = 6.02 wt%.

3.9.2.6 Reaction of ^{13}C di-labelled ethylene with CH_3ReO_3/Al_2O_3.

CH_3ReO_3/Al_2O_3 (300 mg) was loaded in a reactor of known volume (300 mL). Di-labelled ethylene (0.5 equiv per Re) was added to the powder. The gas phase was analyzed by GC/MS after either 30 min or 15 h to determine the ratio of ethylene isotopomers. The CH_3ReO_3/Al_2O_3 reacted with ethylene for 15h was analyzed by ^{13}C CPMAS solid-state NMR spectroscopy.

3.9.2.7 *In-situ* reaction of ^{13}C di-labelled ethylene with CH_3ReO_3/Al_2O_3 sealed in a glass insert.

CH_3ReO_3/Al_2O_{3-500} (30 mg, 5.1 10^{-3} mmol of Re) was loaded into a glass insert fitting into a 4 mm solid-state NMR rotor. ^{13}C di-labelled ethylene (2.6 10^{-3} mmol of ethylene) was added into the glass insert. The glass insert was flame-sealed, and inserted into the 4 mm rotor for solid-state NMR measurements.

3.9.3 Computational method.

The DFT calculations were performed in the Generalized Gradient Approximation (GGA) using the Perdew-Wang (PW91) functional,[72] as implemented in the VASP 4.6 code.[73,74] The Projected Augmented Wave (PAW) method was adopted.[75] A tight convergence of the plane-wave expansion was obtained with a kinetic energy cut-off of 400 eV, in accordance with the selected PAW atomic radii. The (110) surfaces of ɣ-Al_2O_3 are based on our previously established models.[74] Test calculations show that 8-layers thick slabs (unit formula $Al_{32}O_{48}$) yield converged adsorption energies. The Brillouin zone integration was performed with a 3×3×1 k-point grid generated by the Monkhorst-Pack algorithm. In order to reproduce the

properties of extended surfaces, the bottom two layers were kept fixed during the calculations at bulk coordinates, while the top layers were allowed to relax. The Climbing Image Nudged Elastic Band method (CI-NEB) was used to determine the transition states, with sets of 8 images. The transition states (TS) obtained were converged to 0.01 eV/Å forces with a quasiNewton algorithm and validated with a vibrational analysis. [76,77] For NMR calculations the Materials Studio CASTEP code (version 5.5) was used on the structures optimized with VASP. Carbon and proton chemical shifts were were referenced to tetramethylsilane. We used the PBE functional[78,79] and on-the-fly generated pseudopotentials with a cut-off energy of 490 eV. The calculations were carried out on the ETHZ "Brutus" cluster using 8 to 64 cores. Figures of the structures were produced with the XCrySDen program.[80]

For PDOS calculation, the contribution of the *s*- and *p*-orbitals of the carbon atom of CH_3ReO_3 to the density of states (DOS) was evaluated on the optimized structures of the molecule, the enolic form, the μ-CH_2 and the alkylidene species of the grafted structure. The DOS was calculated with VASP using a dense k-point grid (9x9x1) and the projected density of states (PDOS) was extracted with the p4vasp program.[80] In order to assist the interpretation of the PDOS, molecular orbital calculations were performed for MTO and its enolic tautomer. These calculations were performed with the Gaussian 09 program package using the B3PW91 density functional.[81] The LANL2DZ basis set was used[82] for Re, augmented by f-polarization functions[83], while for C, H and O the 6-311++G(d,p) basis set was used.

3.10 References.

(1) Banks, R. L.; Bailey, G. C. *Ind. Eng. Chem. Prod. Rd.* **1964**, *3*, 170.

(2) Chauvin, Y.; Commereuc, D. *J. Chem. Soc., Chem. Commun.* **1992**, 462.

(3) Ivin, K. J.; Mol, J. C. *Olefin Metathesis and Metathesis Polymerization*, 1997.

(4) Lwin, S.; Wachs, I. E. *ACS Catal.* **2014**, *4*, 2505.

(5) Schrock, R. R. *Angew. Chem. Int. Ed.* **2006**, *45*, 3748.

(6) Murdzek, J. S.; Schrock, R. R. *Organometallics* **1987**, *6*, 1373.

(7) Schrock, R. R.; Murdzek, J. S.; Bazan, G. C.; Robbins, J.; DiMare, M.; O'Regan, M. *J. Am. Chem. Soc.* **1990**, *112*, 3875.

(8) Nguyen, S. T.; Johnson, L. K.; Grubbs, R. H.; Ziller, J. W. *J. Am. Chem. Soc.* **1992**, *114*, 3974.

(9) Scholl, M.; Ding, S.; Lee, C. W.; Grubbs, R. H. *Org. Lett.* **1999**, *1*, 953.

(10) Hoveyda, A. H. *J. Org. Chem.* **2014**, *79*, 4763.

(11) Lawrenson, M. J.; A, U., Ed. M.J. Lawrenson, US Patent US3974233A, 1976.

(12) Mol, J. C. *Catal. Today* **1999**, *51*, 289.

(13) Mol, J. C. *J. Mol. Catal. A* **2004**, *213*, 39.

(14) Feldman, J.; Davis, W. M.; Schrock, R. R. *Organometallics* **1989**, *8*, 2266.

(15) Feldman, J.; Davis, W. M.; Thomas, J. K.; Schrock, R. R. *Organometallics* **1990**, *9*, 2535.

(16) Solans-Monfort, X.; Clot, E.; Copéret, C.; Eisenstein, O. *J. Am. Chem. Soc.* **2005**, *127*, 14015.

(17) Blanc, F.; Berthoud, R.; Copéret, C.; Lesage, A.; Emsley, L.; Singh, R.; Kreickmann, T.; Schrock, R. R. *Proc. Nat. Acad. Sci. U.S.A.* **2008**, *105*, 12123.

(18) Solans-Monfort, X.; Copéret, C.; Eisenstein, O. *Organometallics* **2012**, *31*, 6812.

(19) Mougel, V.; Copéret, C. *Chem. Sci.* **2014**, *5*, 2475.

(20) Mougel, V.; Santiago, C. B.; Zhizhko, P. A.; Bess, E. N.; Varga, J.; Frater, G.; Sigman, M. S.; Copéret, C. *J. Am. Chem. Soc.* **2015**, *137*, 6699.

(21) Popoff, N.; Mazoyer, E.; Pelletier, J.; Gauvin, R. M.; Taoufik, M. *Chem. Soc. Rev.* **2013**, *42*, 9035.

(22) Tian, H.; Roberts, C. A.; Wachs, I. E. *J. Phys. Chem. C* **2010**, *114*, 14110.

(23) Debecker, D. P.; Stoyanova, M.; Rodemerck, U.; Gaigneaux, E. M. *J. Mol. Catal. A* **2011**, *340*, 65.

(24) Imamoğlu, Y. *Metathesis Polymerization of Olefins and Polymerization of Alkynes*; Kluwer Academic, 1998.

(25) Moffat, A. J.; Clark, A.; Johnson, M. M. *J. Catal.* **1971**, *22*, 379.

(26) Copéret, C.; Chabanas, M.; Petroff Saint-Arroman, R.; Basset, J.-M. *Angew. Chem. Int. Ed.* **2003**, *42*, 156.

(27) Rhers, B.; Salameh, A.; Baudouin, A.; Quadrelli, E. A.; Taoufik, M.; Copéret, C.; Lefebvre, F.; Basset, J.-M.; Solans-Monfort, X.; Eisenstein, O.; Lukens, W. W.; Lopez, L. P. H.; Sinha, A.; Schrock, R. R. *Organometallics* **2006**, *25*, 3554.

(28) Salameh, A.; Joubert, J.; Baudouin, A.; Lukens, W.; Delbecq, F.; Sautet, P.; Basset, J. M.; Copéret, C. *Angew. Chem. Int. Ed.* **2007**, *46*, 3870.

(29) Blanc, F.; Basset, J.-M.; Copéret, C.; Sinha, A.; Tonzetich, Z. J.; Schrock, R. R.; Solans-Monfort, X.; Clot, E.; Eisenstein, O.; Lesage, A.; Emsley, L. *J. Am. Chem. Soc.* **2008**, *130*, 5886.

(30) Wischert, R.; Copéret, C.; Delbecq, F.; Sautet, P. *Angew. Chem. Int. Ed.* **2011**, *50*, 3202.

(31) Conley, M. P.; Mougel, V.; Peryshkov, D. V.; Forrest, W. P.; Gajan, D.; Lesage, A.; Emsley, L.; Copéret, C.; Schrock, R. R. *J. Am. Chem. Soc.* **2013**, *135*, 19068.

(32) Copéret, C.; Comas-Vives, A.; Conley, M. P.; Estes, D.; Ninez-Zarur, F.; Fedorov, A.; Mougel, V.; Nagae, H.; Zhizhko, P. *Chem. Rev.* **2015**, *in press*.

(33) Chabanas, M.; Baudouin, A.; Copéret, C.; Basset, J.-M. *J. Am. Chem. Soc.* **2001**, *123*, 2062.

(34) Chabanas, M.; Copéret, C.; Basset, J.-M. *Chem. –Eur. J.* **2003**, *9*, 971.

(35) Copéret, C. *Dalton Trans.* **2007**, 5498.

(36) Rendón, N.; Berthoud, R.; Blanc, F.; Gajan, D.; Maishal, T.; Basset, J.-M.; Copéret, C.; Lesage, A.; Emsley, L.; Marinescu, S. C.; Singh, R.; Schrock, R. R. *Chem. –Eur. J.* **2009**, *15*, 5083.

(37) Gajan, D.; Rendon, N.; Wampler, K. M.; Jean-Marie, B.; Copéret, C.; Lesage, A.; Emsley, L.; Schrock, R. R. *Dalton Trans.* **2010**, *39*, 8547.

(38) Copéret, C. *Beilstein J. Org. Chem.* **2011**, *7*, 13.

(39) Conley, M. P.; Forrest, W. P.; Mougel, V.; Copéret, C.; Schrock, R. R. *Angew. Chem. Int. Ed.* **2014**, *126*, 14445.

(40) Valla, M.; Stadler, D.; Mougel, V.; Copéret, C. *Angew. Chem. Int. Ed.* **2015**, n/a.

(41) Lwin, S.; Keturakis, C.; Handzlik, J.; Sautet, P.; Li, Y.; Frenkel, A. I.; Wachs, I. E. *ACS Catal.* **2015**, *5*, 1432.

(42) Lwin, S.; Wachs, I. E. *ACS Catal.* **2015**, *5*, 6823.

(43) Evert Verkuijlen, F. K., Johannes C. Mol, Cornelis Boelhouwer *J.C.S. Chem. Comm.* **1977**, 198.

(44) Peter Esser, A. R., Martin Sturmann, Ingo Wohrle 2001; Vol. US20030054956 A1.

(45) Salameh, A.; Baudouin, A.; Basset, J. M.; Copéret, C. *Angew. Chem. Int. Ed.* **2008**, *47*, 2117.

(46) Herrmann, W. A.; Wagner, W.; Flessner, U.; Volkhardt, U.; Komber, H. *Angew. Chem. Int. Ed.* **1991**, *103*, 1704.

(47) Buffon, R.; Auroux, A.; Lefebvre, F.; Leconte, M.; Choplin, A.; Basset, J. M.; Herrmann, W. A. *J. Mol. Catal.* **1992**, *76*, 287.

(48) Rost, A. M. J.; Schneider, H.; Zoller, J. P.; Herrmann, W. A.; Kuhn, F. E. *J. Organomet. Chem.* **2005**, *690*, 4712.

(49) Salameh, A.; Baudouin, A.; Soulivong, D.; Boehm, V.; Roeper, M.; Basset, J.-M.; Copéret, C. *J. Catal.* **2008**, *253*, 180.

(50) Moses, A. W.; Raab, C.; Nelson, R. C.; Leifeste, H. D.; Ramsahye, N. A.; Chattopadhyay, S.; Eckert, J.; Chmelka, B. F.; Scott, S. L. *J. Am. Chem. Soc.* **2007**, *129*, 8912.

(51) Verkuijlen, E.; Kapteijn, F.; Mol, J. C.; Boelhouwer, C. *J. Chem. Soc., Chem. Commun.* **1977**, 198.

(52) Valla, M.; Conley, M. P.; Copéret, C. *Catal. Sci. Technol.* **2015**, *5*, 1438.

(53) Wischert, R.; Copéret, C.; Delbecq, F.; Sautet, P. *ChemCatChem* **2010**, *2*, 812.

(54) Wischert, R.; Laurent, P.; Copéret, C.; Delbecq, F.; Sautet, P. *J. Am. Chem. Soc.* **2012**, *134*, 14430.

(55) Handzlik, J.; Sautet, P. *J. Phys. Chem. C* **2010**, *114*, 19406.

(56) Joubert, J.; Salameh, A.; Krakoviack, V.; Delbecq, F.; Sautet, P.; Copéret, C.; Basset, J. M. *J. Phys.Chem. B* **2006**, *110*, 23944.

(57) Grinev, V. E.; Khalif, V. A.; Aptekar, E. L.; Krylov, O. V. *B. Acad. Sci. U.S.S.R. Ch.* **1981**, *30*, 1338.

(58) Grinev, V. E.; Madden, M.; Khalif, V. A.; Aptekar, E. L.; Aldag, A. W.; Krylov, O. V. *Kinet. Catal.* **1983**, *24*, 641.

(59) Flatt, B. T.; Grubbs, R. H.; Blanski, R. L.; Calabrese, J. C.; Feldman, J. *Organometallics* **1994**, *13*, 2728.

(60) Toreki, R.; Vaughan, G. A.; Schrock, R. R.; Davis, W. M. *J. Am. Chem. Soc.* **1993**, *115*, 127.

(61) Webber, A. L.; Elena, B.; Griffin, J. M.; Yates, J. R.; Pham, T. N.; Mauri, F.; Pickard, C. J.; Gil, A. M.; Stein, R.; Lesage, A.; Emsley, L.; Brown, S. P. *Phys. Chem. Chem. Phys.* **2010**, *12*, 6970.

(62) Salager, E.; Stein, R. S.; Steuernagel, S.; Lesage, A.; Elena, B.; Emsley, L. *Chem. Phys. Lett.* **2009**, *469*, 336.

(63) Digne, M.; Sautet, P.; Raybaud, P.; Euzen, P.; Toulhoat, H. *J. Catal.* **2002**, *211*, 1.

(64) Digne, M.; Sautet, P.; Raybaud, P.; Euzen, P.; Toulhoat, H. *J. Catal.* **2004**, *226*, 54.

(65) Krokidis, X.; Raybaud, P.; Gobichon, A. E.; Rebours, B.; Euzen, P.; Toulhoat, H. *J. Phys. Chem. B* **2001**, *105*, 5121.

(66) Solans-Monfort, X.; Copéret, C.; Eisenstein, O. *J. Am. Chem. Soc.* **2010**, *132*, 7750.

(67) Solans-Monfort, X.; Copéret, C.; Eisenstein, O. *Organometallics* **2015**, *34*, 1668.

(68) Duer, M. J. In *Solid-State NMR Spectroscopy Principles and Applications*; Blackwell Science Ltd: 2007, p 216.

(69) Herzfeld, J.; Berger, A. E. *J. Chem. Phys.* **1980**, *73*, 6021.

(70) Herrmann, W. A.; Scherer, W.; Fischer, R. W.; Blumel, J.; Kleine, M.; Mertin, W.; Gruehn, R.; Mink, J.; Boysen, H.; Wilson, C. C.; Ibberson, R. M.; Bachmann, L.; Mattner, M. *J. Am. Chem. Soc.* **1995**, *117*, 3231.

(71) Herrmann, W. A.; Kuehn, F. E.; Fischer, R. W.; Thiel, W. R.; Romao, C. C. *Inorg. Chem.* **1992**, *31*, 4431.

(72) Perdew, J. P.; Wang, Y. *Phys. Rev. B* **1992**, *45*, 13244.

(73) Kresse, G.; Furthmüller, J. *Phys. Rev. B* **1996**, *54*, 11169.

(74) Kresse, G.; Furthmüller, J. *Comp. Mater. Sci.* **1996**, *6*, 15.

(75) Blöchl, P. E. *Phys. Rev. B* **1994**, *50*, 17953.

(76) Henkelman, G.; Uberuaga, B. P.; Jónsson, H. *J. Chem. Phys.* **2000**, *113*, 9901.

(77) Henkelman, G.; Jónsson, H. *J. Chem. Phys.* **2000**, *113*, 9978.

(78) Perdew, J. P.; Burke, K.; Ernzerhof, M. *Phys. Rev. Lett.* **1996**, *77*, 3865.

(79) Perdew, J. P.; Burke, K.; Ernzerhof, M. *Phys. Rev. Lett.* **1997**, *78*, 1396.

(80) Kokalj, A. *J. Mol. Graph. Model.* **1999**, *17*, 176.

(81) Becke, A. D. *J. Chem. Phys.* **1993**, *98*, 5648.

(82) Hay, P. J.; Wadt, W. R. *J. Chem. Phys.* **1985**, *82*, 299.

(83) Ehlers, A. W.; Böhme, M.; Dapprich, S.; Gobbi, A.; Höllwarth, A.; Jonas, V.; Köhler, K. F.; Stegmann, R.; Veldkamp, A.; Frenking, G. *Chem. Phys. Lett.* **1993**, *208*, 111.

Chapter 4: Characterization of the Active site of Re_2O_7/Al_2O_3 activated with Me_4Sn.

4.1 Individual contribution.

Reproduced with permission from The Royal Society of Chemistry from:
Valla, Maxence; Conley, Matthew P.; Copéret, Christophe; *Catal. Sci. Technol.*, **2015**, 5, 1438-1442.

All experiments and spectroscopic analyses were planned and performed by M. Valla. All authors participated to the scientific discussion and contributed to the manuscript.

4.2 Introduction.

The ethenolysis of 2-butenes to form propene is a central reaction in the Lummus process. This reaction is catalysed by the heterogeneous WO_3/SiO_2 alkene metathesis catalyst at temperatures above 400 °C.[1-4] Related heterogeneous catalysts, such as MoO_3/SiO_2 or MoO_3/SiO_2-Al_2O_3 operate at lower temperatures between 100 and 300 °C,[5-7] while Re_2O_7/Al_2O_3 catalyses this reaction at temperatures as low as 25 °C.[8-10] In general, these heterogeneous metathesis catalysts are incompatible with alkenes containing functional groups unless pre-activated. These catalysts are usually prepared by introducing high-valent metal oxide precursors to the high surface area support by incipient wetness impregnation followed by calcination to form isolated metal sites on the support surface. This preparation technique leads to complicated mixtures of surface sites with a low concentration of catalytically active sites,[11,12] which are difficult to study and to understand at the molecular level.

One approach to studying these heterogeneous catalysts is the synthesis of well-defined supported catalysts by grafting molecular – Mo–, W– or Re–alkylidene – precursors on partially dehydroxylated surfaces.[13-19] For example, Re(≡C-^{t}Bu)(=CH-^{t}Bu)(-CH_2-^{t}Bu)$_2$ grafted on silica forms a heterogeneous catalyst with high concentrations of active sites, fully characterized by spectroscopic techniques and compatible with functionalized alkenes.[18-20] In some cases, these well-defined environments can also lead to the determination of intermediates in the alkene

metathesis catalytic cycle,[15,17,21] which is currently not possible for the classical catalysts.

In the context of pure metal oxide heterogeneous catalysts, we showed that $MeReO_3$ supported on alumina has similar reactivity patterns in propene metathesis as the parent Re_2O_7/Al_2O_3 catalyst.[22] Surprisingly, $MeReO_3/Al_2O_3$ and related systems also catalyse the metathesis of ethylene and ethyl oleate, an alkene containing an ester functional group, both of which are unreactive towards the Re_2O_7/Al_2O_3 catalyst.[22-29] Detailed NMR and computational studies of $MeReO_3/Al_2O_3$ revealed that two major surface Re-species are present in this material (Scheme 4.1).[22,30] The major species (85-90 %) is $MeReO_3$ coordinated to a surface Al by a Re=O group and is inactive (oxo species). The minor species (10-15 %) corresponds to a μ-methylene bridging ligand in which a C-H bond in $MeReO_3$ is activated on an Al–O bond to form a methylene group bound to Re and Al (μ-methylene species). The oxo-bound and μ-methylene species are distinguishable by their characteristic NMR chemical shift. The signal for the oxo-bound complex appears at 30 ppm, while the μ-methylene is at 66 ppm. From titration and selective labelling experiments the minor μ-methylene surface species is active in metathesis.[22,27,30]

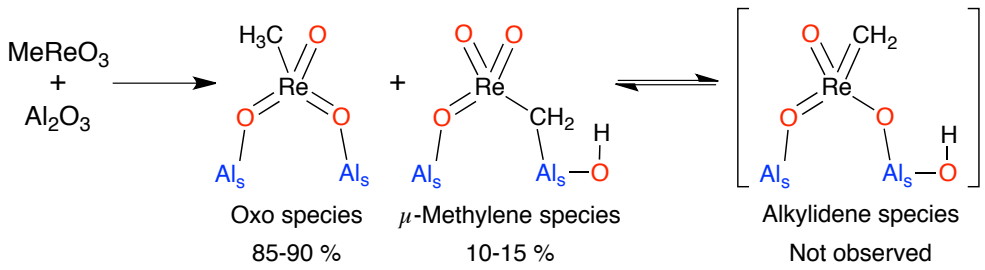

Scheme 4. 3. Surface species resulting from the grafting of $MeReO_3$ on Al_2O_3: oxo and μ-methylene species. Al_s corresponds to surface aluminium atoms.

Activation of Re_2O_7/Al_2O_3 with Me_4Sn forms $Me_4Sn/Re_2O_7/Al_2O_3$ that displays catalytic properties more similar to $MeReO_3/Al_2O_3$ than Re_2O_7/Al_2O_3. For instance, $Me_4Sn/Re_2O_7/Al_2O_3$ is active in both ethylene and ethyl oleate self-metathesis reactions. Spectroscopic studies of Re_2O_7/Al_2O_3 show that most Re-sites are isolated from one another and adopt a tetrahedral geometry,[11,31-35] and contacting Re_2O_7/Al_2O_3 with Me_4Sn was proposed to result in a surface alkylidene.[36] In view of the similar reactivity patterns between $Me_4Sn/Re_2O_7/Al_2O_3$ and $MeReO_3/Al_2O_3$ we investigated the role of Me_4Sn in the activation step of Re_2O_7/Al_2O_3 by solid-state NMR spectroscopy.

4.3 Results and Discussion.

Re_2O_7/Al_2O_3 (8 wt % Re) was synthesized by incipient wetness impregnation of perrhenic acid on alumina followed by calcination at 500 °C for 16 h.[37] Contacting Re_2O_7/Al_2O_3 with a solution of Me_4Sn in CCl_4 generates $Me_4Sn/Re_2O_7/Al_2O_3$.[38] This activated material catalyses the self-metathesis of propene. For instance, $Me_4Sn/Re_2O_7/Al_2O_3$ converts 450 equivalent of propene into the equilibrium mixture of ethene (*ca.* 15%), propene (*ca.* 65%) and 2-butenes (*ca.* 20% in *E*/*Z* isomers of 3:1 ratio) in 90 min at 25 °C.[39] Contacting non-labelled and carbon-13 di-labelled ethylene with $Me_4Sn/Re_2O_7/Al_2O_3$ results in a statistical mixture of isotopomers, indicating that the activated material catalyses ethylene self-metathesis, in contrast to Re_2O_7/Al_2O_3.[25]

The number of active sites in $Me_4Sn/Re_2O_7/Al_2O_3$ was evaluated by contacting the catalysts with 0.4 equiv. of carbon-13 di-labelled ethylene, with respect to Re, for 15 h at 25 °C. A mixture of di-labelled, mono-labelled and non-labelled ethylene isotopomers was obtained in 81/14/5 ratio, respectively. The quantity of unlabelled carbons in the gas phase is directly related to the number of exchangeable active sites because the $Me_4Sn/Re_2O_7/Al_2O_3$ was activated with natural abundance $SnMe_4$. This is a similar procedure used in Chapter 2 of this thesis. Considering that only 0.4 equiv. of labelled ethylene was added (per Re centre) to the catalyst, the number of active sites is ca. 5% in $Me_4Sn/Re_2O_7/Al_2O_3$, which is slightly lower than in $MeReO_3/Al_2O_3$ (ca. 10-15 %).[22,27]

The ^{13}C CPMAS NMR of $Me_4Sn/Re_2O_7/Al_2O_3$ contains a signal at 0 ppm (Figure 4.1a), consistent with the presence of a surface methyltin group.[40] We also found that small amounts of Me_3SnCl were formed during the activation process from ^{119}Sn NMR and GC-MS analyses.

After reacting $Me_4Sn/Re_2O_7/Al_2O_3$ with carbon-13 di-labelled ethylene (0.4 equiv./Re), the ^{13}C CPMAS NMR contains signals at 66, 30, 18, 10 along with the surface methyltin peak at 0 ppm (Figure 4.1b). The signals at 10 and 18 ppm were previously attributed to the formation of ethylene oligomers on the Al_2O_3 surface.[22,27,28] The signals at 30 and 66 ppm are similar to those obtained in carbon-13 labelled $*MeReO_3/Al_2O_3$ shown in Figure 4.1d.[22] These peaks were previously assigned to the oxo-, and the μ-methylene surface species shown in Scheme 1.[22,27,28] The observation of both μ-methylene and oxo species after exposure to ^{13}C-labelled

ethene indicates that these species probably interconvert; possibly through H-transfer or tautomerization processes (Scheme 4.2).

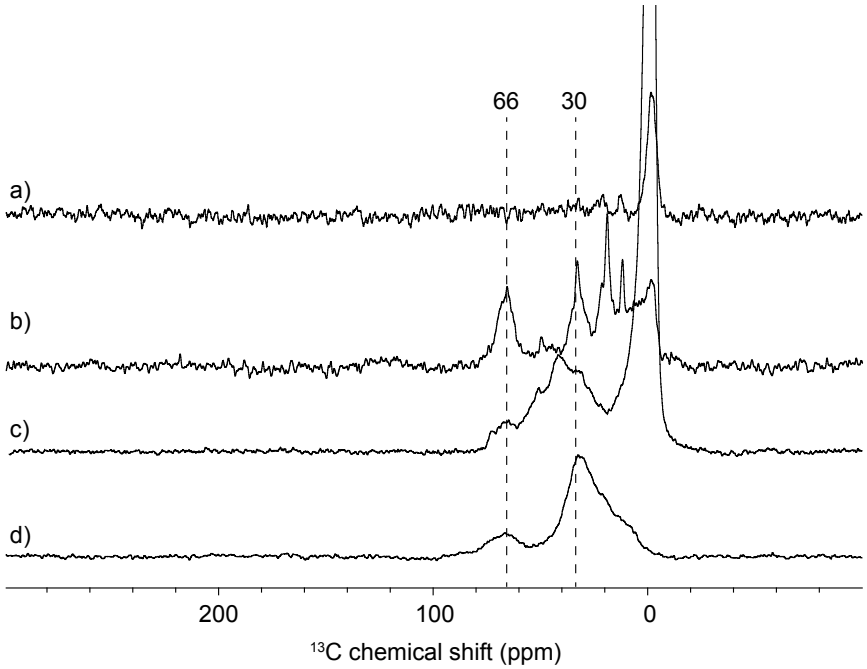

Figure 4. 12. ^{13}C CPMAS spectra of supported Re-based catalysts on alumina. For all the spectra the contact time was set to 0.6 ms and the recycling delay was 1 sec. a) $Me_4Sn/Re_2O_7/Al_2O_3$, 400 MHz, 60k scans, b) Spectrum of $Me_4Sn/Re_2O_7/Al_2O_3$ contacted with 2-^{13}C *C_2H_4 100k scans, c) *$Me_2Me_2Sn/Re_2O_7/Al_2O_3$, 80k scans, 400 MHz and d) ^{13}C labeled *$MeReO_3/Al_2O_3$, 5k scans, 700 MHz.

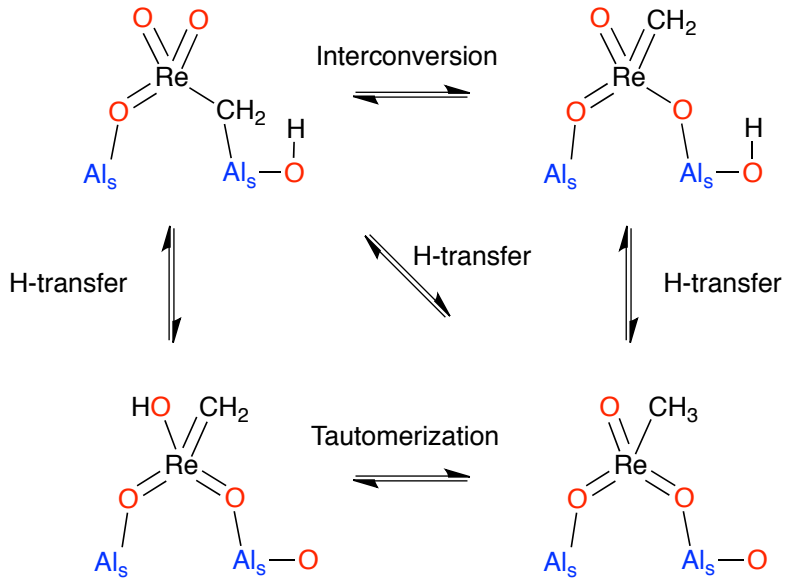

Scheme 4. 4. Reaction scheme of the possible interconversion between the methylene, the alkylidene and the oxo-species through tautomerization or H-transfer.

The surface Re-species generated, after contacting $Me_4Sn/Re_2O_7/Al_2O_3$ with carbon-13 labelled ethylene, are in low concentration. To determine the spectroscopic

signature of $Me_4Sn/Re_2O_7/Al_2O_3$ we synthesized the carbon-13 enriched material by treating Re_2O_7/Al_2O_3 with $*Me_2Me_2Sn$. The ^{13}C CPMAS spectrum of $*Me_2Me_2Sn/Re_2O_7/Al_2O_3$ contains an intense signal at 0 ppm associated with carbon-13 enriched methyltin compounds as well as the two signals at 66 and 30 ppm, as already observed in Figure 4.1b. The close chemical shift agreement between $*Me_2Me_2Sn/Re_2O_7/Al_2O_3$ (Figure 4.1c) and $MeReO_3/Al_2O_3$ (Figure 4.1d) also supports the assignment of these peaks as the μ-methylene and oxo species, respectively.[22,27,28] The peak assigned to oxo species at 40 and 51 ppm in Figure 1c are shifted to higher frequency in comparison to $MeReO_3/Al_2O_3$. This may be due to Re=O units binding to different alumina sites on the surface. However, these species are inactive in ethylene metathesis since they are not observed in Figure 4.1b. Contacting $*Me_2Me_2Sn/Re_2O_7/Al_2O_3$ with an excess of non-labelled propylene induces a significant decrease in the resonance intensity for the signals at 66 and 40-30 ppm (Figure 4.2).

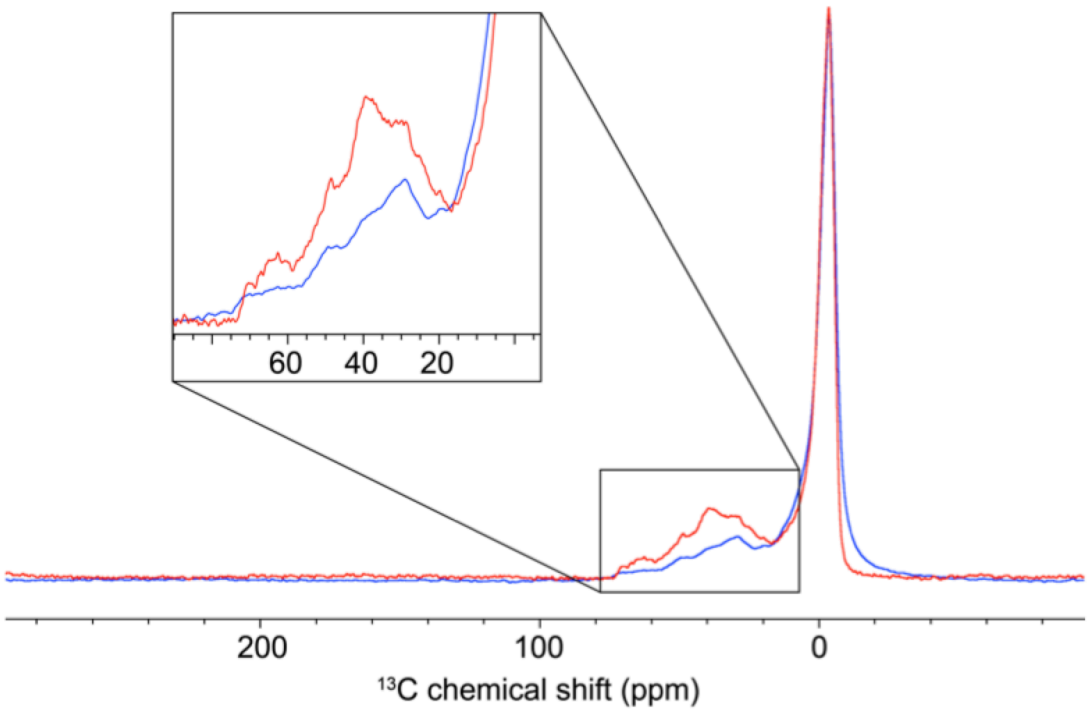

Figure 4. 13. ^{13}C CPMAS spectra of 2-^{13}C-$Me_4Sn/Re_2O_7/Al_2O_3$, 80 k scans, 400 MHz (Red line) and 2-^{13}C-$Me_4Sn/Re_2O_7/Al_2O_3$, contacted with an excess of non-labelled propylene, 80 k scans, 400 MHz For all the spectra the contact time was set to 0.6 ms and the recycling delay was 1 sec.

The reaction of Me_4Sn with Re_2O_7/Al_2O_3 forms a catalyst that has similar reactivity trends and solid-state NMR spectral features as $MeReO_3/Al_2O_3$. The carbon-containing surface species include surface methyltin species, physisorbed Me_3SnCl, μ-methylene and oxo species. Grafting alkyltin species on oxide surfaces[40,41] and reaction of Me_4Sn with $XReO_3$ (X = $OReO_3$, $OCOCF_3$, etc.)[42,43] are well known. In this case, these reactions would form Me_3SnO-Al and $MeReO_3$ (Scheme 4.3). Me_3SnCl formation may arise from the reaction of CCl_4 and Me_3SnO-Al. The μ-methylene and oxo species would arise from the reaction of aluminium bound perrhenate and Me_4Sn to form $MeReO_3$, which further reacts with Al,O sites to provide the active μ-methylene sites along with some adsorbed oxo (Scheme 4.3).[42] Note that free MeReO3 was never isolated on this system and is though to react instantaneously with the surface.

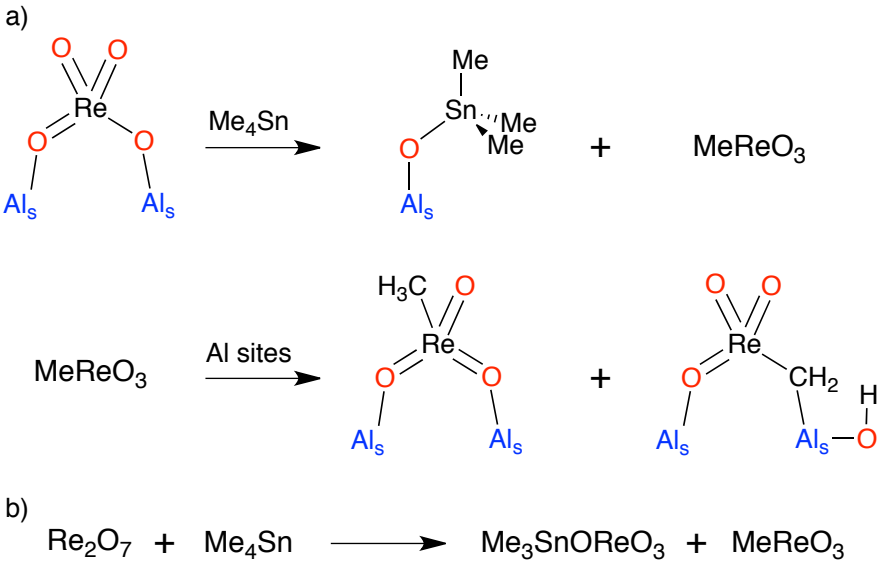

Scheme 4. 5. a) Generation of $MeReO_3$ from surface perrhenate and Me_4Sn, and subsequent reaction of $MeReO_3$ with surface Al sites. b) Formation of $MeReO_3$ by reaction of Re_2O_7 and $SnMe_4$.

4.4 Conclusion.

The activation of Re_2O_7/Al_2O_3 with Me_4Sn results in the formation of μ-methylene (Al-CH_2ReO_3) and oxo species, similar to that found in CH_3ReO_3/Al_2O_3. This explains the similar reactivity of $Me_4Sn/Re_2O_7/Al_2O_3$ and CH_3ReO_3/Al_2O_3 towards functionalized alkenes and ethylene, and distinguishes these catalysts from the pure oxide based Re_2O_7/Al_2O_3.

4.5 Experimental part.

4.5.1 General Procedure

Re_2O_7 and Me_4Sn were purchased from STREM chemicals and Aldrich, respectively. Alumina (Alu C) was obtained from Evonik, and agglomerated by slurring the solid in distilled water, following by a drying under air at 100 °C and sieving to obtain compacted alumina with a grain size of 250–400 μm. All gases were purified by passage through activated 4 Å molecular sieves and BASF copper-catalyst prior to use. Carbon tetrachloride and diethyl ether were purchased from Sigma-Aldrich, THF-d_8 was purchased from Cambridge Isotope Laboratories. THF and diethyl ether were distilled over sodium/benzophenone. Gas analyses were performed on an Agilent Technologies 7890A GC systems equipped with a flame ionization detector and a HP-Al/KCl on fused silica column (50 m x 0.32 mm). GC/MS measurements were performed on an Agilent GC 7820 A equipped with a mass Spectrometer (5975). The column used were HP-Al/KCl on fused silica for alkenes type compounds and HP-88 Agilent column for tin based compounds. Solution NMR spectra were recorded on either 250 or 500 MHz Bruker spectrometers. The solid-state NMR spectra were measured on either 400 or 700 MHz Bruker NMR spectrometers equipped with 4 mm triple resonance probe heads. The method used was ^{1}H-^{13}C cross-polarization magic angle spinning (CP-MAS) using a radio frequency field of 100 kHz on the proton channel.

4.5.2 Preparation of CH_3ReO_3 or $*CH_3ReO_3$ Supported on $Al_2O_{3-(500°C)}$.

These compounds were prepared as previously reported.[22,43] and described in Chap. II Elemental analysis: Re (5.6 wt%).

4.5.3 Preparation of Re_2O_7/Al_2O_3 by Incipient Wetness Impregnation.

Al_2O_3 (5.5 g, Alu C) was impregnated with a solution of 0.78 g of perrhenic acid (99.99% pure) in 4.1 mL of water.[39] The resulting solid was dried at 150 °C (10°C min^{-1} heating ramp) under static air for 16 h, rewetted with 5 mL of water and dried at 300 °C with a ramp of 10 °C min^{-1} for 4 h. This material was calcined under a flow of synthetic air at 500 °C with a ramp of 10 °C min^{-1} for 16 h and evacuated under high vacuum (10^{-5} mBar) line for 60 min. Elemental analysis: Re (8.1 wt%).

4.5.4 Synthesis of $SnMe_2Me^*_2$.

A 2 neck round bottom flask equipped with a dropping funnel and a condenser was loaded with magnesium (2.6 g, 106 mmol, 2.4 equiv) and 150 mL of diethyl ether. ^{13}C labelled idodomethane (6.2, 44 mmol, 2.2 equiv) was added dropwise to the suspension. The magnesium slowly disappears and a solid was formed in the solution. After one hour the mixture was cooled to 0 °C and a solution of dichlorodimethyltin (20 mmol, 1 equiv) in 40 mL of ether was added dropwise for 30 min. The reaction mixture was warmed to room temperature and maintained at this temperature overnight. 1 M HCl (20 mL) was added to the mixture and the phases were separated. The aqueous phase was extracted with diethyl ether (3 x 20 mL). The combined organic phases were dried over anhydrous $MgSO_4$. After 3 successive careful distillations of the azeotrope diethyl ether / Me_4Sn, the desired product was obtained with a yield of 11 % (bp 74 °C at 1 atm). ^1H (250 MHz, C_6D_6) δ: 0.12 (s, Me_4Sn J_{H-C}=120 Hz).

4.5.5 Preparation of $Me_4Sn/Re_2O_7/Al_2O_3$.

Representative procedure. To Re_2O_7/Al_2O_3 (500 mg) suspended in 1 mL of CCl_4 in a 50 mL Schlenck under Argon was added Me_4Sn (0.1 mL, 0.56 mmol). The reaction mixture was stirred for 30 min at room temperature, and the colour changed from white to brown. The solid was isolated by filtration, and washed three times with 1 mL of CCl_4. Elemental analysis: Re (6.7 wt%) and Sn (1.1 wt%).Preparation of $SnMe_2Me_2$* –activated Re_2O_7/Al_2O_3. This compound was prepared as described above using $SnMe_2Me_2$* in place of Me_4Sn.[44]

4.5.6 Extraction of $Me_4Sn/Re_2O_7/Al_2O_3$ with THF-d_8.

To $Me_4Sn/Re_2O_7/Al_2O_3$ (500 mg) was suspended in 1 mL of dry THF d_8 under inert atmosphere. The mixture was stirred 16 h. The resulting liquid was analysed by ^{119}Sn solution NMR and by GC-MS. It revealed the presence of unreacted Me_4Sn, CCl_4 and Me_3SnCl.

4.5.7 Reaction of Carbon-13 Di-labelled Ethylene with Me_4Sn–Activated Re_2O_7/Al_2O_3.

$Me_4Sn/Re_2O_7/Al_2O_3$ (200 mg) was loaded in a 110 mL glass reactor and contacted with carbon-13 di-labelled ethene (0.4 equiv per Re metal centre). After 15 h at room temperature, the gas phase was analysed by GC and GC/MS showing the presence of di-, mono- and non-labelled ethene (di-labelled 81 %, mono-labelled 14 % and non-

labelled 5 %). The number of non labelled carbon is therefore 12% in the gas phase, this number is multiplied by the number of equivalent of ethylene added per Re centre. Therefore, the calculated number of active sites is 5%.

4.5.8 Reaction of Carbon-13 Di-labelled and Non-labelled Ethylene with Me_4Sn–Activated Re_2O_7/Al_2O_3.

$Me_4Sn/Re_2O_7/Al_2O_3$ (200 mg) was loaded in a 110 mL glass reactor and contacted with 20 equiv. of non-labelled ethene and 10 equivalent of ^{13}C di-labelled ethene and left for 24 hours to react at 25°C. The resulting gas phase was analysed by GC-MS leading a 45/39/16 mixture of non-labelled, mono labelled and di-labelled ethylene (di-labelled 16 %, mono-labelled 39 % and non-labelled 45 %).

4.6 References.

(1) Banks, R. L.; Bailey, G. C. *Ind. Eng. Chem. Prod. Rd.* **1964**, *3*, 170.

(2) Mol, J. C. *J. Mol. Catal. A* **2004**, *213*, 39.

(3) Popoff, N.; Mazoyer, E.; Pelletier, J.; Gauvin, R. M.; Taoufik, M. *Chem. Soc. Rev.* **2013**, *42*, 9035.

(4) Lwin, S.; Wachs, I. E. *ACS Catal.* **2014**, *4*, 2505.

(5) Ivin, K. J.; Mol, J. C. *Olefin Metathesis and Metathesis Polymerization*, 1997.

(6) Tian, H.; Roberts, C. A.; Wachs, I. E. *J. Phys. Chem. C* **2010**, *114*, 14110.

(7) Debecker, D. P.; Stoyanova, M.; Rodemerck, U.; Gaigneaux, E. M. *J. Mol. Catal. A* **2011**, *340*, 65.

(8) Lawrenson, M. J.; A, U., Ed. M.J. Lawrenson, US Patent US3974233A, 1976.

(9) Mol, J. C. *Catal. Today* **1999**, *51*, 289.

(10) Imamoğlu, Y. *Metathesis Polymerization of Olefins and Polymerization of Alkynes*; Kluwer Academic, 1998.

(11) Chauvin, Y.; Commereuc, D. *J. Chem. Soc., Chem. Commun.* **1992**, 462.

(12) Moffat, A. J.; Clark, A.; Johnson, M. M. *J. Catal.* **1971**, *22*, 379.

(13) Copéret, C.; Chabanas, M.; Petroff Saint-Arroman, R.; Basset, J.-M. *Angew. Chem. Int. Ed.* **2003**, *42*, 156.

(14) Copéret, C. *Dalton Trans.* **2007**, 5498.

(15) Mougel, V.; Copéret, C. *Chem. Sci.* **2014**, *5*, 2475.

(16) Conley, M. P.; Mougel, V.; Peryshkov, D. V.; Forrest, W. P.; Gajan, D.; Lesage, A.; Emsley, L.; Copéret, C.; Schrock, R. R. *J. Am. Chem. Soc.* **2013**, *135*, 19068.

(17) Conley, M. P.; Forrest, W. P.; Mougel, V.; Copéret, C.; Schrock, R. R. *Angew. Chem. Int. Ed.* **2014**, *126*, 14445.

(18) Chabanas, M.; Baudouin, A.; Copéret, C.; Basset, J.-M. *J. Am. Chem. Soc.* **2001**, *123*, 2062.

(19) Chabanas, M.; Copéret, C.; Basset, J.-M. *Chem. –Eur. J.* **2003**, *9*, 971.

(20) Leduc, A.-M.; Salameh, A.; Soulivong, D.; Chabanas, M.; Basset, J.-M.; Copéret, C.; Solans-Monfort, X.; Clot, E.; Eisenstein, O.; Böhm, V. P. W.; Röper, M. *J. Am. Chem. Soc.* **2008**, *130*, 6288.

(21) Blanc, F.; Berthoud, R.; Copéret, C.; Lesage, A.; Emsley, L.; Singh, R.; Kreickmann, T.; Schrock, R. R. *Proc. Nat. Acad. Sci. U.S.A.* **2008**, *105*, 12123.

(22) Salameh, A.; Joubert, J.; Baudouin, A.; Lukens, W.; Delbecq, F.; Sautet, P.; Basset, J. M.; Copéret, C. *Angew. Chem. Int. Ed.* **2007**, *46*, 3870.

(23) Herrmann, W. A.; Wagner, W.; Flessner, U.; Volkhardt, U.; Komber, H. *Angew. Chem. Int. Ed.* **1991**, *103*, 1704.

(24) Rost, A. M. J.; Schneider, H.; Zoller, J. P.; Herrmann, W. A.; Kuhn, F. E. *J. Organomet. Chem.* **2005**, *690*, 4712.

(25) McCoy, J. R.; Farona, M. F. *J. Mol. Catal.* **1991**, *66*, 51.

(26) Buffon, R.; Auroux, A.; Lefebvre, F.; Leconte, M.; Choplin, A.; Basset, J. M.; Herrmann, W. A. *J. Mol. Catal.* **1992**, *76*, 287.

(27) Salameh, A.; Baudouin, A.; Soulivong, D.; Boehm, V.; Roeper, M.; Basset, J.-M.; Copéret, C. *J. Catal.* **2008**, *253*, 180.

(28) Salameh, A.; Baudouin, A.; Basset, J. M.; Copéret, C. *Angew. Chem. Int. Ed.* **2008**, *47*, 2117.

(29) Moses, A. W.; Raab, C.; Nelson, R. C.; Leifeste, H. D.; Ramsahye, N. A.; Chattopadhyay, S.; Eckert, J.; Chmelka, B. F.; Scott, S. L. *J. Am. Chem. Soc.* **2007**, *129*, 8912.

(30) Wischert, R.; Copéret, C.; Delbecq, F.; Sautet, P. *ChemCatChem* **2010**, *2*, 812.

(31) Tsuda, N.; Fujimori, A. *J. Catal.* **1981**, *69*, 410.

(32) Duquette, L. G.; Cieslinski, R. C.; Jung, C. W.; Garrou, P. E. *J. Catal.* **1984**, *90*, 362.

(33) Hardcastle, F. D.; Wachs, I. E.; Horsley, J. A.; Via, G. H. *J. Mol. Catal.* **1988**, *46*, 15.

(34) Vuurman, M. A.; Stufkens, D. J.; Oskam, A.; Wachs, I. E. *J. Mol. Catal.* **1992**, *76*, 263.

(35) Schekler-Nahama, F.; Clause, O.; Commereuc, D.; Saussey, J. *Appl. Catal. A* **1998**, *167*, 247.

(36) Ellison, A.; Coverdale, A. K.; Dearing, P. F. *Appl. Catal.* **1983**, *8*, 109.

(37) Daniell, W.; Weingand, T.; Knözinger, H. *J. Mol. Catal. A* **2003**, *204,Äì205*, 519.

(38) Evert Verkuijlen, F. K., Johannes C. Mol, Cornelis Boelhouwer *J.C.S. Chem. Comm.* **1977**, 198.

(39) Andreini, A.; Xu, X. D.; Mol, J. C. *Appl. Catal.* **1986**, *27*, 31.

(40) Nedez, C.; Theolier, A.; Lefebvre, F.; Choplin, A.; Basset, J. M.; Joly, J. F. *J. Am. Chem. Soc.* **1993**, *115*, 722.

(41) Nedez, C.; Lefebvre, F.; Choplin, A.; Niccolai, G. P.; Basset, J. M.; Benazzi, E. *J. Am. Chem. Soc.* **1994**, *116*, 8638.

(42) Herrmann, W. A.; Kuchler, J. G.; Felixberger, J. K.; Herdtweck, E.; Wagner, W. *Angew. Chem. Int. Ed.* **1988**, *27*, 394.

(43) Herrmann, W. A.; Kuehn, F. E.; Fischer, R. W.; Thiel, W. R.; Romao, C. C. *Inorg. Chem.* **1992**, *31*, 4431.

(44) Verkuijlen, E.; Kapteijn, F.; Mol, J. C.; Boelhouwer, C. *J. Chem. Soc., Chem. Commun.* **1977**, 198.

Chapter 5: Atomic Description of the Interface Between Silica and Alumina in Aluminosilicates Through Dynamic Nuclear Polarization Surface-Enhanced NMR Spectroscopy.

5.1 Individual Contribution.

Reprinted with permission from:

Valla, M.; Rossini, A.J.; Caillot, M.; Chizallet, C.; Raybaud, P.; Digne, M.; Chaumonnot, A.; Lesage, A.; Emsley, L.; van Bokhoven, J.A. and Copéret, C. *J. Am. Chem. Soc.*, **2015**, 137, 10710-10719.

Copyright 2015 American Chemical society.

Spectroscopic experiments and analyses were planned by M. Valla with the help of A. J. Rossini. The samples were synthesized by M. Caillot. All calculations were done by C. Chizallet and P. Raybaud. All authors contributed to the manuscript.

5.2 Introduction.

Amorphous aluminosilicates (ASAs) are ubiquitous in catalysis, and are used both as a catalyst and catalyst support for single-sites, metal sulfides and metal nanoparticles as they have high surface areas, combined with mild acidic properties alternative to zeolite in industrial reaction conditions.[1-3] They are known to dehydrate ethanol to ethylene as well as to catalyze the isomerization of *m*-xylene.[4] They are also industrially used in refining technology to convert heavy fractions of crude oil and as supports for hydro-treating catalysts thanks to the tolerance of their acid sites to hetero-elements containing organic molecules. [5-8] They show promising properties in the production of fine chemicals,[1,2,9,10] and the conversion of biomass.[11,12] They are also known in the Re chemistry and especially with the metathesis reaction. When CH_3ReO_3 or Re_2O are supported on aluminosilicate type supports, they exhibit much higher activity in metathesis. It is therefore very important to understand such support

and their reaction with Re type catalyst. This chapter will be dedicated to the understanding of the simple support.

The activity of aluminosilicate arises from their acid/base properties. The presence of both aluminum and silicon atoms at the surface of the materials induces Brønsted acidity to the surface hydroxyls.[2,13-16] However, the complex distribution of silicon and aluminum and the amorphous character of the material make the correlation between structure and activity very difficult to establish; the structure of the catalytically active sites are still a matter of debate.[14,17-20] The original structural models of ASA proposed that the Brønsted acidity arises from protons compensating the electronic charge of the surface[21,22] or from HO-Al groups close to silanol groups.[23] Since these original pioneering works, numerous additional structural models have been proposed. Based on probe molecule adsorption, it has been suggested that the acidic sites are similar to those of zeolites, i.e. bridging Si-OH-Al groups.[14,20,24] In contrast to depositing aluminum or silicon precursors, co-impregnation yields sites of similar strength as zeolites.[16] Other studies have concluded that the acidic sites are silanol groups in the vicinity of aluminum atoms (but not bridging the OH). In this case, the nature of Al atoms in the vicinity of the acidic groups is also a subject of discussion: tetrahedral Al(IV), five-coordinate Al(V)[18,25] and unsaturated Al(III) sites have all been proposed.[17,18] All these structural propositions are based on interpretation of complex spectral data. For instance, the assignments of OH infrared stretching frequencies have been debated.[26-28] In particular, the vibrational properties of probes such as CO or pyridine are not unambiguously specific to given ASA surface sites.[29,30] Additionally, the numerous preparation routes give rise to a broad range of materials with varying structure, acidity and active sites.[16] Even the surfaces that are formed by using well-defined methods are heterogeneous in nature.[16] More recently, pseudo-bridging silanol groups have also been proposed to be active sites based on DFT calculations.[19]

An efficient synthesis of ASA materials involves the controlled grafting of aluminum alkoxide or silicon alkoxide precursors onto a silica or alumina surface under anhydrous conditions at low temperatures, thus forming Al_2O_3 on SiO_2 (Al/SiO_2) or SiO_2 on Al_2O_3 (Si/Al_2O_3), respectively.[16,31-33] This approach has the advantage of providing a homogeneous and regular deposition. The anhydrous conditions prevent the pre-hydrolysis of the precursor and inhomogeneous deposition.

In addition, the amount of precursor grafted on the surface is mainly directed by the size of the alkyl chain of the precursor used. High Al and Si loadings may be achieved through successive grafting steps for both Al/SiO_2 and Si/Al_2O_3. The stoichiometric adsorption and further dehydration of ethanol enabled the quantification of the surface density of active sites.[33] Even with a controlled deposition synthesis of ASA materials, Si/Al_2O_3 and Al/SiO_2 still have multiple types of Brønsted acid sites on their surface. Comparing these data to the catalytic activity for *m*-xylene isomerization revealed a moderate intrinsic acidity of these materials with respect to zeolites, Si/Al_2O_3 being the more reactive.[33] Grafting of the silicon precursor occurred first on the (100) surface. Brønsted acidity only appeared upon grafting the (110) surface.[8,32-34]

While NMR spectroscopy is a valuable tool to obtain insights into the nature of Al and Si species on ASA,[18,35-39] unambiguous identification of the most relevant surface sites has not been achieved yet, one reason being the small amount of surface sites combined with the low sensitivity of NMR. Dynamic Nuclear Polarization Surface Enhanced Spectroscopy (DNP SENS)[40-42] has recently been introduced to characterize materials and in particular their surfaces. In a DNP SENS experiment, the sample is impregnated with a small volume of a solution containing a persistent radical that acts as the DNP polarizing agent.[40-42] Impregnation brings the solvent and DNP polarizing agent (usually a nitroxide biradical)[43] into contact with the surface. DNP at low temperatures[44,45] (ca. 100 K) is then used to enhance the polarization of protons of the solvent and surface functionality.[43-45] The DNP enhanced proton polarization is then transferred to the surface hetero-nuclei by cross-polarization (CP)[46] or other coherence transfer methods.[40-42,46-48] For inorganic materials, signals from NMR active nuclei residing at the surface of the material are selectively enhanced since only the surface nuclei are in proximity to the protons of the solvent and/or surface functionalities. DNP SENS routinely provides sensitivity enhancements of two orders of magnitude,[49,50] enabling NMR experiments that would normally require isotopic labeling and/or prohibitively long signal averaging periods.[40-42,48]

Here, we apply DNP SENS for the detailed characterization of ASA materials prepared via controlled grafting approach, so as to provide an unambiguous characterization of the interface between silica and alumina for two well-defined

series of samples: silica deposited on alumina (Si/Al_2O_3) and alumina deposited on silica (Al/SiO_2) materials. DNP NMR has recently been applied to characterize materials such as alumina, silica and β-zeolite surfaces.[51-57] Here DNP SENS allows sensitivity enhancements of several orders of magnitude, thus enabling the acquisition of natural abundance ^{29}Si-^{27}Al scalar and dipolar hetero-nuclear correlation spectra, providing structural insight into the alumina/silica interface of these materials. Calculations of NMR signatures of surface sites of Si/Al_2O_3 on a aluminosilicate model by periodic density functional theory (DFT) calculations, which have proven to be efficient for the assignment of NMR spectra of various oxides,[58-66] allow us not only to propose a structure for the interface between the alumina and the silica but also to propose structural models of the Brønsted acid sites of ASA.

5.3 Probing the Structure of Aluminum on Silica Using Dynamic Nuclear Polarization Surface Enhanced NMR.

The samples with increasing loadings of aluminum (*i.e.* 5.7 w%, 15 w% and 24.8 w% of Al_2O_3 on SiO_2 noted Al/SiO_2) were analyzed with ^{1}H-^{27}Al cross-polarization magic angle spinning (CPMAS) solid-state NMR spectroscopy. Indirect ^{1}H DNP coupled with CPMAS enables the selective enhancement of the NMR signals of the surface ^{27}Al nuclei which are nearby to ^{1}H nuclei of the surface hydroxyl groups and solvent molecules.[51] Here a short contact time of 0.6 ms was employed in ^{1}H-^{27}Al CPMAS experiments since it is well known that with short contact times the CP experiment is very selective and only nuclei in close proximity to protons will be excited. CP transfers to more distant sub-surface will also be less efficient due to dipolar truncation, ensuring that only surface nuclei are detected.[55] ^{1}H DNP enhancements were measured with CP to ^{27}Al ($\varepsilon_{Al\,CP}$) and were between 5 and 8 for the different samples at 600 MHz/395 GHz (Figure 5.1). (Note that previous studies indicate that the overall sensitivity enhancement, as compared to a dry sample at room temperature, is usually similar to the ε value under these conditions).[49] DNP enhanced ^{1}H-^{27}Al CPMAS spectra were also acquired at 400 MHz/263 GHz and higher ($\varepsilon_{Al\,CP}$) signal enhancements between 51-80 were observed (Figure A.5.1). The resolution of the ^{27}Al solid-state NMR spectra is greatly improved at higher magnetic field, as expected for quadrupolar nuclei such as ^{27}Al. Therefore, our analysis of 1D spectra focuses on the high field spectra.

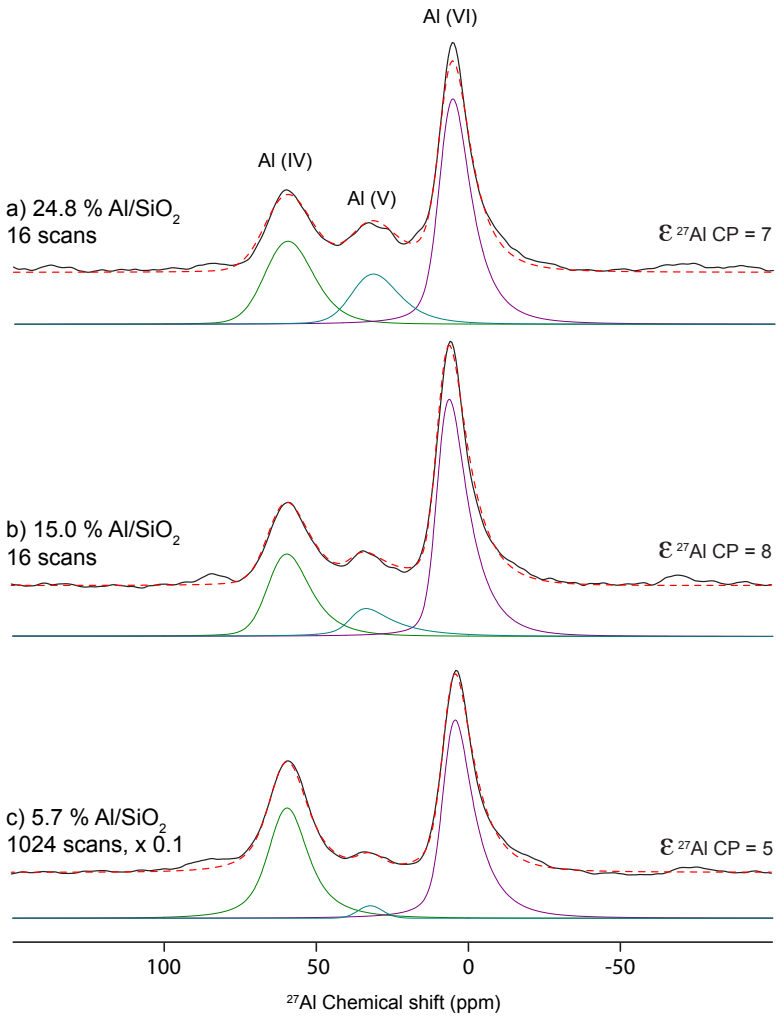

Figure 5. 1. DNP enhanced 600 MHz ^{1}H-^{27}Al CPMAS spectra of (a) 24.8 %, (b) 15% and (c) 5.7% Al_2O_3 on SiO_2. Experimental spectra (black trace), total fits (red dashed trace) and deconvolutions of individual sites (lower traces) are shown. All spectra were acquired with a 12.5 kHz spinning frequency and a CP contact time of 0.6 ms. The recycling delay was set to 3.5 sec. On the right hand side of each spectrum the ^{27}Al DNP enhancement is shown. Decomposition of the spectra was performed using the Gaussian isotropic model (GIM) (Czjzek, d=5) implemented in the DMFit program. The mean isotropic chemical shift (δ_{iso}), the width of the Gaussian distribution of isotropic chemical shifts ($\Delta\delta_{iso}$), the mean quadrupolar coupling constant (C_Q) and the relative integrated intensities were obtained from the fits.

In all samples, three peaks centered around 6, 33 and 60 ppm are assigned respectively to hexa- Al(VI), penta- Al(V) and tetra-coordinated Al(IV) aluminum sites, similarly to what is observed for γ-alumina, albeit with a larger component of Al(V),[51,66-69] in agreement with previous NMR measurements.[18,35,37,38] The shape of the peaks in the spectra evolves as the concentration of alumina on SiO_2 changes. We also note that as the Al loading increases, the intensity of the ^{27}Al CPMAS spectra also substantially increases (Figure A.5.1). The one-dimensional ^{27}Al DNP SENS CPMAS spectra were fit

to a Cjzek model implemented in DMFit program to model the broad and featureless ^{27}Al resonances characteristics of distributions of quadrupole and chemical shift parameters (Figure 5.1).[70]

The fits enabled the determination of the relative ratio of each species, the isotropic chemical shift and the quadupolar constant (Table 5.1 and Figure A.5.2). The fits show that for Al/SiO_2 the relative amount of Al(V) (2, 11 and 17 %) increases with higher aluminum loading. All the peaks have very similar mean quadripolar coupling constant (C_Q), comprised between 2.4 and 5.1 MHz, with no influence of the concentration of Al on SiO_2.

Table 5. 1. Results of the simulation (Gaussian Isotropic Model) of the 600 MHz ^{1}H-^{27}Al CPMAS with saturation cycle. The mean isotropic chemical shift (δ_{iso}), the width of the Gaussian distribution of the chemical shift ($\triangle\delta_{iso}$), the mean quadrupolar coupling constant (CQ) and the relative integrated intensities are presented.

		5.7% Al/SiO_2		
Site	Percent	δ_{iso} (ppm)	$\Delta\delta_{iso}$ (ppm)	C_Q (MHz)
Al^{IV}	40.4	61.3	9.8	3.1
Al^{V}	2.4	33.9	8.8	2.4
Al^{VI}	57.2	7.6	6.2	4.5
		15.0% Al/SiO_2		
Site	Percent	δ_{iso} (ppm)	$\Delta\delta_{iso}$ (ppm)	C_Q (MHz)
AlI^{IV}	27.9	64.5	11.2	4.9
Al^{V}	10.8	38.1	7	5.7
Al^{VI}	61.3	10.1	6.2	4.8
		24.8% Al/SiO_2		
Site	Percent	δ_{iso} (ppm)	$\Delta\delta_{iso}$ (ppm)	C_Q (MHz)
AlI^{IV}	27.7	64.6	14.9	4.5
Al^{V}	17.1	37	13	5.1
Al^{VI}	55.2	9.1	7.26	4.3

For Al/SiO_2 all of the 1D DNP enhanced ^{29}Si CPMAS NMR spectra show a major peak centered at around –100 ppm and a reduced intensity "tail" at around –85 ppm (Figure 5.2). The major peak at –100 ppm indicates that most silicon atoms are present as Q_4 sites. As the aluminum loading increases the intensity of the tail increases and moves towards more positive chemical shift. Silicon with multiple neighboring aluminum atoms and/or protons bound to the coordinating oxygen atoms should exhibit more positive chemical shifts (see next section, regarding Si/Al_2O_3 samples).[4,71,72]

It is indeed well known from experiments on crystalline materials that substitution of aluminum atoms into neighboring tetrahedral sites around tetrahedral silica induces a positive displacement of the ^{29}Si chemical shift.[71-75] From solid-state NMR experiments performed on amorphous silica it is also

known that Si atoms with protons bound to coordinating oxygen atoms are also displaced to higher ^{29}Si chemical shifts.[4,71,72,76] Finally, we note that 1D ^{29}Si CPMAS experiments and 2D ^{29}Si-^{27}Al INEPT-HETCOR experiments used 3 ms and 6 ms contact times, respectively, since these relatively long contact times gave the most signal. However, ^{29}Si CPMAS spectra of 17.1 % Si/Al_2O_3 acquired with contact times of 1-6 ms showed only minor variation in the observed ^{29}Si chemical shifts with contact time (Figure A.5.4). This suggests that even at relatively long contact times only the surface of material is probed.

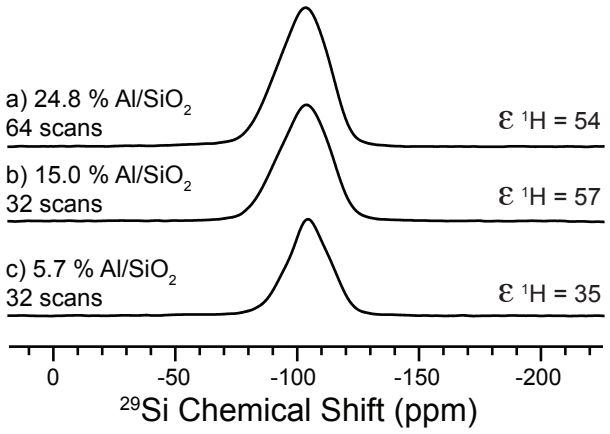

Figure 5. 2. 400 MHz/263 GHz DNP SENS ^{1}H-^{29}Si CPMAS solid-state NMR spectra. a) 24.8 w% Al/SiO_2, b) 15.0 w% Al/SiO_2, c) 5.7 w% Al/SiO_2. For ^{29}Si measurement DNP enhancement was measured by directly observing the ^{1}H spectrum, since the acquisition of a ^{29}Si CPMAS spectrum without DNP required too long for signal averaging. All spectra were acquired with a 12.5 kHz spinning frequency and a CP contact time of 3.0 ms for ^{29}Si. ^{1}H-^{29}Si CPMAS spectrum of the starting silica is available Figure A4.3.

In addition, with increasing Al-loading, the relative number of Al(IV) sites decreases. We suspect that at high loading, the conversion of Al(IV) species into Al(V) is due to the increased ionicity of the framework, leading to preferred higher coordination number. Indeed, intrinsically, the Al-O bond is more ionic than the Si-O bond as expected from the respective electronegativity values of Al, Si and O and the definition of ionicity given by Pauling.[77-79] Simultaneously, the ratio of six-coordinate Al sites remains at around 60% of the total aluminum atoms.

To obtain direct insight into the bonding between Al and SiO_2, DNP SENS ^{29}Si-^{27}Al INEPT was used to obtain two-dimensional ^{29}Si and ^{27}Al hetero-nuclear correlation (HETCOR) spectra of Al/SiO_2 (Figure 5.3). We note that the ^{29}Si-^{27}Al correlation experiments are very challenging due to the low natural

isotopic abundance of ^{29}Si (natural abundance of 4.7 %) and inefficient polarization transfer to/from quadrupolar ^{27}Al nuclei. Therefore, 2D ^{29}Si-^{27}Al correlation experiments were performed at 400 MHz/263 GHz where substantially higher DNP enhancements and NMR sensitivity were obtained. The HETCOR spectra were obtained with ^{29}Si-^{27}Al scalar couplings to selectively observe scalar coupled aluminum and silicon atoms linked by bridging oxygen (black traces). HETCOR spectra were also obtained with ^{29}Si-^{27}Al dipolar couplings by applying dipolar recoupling during the evolution period to observe both bonded and non-bonded, but proximate, aluminum and silicon atoms (red contours/traces).

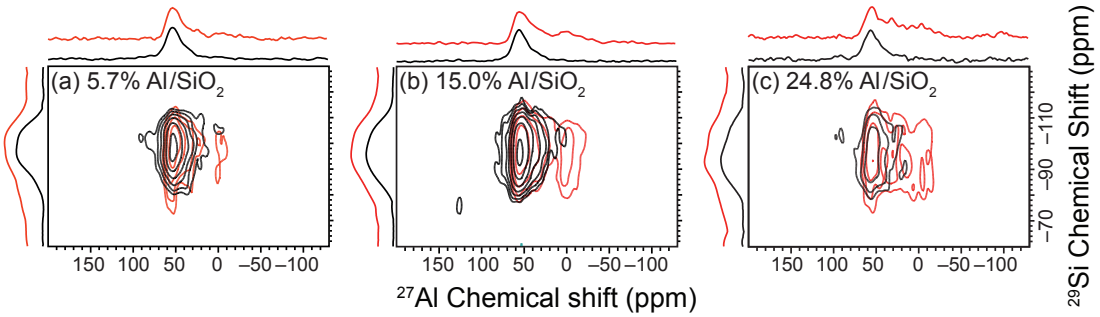

Figure 5. 3. 400 MHz/263 GHz DNP SENS scalar refocused INEPT (black traces/contours) and dipolar refocused R^3-INEPT (red traces/contours) ^{29}Si-^{27}Al hetero-nuclear correlation spectra of (a) 5.7 w% Al/SiO_2, (b) 15.0 w% Al/SiO_2, (c) 24.8 w% Al/SiO_2. All spectra were acquired with a 12.5 kHz MAS frequency. Projections of the 2D spectra are shown along the horizontal and vertical axes. For dipolar correlation experiments 96 total rotor cycles (*N*, Figure A.5.5) of recoupling were used, while for scalar correlation experiments, 420 total rotor cycles of evolution were used. Spectra were acquired with between 16 and 80 scans per increment, 28 t_1 increments and a rotor synchronized t_1 increment of 80 ms. Recycle delays were optimized for sensitivity and were between 3.8 s and 5.0 s. The pulse sequences used to acquire the 2D spectra are illustrated in Figure A.5.5.

The scalar HETCOR spectra (black contours/traces) indicate that in all cases the silica tetrahedra are primarily bound to aluminum tetrahedra in Al/SiO_2 (fits of the projected ^{27}Al dimension for both scalar and dipolar spectrum are provided in the SI, see Figure A.5.6-7 and Table A.5.1-2). The dipolar ^{29}Si-^{27}Al correlation spectra (Figure 5.3, red traces) show correlations between ^{29}Si Q_4 sites with ^{27}Al (IV) and additional weak correlations between silicon and octahedral aluminum Al(VI) in all cases (Figure A.5.7 and Table A.5.2). This result is consistent with earlier NMR analysis on co-gelled ASA samples with high silica content.[36] The relative intensity of the latter correlations increases as the aluminum loading level is increased. As the dipolar correlation experiment

gives correlations through space, the observed correlations to the octahedral Al-sites are very weak and likely arise from coupling to proximate, non-bonded Al-octahedra. Note that at this stage, the correlation with Al(V) nuclei cannot be excluded, but does not appear on the correlation plots probably due to low sensitivity of ^{29}Si-^{27}Al correlation experiments and the reduced resolution of the ^{27}Al spectra at 9.4 T. We note that DNP enhanced ^{1}H-^{27}Al and ^{1}H-^{29}Si dipolar HETCOR spectra were also acquired (Figure A.5.9-10). However, both the ^{1}H-^{29}Si and ^{1}H-^{27}Al HETCOR spectra generally show correlations to a very broad range of ^{1}H chemical shifts (ca. 0.5 to 10 ppm), which likely reflects the diverse range of proton environments at the surface (i.e, hydroxyl, water, adsorbed solvent molecules, acidic protons, etc.). The most intense ^{1}H peaks in the HETCOR spectra are centered around 4.5-5 ppm and ca. 6.2 ppm. These ^{1}H chemical shifts likely correspond to adsorbed H_2O and TCE solvent molecules (solvent used to impregnate the samples with radicals), respectively. The ^{1}H peaks in the HETCOR spectra are also rather featureless which prevents useful structural information from being obtained.

In summary, the scalar and dipolar DNP SENS ^{29}Si-^{27}Al HETCOR spectra indicate that the majority of aluminum species that are bound to the silica surface via Si Q_4 sites are Al(IV) and as the loading increases, the number of Al(VI) proximate to the silica surface increases (Scheme 5.1).

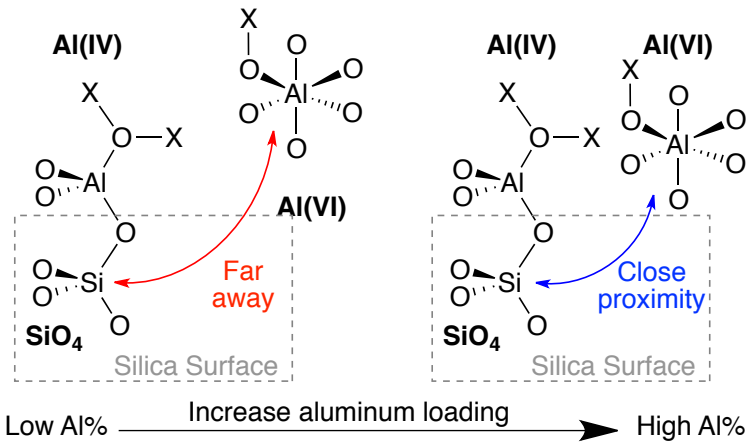

Scheme 5. 1. Representation of the Al/SiO_2 interface depicting direct bonding between tetrahedral aluminum and silicon sites and the proximity of octahedral aluminum sites. X= Al, Si or H. Homocondensation of the alkoxides is possible and would lead to the formation Al-O-Al type species.

5.4 Probing the structure of Silica on Alumina Using Dynamic Nuclear Polarization Surface Enhanced NMR and First Principle Calculations.

Si/Al_2O_3 prepared by the deposition of SiO_2 on Al_2O_3 via a molecular approach was also investigated by DNP SENS. ^1H-^{27}Al CPMAS spectra were recorded for the Si/Al_2O_3 samples (Figure 5.4). Higher DNP enhancements of 7-20 were obtained for Si/Al_2O_3 as compared to enhancements of 5-8 observed for Al/SiO_2 at 600 MHz/395 GHz. The larger enhancements observed for Si/Al_2O_3 samples (51-80 at 400 MHz/263 GHz) as compared to Al/SiO_2 ($e_{Al\ CP}$ of 114-153 at 400 MHz/263 GHz) could reflect more suitable dielectric properties of alumina.[80] However, other factors such as the degree of oxygen removal[80] and/or interaction/aggregation of the radicals could also impact the observed DNP enhancements.

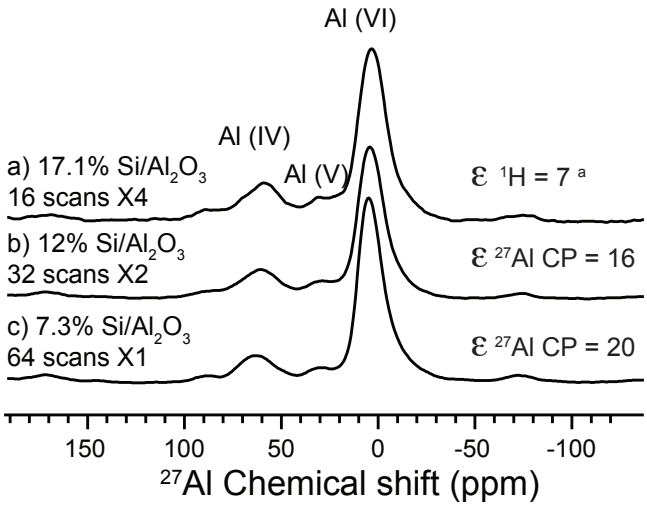

Figure 5. 4. DNP enhanced ^1H-^{27}Al CPMAS solid-state NMR spectra acquired at 600 MHz/395 GHz. a) 17.1 w% Si/Al_2O_3, b) 12 w% Si/Al_2O_3 and c) 7.3 w% Si/Al_2O_3. Spectra for all of these samples were also measured on a 400 MHz DNP spectrometer (Figure A.5.1). ^1H-^{27}Al CPMAS of the starting alumina is available Figure A.5.10.

Once again, three distinct resonances centered around 9, 36 and 65 ppm were observed in the ^1H-^{27}Al CPMAS spectra and are assigned to Al(VI), Al(V) and Al(IV) aluminum atoms. Given the sensitivity of the ^{27}Al NMR chemical shifts and quadrupole parameters to hydration and the challenge of accurately modeling water coordination/hydration of the surface we did not consider the calculated ^{27}Al NMR spectra.[66]

Fits of the ^{27}Al CPMAS spectra shows the relative ratios of the Al(VI):Al(V):Al(IV) sites is approximately 75:5:20 for all silica loading levels, i.e.,

there is not a strong variation in the relative intensities of the different aluminum sites with increasing SiO_2 loading level (Figure A.5.11 and Table A.5.4). However, as the loading of SiO_2 is increased and the alumina surface becomes covered the absolute intensity of the ^{27}Al CPMAS spectra is observed to decrease (Figure A4.1). In addition, we may also expect a different intrinsic behavior of Al/SiO_2 and Si/Al_2O_3 interface. In Si/Al_2O_3 we expect that Al(V) sites result from the reconstruction-amorphization process as reported in ref [19]; the rigid alumina framework imposes structural constraints and likely limits the formation of a large number of Al(V) even at high silica content. In contrast for Al/SiO_2, monomeric aluminum species deposited on the silica surface are intrinsically more flexible, thus allowing the formation of Al(V) from Al(IV) species (*vide supra*).

Once again high quality ^{1}H-^{29}Si CPMAS spectra could be rapidly acquired (ca. 5 minutes for a one dimensional spectrum). The DNP enhanced ^{1}H-^{29}Si CPMAS spectra of Si/Al_2O_3 are shown for three different silicon loadings of 7.3, 12.0 and 17.1 w% (Figure 5.5). The ^{29}Si DNP SENS CPMAS spectra of Si/Al_2O_3 can be decomposed into three components at -83, -93 and -100 ppm (Figure A.5.13-14).

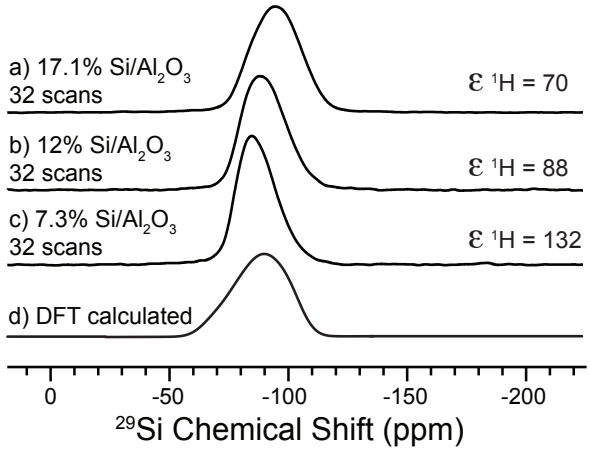

Figure 5. 5. 400 MHz/263 GHz DNP SENS ^{1}H-^{29}Si CPMAS solid-state NMR spectra. a) 17.1 w% Si/Al_2O_3, b) 12 w% Si/Al_2O_3 and c) 7.3 w% Si/Al_2O_3. For ^{29}Si measurement DNP enhancement was measured by directly observing the ^{1}H spectrum, since the acquisition of a ^{29}Si CPMAS spectrum without DNP required too long for signal averaging. (d) DFT calculated spectrum, for all ^{29}Si nucleus, independently of their proximity to ^{1}H. The model corresponds to a 14% Si/Al_2O_3. All spectra were acquired with a 12.5 kHz spinning frequency and a CP contact time of 0.6 ms for ^{27}Al and 3.0 ms for ^{29}Si.

The calculated ^{29}Si chemical shifts of the various surface sites are distributed between –78 to –99 ppm, consistent with the experimental observations. Applying Gaussian broadening to this distribution leads to the simulated spectrum reported in Figure 5.5.d. The position of the maximum is enclosed between those of the

experimental spectra of the 12% and 17.1% Si/Al_2O_3 sample. The DFT model is representative of a perfectly dispersed silica over-layer, without multilayers, which may explain the slightly different shape of the simulated spectrum as compared to the experiment; the DFT simulated spectrum is slightly more intense at negative chemical shifts, and less intense at the more positive chemical shift tail (Figure A.5.15). Reducing the broadening for the simulated spectrum leads to a three-component spectrum (Figure A.5.16), centered at around -80, -92 and -97 ppm. Excluding the Si atoms that do not have any hydrogen as second neighbors from the simulation does not affect the shape of the spectrum. All surface Si are likely observed since the contact time used for the ^{1}H-^{29}Si CPMAS experiment is long (3ms).

On the basis of DFT calculation, we can propose an assignment of the spectra of the Si/Al_2O_3 samples. Note however that the presence of various environments around similar ^{29}Si (Figure 5.6), *e.g.* various Si-O-Si and Si-O-Al angles and bond lengths, coordination numbers of Al atoms, presence of additional Al atoms non-covalently bonded but in close proximity to Si-O, will lead to a distribution of chemical shifts, only modeled in part here.

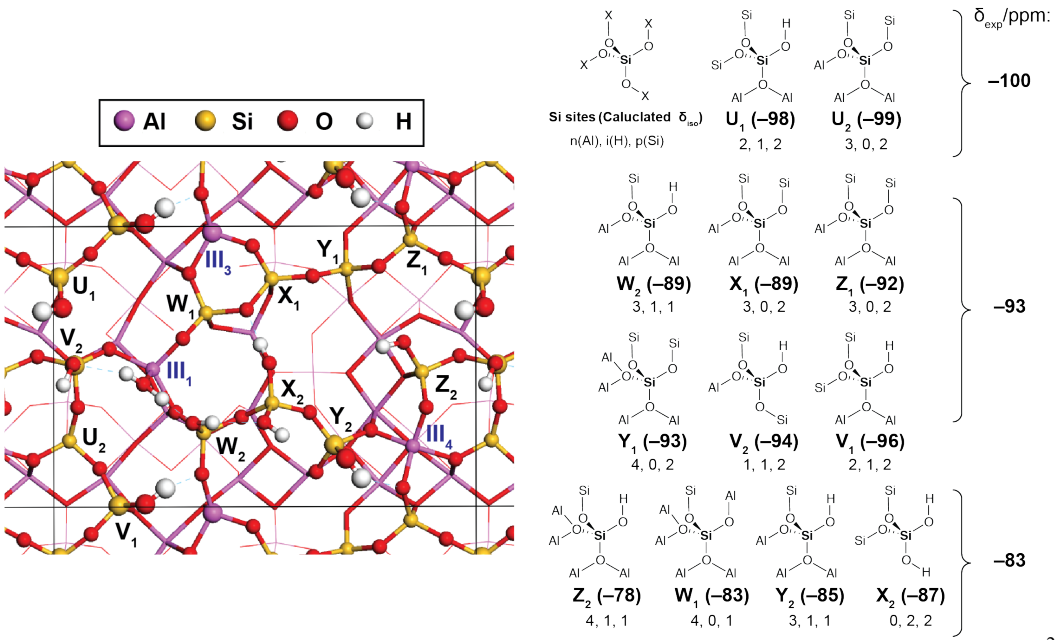

Figure 5. 6. On the left, top view of the Si/Al_2O_3 DFT model employed with θ_{OH} = 5.4 nm^{-2}, constructed from the silication of the (100) γ-Al_2O_3 surface. The terminology for Si and outermost surface Al atoms is given in black and blue respectively. See Figure A.5.17, Table A.5.5 for more details on local environments and side views. On the right, schematic representation of each Si sites with in parenthesis the DFT-computed ^{29}Si chemical shifts, the number and the nature of second neighbors for each Si atom on the ASA model employed. The environment of Si is noted Si(nAl, iH, pSi), by extension of the terminology from previous work.[75] n+i+p can be larger than four because of the significant ionicity of the framework (some oxygen are more than twofold coordinated). According to the decomposition, DFT calculated peaks were lumped into three sub-groups centered around the experimental peaks: $\delta < -96$ ppm ; $-96 \text{ ppm} \leq \delta \leq -88$ ppm; $-88 \text{ ppm} < \delta$.

In agreement with previous empirical assignments, based on the analysis of crystalline and amorphous alumino-silicates,[71-75] both H and Al second neighbors are at the origin of the increase of the chemical shift of ^{29}Si nucleus (Figure 5.7): the Z_2 site, corresponding to -78 ppm chemical shift, is surrounded by the highest number of Al neighbors (n=4) together with a proton.[71-74] Considering that all oxygen atoms surrounding a Si atom are two-fold coordinated (as in silica), an empirical assignment (Figure A.5.18) and model (Figure 5.7) can be drawn for each Si atom in silicates based on the number of H s (i) and Al (n) neighbors, where the chemical shift of a specific Si site is positively shifted by (10i + 5n) ppm from the chemical shift of pure SiO_2 (Q_4 sites, d_{iso} = –110 ppm) as a reference (see eq. 1).[71-74]

$$d_{iso}{}^{29}Si(i,n) = ((10i + 5n) – 110) \text{ ppm} \quad (1)$$

However, in the presence of alumina, a more ionic support than silica, oxygen atoms can adopt higher than two-fold coordination. In alumina, the coordination number of oxygen atoms can be as high as four, so that higher coordination may be expected at the Si/Al interface. If we denote the environment of a given Si as Si(nAl, iH, pSi) to note the number of its second neighbors, DFT calculations show that n+i+p can exceed four. This can be related to the so-called "O tricluster" suspected for aluminosilicate glasses.[4,65,81-83] We can extend this concept to an "O tetracluster" on our silicate alumina surface model. This leads to a deviation (below 10 ppm) of the empirical model chemical shifts (Figure 5.7) since the ^{29}Si chemical shift cannot be simply related to the nature and number of second neighbors.

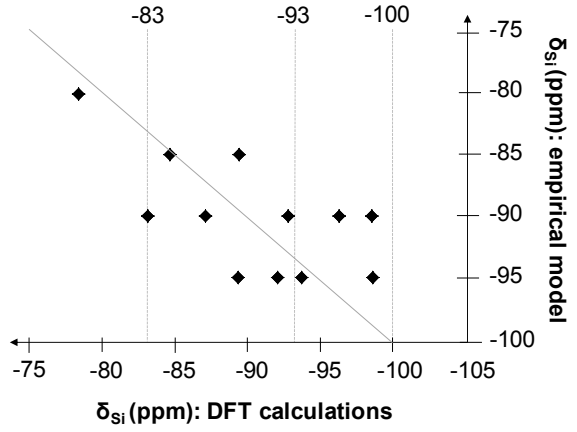

Figure 5. 7. Comparison of ^{29}Si chemical shifts calculated by DFT and an empirical model (see Figure A.5.18), derived from the analysis of the literature data available, assuming twofold coordination for all O atoms, and constant chemical shift variation by +10 ppm for each ^{1}H and +5 ppm for each Al second neighbor.[71-75] The experimental ^{29}Si chemical shifts of our Si/Al_2O_3 samples are represented with the dotted vertical lines. The plain line depicts the diagonal of the parity plot.

To assign the experimental ^{29}Si CPMAS NMR spectra, we compared the DFT calculated chemical shifts to the three experimental chemical shifts obtained from deconvolution of the ^{29}Si CPMAS spectrum of 17.1% Si/Al_2O_3 (Figure A.5.6). The -93 and -100 ppm peaks are clearly related to a higher number of Si atoms as second neighbors than the -83 ppm peak. The -83 and -93 ppm peaks correspond generally, but not necessarily, to a high number of Al as second neighbors (example: X_2), as several H as second neighbors can also lead to increase in chemical shifts.[74] Experimental evaluation of the peak intensities shows that at high silicon loading, Si species giving signal around -93 ppm (and in a lower extent, -100 ppm) become dominant, whereas the -83 ppm signal vanishes, consistent with the existence of more numerous Si as second neighbors. This can be related to the formation of a SiO_2 multilayer and a pure silica network. At low loading the -83 ppm peak increases dramatically consistent with the first layer of silicate bonding directly to the surface of Al_2O_3.

Scalar two-dimensional ^{29}Si-^{27}Al DNP SENS INEPT HETCOR spectra of Si/Al_2O_3 (Figure 5.8) show that the silica tetrahedra are primarily bonded to the aluminum tetrahedra (decompositions of the projection of the ^{27}Al dimension for both scalar and dipolar HETCOR spectra are given in Figure A.5.6-7 and Table A.5.2-3.

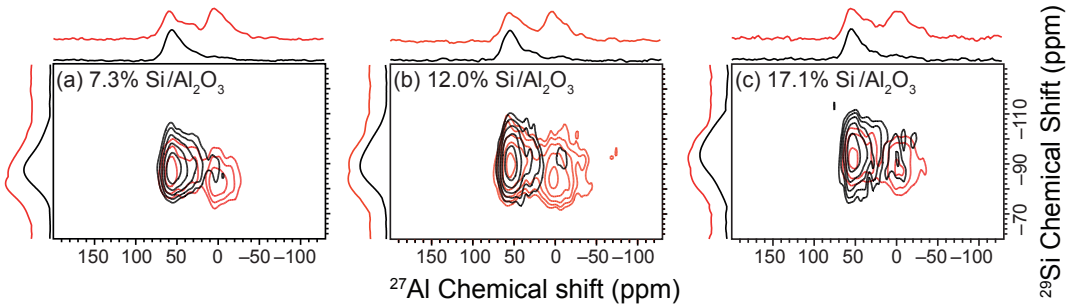

Figure 5. 8. 400 MHz/263 GHz DNP SENS scalar refocused INEPT (black traces/contours) and dipolar refocused R^3-INEPT (red traces/contours) ^{29}Si-^{27}Al hetero-nuclear correlation spectra of h) 17.1 w% Si/Al_2O_3, i) 12 w% Si/Al_2O_3 and j) 7.3 w% Si/Al_2O_3. All spectra were acquired with a 12.5 kHz MAS frequency. Projections of the 2D spectra are shown along the horizontal and vertical axes. For dipolar correlation experiments 96 total rotor cycles of recoupling were used, while for scalar correlation experiments, 420 total rotor cycles of evolution were used. Spectra were acquired with between 16 and 80 scans per increment, 28 t_1 increments and a rotor synchronized t_1 increment of 80 ms. Recycle delays were optimized for sensitivity and were between 3.8 s and 5.0 s.

However, in the scalar HETCOR spectra weak correlations to octahedral aluminum sites are observed, and the relative intensities of these correlations are constant (within the uncertainty of the measurement) with increasing loading of Si on

alumina (Figure A.5.6 and Table A.5.2). This is consistent with the high intensity of the octahedral aluminum sites observed in the 1D ^{27}Al CPMAS spectra of Si/Al_2O_3.

The dipolar ^{29}Si-^{27}Al HETCOR spectra of Si/Al_2O_3 show more intense correlations to octahedral aluminum sites, and penta-coordinate aluminum, in particular for the lowest Si loading. The relative intensity of the correlations to the octahedral and penta-coordinate aluminum sites is also increased in Si/Al_2O_3 as compared to the corresponding HETCOR spectra of Al/SiO_2 due to the presence of 6- and 5-fold coordination of aluminum sites on the alumina surface and therefore the close proximity with the ^{29}Si nuclei (Figure A.5.7 and Table A.5.3). To explain this, we analyzed the Si to Al proximity in our DFT model (Figure A.5.19). From this, we expect correlations with all types of Al atoms (IV, V, VI), but clearly the environment of Si is richer in Al(IV) than *a priori* expected from the structure of the alumina surface (on the (100) alumina orientation used for the simulation, no Al(IV) are exposed at the surface).[84,85] This can be interpreted as an Al(VI) to Al(IV) and Al(V) to Al(IV) conversion induced by silica. This conversion is likely driven by the higher degree of covalence of silica as compared to alumina, which favors lower coordination numbers. This is in line with the higher Al(IV)/Al(VI) ratio observed as silica content increases in ASA, which was known from classical ^{27}Al NMR.[18,37,38] Note that the Al(IV) giving signal in the ^{29}Si-^{27}Al HETCOR spectra (Figure 5.3 and 4.8) appears at slightly lower isotropic chemical shifts (62-66 ppm, Figure A.5.7 and Table A.5.3) than in the 1D DNP enhanced ^{27}Al CPMAS NMR spectra (66-73 ppm). This can be related to the DFT results, which show that the isotropic chemical shift of Al(IV) is reduced when silicon is present as second neighbor (Figure A.5.9). This is qualitatively comparable to observations from calculations on aluminosilicate glasses, even if the strength of the effect is different.[76] Note also that the ^{29}Si nuclei detected in ^{29}Si-^{27}Al HETCOR appear at more positive chemical shifts than in the 1D ^{29}Si CPMAS NMR spectrum. This is because Si sites which neighbor Al will give rise to more positive ^{29}Si chemical shifts than Si near to only Si.

In summary, the 1D ^{27}Al and ^{29}Si and 2D ^{29}Si-^{27}Al correlation spectra suggest that grafting of silica onto alumina primarily results in the formation of bonds between SiO_4 tetrahedra and tetrahedral Al(IV) sites, however, some SiO_4 tetrahedra are bonded to octahedral Al sites. Since SiO_2 is deposited onto Al_2O_3, most Si atoms will be proximate to the aluminum surface resulting in more intense correlations

between Si and octahedral/penta-coordinated aluminum atoms. The observation of more negative ^{29}Si chemical shifts with increasing Si loading level is also consistent with formation of a SiO_2 multi-layer at higher loading level.

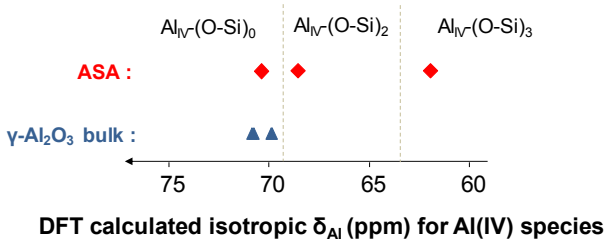

Figure 5. 9. DFT calculated dependence on Al(IV) isotropic chemical shift as a function of the number of Si as second neighbors of Al. γ-Al_2O_3 serves as reference with no Si as second neighbors. In Al_{IV}-$(OSi)_x$, IV refers tetra-coordinate aluminum and x to the number of (OSi) bound to Al.

Taken together the variation in the intensities of the DNP SENS 1D and 2D NMR with the loading levels can be used to propose some simple structural models (Scheme 5.2). On Si/Al_2O_3, the population of Al(VI) is more abundant that on Al/SiO_2 (from ^{27}Al DNP SENS). Many Si nuclei are bonded to OH groups, and are connected to Al(IV) as second neighbors, being also quite close to Al(VI) and Al(V) species. This strong connection to Al(IV) atoms is linked to the locally strong covalence of ASA as compared to alumina. As the silica loading increases there is an overall increase in the intensity of signal with more negative chemical shifts. This suggests that increasing loading of SiO_2 results in the formation of a SiO_2 multilayer, likely a pure silica network. On the other hand, when Al is grafted onto silica in Al/SiO_2 the relative intensity of the tetrahedral sites is higher, due to the high covalence of the host matrix (silica). However, as the Al-loading increases, an Al_2O_3 over-layer begins to form and relative ratio of tetrahedral to six-coordinate sites decreases to converge towards this of pure γ-alumina (3/1). Interestingly, the relative amount of penta-coordinated aluminum sites at the surface increases with the grafting of alumina, suggesting that more defected alumina surface sites may result as the loading level is increased, thereby confirming previous propositions.[32]

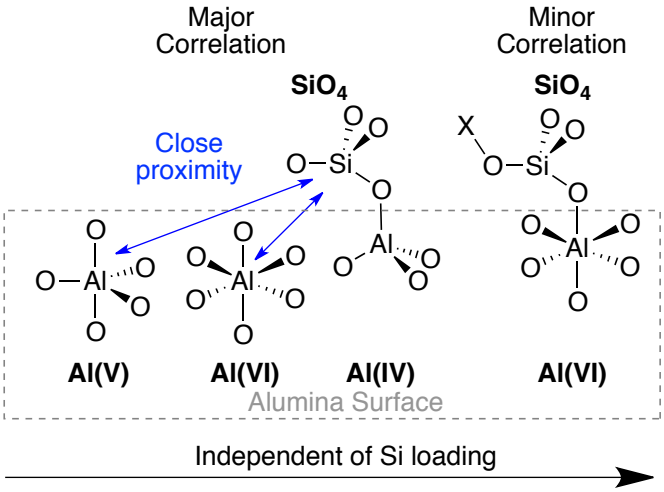

Scheme 5. 2. Representation of the Si/Al_2O_3 interface depicting direct bonding between tetrahedral aluminum silicon sites and close proximity of octahedral aluminum sites. X= Al, Si or H. Homocondensation of the alkoxides is possible and would lead to the formation Si-O-Si type species. These structures represent an equilibrium population.

5.5 Relation to Brønsted Acidity and Proposal for its Structure.

The present NMR data, in particular the correlation experiments, yields new insight into the atomistic structure of the Brønsted acid sites of ASA materials. Table 5.2 quantifies the Brønsted acid sites.[16,31-33] On Al/SiO_2 samples, the occurrence of Si(IV) - Al(IV) connectivity as the aluminum loading increases is associated with a higher concentration of acid sites per Al atom on these samples.[33] Previous measurements of the concentration of Brønsted acid sites have shown that there are more Brønsted acid sites per deposited aluminum at low Al loading levels. The DNP SENS ^{27}Al CPMAS spectra also show that there is an increase in the relative amount of Al(IV) sites at low loading levels. Taken together, these two results strongly suggest that the formation of Brønsted acid sites is related to the presence of Al(IV) on the Al/SiO_2 surface. This finding substantiates previous observations.[86] Silicon connected to aluminum with higher coordination number would be inefficient in forming Brønsted acid sites.

Table 5. 2. Coverage by aluminum species and surface density of Brønsted acid sites.[31,33]

Sample	Brønsted acid sites (nm^{-2})	Brønsted acid sites Per Al atom ($\times10^{-2}$, Al $exposed^{-1}$)
5.7% Al_2O_3/SiO_2	0.20	15.4
15% Al_2O_3/SiO_2	0.39	6.7
24.8% Al_2O_3/SiO_2	0.52	7.3
7.3% SiO_2/Al_2O_3	0.04	0.5
12% SiO_2/Al_2O_3	0.11	1.5
17.1% SiO_2/Al_2O_3	0.19	5.2

The results on Al/SiO_2 materials show that the low coordination of the aluminum atoms and the presence of silica as a matrix are both crucial parameters for obtaining Brønsted acid sites in ASAs. Gathering such conditions by grafting silicon species on the Al_2O_3 surface is more difficult for two main reasons. On the one hand, the coordination of the aluminum atoms populating the Al_2O_3 surface is on average closer to six than to four, higher than that of the first aluminum species deposited in Al/SiO_2 samples. On the other hand, a significant amount of deposited silicon species is required so as to change the covalence of the surface aluminum species in such a way that it induces the formation of reactive sites. Hence the number of Brønsted acid sites per exposed aluminum atom in Si/Al_2O_3 samples increases with the silica loading and consequent coverage of aluminum surface species.

Hensen *et al.*[20] categorized the acid sites of ASAs in two main types, the strongest ones being bridging acid sites such as in zeolites, and the milder ones being specific to ASAs, with different structures. Experimental and computational data combined suggest that the structures of the acid sites of ASAs are bridging hydroxyl between Si(IV) and Al(IV), possibly associated with pseudo-bridging silanols (PBS) for Si/Al_2O_3 materials (Scheme 5.3).[19,29,79,87] Such sites are defined as silanols being non-covalently bonded to aluminum atoms (electrostatic interaction between aluminum atoms and oxygen of the silanol, shown as dashed line in Scheme 5.3). According to calculations such species can be protonated by basic probe molecules (B) such as lutidine, by closing the Si-O•••Al bridge, yielding Si-O-Al anionic species and BH^+, in agreement with ref. 17.[30,79] Moreover, the intrinsic protonation and cracking abilities of such PBS sites have recently been compared to bridging acid sites of a zeolite in DFT calculations, and these specific structures would

account for the milder acidity of PBS and corroborate the main role of the interaction between the alumina support and deposited silicon species.[87] In the present work, on the basis of the NMR spectra, we suggest that the acceptor Al atom is likely in tetrahedral coordination, and that the silicon bearing the silanol is covalently bonded to other Al(IV) ions (Scheme 5.3). However, all PBS sites are covalently connected to only Al(VI) and Al(V) in the DFT model discussed here, due to the high aluminum content. While it is hard to make an unambiguous prediction of the ^{29}Si NMR chemical shift for sites depicted in Scheme 5.3, the two PBS sites, V_1 and Z_2 in Figure 5.6, can be considered as prototypical examples: they are characterized by very distinct calculated chemical shifts of -96 and -78 ppm respectively. This large difference of calculated chemical shifts, for similar species, shows that 1D NMR cannot be used to identify the Brønsted acid sites of ASA. In contrast, NMR correlation experiments, which probe Al(IV) to Si(IV) proximity, a requirement for Brønsted acidity, are therefore better suited to characterize such species.

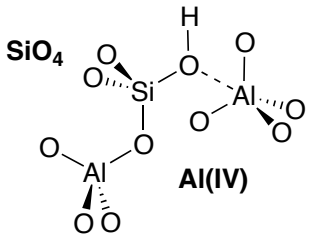

Scheme 5. 3. Proposal for a possible structure of Brønsted acid sites on ASA (Si/Al_2O_3): Pseudo-Bridging Silanol in connection with Al(IV) species.

5.6 Conclusion .

Combining DNP SENS, including 2D scalar and dipolar ^{29}Si-^{27}Al INEPT, and DFT calculations on ASA materials has allowed for a detailed atomic level description of (i) the connectivity between Si and Al nuclei on ASA surfaces, as a function of their coordination number and local environment, (ii) structural insight into the nature of Brønsted acid sites, which unifies the behavior of solids obtained by grafting either Al on silica, or Si on alumina.

On silica and alumina surfaces, molecular Si and Al precursor are preferentially grafted as "(IV)-to-(IV)"-coordinated mixed layer: the deposited silicon species are preferentially attached to Al(IV) sites issued from Al atoms of various coordinations of γ-alumina, with strong Si(IV)-Al(IV) connectivity. Similarly, the first deposited

aluminum species on silica in Al/SiO_2 are Al(IV) tetrahedrally coordinated species. This specific surface site connectivity eventually enables the formation of Brønsted acid sites. Such acid sites may be formulated as bridging hydroxyls in connection with Al(IV) species, such as pseudo-bridging silanol in Al/SiO_2. While an atomic level description of the interface of ASAs remains complex because each preparation technique makes a unique structure, the present study lays the foundation for the determination of the structure of the Brønsted active sites in the large family of alumino-silicates with the ultimate goal to establish structure-activity relationships and to use more rational development of solid acid catalysts.

5.7 Experimental Part.

5.7.1 Silica on Alumina Materials.

Si/Al_2O_3 samples were prepared by contacting excess tetraethyl-orthosilicate dissolved in dry toluene with γ-alumina (resulting from calcination at 540°C of Pural SB3, Sasol) in inert atmosphere (argon). After elimination of the unreacted precursor molecules, the samples were dried at 100°C and further calcined at 500°C (10°C per min ramp) under flow of air for 4h. The 7.3 w% of SiO_2 Si/Al_2O_3 sample was obtained after one grafting step; 12.0 and 17.1 w% of SiO_2 Si/Al_2O_3 samples were obtained after completion of two and three grafting steps, respectively. In all cases the final composition was determined by X-ray fluorescence spectroscopy.

5.7.2 Alumina on Silica Materials.

A similar procedure was applied for the preparation of the Al/SiO_2 samples. Aluminum isopropoxide dissolved in dry toluene was contacted with silica in inert atmosphere (Silica gel beads from Grace). The amount of aluminum precursor was adapted to obtain either 5.7 w% of Al_2O_3 or 15.0 w% of Al_2O_3 after one grafting step; 24.8 w% Al/SiO_2 was obtained after a second grafting step.

5.7.3 Dynamic Nuclear Polarization Surface Enhanced NMR Spectroscopy.

For DNP SENS[40,42] experiments the nitroxide biradical polarizing agents bCTbK [47] or TEKPol were used.[88]Incipient wetness impregnation with 1,1,2,2-tetrachloroethane (TCE) biradical solution [42,89] with a concentration of 14 to 16 mM biradical was used to prepare the samples for DNP experiments. The impregnated samples were packed into sapphire rotors and the sample was frozen at 100 K inside

the low temperature 3.2 mm MAS probe head. Samples were typically subjected to multiple insert-eject cycles and left under an eject gas flow prior to insertion in order to reduce the amount of oxygen in the TCE solution and increase DNP enhancements.[80] Experiments were performed with a 400 MHz (9.4 T)/263 GHz Bruker DNP system or a 600 MHz (14.1 T)/395 GHz Bruker DNP system.[90] The sweep coil of the main magnetic field was set so that microwave irradiation occurred at the ^{1}H positive enhancement maximum of nitroxide biradicals. Standard ramped cross-polarization (CP)[46] was then used to transfer polarization from the ^{1}H nuclei to the nucleus of interest (^{29}Si or ^{27}Al). For ^{1}H-^{27}Al CP experiments a low ^{27}Al spin lock radiofrequency field less than 20 kHz was employed in order to maximize the efficiency of the CP transfers. Two-dimensional ^{29}Si-^{27}Al scalar correlation spectra were acquired with a refocused INEPT pulse sequence (Figure A.5.5). ^{29}Si-^{27}Al dipolar correlation spectra were acquired with a dipolar refocused R^{3}-INEPT pulse sequence[91] where first order rotary resonance recoupling (R^{3})[92] was employed to recouple ^{29}Si-^{27}Al dipolar couplings. In all cases initial ^{29}Si magnetization was generated with ^{1}H-^{29}Si CP with a 6 ms contact time. We also tested a ^{29}Si-^{27}Al population transfer-HMQC pulse sequences[93] (with detection of ^{29}Si) to obtain scalar correlation spectra, however, the INEPT type sequences (with ^{27}Al detection) were found to provide superior sensitivity. ^{1}H-^{27}Al and ^{1}H-^{29}Si HETCOR experiments were performed with *e*-DUMBO$_{1\text{-}22}$ homonuclear decoupling applied during the t_1 evolution period.[94] The States-TPPI procedure was applied to achieve quadrature detection in the indirect dimension. The one-dimensional ^{27}Al DNP SENS CPMAS spectra were fit to a Cjzek model implemented in DMFit program in order to model the broad and featureless ^{27}Al resonances characteristics of distributions of quadrupole and chemical shift parameters.[70] The fits enabled the determination of the relative ratio of each species, the isotropic chemical shift (δ_{iso}), the Gaussian distribution of the chemical shifts ($\Delta\delta_{iso}$) and the quadrupolar coupling constant

5.7.4 Density Functional Theory.

Density Functional Theory (DFT) calculations were performed starting from the periodic ASA model previously established[19], according to a SiO_2/Al_2O_3 type, for θ_{OH} = 5.4 nm^{-2} and θ_{Si} = 6.5 nm^{-2}. This model was obtained by calculating the interaction of silicic compounds (silicic acid and a silica film) on a γ -Al_2O_3 model previously described by Digne *et al*.[84,85] Molecular dynamics simulations revealed

amorphization as well as mixing between the silica and alumina phases, by extraction of some aluminum atoms from the alumina layer to the silica one. The step-by-step simulation of hydration led to models containing OH groups. Shielding tensor computation were carried out with the CASTEP code [95], using the generalized gradient approximation of Perdew, Burke, and Ernzerhof PBE[96], and ultrasoft pseudopotentials[97] (cutoff energy 550 eV). A 1x1x2 k-points mesh was used. The gauge including projector augmented wave (GIPAW) algorithm[98] was applied. Due to computer memory constraints, the size of the systems modeled was reduced compared to the original geometry, by removing the lowermost atoms from the cell and saturating the resulting dangling bonds with water molecules to avoid unphysical electrostatic effects. The isotropic shielding (σ_{iso}), quadrupolar coupling constants (C_Q) and asymmetry parameters (η) of ^{1}H, ^{27}Al, ^{29}Si were calculated. Tetramethylsilane (for ^{1}H and ^{29}Si) and α-Al_2O_3 (for ^{27}Al) were used as references for chemical shifts calculations.

5.8 References.

(1) Corma, A. *Chem. Rev.* **1995**, *95*, 559.

(2) Busca, G. *Chem. Rev.* **2007**, *107*, 5366.

(3) Perez-Ramirez, J.; Christensen, C. H.; Egeblad, K.; Christensen, C. H.; Groen, J. C. *Chem. Soc. Rev.* **2008**, *37*, 2530.

(4) Stebbins, J. F.; Xu, Z. *Nature* **1997**, *390*, 60.

(5) Moses, A. W.; Raab, C.; Nelson, R. C.; Leifeste, H. D.; Ramsahye, N. A.; Chattopadhyay, S.; Eckert, J.; Chmelka, B. F.; Scott, S. L. *J. Am. Chem. Soc.* **2007**, *129*, 8912.

(6) Motokura, K.; Tada, M.; Iwasawa, Y. *J. Am. Chem. Soc.* **2007**, *129*, 9540.

(7) Alphazan, T.; Bonduelle-Skrzypczak, A.; Legens, C. l.; Gay, A.-S.; Boudene, Z.; Girleanu, M.; Ersen, O.; Copéret, C.; Raybaud, P. *ACS Catal.* **2014**, 4320.

(8) Bertoncini, F.; Bonduelle-Skrypczak, A.; Francis, J.; Guillon, E. *Catalysis by Transition Metal Sulphides: From Molecular Theory to Industrial Application*; (Eds.: Raybaud, P.; Toulhoat, H.), Technip Paris, **2013**, Chap. 3.4, pp. 609.

(9) Thieuleux, C.; Maraval, A.; Veyre, L.; Copéret, C.; Soulivong, D.; Basset, J.-M.; Sunley, G. J. *Angew. Chem. Int. Ed.* **2007**, *46*, 2288.

(10) Weitkamp, J. *ChemCatChem* **2012**, *4*, 292.

(11) Bond, J. Q.; Alonso, D. M.; Wang, D.; West, R. M.; Dumesic, J. A. *Science* **2010**, *327*, 1110.

(12) Hahn, M. W.; Copeland, J. R.; van Pelt, A. H.; Sievers, C. *ChemSusChem* **2013**, *6*, 2304.

(13) Marcilly, C. *J. Catal.* **2003**, *216*, 47.

(14) Hensen, E. J. M.; Poduval, D. G.; Degirmenci, V.; Ligthart, D. A. J. M.; Chen, W.; Mauge, F.; Rigutto, M. S.; van Veen, J. A. R. *J. Phys. Chem. C* **2012**, *116*, 21416.

(15) Koekkoek, A. J. J.; van Veen, J. A. R.; Gerrtisen, P. B.; Giltay, P.; Magusin, P. C. M. M.; Hensen, E. J. M. *Micropor. Mesopor. Mater.* **2012**, *151*, 34.

(16) Caillot, M.; Chaumonnot, A.; Digne, M.; van Bokhoven, J. A. *J. Catal.* **2014**, *316*, 47.

(17) Trombetta, M.; Busca, G.; Rossini, S.; Piccoli, V.; Cornaro, U.; Guercio, A.; Catani, R.; Willey, R. J. *J. Catal.* **1998**, *179*, 581.

(18) Crépeau, G.; Montouillout, V.; Vimont, A.; Mariey, L.; Cseri, T.; Maugé, F. *J. Phys.Chem. B* **2006**, *110*, 15172.

(19) Chizallet, C.; Raybaud, P. *Angew. Chem. Int. Ed.* **2009**, *48*, 2891.

(20) Poduval, D. G.; van Veen, J. A. R.; Rigutto, M. S.; Hensen, E. J. M. *Chem. Commun.* **2010**, *46*, 3466.

(21) Thomas, C. L. *Ind. Eng. Chem.* **1949**, *41*, 2564.

(22) Tamele, M. W. *Discuss. Faraday Soc.* **1950**, *8*, 270.

(23) Hansford, R. C. *Ind. Eng. Chem.* **1947**, *39*, 849.

(24) Xu, B.; Sievers, C.; Lercher, J. A.; van Veen, J. A. R.; Giltay, P.; Prins, R.; van Bokhoven, J. A. *J. Phys. Chem. C* **2007**, *111*, 12075.

(25) Huang, J.; van Vegten, N.; Jiang, Y.; Hunger, M.; Baiker, A. *Angew. Chem. Int. Ed.* **2010**, *49*, 7776.

(26) de Boer, J. H. *Discuss. Faraday Soc.* **1971**, *52*, 109.

(27) Blonski, S.; Garofalini, S. H. *J. Phys. Chem.* **1996**, *100*, 2201.

(28) Hwang, C.-P.; Yeh, C.-T. *J. Catal.* **1999**, *182*, 48.

(29) Leydier, F.; Chizallet, C.; Chaumonnot, A.; Digne, M.; Soyer, E.; Quoineaud, A.-A.; Costa, D.; Raybaud, P. *J. Catal.* **2011**, *284*, 215.

(30) Leydier, F.; Chizallet, C.; Costa, D.; Raybaud, P. *Chem. Commun.* **2012**, *48*, 4076.

(31) Caillot, M.; Chaumonnot, A.; Digne, M.; Bokhoven, J. A. V. *ChemCatChem* **2013**, *5*, 3644.

(32) Caillot, M.; Chaumonnot, A.; Digne, M.; Poleunis, C.; Debecker, D. P.; van Bokhoven, J. A. *Micropor. Mesopor. Mater.* **2014**, *185*, 179.

(33) Caillot, M.; Chaumonnot, A.; Digne, M.; Van Bokhoven, J. A. *ChemCatChem* **2014**, *6*, 832.

(34) Toulhoat, H.; Raybaud, P.; Benazzi, E. *J. Catal.* **2004**, *221*, 500.

(35) Gilson, J.-P.; Edwards, G. C.; Peters, A. W.; Rajagopalan, K.; Wormsbecher, R. F.; Roberie, T. G.; Shatlock, M. P. *J. Chem. Soc., Chem. Commun.* **1987**, 91.

(36) Man, P. P.; Peltre, M. J.; Barthomeuf, D. *J Chem. Soc. Faraday T.* **1990**, *86*, 1599.

(37) Dorémieux-Morin, C.; Martin, C.; Brégeault, J.-M.; Fraissard, J. *Appl. Catal.* **1991**, *77*, 149.

(38) De Witte, B. M.; Grobet, P. J.; Uytterhoeven, J. B. *J. Phys. Chem.* **1995**, *99*, 6961.

(39) Omegna, A.; van Bokhoven, J. A.; Prins, R. *J. Phys.Chem. B* **2003**, *107*, 8854.

(40) Lesage, A.; Lelli, M.; Gajan, D.; Caporini, M. A.; Vitzthum, V.; Miéville, P.; Alauzun, J.; Roussey, A.; Thieuleux, C.; Mehdi, A.; Bodenhausen, G.; Copéret, C.; Emsley, L. *J. Am. Chem. Soc.* **2010**, *132*, 15459.

(41) Lelli, M.; Gajan, D.; Lesage, A.; Caporini, M. A.; Vitzthum, V.; Miéville, P.; Héroguel, F.; Rascón, F.; Roussey, A.; Thieuleux, C.; Boualleg, M.; Veyre, L.; Bodenhausen, G.; Coperet, C.; Emsley, L. *J. Am. Chem. Soc.* **2011**, *133*, 2104.

(42) Rossini, A. J.; Zagdoun, A.; Lelli, M.; Lesage, A.; Copéret, C.; Emsley, L. *Acc. Chem. Res.* **2013**, *46*, 1942.

(43) Song, C.; Hu, K.-N.; Joo, C.-G.; Swager, T. M.; Griffin, R. G. *J. Am. Chem. Soc.* **2006**, *128*, 11385.

(44) Maly, T.; Debelouchina, G. T.; Bajaj, V. S.; Hu, K.-N.; Joo, C.-G.; Mak–Jurkauskas, M. L.; Sirigiri, J. R.; van der Wel, P. C. A.; Herzfeld, J.; Temkin, R. J.; Griffin, R. G. *J. Chem. Phys.* **2008**, *128*, 052211.

(45) Ni, Q. Z.; Daviso, E.; Can, T. V.; Markhasin, E.; Jawla, S. K.; Swager, T. M.; Temkin, R. J.; Herzfeld, J.; Griffin, R. G. *Acc. Chem. Res.* **2013**, *46*, 1933.

(46) Pines, A.; Gibby, M. G.; Waugh, J. S. *J. Chem. Phys.* **1972**, *56*, 1776.

(47) Zagdoun, A.; Casano, G.; Ouari, O.; Lapadula, G.; Rossini, A. J.; Lelli, M.; Baffert, M.; Gajan, D.; Veyre, L.; Maas, W. E.; Rosay, M.; Weber, R. T.; Thieuleux, C.; Coperet, C.; Lesage, A.; Tordo, P.; Emsley, L. *J. Am. Chem. Soc.* **2012**, *134*, 2284.

(48) Perras, F. A.; Kobayashi, T.; Pruski, M. *J. Am. Chem. Soc.* **2015**, *137*, 8336.

(49) Rossini, A. J.; Zagdoun, A.; Lelli, M.; Gajan, D.; Rascon, F.; Rosay, M.; Maas, W. E.; Coperet, C.; Lesage, A.; Emsley, L. *Chem. Sci.* **2012**, *3*, 108.

(50) Kobayashi, T.; Lafon, O.; Lilly Thankamony, A. S.; Slowing, I. I.; Kandel, K.; Carnevale, D.; Vitzthum, V.; Vezin, H.; Amoureux, J.-P.; Bodenhausen, G.; Pruski, M. *Phys. Chem. Chem. Phys.* **2013**, *15*, 5553.

(51) Vitzthum, V.; Mieville, P.; Carnevale, D.; Caporini, M. A.; Gajan, D.; Copéret, C.; Lelli, M.; Zagdoun, A.; Rossini, A. J.; Lesage, A.; Emsley, L.; Bodenhausen, G. *Chem. Commun.* **2012**, *48*, 1988.

(52) Lafon, O.; Thankamony, A. S. L.; Kobayashi, T.; Carnevale, D.; Vitzthum, V.; Slowing, I. I.; Kandel, K.; Vezin, H.; Amoureux, J.-P.; Bodenhausen, G.; Pruski, M. *J. Phys. Chem. C* **2013**, *117*, 1375.

(53) Wolf, P.; Valla, M.; Rossini, A. J.; Comas-Vives, A.; Núñez-Zarur, F.; Malaman, B.; Lesage, A.; Emsley, L.; Copéret, C.; Hermans, I. *Angew. Chem. Int. Ed.* **2014**, *53*, 10179.

(54) Gunther, W. R.; Michaelis, V. K.; Caporini, M. A.; Griffin, R. G.; Román-Leshkov, Y. *J. Am. Chem. Soc.* **2014**, *136*, 6219.

(55) Lee, D.; Duong, N. T.; Lafon, O.; De Paëpe, G. *J. Phys. Chem. C* **2014**, *118*, 25065.

(56) Lee, D.; Monin, G.; Duong, N. T.; Lopez, I. Z.; Bardet, M.; Mareau, V.; Gonon, L.; De Paëpe, G. *J. Am. Chem. Soc.* **2014**, *136*, 13781.

(57) Lee, D.; Hediger, S.; De Paëpe, G. *Solid State Nucl. Magn. Reson.* **2015**, *66–67*, 6.

(58) Profeta, M.; Benoit, M.; Mauri, F.; Pickard, C. J. *J. Am. Chem. Soc.* **2004**, *126*, 12628.

(59) Gervais, C.; Profeta, M.; Babonneau, F.; Pickard, C. J.; Mauri, F. *J. Phys.Chem. B* **2004**, *108*, 13249.

(60) Kučera, J.; Nachtigall, P. *Micropor. Mesopor. Mater.* **2005**, *85*, 279.

(61) Chizallet, C.; Costentin, G.; Lauron-Pernot, H.; Che, M.; Bonhomme, C.; Maquet, J.; Delbecq, F.; Sautet, P. *J. Phys. Chem. C* **2007**, *111*, 18279.

(62) Sklenak, S.; Dědeček, J.; Li, C.; Wichterlová, B.; Gábová, V.; Sierka, M.; Sauer, J. *Angew. Chem. Int. Ed.* **2007**, *46*, 7286.

(63) Tielens, F.; Gervais, C.; Lambert, J. F.; Mauri, F.; Costa, D. *Chem. Mat.* **2008**, *20*, 3336.

(64) Brouwer, D. H.; Cadars, S.; Eckert, J.; Liu, Z.; Terasaki, O.; Chmelka, B. F. *J. Am. Chem. Soc.* **2013**, *135*, 5641.

(65) Charpentier, T.; Menziani, M. C.; Pedone, A. *RSC Adv.* **2013**, *3*, 10550.

(66) Wischert, R.; Florian, P.; Copéret, C.; Massiot, D.; Sautet, P. *J. Phys. Chem. C* **2014**, *118*, 15292.

(67) Kunath-Fandrei, G.; Bastow, T. J.; Hall, J. S.; Jaeger, C.; Smith, M. E. *J. Phys. Chem.* **1995**, *99*, 15138.

(68) Lee, S. K.; Park, S. Y.; Yi, Y. S.; Moon, J. *J. Phys. Chem. C* **2010**, *114*, 13890.

(69) Sarou-Kanian, V.; Gleizes, A. N.; Florian, P.; Samélor, D.; Massiot, D.; Vahlas, C. *J. Phys. Chem. C* **2013**, *117*, 21965.

(70) Massiot, D.; Fayon, F.; Capron, M.; King, I.; Le Calvé, S.; Alonso, B.; Durand, J.-O.; Bujoli, B.; Gan, Z.; Hoatson, G. *Magn. Reson. Chem.* **2002**, *40*, 70.

(71) Lippmaa, E.; Maegi, M.; Samoson, A.; Engelhardt, G.; Grimmer, A. R. *J. Am. Chem. Soc.* **1980**, *102*, 4889.

(72) Lippmaa, E.; Maegi, M.; Samoson, A.; Tarmak, M.; Engelhardt, G. *J. Am. Chem. Soc.* **1981**, *103*, 4992.

(73) Murdoch, J. B.; Stebbins, J. F.; Carmichael, I. S. E. *Am. Mineral.* **1985**, *70*, 332.

(74) Maciel, G. E.; Sindorf, D. W. *J. Am. Chem. Soc.* **1980**, *102*, 7606.

(75) Sato, S.; Sodesawa, T.; Nozaki, F.; Shoji, H. *J. Mol. Catal.* **1991**, *66*, 343.

(76) Gambuzzi, E.; Pedone, A.; Menziani, M. C.; Angeli, F.; Caurant, D.; Charpentier, T. *Geochim. Cosmochim. Ac.* **2014**, *125*, 170.

(77) Pauling, L. *The Nature of the Chemical Bond and the Structure of Molecules and Crystals: An Introduction to Modern Structural Chemistry*; Cornell University Press, 1960.

(78) Chizallet, C.; Digne, M.; Arrouvel, C.; Raybaud, P.; Delbecq, F.; Costentin, G.; Che, M.; Sautet, P.; Toulhoat, H. *Top. Catal.* **2009**, *52*, 1005.

(79) Chizallet, C.; Raybaud, P. *ChemPhysChem* **2010**, *11*, 105.

(80) Kubicki, D. J.; Rossini, A. J.; Purea, A.; Zagdoun, A.; Ouari, O.; Tordo, P.; Engelke, F.; Lesage, A.; Emsley, L. *J. Am. Chem. Soc.* **2014**, *136*, 15711.

(81) Farnan, I. *Nature* **1997**, *390*, 14.

(82) Benoit, M.; Ispas, S.; Tuckerman, M. E. *Phys. Rev. B* **2001**, *64*, 224205.

(83) Benoit, M.; Profeta, M.; Mauri, F.; Pickard, C. J.; Tuckerman, M. E. *J. Phys.Chem. B* **2005**, *109*, 6052.

(84) Digne, M.; Sautet, P.; Raybaud, P.; Euzen, P.; Toulhoat, H. *J. Catal.* **2002**, *211*, 1.

(85) Digne, M.; Sautet, P.; Raybaud, P.; Euzen, P.; Toulhoat, H. *J. Catal.* **2004**, *226*, 54.

(86) Védrine, J.; Barthomeuf, D.; Dalmai, G.; Trambouze, Y.; Imelik, B.; Prettre, M. *C. R. Acad. Sc. Paris* **1968**, *267*, 118.

(87) Leydier, F.; Chizallet, C.; Costa, D.; Raybaud, P. *J. Catal.* **2015**, *325*, 35.

(88) Zagdoun, A.; Casano, G.; Ouari, O.; Schwarzwälder, M.; Rossini, A. J.; Aussenac, F.; Yulikov, M.; Jeschke, G.; Copéret, C.; Lesage, A.; Tordo, P.; Emsley, L. *J. Am. Chem. Soc.* **2013**, *135*, 12790.

(89) Zagdoun, A.; Rossini, A. J.; Gajan, D.; Bourdolle, A.; Ouari, O.; Rosay, M.; Maas, W. E.; Tordo, P.; Lelli, M.; Emsley, L.; Lesage, A.; Coperet, C. *Chem. Commun.* **2012**, *48*, 654.

(90) Rosay, M.; Tometich, L.; Pawsey, S.; Bader, R.; Schauwecker, R.; Blank, M.; Borchard, P. M.; Cauffman, S. R.; Felch, K. L.; Weber, R. T.; Temkin, R. J.; Griffin, R. G.; Maas, W. E. *Phys. Chem. Chem. Phys.* **2010**, *12*, 5850.

(91) Trebosc, J.; Hu, B.; Amoureux, J. P.; Gan, Z. *J. Mag. Res.* **2007**, *186*, 220.

(92) Oas, T. G.; Griffin, R. G.; Levitt, M. H. *J. Chem. Phys.* **1988**, *89*, 692.

(93) Wang, Q.; Trebosc, J.; Li, Y.; Xu, J.; Hu, B.; Feng, N.; Chen, Q.; Lafon, O.; Amoureux, J.-P.; Deng, F. *Chem. Commun.* **2013**, *49*, 6653.

(94) Elena, B.; de Paëpe, G.; Emsley, L. *Chem. Phys. Lett.* **2004**, *398*, 532.

(95) Clark, S. J.; Segall, M. D.; Pickard , C. J.; Hasnip, P. J.; Probert, M. I. J.; Refson, K.; Payne, M. C. *Z. Kristallogr.* **2005**, *220*, 567.

(96) Perdew, J. P.; Burke, K.; Ernzerhof, M. *Phys. Rev. Lett.* **1996**, *77*, 3865.

(97) Yates, J. R.; Pickard, C. J.; Mauri, F. *Phys. Rev. B* **2007**, *76*, 024401.

(98) Pickard, C. J.; Mauri, F. *Phys. Rev. B* **2001**, *63*, 245101.

Chapter 6: Generation of Metathesis Active Supported Re Oxo Alkylidene.

6.1 Individual Contribution.

Reproduced with permission from *John Wiley and Sons* and *Angewandte Chemie International Edition* from:

Valla, Maxence; Stadler, David; Mougel, Victor; Copéret, Christophe; *Angew. Chem. Int. Ed.,* **2016**, 55, 1124-1127.

Synthesis, characterization and catalytic test were done by Maxence Valla and David Stadler. Victor Mougel helped with the XRD measurement and the catalytic tests. Maxence Valla, Victor Mougel and Christophe Copéret participated to the scientific discussion and contributed to the writing process of the manuscript.

6.2 Introduction.

With its high efficiency and atom economy, metathesis has become one of the pillars of the petrochemical and chemical industry, and a key reaction for the development of fine chemicals through more sustainable processes.[1,2] In heterogeneous catalysis, metathesis mainly relies on supported Mo, W and Re oxides. Of these, Re_2O_7/Al_2O_3 and Re_2O_7/SiO_2-Al_2O_3 are unique, because of their room temperature activity and their compatibility with functional groups upon activation with R_4Sn.[2-11] It is currently thought that a perrhenate surface species coordinated to Al Lewis sites is the origin of the active species (Scheme 6.1a)[1,2] but the expected rhenium alkylidene propagating species have never been observed experimentally (Scheme 6.1b).

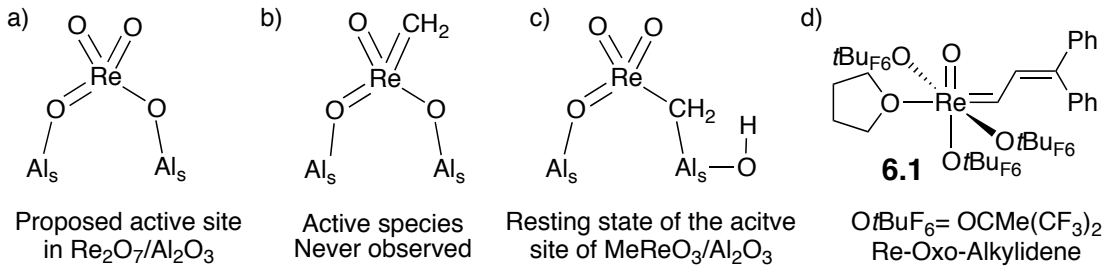

Scheme 6. 1. a) Proposed active sites in the heterogeneous catalysts Re_2O_7/Al_2O_3 b) Putative Re oxo Alkylidene active species of Re-based heterogeneous catalyst. c) Resting state of the active site (μ-methylene) in $MeReO_3/Al2O_3$ and d) $Re(O)(=CH–CH=CPh_2)(OtBu_{F6})_3(THF)$.

Most recent studies have focused on using supported CH_3ReO_3/Al_2O_3 as a possible model for Re_2O_7/Al_2O_3 and related systems.[12-20] However, while highly active in alkene metathesis, the expected alkylidene intermediates have never been observed in these systems. Instead, μ-methylene species have been identified, and correspond to a resting state of the catalyst (Scheme 6.1c). To date, (≡SiO)Re(≡C*t*Bu)(=CH*t*Bu)(CH_2*t*Bu) is the only well-defined supported rhenium alkylidene complex synthesized and active in metathesis.[21-24] Nonetheless, the absence of oxo ligands makes it difficult to relate the activity of that species with the classical heterogeneous catalysts. While recent reports have shown that molecular and silica-supported W oxo alkylidene complexes are highly efficient alkene metathesis catalysts,[25-31] analogous Re oxo alkylidenes surface species have remained elusive. Only few molecular rhenium oxo alkylidene molecular complexes are known,[32,33] and Re(O)(=CH–CH=CPh_2)($OtBu_{F6}$)$_3$(THF) ($OtBu_{F6}$ = $OCMe(CF_3)_2$) (**6.1,** Scheme 6.1d) is the only reported active alkene metathesis catalyst when activated with Lewis acids such as $GaBr_3$ or $AlCl_3$.[33]

Here, we explore the formation of well-defined active supported Re oxo alkylidene species through Surface Organometallic Chemistry,[34-36] and show that the incorporation of Al Lewis acid sites on silica is essential for metathesis activity.

6.3 Grafting of Re(O)(=CH–CH=CPh_2)($OtBu_{F6}$)$_3$(THF) on Partially Dehydroxylated SiO_2.

Carbon-13 labelled Re(O)(=*CH–*CH=CPh_2)($OtBu_{F6}$)$_3$(THF) was synthetized and characterized by liquid state NMR (Figure A.6.1-2). This complex will be called **6.1***. Grafting **6.1** (1.05 equiv.) on silica partially dehydroxylated at 700 °C (SiO_{2-700}) yields a dark red material with 0.8-0.9 equiv. of $tBu_{F6}OH$ per initial surface OH released. The decrease of the isolated silanol band at 3747 cm^{-1} in the IR spectrum (see Figure 6.1) is consistent with the consumption of surface silanol sites and the formation of (≡SiO)Re(O)(=CH–CH=CPh_2)($OtBu_{F6}$)$_2$(THF) **6.2a**, as the main surface species (Scheme 6.2). The appearance of carbon sp^2 vibration between 3000 and 3100 cm^{-1} and the appearance of carbon sp3 between 2800 and 3000 cm^{-1} confirm the well grafting of 6.1 and generation of the surface species **6.2a** and **6.2b**. The Re

loading of 3.03 wt% is consistent with the grafting on 72% of the surface silanol moieties, consistent with the observation of residual silanol by IR (Figure 6.1).

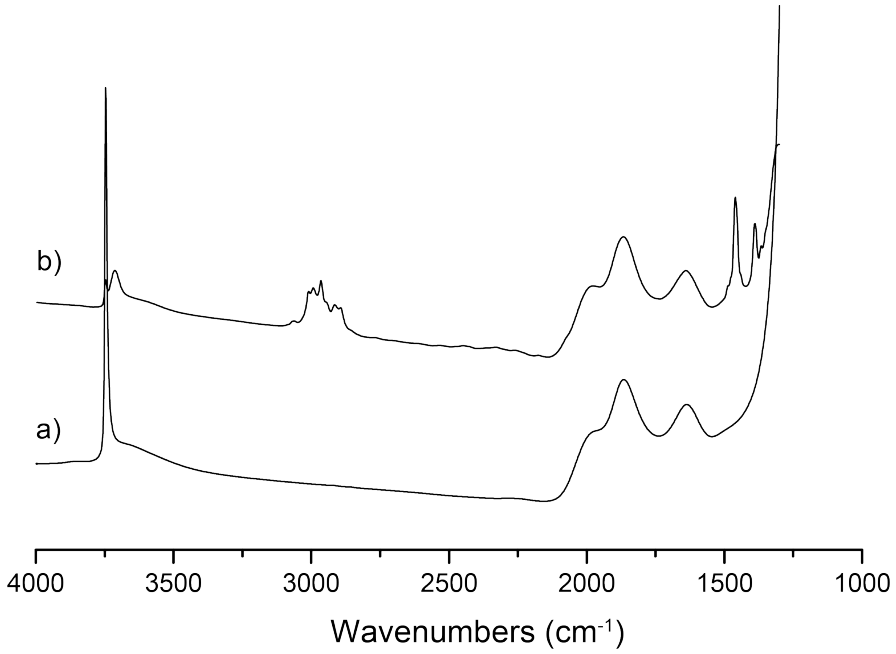

Figure 6. 1. FT-IR spectra of (a) $SiO_{2-(700)}$ and (b) $Re(O)(=CH–CH=CPh_2)(OtBu_{F6})_3(THF)$ grafted on $SiO_{2-(700)}$. 16 scans.

Carbon, fluorine and proton elemental analysis (4.5 wt% C, 0.41 wt% H and 3.12 wt% F) are consistent with the expected values for **6.2a** present as a major surface species (C/Re: 23 C measured, 27 expected; H/Re: 26 H meas., 26 exp. and F/Re: 10 F meas., 12 exp.) along with a minor amount of bis-grafted species **6.2b** (C/Re: 19, H/Re: 23 and F/Re: 6) as shown in Scheme 6.2.

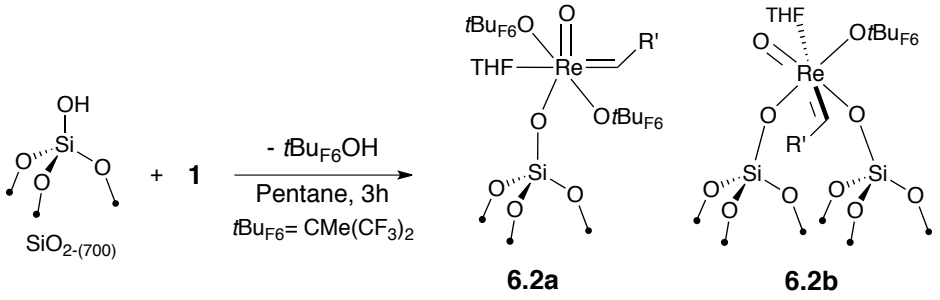

$Scheme 6. 2. Grafting of **1** on $SiO_{2-(700)}$ yielding $(\equiv SiO)Re(O)(=CH–CH=CPh_2)(OtBu_{F6})_2(THF)$ (**2**). R' = CH-CH=CPh_2.

The surface species was further characterized by solid-state NMR. The ^1H MAS NMR spectrum displays two peaks at 12.4 and 9.5 ppm assigned to the α- and β-C-H of the alkylidene ligand, respectively, along with the other resonances associated with phenyl (7.4 ppm), THF (4.4 and 1.8 ppm) and $tBuF_6O$ (1.8 ppm) moieties (See Figure A.6.3). The presence of the alkylidene ligand was confirmed by the observation of the

two signals at 280 and 167 ppm associated to the α- and β-carbons in ^{13}C Cross-Polarization (CP) MAS NMR spectrum of the corresponding carbon-13 labeled complex **6.2*** (grafting of **6.1*** on SiO_2 dehydroxylated at 700°C). The signals observed at 69 and 24 ppm correspond to THF (Figure 6.2).

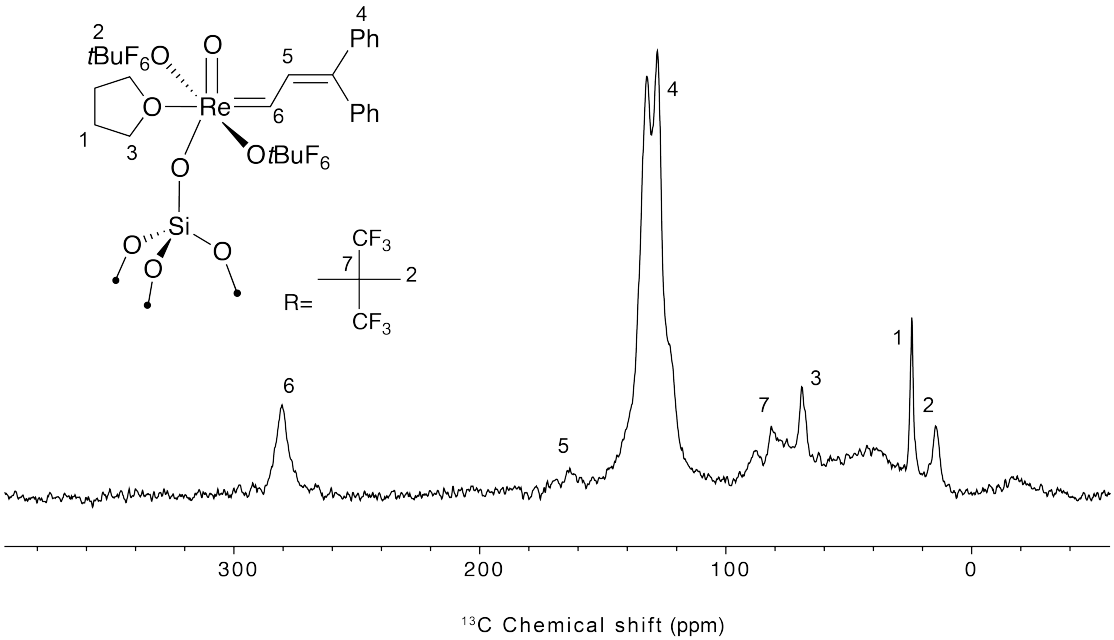

Figure 6. 2. ^{13}C CP-MAS NMR spectrum of $Re(O)(=CH–CH=CPh_2)(OtBu_{F6})_3(THF)$ grafted on $SiO_{2-(700)}$ at 400 MHz, d1= 1 sec, 10 kHz spinning speed. Contact time was set to 1.5 msec and the recycling delay was set to 1 sec.

However, in contrast to the isoelectronic alkylidyne alkylidene complex (≡SiO)Re(≡CtBu)(=CHtBu)(CH_2tBu), **6.2** does not present any significant self-metathesis activity.[21,23] By analogy with the activation of molecular W oxo alkylidene complexes by $B(C_6F_5)_3$,[25,26] metathesis with **6.2** was carried out in the presence of 1 equiv. of $B(C_6F_5)_3$, allowing a conversion of 19% after 24h in *cis*-4-nonene self-metathesis (0.1 mol% loading). In the case of tungsten, the crystal structure of the complex with the borate activator coordinating the oxo ligand was isolated, the same behaviour is expected on the surface.

6.4 Activation of $Re(O)(=CH–CH=CPh_2)(OtBu_{F6})_3(THF)$on Tailored Made Silica-Alumina Support.

When contacted with a Lewis acid molecule, here $B(C_6F_5)_3$, **6.2** becomes active in the self metathesis of *cis*-4-nonene. Therefore, we reasoned that tailoring a support combining both an anchoring OH site and a Lewis acid site in close proximity could

provide an optimal support for rhenium oxo alkylidene complexes.[18] Using a thermolytic precursor approach,[37] the formation of isolated metal silicate with adjacent OH groups is possible through the grafting of molecular tertbutoxysiloxide complexes followed by a thermolysis step under vacuum.[28,37,38] We thus explored the formation of Al silicates exploiting a similar strategy to provide Al Lewis acid sites in proximity to silanol anchoring sites.

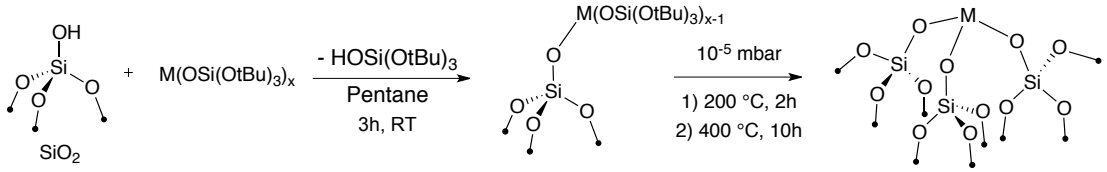

Scheme 6. 3. General reaction pathway for the grafting of Metal siloxide followed by the thermolysis step.

$Al(OSi(OtBu)_3)_3$ was obtained in 87% yield by protonolysis of $Al(i Bu)_3$ with 3 equiv of $(tBuO)_3SiOH$ (Scheme 6.4). The temperature sensitive complex was characterized by single crystal X-ray diffraction (Scheme 6.4, and Table A6.1-3). This compound, $Al(OSi(OtBu)_3)_3$, displays a distorted tetrahedral coordination with one bidentate κ^2-siloxy ligand, (Scheme 6.4).

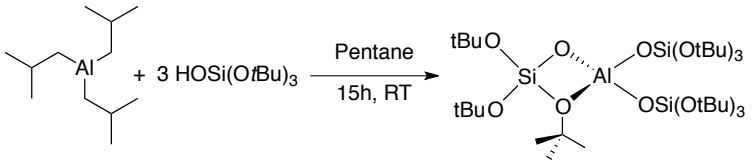

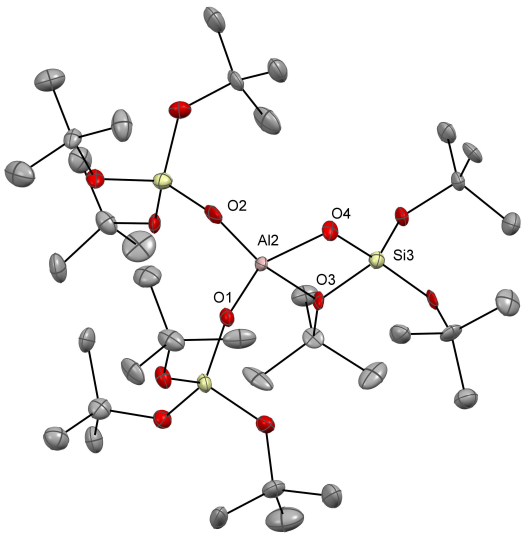

Scheme 6. 4. Top: Reaction pathway for the synthesis of tris-tert-butoxysiloxyaluminum. Bottom: Thermal ellipsoid plot at the 50% probability of $Al(OSi(OtBu)_3)_3$. Hydrogen atoms have been omitted for clarity.

The complex was also characterized by NMR. Low temperature high field solid state NMR (-30°C, 850 MHz) allowed the single fitting of the aluminum quadrupolar pattern with a δ_{iso} of 53.7 ppm and a C_Q value of 19.5 MHz (Figure 6.3) which is in line with a four–coordinate ^{27}Al.

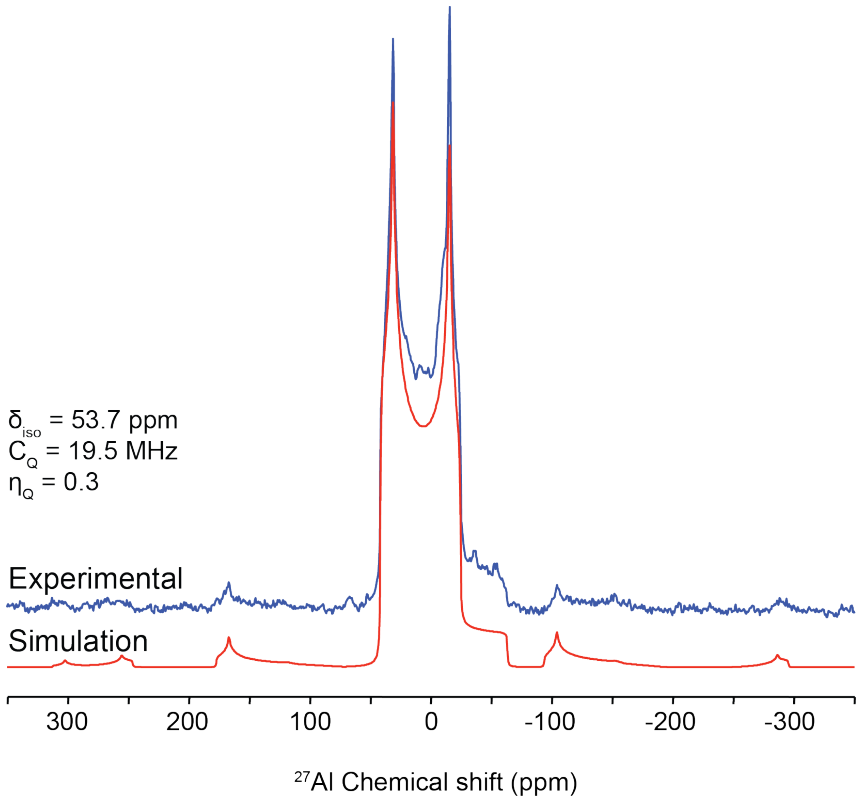

Figure 6. 3. ^{27}Al spin echo NMR spectrum of Al(OSi(OtBu)3)3, 2 echo periods (64 μs), 850 MHz, 30 kHz spinning speed, -30°C, ^{27}Al RF field of 20 kHz (blue trace). Simulation of the experimental spectrum fit to a Cjzek model implemented in DMFit program (red trace).

However, in contrast to the related Cr(III) analogue,[38] $Al(OSi(OtBu)_3)_3$ does not readily graft on silica. Alternatively, impregnation of this complex on $SiO_{2-(700)}$ at room temperature followed by a thermolysis step at 400 °C under high vacuum (10^{-5} mBar) affords a colorless material, **Al@SiO$_2$** with unchanged surface area (Scheme 6.5).

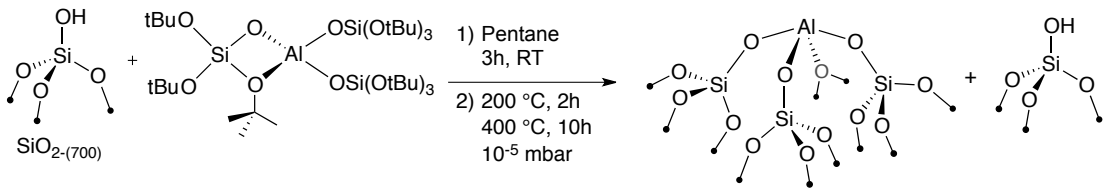

Scheme 6. 5. Synthetic route to @SiO2. The first step is the impregnation of Al tris-tert-butoxysiloxid followed by its thermolysis under high vacuum.

The absence of C-H containing groups was confirmed by IR spectroscopy. The surface silanols stretch is slightly red-shifted to 3743 cm^{-1}, by comparison to

isolated silanol sites, consistent with interaction with nearby Lewis acid sites (see Figure A.6.4).[38-40] The presence of Lewis acid sites was confirmed by monitoring pyridine adsorption on the support by IR. After exposure to a large excess of pyridine, the IR spectrum of **Al@SiO$_2$** reveals 3 bands at 1626, 1497 and 1458 cm^{-1}, characteristic of surface Lewis acid single sites (Figure 6.4).[41] The retention of these peaks (pyridine) upon high vacuum (10^{-5} mbar) and temperature treatment (450°C) indicates the presence of strong Lewis acid sites.

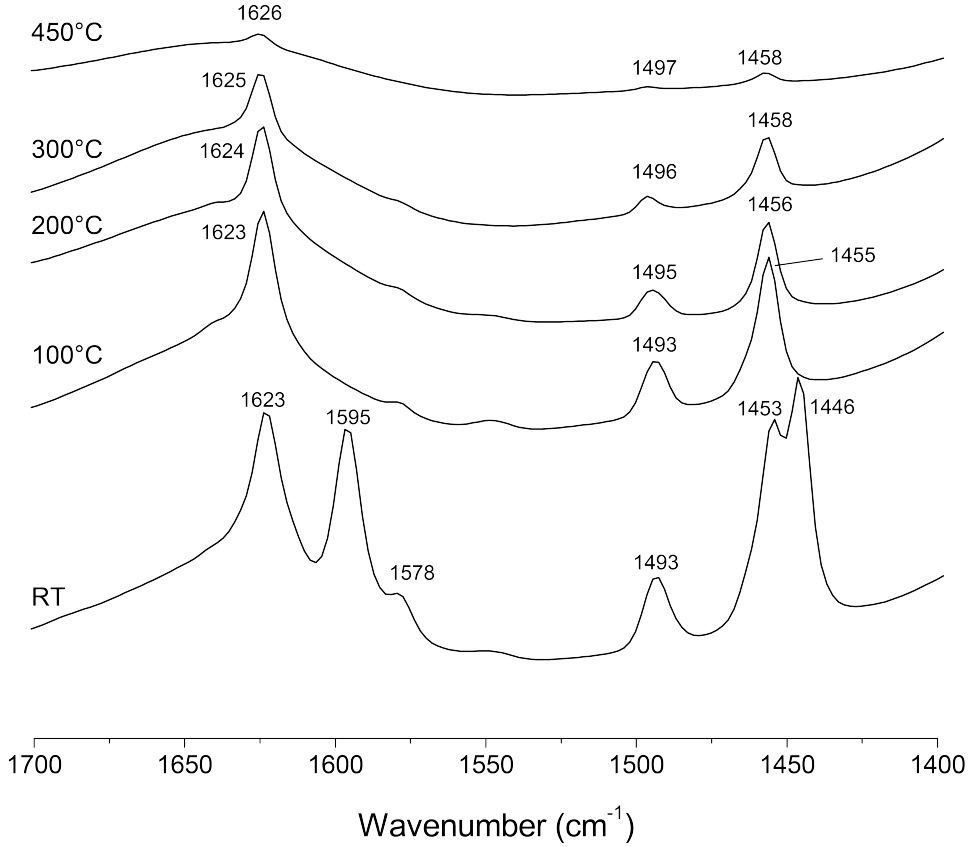

Figure 6. 4. Adsorption of pyridine on Al@SiO$_2$ followed by treatment under high vacuum and different temperature ranging from RT to 450°C. FT-IR spectra zoomed in the δ (C-H) vibration region (1700-1400 cm^{-1})

Al elemental analysis (0.6 %) and titration of surface hydroxyls by excess methylmagnesium bromide (0.54 mmol of CH_4 released per gram of support) show the presence of 0.75 Al.nm^{-2} and 1.6 OH per nm^{-2}. This density corresponds to roughly to 2.1 OH functionalities per Al sites. ^{27}Al spin echo NMR spectrum, measured on a 1 GHz spectrometer at 60 kHz, shows a highly resolved spectrum (Figure 6.5), which can be deconvolved into two components with one major peak (93% integral) with a chemical shift and a quadrupolar constant (C_Q) of 65.7 ppm and 17.5 MHz, respectively. These values are very close to the values found for the molecular complex (*see above*) consistent with a tetra-coordinated Al surface site.

The minor peak (7% integral) has a chemical shift of 21.8 ppm and a C_Q of 12 MHz and is probably associated with the presence of a more symmetric environment such as a five-coordinate surface Al site resulting from the coordination of an additional siloxane bridge.[42]

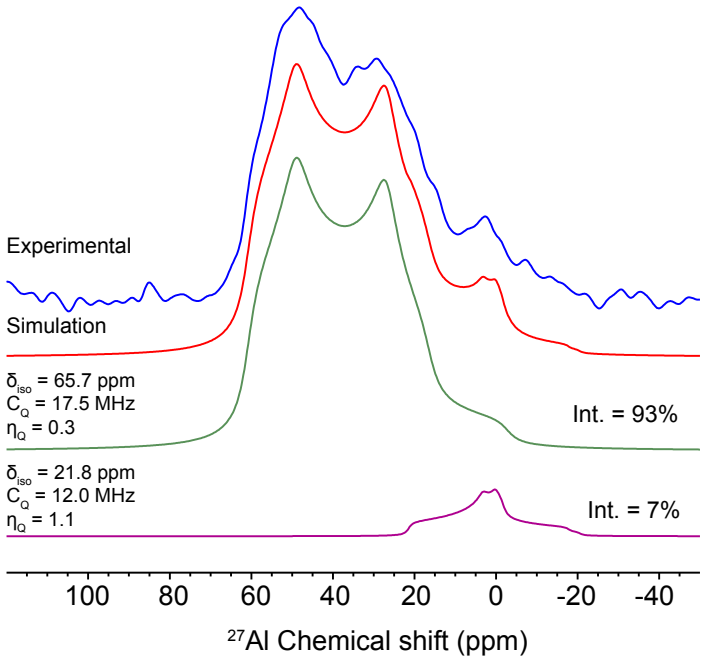

Figure 6. 5. ^{27}Al spin echo MAS with full echo acquisition of **Al@SiO$_2$**, 1 GHz, 60 kHz spinning speed. 15k scans with a recycling delay of 1s. The radio frequency field was calculated to be at 25 kHz according to Al nitrate reference sample.

Grafting of 1 equiv. of **6.1** (with respect to Al) on **Al@SiO$_2$** yielded a dark purple solid containing 3.51 wt% Re. While 0.8-0.9 equiv. of $tBu_{F6}OH$ was released, no THF was observed in solution. In addition, carbon and proton elemental analysis (5.80 wt% C, 0.44 wt% H and 3.65 wt% F) are consistent with the expected values for **6.3** (Scheme 6.6), (≡SiO)Re(O)(=CH–CH=CPh$_2$)(OtBu_{F6})$_2$(THF)/Al (C/Re: 27 C meas., 26 exp.; H/Re: 23 H meas.; 26 exp., F/Re: 10.3 F meas., 12 exp.). This corresponds to the grafting of 0.86 equiv. of the alkylidene on the **Al@SiO$_2$** surface with respect to the Al sites.

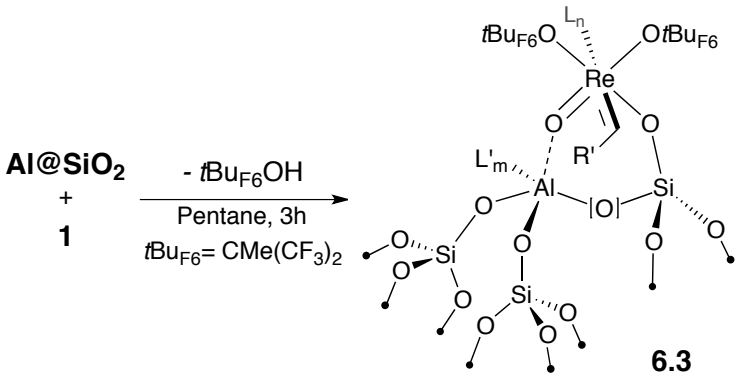

Scheme 6. 6. Grafting of **6.1** on Al@SiO_2 yields **6.3**. L = C_4H_8O, n = 0 or 1, L' = C_4H_8O or siloxane bridge (Si-O-Si), m = 0,1. The brackets indicate that the Al and Si are not necessarily directly bounded to each other through an oxygen bridge but can be separated by additional SiO_3 units. R' = CH-CH=CPh_2.

IR spectroscopy revealed a sharp decrease of the isolated silanol peak at 3743 cm^{-1} upon grafting of **6.1** and the concomitant appearance of a broad band centred at 3640 cm^{-1} assigned to silanols in interaction with the surface complex (see Figure 6.6).[43] Sp^3 ν(C-H) vibration can be observed between 3000 and 2750 cm^{-1} while sp^2 ν(C-H) can be observed above 3000 cm^{-1} indicating the presence of the ligands on the surface of the support.

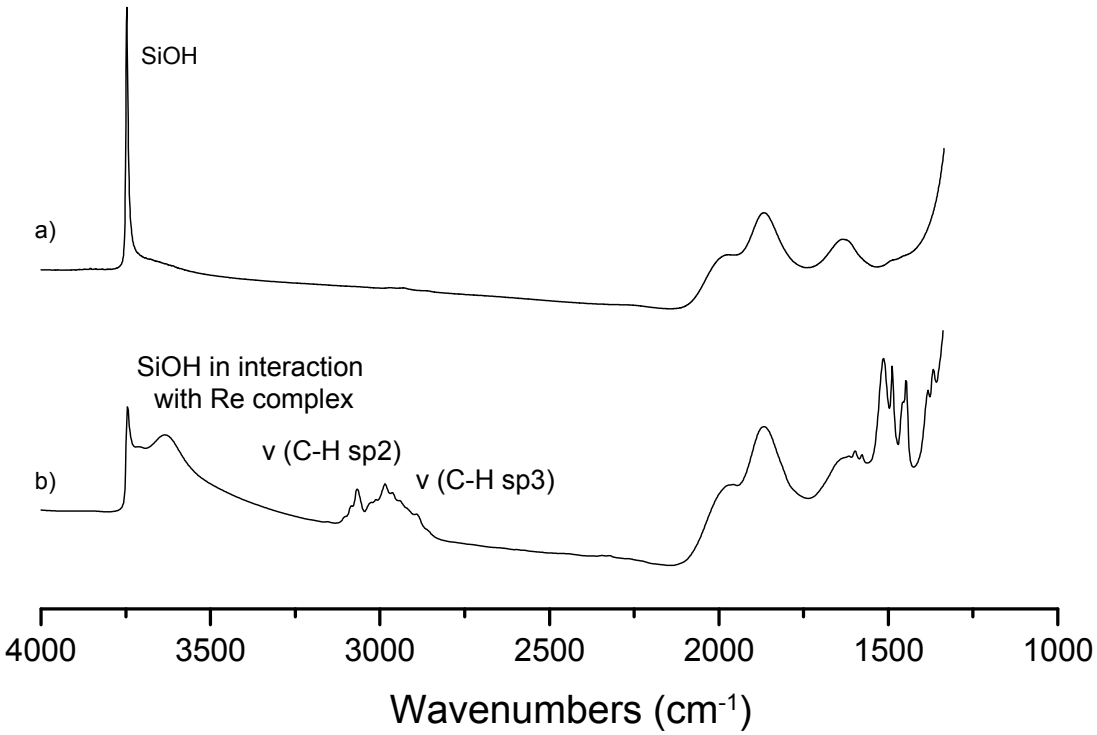

Figure 6. 6. IR spectra of **Al@SiO_2** (a) and Re(O)(=CH–CH=CPh_2)($OtBu_{F6}$)$_3$(THF) grafted on **Al@SiO_2** (b).

^{1}H NMR spectroscopy indicates the presence of an alkylidene species after grafting, evidenced with the peak at 12.3 ppm and at 9.6 ppm corresponding to the α- and β-C-H of the alkylidene ligand (see Figure A.6.5), and the resonances associated with phenyl (7.6 ppm), THF (4.5 and 1.9 ppm) and $tBuF_6O$ (1.9 ppm) groups. The corresponding 20% carbon-13 labelled surface species exhibits very similar NMR chemical shifts than **6.2** (Figure 6.7), but the alkylidene carbon displays a much larger chemical shift anisotropy (CSA). In fact, while it was not possible to measure the chemical shift anisotropy at a spinning speed of 10 kHz for the alkylidene signal of **6.2**, the surface complex **6.3** exhibits a broad spinning side band manifold and thereby a larger CSA (δ_{iso} = 281 ppm, Ω = 467 ppm, k = 0.3, see Figure A.6.6, consistent with a restricted dynamic of the Re alkylidene surface sites.

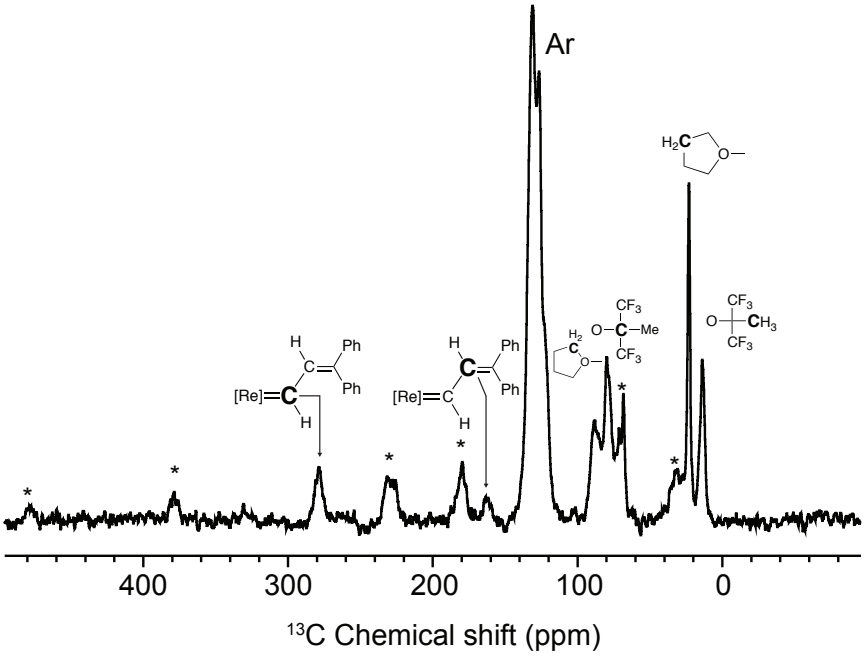

Figure 6. 7. a) ^{1}H-^{13}C CPMAS signature of Re(O)(=CH–CH=CPh$_2$)(OtBu$_{F6}$)$_3$(THF) supported on **Al@SiO$_2$,** 400 MHz, recycling delay was set to 1 sec, 10 KHz spinning speed, contact time was set to 1 msec.

In addition, ^{27}Al NMR shows the presence of two Al sites of approximately equivalent intensities, but lower C_Q than the original Al sites, at δ/C_q = 58.9 ppm / 10.8 MHz and 42.6 ppm / 12.6 MHz, consistent with a more symmetric environment, associated with coordination of Re=O and/or THF on Al (Scheme 6.6 and Figure 6.8).

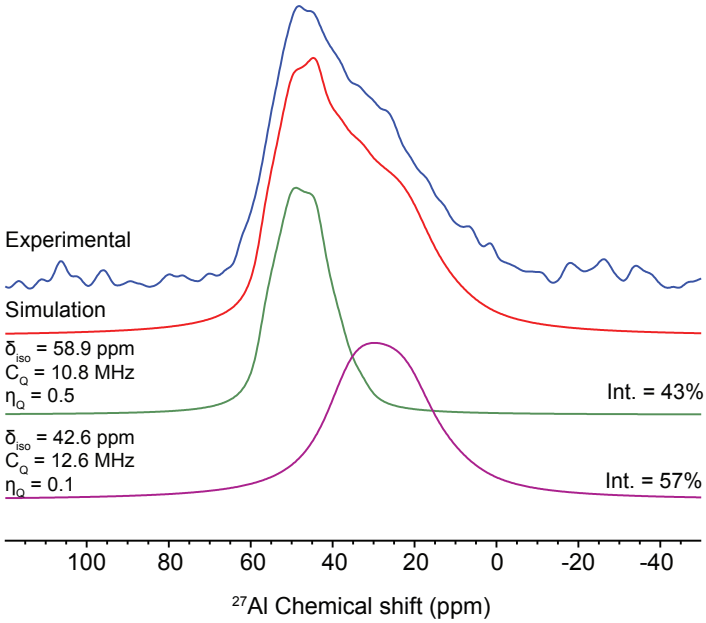

Figure 6. 8. b) ^{27}Al Spin echo MAS with full echo acquisition, 1 GHz, 60 kHz spinning speed. 15k scans with a recycling delay of 1s. The radio frequency field was calculated to be at 25 kHz according to Al nitrate reference sample. Asterisks indicate the spinning side bands.

The ^{27}Al signal can be assigned to be four- and five- coordinate aluminum, which infer the coordination of THF, Re=O or a siloxane bridge. Taken together, these data are consistent with a more rigid oxo alkylidene species grafted to the surface via a surface siloxy ligand and further interacting with adjacent Al sites, as shown in Scheme 6.6.

Unlike its silica-supported analogue **6.2** and the molecular precursor **6.1**, the surface complex **6.3** shows good catalytic performance in the metathesis of cis-4-nonene. At catalyst loading of 0.05 mol% an initial TOF (measured at 3 min, TOF_{3min}) of 22 min^{-1} was observed and equilibrium conversion was reached in 240 min (Table 6.1). Catalytic activity could be maintained even at catalyst loading as low as 100 ppm, reaching thermodynamic conversion in five days. The catalyst is also active in the metathesis of 1-nonene with a TOF_{3min} of 3 min^{-1} at 0.1 mol% catalyst loading. However, it requires ca. 100h to reach quantitative conversion, indicating the deleterious effect of ethylene on activity. The surface complex **6.3** also catalyzes the metathesis of ethyl oleate at 0.2 mol% catalyst loading, reaching 28% conversion with an initial TOF of 0.3 min^{-1} without the need of a co-catalyst, in contrast to Re_2O_7/Al_2O_3.[10]

Table 6. 1. Catalytic activity of **3** in toluene at 30°C.

Substrates	mol %	TOF_{3min} [a]	Time to equilibrium
Cis-4-nonene	0.1	19	<120 min
Cis-4-nonene	0.05	22	<240 min
Cis-4-nonene	0.01	16	130 h
1-nonene	0.1	3	106 h
Ethyl oleate	0.2	0.3	28% after 6h

[a] TOF at 3 min in min^{-1}

6.5 Conclusion.

This study shows that a well-defined alkylidene oxo Re complex can be active for metathesis when the support contains Lewis acid sites, similarly to what has been observed for the classical Re-based metathesis catalyst. Such species catalyse the metathesis of olefins, including oleate esters without any activator, in contrast to Re_2O_7/Al_2O_3. This data further illustrates that the lack of activity of Re_2O_7/Al_2O_3 towards functionalized olefins is probably due to the poisoning by the ester functionality of the Lewis acid sites, needed to generate the alkylidene intermediates and that the role of the Me_4Sn activator is to generate the precursor of the alkylidene prior to catalysis. With this information in hands, we are now further exploring Re_2O_7/Al_2O_3 in hope to track the active sites and reaction intermediates.

6.6 Experimental Part.

6.6.1 General Procedure

All experiments were carried out under dry and oxygen free argon or nitrogen atmosphere using either standard Schlenk or glove-box techniques. The liquid state NMR spectra were performed on 200, 250, or 300 MHz Bruker spectrometers. Pentane, toluene and dichloromethane (DCM) were purified using a double MBraun SPS alumina column, and were degased by three freeze pump cycles. Tetrahydrofuran (THF) and d_6-benzene were purified by distillation over Na/benzaphenone. All the molecular and grafted complexes were stored at –40 °C in a glove-box freezer. Tri-isobutyl aluminum (Aldrich), ^{13}C-bromoform (Cortecnet) and Re_2O_7 (99.99% , Strem) were used as received, and tert-butoxysilanol (Aldrich) was sublimed prior to use, Diphenylcyclopropene was synthesized according to the literature.[44,45] For ^{13}C-labeled diphenylcyclopropene, 40% ^{13}C-labeled bromoform was used.

Fourier Transformed Infrared spectra were acquired under transmission mode on a Bruker Alpha-T spectrometer inside an Ar glove box. Solid-state NMR spectra were recorded on an Avance III 400, 700, 850 and 1000 MHz Bruker spectrometers equipped with a 4 mm probe for ^{13}C measurement, a 2.5 mm probe for ^{1}H measurement or a 1.3 mm probe for ^{27}Al measurement. Cross polarization magic angle spinning (CPMAS) and spin echo type experiments were used to measure ^{13}C and ^{1}H, respectively. The radio frequency (RF) field of proton was always set to 100 kHz while the ^{1}H decoupling was set to 80 kHz. Full spin echo experiments were used to measure ^{27}Al spectra. A RF field of 25 kHz calibrated on a 1M solution of $Al(NO_3)_3$ in water was used.

6.6.2 Synthesis of Diphenylcyclopropene.

6.6.2.1 Synthesis of 1,1-dibromo-2,2-diphenylcyclopropane.

KOtBu (1.8 equiv., 21 g) was added to a solution of 1,1-*diphenylethylene* (1 equiv., 18.8 g, 18.4 ml) in pentane (200 ml) in a 500 ml three necked round bottomed flask. Bromoform (1.9 equiv., 50 g) was added slowly, while the solution was cooled with an ice bath. After the addition, the solution was allowed to room temperature and stirred for three hours. For purification, the precipitate was filtered, dried and refluxed with 2-propanol for 1 hour. The product was filtered and washed with 2-propanol yielding 28.5 g (79 %) of colourless powder. ^{1}H liquid state NMR (250 MHz), CD_2Cl_2, δ (ppm): 2.50 (s), 7.23 – 7.55 (m).

6.6.2.2 Synthesis of 1-bromo-2,2-diphenylcyclopropane.

1,1-Dibromo-2,2-diphenylcyclopropane (1 equiv., 22.7 g) was put in a 500 ml three necked round bottomed flask and dissolved in ether. After $Ti(O^iPr)_4$ (2 mol%, 0.39 g, 0.41 ml) was added, the solution was cooled to 0 °C. EtMgBr (1.3 equiv., 12 g, 30 ml) was then added dropwise. After the addition, the solution was allowed to room temperature and stirred for 30 minutes. The reaction was quenched with water and a solution of H_2O and H_2SO_4 (5:1). The ethereal layer was separated and the aqueous layer was extracted twice with ether. The ethereal layer was washed with brine and water, and dried over $MgSO_4$. For purification, the obtained mixture was filtered through a short column of silica gel yielding 14.7 g of white powder (78 %). ^{1}H liquid state NMR (250 MHz), CD_2Cl_2,**δ**(ppm): 1.29 (s, impurity : diphenylcyclopropane), 1.85 (dt), 3.71 (dd), 7.15 – 7.44 (m)

6.6.2.3 Synthesis of Diphenylcyclopropene.

1-*Bromo*-2,2-*diphenylcyclopropane* (1 equiv., 5.94 g) was dissolved in DMSO (30 ml) and added dropwise (dropping funnel) to a solution of ^{t}BuOK (1.2 equiv., 2.93 g) in DMSO (200 ml) in a 500 ml three necked round bottomed flask. The reaction turned dark green and was stirred for one day at room temperature. For workup, the solution was poured in ice-cold water. The aqueous layer was extracted three times with hexane. The combined organic layers were washed with water (three times), brine and then dried over $MgSO_4$. The solvent was then evaporated and the resulting oil was purified by column chromatography to yield yellowish oil, which was dried under high vacuum (10^{-5} mBar). ^{1}H liquid state NMR (250 MHz), CDCl3, δ (ppm): 1.36 (s), 7.22 - 7.38 (m), 7.54 (s). 18% impurity (calculated by NMR). Two peaks were observed by GC-MS, one corresponding to the diphenylcyclopropene, the other to diphenylcyclopropane.

6.6.2.4 Synthesis of 19% ^{13}C labelled diphenylcyclopropene.

19% ^{13}C labelled diphenylcyclopropene was synthesized using the same procedure described above with 2.5 g of ^{13}C labelled bromoform mixed with 7.5 g of non-labelled bromoform.

6.6.3 Synthesis of Re and Al Based Molecular Complexes.

6.6.3.1 Synthesis of $Re(O)(OtBuF_6)_3(THF)_2$.

$Re(O)Cl_3(PPh_3)_2$ was recrystallized from a large amount of benzene to obtain a yellow/green compound. A suspension of $ReOCl_3(PPh_3)_2$ (1 equiv., 2.78 g) in DCM (30 ml) in a 50 ml Schlenk was added to a stirred suspension of $KOC(CF_3)_2Me$ (3 equiv., 2.2 g) in DCM (60 ml) in a 250 ml Schlenk at 0°C. The reaction was brought to room temperature and turned from yellow to purple. After stirring the solution for 1 hour, the solvent was removed *in vacuo*. The obtained solid was extracted with 10 ml of pentane (seven times) and filtered with a sintered frit to give a dark violet liquid. After the evaporation of the solvent, the resulting violet microcrystalline powder was recrystallized seven times from pentane: THF (20 : 1) at -40°C. The product was obtained as pure blue crystals. Yield: 26.3 % (0.8 g). ^{1}H liquid state NMR (250 MHz), C_6D_6, **δ** (ppm): 1.21 (t), 1.69 (s), 3.61 (t).

6.6.3.2 Synthesis of Re(O)(=CH–CH=CPh$_2$)(OtBu$_{F6}$)$_3$(THF) (OtBu$_{F6}$ = OCMe(CF$_3$)$_2$) (**1**) and Re(O)(=*CH–*CH=CPh$_2$)(OtBu$_{F6}$)$_3$(THF) (**1***).

A solution of diphenylcyclopropene or 20% ^{13}C labeled Diphenylcylopropene (1 equiv., 38 mg) in dichloromethane was added to a solution of Re(O)(OtBu$_{F6}$)$_3$(THF)$_2$ (1 equiv., 160 mg) in DCM. The reaction turned red immediately and was stirred for 20 hours at room temperature. After evacuation of the solvent under vacuum the resulting powder was recrystallized from pentane at -40 ˚C to give a red-brown microcrystalline powder. The solid and the liquid were separated and dried *in vacuo* yielding the desired compound (yield= 27%). ^{1}H liquid state NMR (250 MHz), CD_2Cl_2, **δ** (ppm): 1.36 (s), 1.45 (s), 4.01 (s), 6.74 – 7.47 (m), 9.36 (d, J_{HH} = 11 Hz), 12.32 (d, J_{HH} = 11 Hz).

6.6.3.3 Synthesis of *Al(OSi(OtBu)$_3$)$_3$*.

To a solution of 8.2 g of tris(*ter*-butoxy)silanol (31.05 mmol, 3 equiv.) in pentane (80 mL) was added dropwise at room temperature 2.6 mL (10.35 mmol, 1 equiv.) of triisobutylaluminum. After 16 h under stirring at room temperature, the reaction mixture was concentrated to 20 mL and stored at -20°C for 1 day. The desired compound was collected by filtration affording 7.3 g (2.02 mmol, yield of 87%) of the title compound as colorless crystals. In solid state the compound decomposes within hours at room temperature but can be stored for extensive periods of time at -40°C without signs of decomposition. Single crystal (Summary of data CCDC 1432995) was obtained by crystallization of the compound in a minimum amount of pentane overnight at -40°C. ^{1}H (200 MHz, δ/ppm, C_6D_6) δ: 1.51 (s, 27 H). ^{13}C (200 MHz, C_6D_6) δ: 32, 73.

6.6.4 Preparation and Characterization of the Support.

6.6.4.1 Generation of silica partially dehydroxylated at 700°C.

Silica (Degussa Aerosil, 200 m^2/g) was compacted with distilled water, calcined at 500 °C under air for 4 h, treated under high vacuum (~10^{-5} mbar) at 500 °C for 12 h, and then at 700 °C for 12 h (support referred to as $SiO_{2\text{-}(700)}$).

6.6.4.2 Preparation of **Al@SiO$_2$**.

To a suspension of $SiO_{2\text{-}(700)}$ (3 g, 0.033 mmol ≡$SiOH_{surf}$) in pentane (2 mL) was added at room temperature a solution of *Al(OSi(OtBu)$_3$)$_3$* (700 mg, 0.86 mmol, 1.1 equiv) in pentane (10 mL), and the reaction mixture was slowly stirred at room

temperature for 3 h. The solid was collected by filtration and washed with five suspension/filtration cycles in benzene (3 x 5 mL). The resulting solid was dried thoroughly in high vacuum (~10^{-5} mbar) at room temperature for 1h and then loaded into a reactor and placed under high vacuum (10^{-5} mbar) and heated to 200 °C (1 °C/min) and kept at 200°C for 4 h, then heated to 400 °C (1 °C/min) and kept at 400°C for 10 h. The reactor was cooled to ambient temperature under vacuum, and $Al_{IV}@SiO_2$ was stored in an Ar filled glovebox. Elemental analysis: Al 0.9 %.

6.6.4.3 Titration of the surface hydroxyl on **Al@SiO$_2$** *surface*.

In a 50 mL Schlenck equipped with a dropping funnel was loaded 200 mg of Al@SiO_2 support. The surface was wetted with 5 mL of freshly distilled diethyl ether while 2 mL of methylmagnesium bromide was loaded in the dropping funnel. The system was put under atmosphere of ether. Dropwise, the Grignard reagent was added to the support while release of methane was observed. After 3 hours of reaction, the gas phase was transferred to a 6.1 L balloon and aliquot of the resulting gas phase were measured by GC. The amount of methane was quantified and thus the concentration of surface hydroxyls could be evaluated (0.54 mmol.g^{-1}).

6.6.4.4 Adsorption of pyridine on **Al@SiO$_2$** *support*.

A 50 mg pullet of **Al@SiO$_2$** support was pressed and inserted in a glass pullet holder. The pullet was loaded on a 300 mL glass reactor equipped with a connection to high vacuum line and CaF_2 IR transparent windows allowing *in-situ* measurement of infrared spectra. After evacuating the system under high vacuum (10^{-5} mBar), an excess of pyridine dried over P_2O_5 was vacuum transferred on the support and left to react for 1 hour. The resulting solid was evacuated at given temperature (25°C, 150°C, 300°C and 450°C) under high vacuum for 3 hours and transmission infrared spectrum were measured.

6.6.5 Grafting of the Re-oxo-alkylidene complexes on the supports.

6.6.5.1 Grafting of Re(O)(=CH–CH=CPh$_2$)(OtBu$_{F6}$)$_3$(THF) (OtBu$_{F6}$ = OCMe(CF$_3$)$_2$) on SiO_2.

To a suspension of SiO_2 (100 mg, 0.026 mmol $SiOH_{surf}$) in pentane (2 mL) was added at room temperature a solution of Re(O)(=CH–CH=CPh$_2$)(OtBu$_{F6}$)$_3$(THF) (27.5 mg, 0.027 mmol, 1.05 equiv. with respect to surface silanol) in pentane (4 mL) was added. The reaction mixture was slowly stirred at room temperature for 3 h. The

solid was collected by filtration and washed with five suspension/filtration cycles in pentane (3 x 5 mL). The resulting solid was dried thoroughly in high vacuum (~10^{-5} mbar) at room temperature for 1h yielding the title compound as dark purple powder. Elemental Analysis: 3.13 wt% Re, 5.57 wt% C, 0.39 wt% H and 2.68 wt% F.

6.6.5.2 Grafting of Re(O)(=CH–CH=CPh_2)($OtBu_{F6}$)$_3$(THF) ($OtBu_{F6}$ = $OCMe(CF_3)_2$) on **Al@SiO_2**.

To a suspension of **Al@SiO_2** (150 mg, 0.081 mmol $SiOH_{surf}$) in pentane (2 mL) was added at room temperature a solution of Re(O)(=CH–CH=CPh_2)($OtBu_{F6}$)$_3$(THF) (39 mg, 0.04 mmol, 1 equiv. with respect to Al) in pentane (4 mL) was added. The reaction mixture was slowly stirred at room temperature for 3 h. The solid was collected by filtration and washed with five suspension/filtration cycles in pentane (3 x 5 mL). The resulting solid was dried thoroughly in high vacuum (~10^{-5} mbar) at room temperature for 1h yielding the title compound as a purple powder. Elemental Analysis: 3.51 wt% Re, 5.80 wt% C, 0.44 wt% H and 3.14 wt% F.

6.6.5.3 Grafting of Re(O)(=*CH–*CH=CPh_2)($OtBu_{F6}$)$_3$(THF) ($OtBu_{F6}$ = $OCMe(CF_3)_2$) on **Al@SiO_2**.

Grafting was conducted as described above using the labelled compound Re(O)(=*CH–*CH=CPh_2)($OtBu_{F6}$)$_3$(THF) ($OtBu_{F6}$ = $OCMe(CF_3)_2$).

6.7 References.

(1) Ivin, K. J.; Mol, J. C. *Olefin Metathesis and Metathesis Polymerization*, 1997.

(2) Lwin, S.; Wachs, I. E. *ACS Catal.* **2014**, *4*, 2505.

(3) Banks, R. L.; Bailey, G. C. *Ind. Eng. Chem. Prod. Rd.* **1964**, *3*, 170.

(4) Evert Verkuijlen, F. K., Johannes C. Mol, Cornelis Boelhouwer *J.C.S. Chem. Comm.* **1977**, 198.

(5) Mol, J. C. *J. Mol. Catal. A* **2004**, *213*, 39.

(6) Popoff, N.; Mazoyer, E.; Pelletier, J.; Gauvin, R. M.; Taoufik, M. *Chem. Soc. Rev.* **2013**, *42*, 9035.

(7) Lawrenson, M. J.; A, U., Ed. M.J. Lawrenson, US Patent US3974233A, 1976.

(8) Mol, J. C. *Catal. Today* **1999**, *51*, 289.

(9) Imamoğlu, Y. *Metathesis Polymerization of Olefins and Polymerization of Alkynes*; Kluwer Academic, 1998.

(10) Valla, M.; Conley, M. P.; Copéret, C. *Catal. Sci. Technol.* **2015**, *5*, 1438.

(11) Lwin, S.; Keturakis, C.; Handzlik, J.; Sautet, P.; Li, Y.; Frenkel, A. I.; Wachs, I. E. *ACS Catal.* **2015**, *5*, 1432.

(12) Herrmann, W. A.; Wagner, W.; Flessner, U.; Volkhardt, U.; Komber, H. *Angew. Chem. Int. Ed.* **1991**, *103*, 1704.

(13) Rost, A. M. J.; Schneider, H.; Zoller, J. P.; Herrmann, W. A.; Kuhn, F. E. *J. Organomet. Chem.* **2005**, *690*, 4712.

(14) McCoy, J. R.; Farona, M. F. *J. Mol. Catal.* **1991**, *66*, 51.

(15) Buffon, R.; Auroux, A.; Lefebvre, F.; Leconte, M.; Choplin, A.; Basset, J. M.; Herrmann, W. A. *J. Mol. Catal.* **1992**, *76*, 287.

(16) Salameh, A.; Joubert, J.; Baudouin, A.; Lukens, W.; Delbecq, F.; Sautet, P.; Basset, J. M.; Copéret, C. *Angew. Chem. Int. Ed.* **2007**, *46*, 3870.

(17) Salameh, A.; Baudouin, A.; Soulivong, D.; Boehm, V.; Roeper, M.; Basset, J.-M.; Copéret, C. *J. Catal.* **2008**, *253*, 180.

(18) Salameh, A.; Baudouin, A.; Basset, J. M.; Copéret, C. *Angew. Chem. Int. Ed.* **2008**, *47*, 2117.

(19) Moses, A. W.; Raab, C.; Nelson, R. C.; Leifeste, H. D.; Ramsahye, N. A.; Chattopadhyay, S.; Eckert, J.; Chmelka, B. F.; Scott, S. L. *J. Am. Chem. Soc.* **2007**, *129*, 8912.

(20) Lai, Y.-Y.; Bornand, M.; Chen, P. *Organometallics* **2012**, *31*, 7558.

(21) Chabanas, M.; Baudouin, A.; Copéret, C.; Basset, J.-M. *J. Am. Chem. Soc.* **2001**, *123*, 2062.

(22) Lesage, A.; Emsley, L.; Chabanas, M.; Copéret, C.; Basset, J.-M. *Angew. Chem. Int. Ed.* **2002**, *41*, 4535.

(23) Chabanas, M.; Copéret, C.; Basset, J.-M. *Chem. –Eur. J.* **2003**, *9*, 971.

(24) Chabanas, M.; Baudouin, A.; Copéret, C.; Basset, J.-M.; Lukens, W.; Lesage, A.; Hediger, S.; Emsley, L. *J. Am. Chem. Soc.* **2003**, *125*, 492.

(25) Peryshkov, D. V.; Schrock, R. R.; Takase, M. K.; Müller, P.; Hoveyda, A. H. *J. Am. Chem. Soc.* **2011**, *133*, 20754.

(26) Peryshkov, D. V.; Forrest, W. P.; Schrock, R. R.; Smith, S. J.; Müller, P. *Organometallics* **2013**, *32*, 5256.

(27) Conley, M. P.; Mougel, V.; Peryshkov, D. V.; Forrest, W. P.; Gajan, D.; Lesage, A.; Emsley, L.; Copéret, C.; Schrock, R. R. *J. Am. Chem. Soc.* **2013**, *135*, 19068.

(28) Conley, M. P.; Delley, M. F.; Siddiqi, G.; Lapadula, G.; Norsic, S.; Monteil, V.; Safonova, O. V.; Copéret, C. *Angew. Chem. Int. Ed.* **2014**, *53*, 1872.

(29) Conley, M. P.; Forrest, W. P.; Mougel, V.; Copéret, C.; Schrock, R. R. *Angew. Chem. Int. Ed.* **2014**, *126*, 14445.

(30) Mougel, V.; Pucino, M.; Copéret, C. *Organometallics* **2015**, *34*, 551.

(31) Schowner, R.; Frey, W.; Buchmeiser, M. R. *J. Am. Chem. Soc.* **2015**, *137*, 6188.

(32) Cai, S.; Hoffman, D. M.; Wierda, D. A. *J. Chem. Soc., Chem. Commun.* **1988**, 1489.

(33) Flatt, B. T.; Grubbs, R. H.; Blanski, R. L.; Calabrese, J. C.; Feldman, J. *Organometallics* **1994**, *13*, 2728.

(34) Copéret, C.; Chabanas, M.; Petroff Saint-Arroman, R.; Basset, J.-M. *Angew. Chem. Int. Ed.* **2003**, *42*, 156.

(35) Tada, M.; Iwasawa, Y. *Coordination Chemistry Reviews* **2007**, *251*, 2702.

(36) Wegener, S. L.; Marks, T. J.; Stair, P. C. *Acc. Chem. Res.* **2012**, *45*, 206.

(37) Lugmair, C. G.; Fujdala, K. L.; Tilley, T. D. *Chem. Mat.* **2002**, *14*, 888.

(38) Delley, M. F.; Núñez-Zarur, F.; Conley, M. P.; Comas-Vives, A.; Siddiqi, G.; Norsic, S.; Monteil, V.; Safonova, O. V.; Copéret, C. *Proc. Nat. Acad. Sci. U.S.A.* **2014**, *111*, 11624.

(39) Héroguel, F.; Siddiqi, G.; Detwiler, M. D.; Zemlyanov, D. Y.; Safonova, O. V.; Copéret, C. *J. Catal.* **2015**, *321*, 81.

(40) Valla, M.; Rossini, A. J.; Caillot, M.; Chizallet, C.; Raybaud, P.; Digne, M.; Chaumonnot, A.; Lesage, A.; Emsley, L.; van Bokhoven, J. A.; Copéret, C. *J. Am. Chem. Soc.* **2015**, *137*, 10710.

(41) Parry, E. P. *J. Catal.* **1963**, *2*, 371.

(42) Wischert, R.; Florian, P.; Copéret, C.; Massiot, D.; Sautet, P. *J. Phys. Chem. C* **2014**, *118*, 15292.

(43) Rhers, B.; Salameh, A.; Baudouin, A.; Quadrelli, E. A.; Taoufik, M.; Copéret, C.; Lefebvre, F.; Basset, J.-M.; Solans-Monfort, X.; Eisenstein, O.; Lukens, W. W.; Lopez, L. P. H.; Sinha, A.; Schrock, R. R. *Organometallics* **2006**, *25*, 3554.

(44) Sandler, S. R. *Org. Synth.* **1977**, *56*, 32.

(45) Rubina, M.; Rubin, M.; Gevorgyan, V. *J. Am. Chem. Soc.* **2002**, *124*, 11566.

Chapter 7: Conclusion and Perspectives

The general aim of this PhD was the development and the understanding at a molecular level of Re-based alkene metathesis catalysts. The understanding of the supports and the characterization of key metathesis surface species on these catalysts were inevitable. It was possible to achieve these goals by using state of the art surface organometallics techniques, which rely on a combined spectroscopic and computational approach, where solid-state NMR spectroscopy occupies a central role.

We further illustrated in **Chapter 2** the high reactivity of highly dehydrated alumina surface, which exposes Al_{III} defect sites. Earlier work reported that such sites coordinate N_2 and activate the σ-bonds of H_2 and CH_4 and that the C-F bond of CH_3F is also activated to yield olefins. Here, we have shown that highly dehydrated alumina also reacts with CH_3OCH_3 to give methane and higher olefin hydrocarbons along with methoxy and formate surface species. These species are formed through a transient oxonium ion intermediate and the promotion of hydrogen transfer between surface species adsorbed on adjacent Al sites. The formation of olefins from DME is proposed to explain the first carbon-carbon formation step in the Methanol-To-Olefin (MTO) process, which uses zeolites as catalysts. In addition, we have shown that this Al_{III} site can coordinate ethylene and activate the C-H bond of ethylene generating Al-vinyl surface species. Worthy of note, no surface alkoxy species are formed in contrast to what is observed in the reaction of propene with alumina. This observation may be important since the related Re_2O_7/Al_2O_3 does not catalyse the metathesis of ethylene in the absence of other olefins, while propene is disproportionated under the same reaction conditions. This finding suggests that the formation of surface alkoxy species may be important to initiate catalytic activity in the Re-based alumina-supported catalysts. Further work on Re_2O_7/Al_2O_3 is clearly needed at this stage.

Towards the goal of understanding this heterogeneous catalyst, we also investigated in **Chapter 3** CH_3ReO_3 supported on Al_2O_3 as a better-defined model of Re_2O_7/Al_2O_3 (Scheme 7.3). We have in particular shown that the μ-methylene species in CH_3ReO_3 supported on Al_2O_3 display a distribution of surface site structures and reactivity. *In situ* solid-state NMR spectroscopy allowed the observation for the first time of the metallacyclobutane reaction intermediates, present in TBP and SP geometries as observed for the corresponding well-defined molecular or silica-supported d^0 group 6 alkylidene complexes. DFT calculations show the critical role of

Al_{III} sites in generating highly active species. In particular, it was shown that the μ-methylene species, with one oxo ligand bound to Al_{III} and the methylene to Al_{IVb}, easily generate TBP and not SP metallacycles, yielding a rather shallow potential energy surfaces, hence the high activity of that sites (Scheme 7.1). Worthy of note the reverse configuration (oxo ligand bound to Al_{IVb} and methylene to Al_{III}) cannot easily generate the alkylidene or metallacyclobutane intermediates, making that site inactive. On the other hand, having the oxo and methylene ligands bound to adjacent Al_{IVa} sites also generate active sites, but they are found to be less active because of the easier formation of a very stable SP metallacycles.

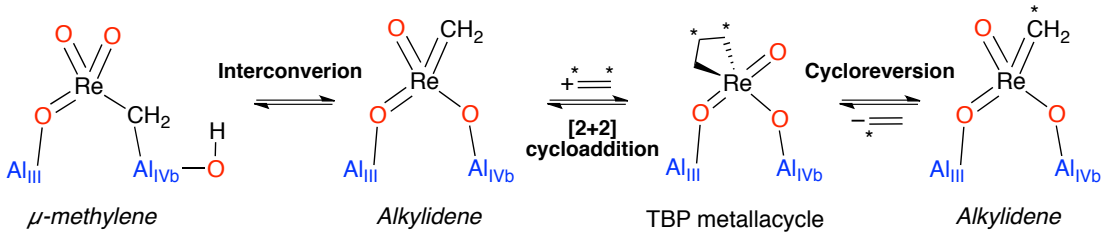

Scheme 7.1. Active metathesis route for CH_3ReO_3.

Finally, the last configuration with oxo and methylene ligands bound to Al_{IVa} and Al_{IVb} sites generate inactive active sites with an octahedral Re sites. This study illustrates the specificity of each Al site in alumina and the importance of Al_{III} sites, formed only upon thermal treatment of the alumina surface at high temperature. DFT calculations on NMR parameters suggest that the higher reactivity of sites having one oxo ligand bound to Al_{III} and the methylene to Al_{IVb} is that it has a strong alkylidene character. This finding may also explain why Re_2O_7/Al_2O_3 activated at 700 °C, temperature corresponding to the highest density of Al_{III} sites on alumina, is the most active catalysts. Furthermore, a parallel can be drawn with the recently proposed surface sites of Re_2O_7/Al_2O_3 (**Chap.** 1, section 1.3.4), where the proposed active species (ReOx-II) is a ReO_4- tetrahedral sites bound to Al_{III} and Al_{IV}, while the inactive species (ReOx-I) correspond to a distorted 6-coordinate ReO_4- having two additional surface oxygen coordinating the Re centre. This finding is very similar compare to what we found with CH_3ReO_3/Al_2O_3 where the most active species are tetrahedral connected to Al_{III} and Al_{IVb} and the inactive species are 6-coordinate and bound to Al_{IVb} and Al_{IVa} sites. Although further work is needed to understand the active sites of Re_2O_7/Al_2O_3 in particular the structures of the metathesis intermediates, the gap is closing.

In view of the similarities of reactivity between CH_3ReO_3/Al_2O_3 and Me_4Sn activated Re_2O_7/Al_2O_3, we also investigated their respective NMR signatures in **Chapter 4**. By using selective carbon-13 labelling approach and solid-state NMR spectroscopy, we could show that the activation of Re_2O_7/Al_2O_3 by Me_4Sn generates surface sites in close resemblance with CH_3ReO_3/Al_2O_3. Since it is known that the reaction of Re_2O_7 and Me_4Sn generates CH_3ReO_3, we propose that the Sn co-catalyst is need to generate *in-situ* CH_3ReO_3 which further reacts with Al_2O_3 sites to form the μ-methylene or the oxo species (Al-O=Re(=O)$_2$(CH_3). One step further toward the understanding of Re_2O_7/Al_2O_3 (Scheme 7.3).

Several reports have shown that silica-aluminas (also called aluminosilicates) are also very good supports for Re-based metathesis catalysts. We have thus investigated in greater details the structure of the support in **Chapter 5**, focusing on the structure of the interface between silica and alumina. This was made possibly by using dynamic nuclear polarization surface enhanced NMR spectroscopy (DNP SENS). In particular, 2D ^{27}Al-^{29}Si INEPT experiments showed that the interface of all aluminosilicate materials prepared by deposition of Si or Al molecular on the complementary support are composed of interconnected tetrahedra of Si and Al via Si-O-Al bonds. Based on this data and DFT calculations, we propose a structure for the Bronsted acidic pseudo bridging silanol as a silanol interacting with an aluminum tetrahedron (Scheme 7.2).

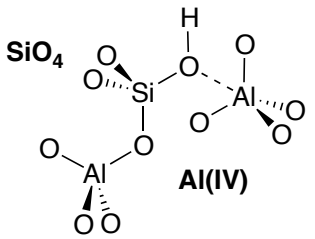

Scheme 7.2. Proposal for a possible structure of Brønsted acid sites on ASA (Si/Al_2O_3):

In **Chapter 6**, we went on trying to generate active oxo alkylidene Re-based catalysts, and showed that such well-defined supported species on silica are inactive. This led us to develop better-defined silica-alumina supports from tailor-made aluminosilicate prepared through the thermolytic precursor approach. We have shown that the corresponding supported oxo alkylidene Re complexes display very good activity, in a broad range of substrate (internal, terminal and functionalized olefins). This work has shown that Re oxo alkylidene are indeed active in metathesis (Scheme 7.3). However, at this stage, it is not clear what is the role of the surface Al sites: do

they activate the Re oxo alkylidene or are they only needed to scavenge THF, which is always present on the inactive molecular complex and silica-supported catalysts. If the Al is essential to activate the Re oxo alkylidene surface species, one can propose to tune the activity of the supported catalyst by tailoring the acidity of the support, by replacing Al, by B, Ga or Sn.

Furthermore, all this PhD dealt with supported rhenium complex with the highest oxidation state (Re^{VII}). However, most of the initiation mechanisms for the generation of the active species of Re_2O_7/Al_2O_3 involve metal centre in lower oxidation states, including for the pseudo-Wittig mechanism, which may involve a Re(V) glycolate species as proposed by Chen *et al*.. Thus the chemistry of supported Re(V) complexes should be studied in greater details. Preliminary results (Appendix A.7.1) show that $Re(V)(=O)(OtBuF_6)_3(THF)_2$ grafted on the tailor-made aluminosilicate discussed above is inactive in the self-metathesis of propylene. However, it becomes highly active upon reaction with diphenyl cyclopropene. Full characterization of the corresponding surface species show that a Re(VII) oxo alkylidene was formed. Further work on well-defined Re(V) complexes is needed; it includes the study of their reactivity towards various olefins in a broader temperature range. This could prove to be helpful to understand the formation of active species in Re-based metathesis catalysts, including Re_2O_7/Al_2O_3.

A final historical note. Understanding Re_2O_7/Al_2O_3 has been a goal since its discovery in 1967. It took 26 years to generate the first well-defined molecular catalysts based on Re(VII) alkylidene, and the corresponding supported version only appeared in 2001(Scheme 7.3). In the mean time, $MeReO_3$ was found to be active in metathesis when activated with molecular or solid Lewis acids. In this work, we have also developed well-defined Re(VII) oxo alkylidene, which are active on Lewis acid containing supports. In addition, detailed surface studies showed that the active sites of $MeReO_3/Al_2O_3$ corresponded to an adsorbed μ-methylene; this work has also shown the role of Al_{III} and Al_{IVb} sites, a finding that parallels what has been recently found for Re_2O_7/Al_2O_3. All the data clearly show the essential role of $Al_{III.}$ in this catalyst. However several questions remain for Re_2O_7/Al_2O_3, as it is still not clear how the metathesis intermediates are formed and how one can further tune this catalyst through a more rational approach.

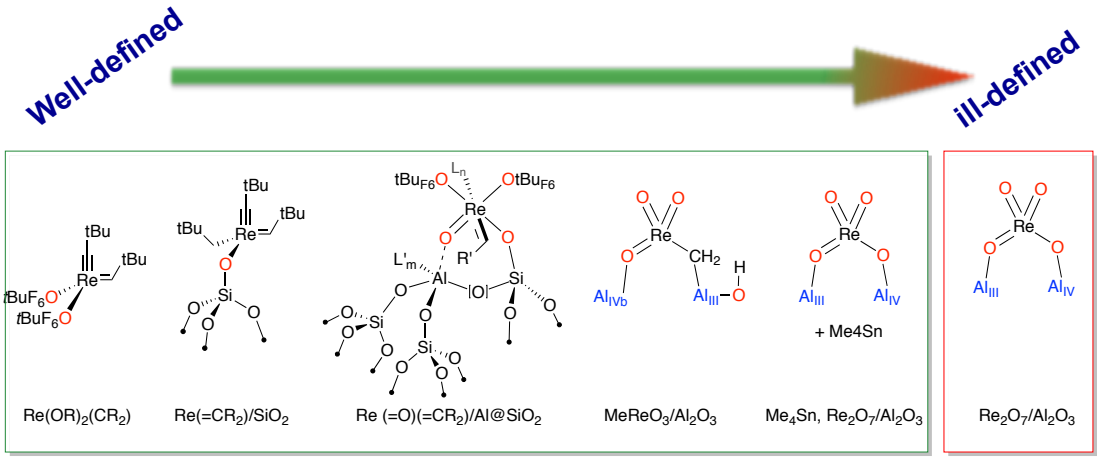

Scheme 7.3 General route from well defined homogeneous catalysts toward the understanding of the ill-defined Re_2O_7/Al_2O_3.

Appendices.

A.1. Appendix to Chapter 2.

Table A.2. 1 Desorbed compounds (molecules/nm^2) from Al_2O_3 (Sba 200, partially dehydroxylated at 700°C) after reaction with dimethyl ether at 300°C.

Hydrocarbon removed from the surface	Molecules per nm^2
Ethylene	$0.5x10^{-2}$
Propylene	$0.5x10^{-2}$
2-butene	$3.1x10^{-2}$
Pentene	$2.1x10^{-2}$
C6	Traces
C7	Traces

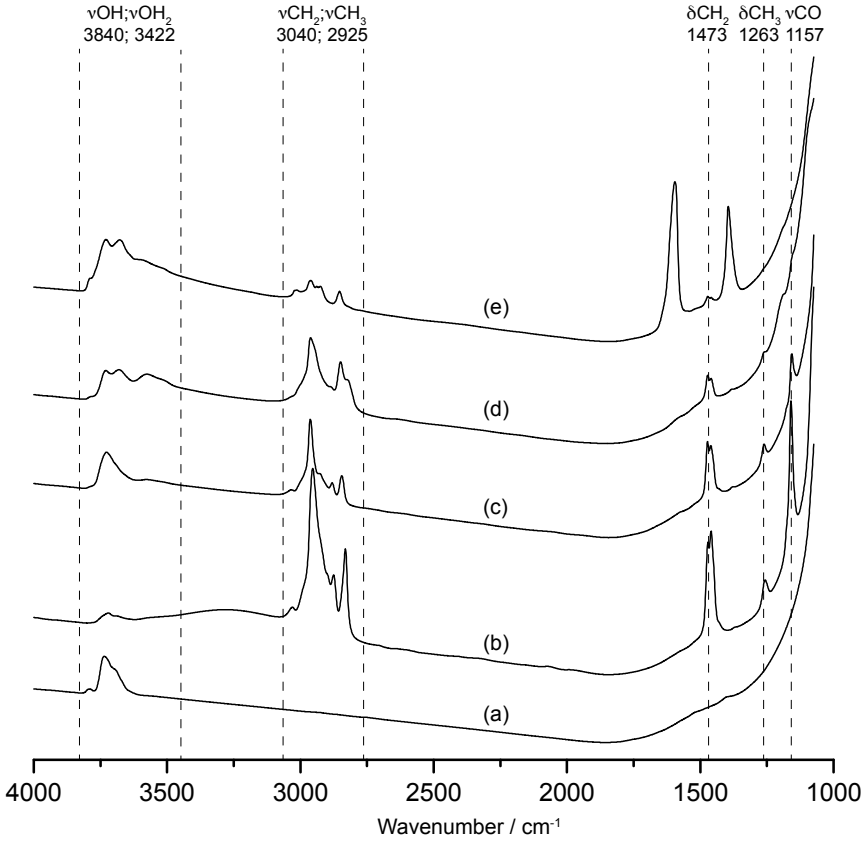

Figure A.2. 1 FT-IR Transmission spectra of Alu C Al_2O_3 (a) partially dehydroxylated at 700°C, (b) contacted with 40 mBar of dimethyl ether at room temperature, (c) after evacuation under high vacuum for 14 h, (d) after reaction with dimethyl ether at 200°C (e) after reaction with dimethyl ether at 300°C. All the spectra were recorded with the gas phase condensed at -190°C. The number of scans was 16.

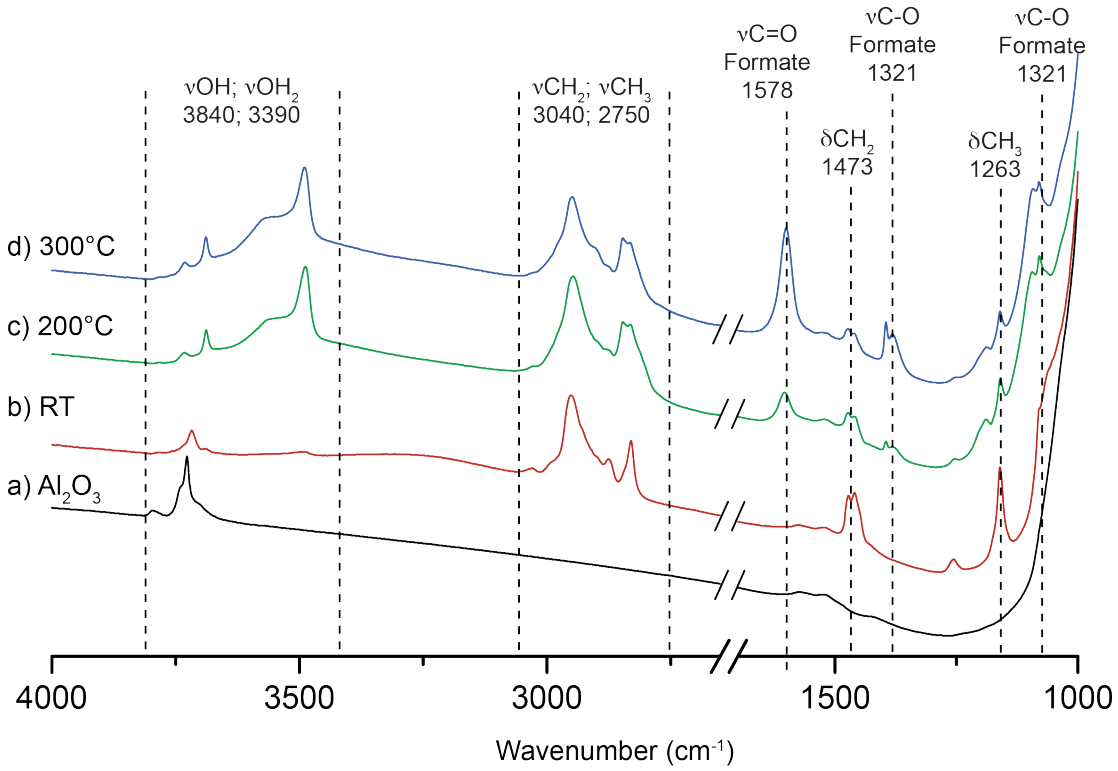

Figure A.2. 2. FT-IR transmission spectra of (a) g-alumina (Sba 200) Al_2O_3 partially dehydroxylated at 700°C, (b) after contacting with 40 mBar of dimethyl ether at room temperature, (c) after evacuation of the gas phase under high vacuum for 14 h (c), after reaction with dimethyl ether at 200°C (d) and after reaction with dimethyl ether at 300°C (e). All the spectra were recorded with the gas phase condensed at –190°C. The number of scans was 16.

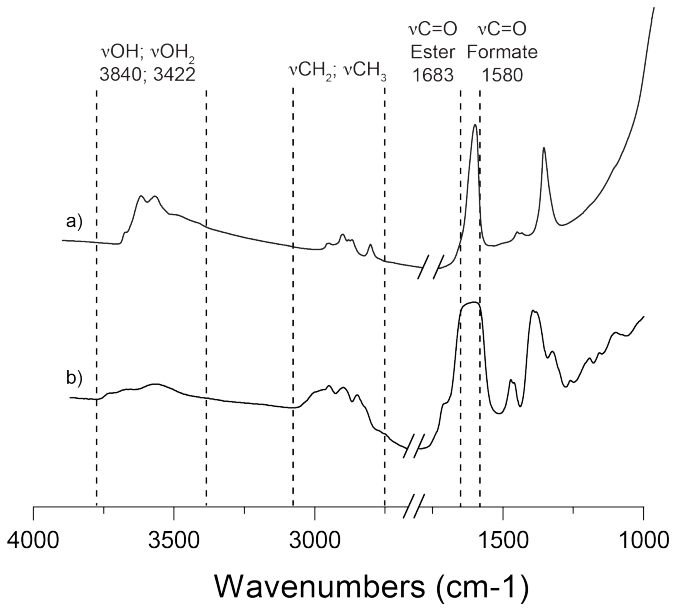

Figure A.2. 3. FT-IR transmission spectrum of a) DME contacted with Al_2O_3 at 300°C and b) methyl formate contacted with AluC (Evonik/Degussa)Al_2O_3 (700°C).

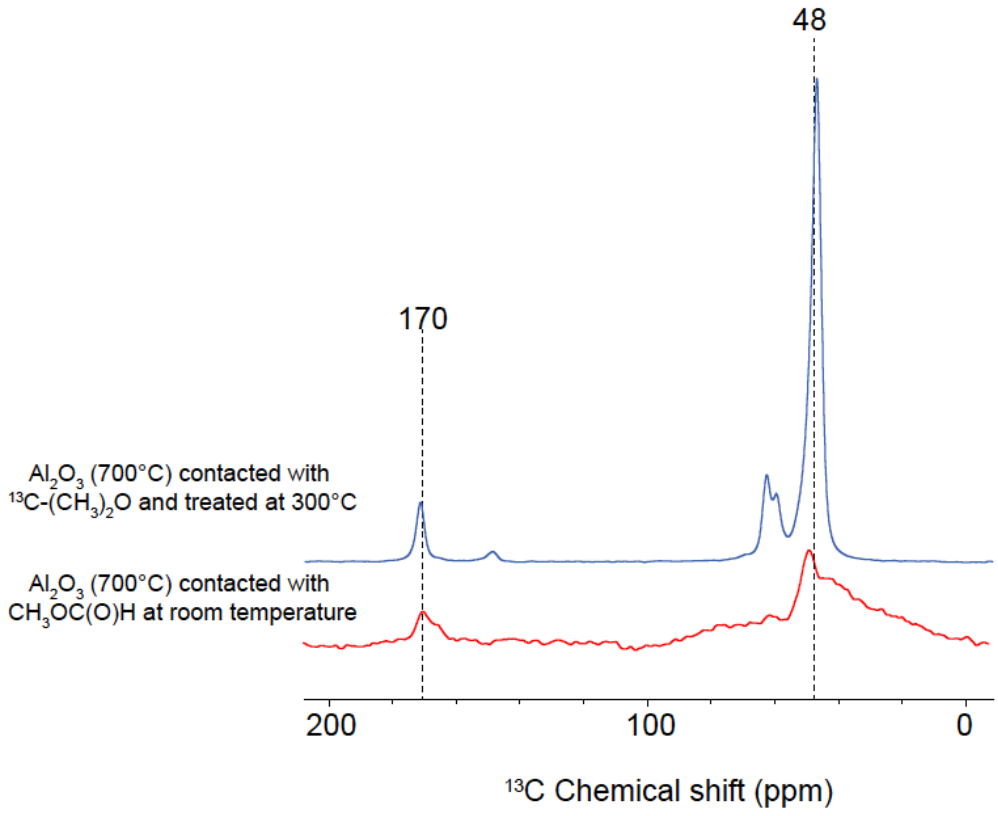

Figure A.2. 4 ^{1}H-^{13}C CPMAS, 400 MHz, 10 kHz, of AluC reacted with 2-^{13}C-$(CH_3)_2O$ at 300°C (blue, top spectrum) and AluC reacted with methyl formate at room temperature (red, bottom spectrum).

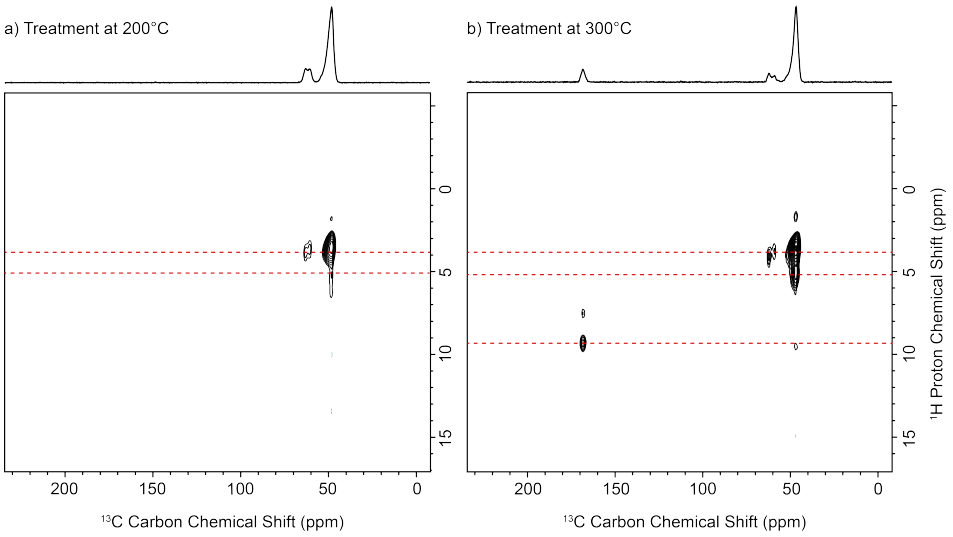

Figure A.2. 5. ^{1}H-^{13}C HETCOR, 400 MHz, 10 kHz, of AluC reacted with 2-^{13}C-$(CH_3)_2O$ at (a) 200°C and at (b) 300°C.

Figures A.2.5a and A.2.5b show similar features: the peaks at 62 and 64 ppm correlate with proton at 3.8 ppm, while the peak at 48 ppm correlates with protons at both 3.8 and 5.3 ppm. The signal at 3.8 ppm could be assigned to be proton attached to a methoxy group where the peak at 5.2 ppm could come from the OH from the alumina surface. Note that on the product treated at 300°C the 5.3 ppm proton have a stronger signal compare to the product treated at 200°C. The signal at 169 ppm correlates with a proton peak at 9.2 ppm, consistent with methyl formate species.

Description of the Model of γ-Al_2O_3 and Computational Details

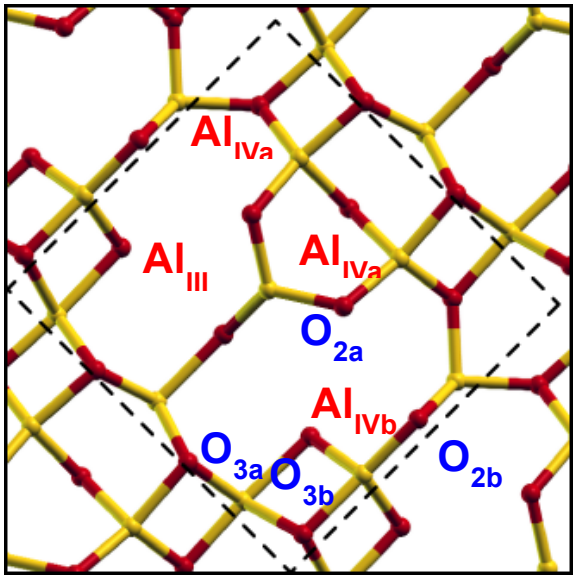

Figure A.2. 6. Model for the 110 termination of the γ-Al_2O_3 fully dehydroxylated (**s0** surface). A dashed line indicates the unit cell. Al: yellow, O: red balls.

For the description of Al_2O_3 we use a model with nonspinel sites occupied, based on the simulated dehydration of boehmite.[1] The g-Al_2O_3 model has three type of Al centers: one tri-coordinated (Al_{III}) and two tetra-coordinated (Al_{IVa} and Al_{IVb}), whose Lewis acidity follows in decreasing order $Al_{(III)} > Al_{IVb} > Al_{IVa}$.

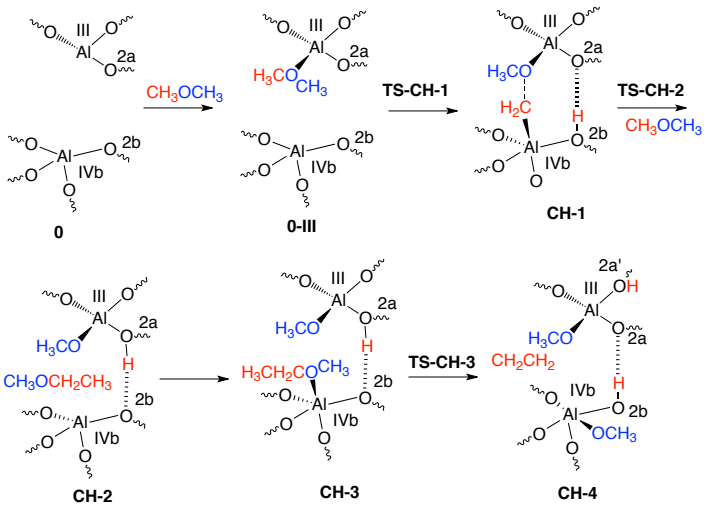

Scheme A.2. 1 Calculated reaction pathway for the reaction of CH_3OCH_3 on g-Al2O3 leading to the formation of $CH_3CH_2OCH_3$ as an intermediate and ethylene as a final product.

In view of the reactivity of methane and H_2 with Al_{III} sites, we examined the C-H bond activation of CH_3OCH_3 starting from **0-III** species This yields **CH-1** which is 105 kJ.mol^{-1} more stable than the separated reactants. During that process, the resulting CH_2 group coordinates to Al_{IVb} and the proton is transferred to the O_{2b} center in close vicinity with the O_{2a} atom, while OCH_3 stays coordinated to Al_{III}. This process is associated with an energy barrier of 144 kJ.mol^{-1} with respect to **0-III** species, a transition-state energy (or in other words an apparent energy barrier) of 12 kJ.mol^{-1} above separated reactants as depicted in Figure A.2.7.

From **CH-1**, the C-H bond activation of second CH_3OCH_3 molecule on "Al–CH_2–OCH_3", a carbenoid species, which can in principle insert in the C-H bond and lead to the formation of a C-C bond. This step is strongly exoenergetic by 177 kJ.mol^{-1} with respect to **CH-1**, and it is associated with an energy barrier of 179 kJ.mol^{-1} (**TS-CH-2**). This step yields $CH_3CH_2OCH_3$, which can further coordinate the adjacent Al_{IVb}, the most acidic Al center after Al_{III}. This step is exoenergetic by 73 kJ.mol^{-1} and corresponds to a reaction energy of –356 kJ.mol^{-1} with respects to the initial reactants (**CH-3** in Scheme A.2.1). $CH_3CH_2OCH_3$ can further react with the alumina surface to yield ethylene with the transfer of OCH_3 to Al_{IVb} and a proton to an adjacent oxygen atom. This step has an energy barrier equal to 132 kJ.mol^{-1}. Overall, the rate-limiting step for the whole pathway for the ethylene formation via the formation of the $CH_3CH_2OCH_3$ intermediate is the C-H insertion, with an energy barrier of 179 kJ.mol^{-}

[1]. Note that the resulting $CH_3CH_2OCH_3$ species could also react in an analogous way to dimethylether in order to form species with longer carbon-carbon bond chains. In Figure A.2.7, it is shown the complete energy profile for this pathway. The apparent activation energy is equal to 73 kJ.mol^{-1}, whereas from the structure in which DME binds the AlIII center (**0-III**) to the highest point in the energy profile (**TS-CH-2**) the energetic difference equals 204 kJ.mol^{-1}.

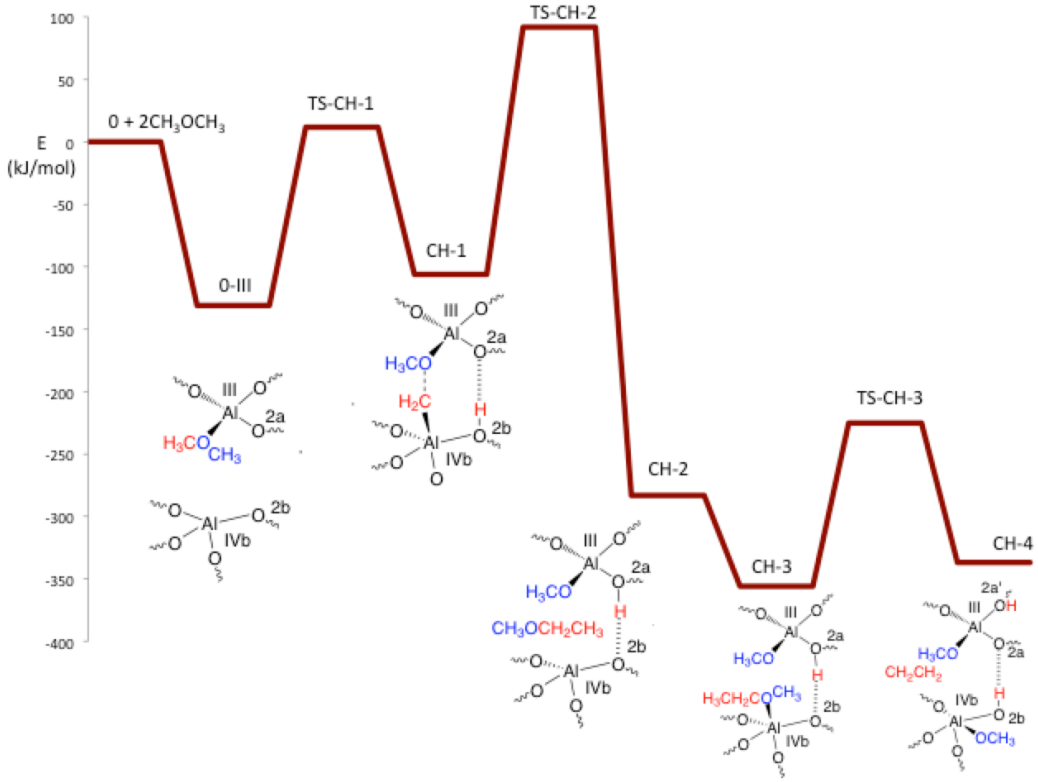

Figure A.2. 7. Energy profile (in kJ.mol^{-1}) for the formation of ethylene with the initial C-H activation of dimethylether.

The **s1b** and **s1b2** surface contain water on the Al_{IVb} center. In the former case (**s1b**) water is adsorbed in a dissociative way and the surface reconstructs as described previously.[6] The **s1b2** surface corresponds to a surface in which water coordinates to Al_{IVb} without initially reconstructing. The energy profiles for the ethylene formation from the **s1a**, **s1b** and **s1b2** surfaces are shown in **Figure S8**. For the **s1b** and **s1b2** surfaces the reaction steps are the same than the ones described on the main text for the **s1a** surface with the difference than in this case the dimethylether molecule initially coordinates to the Al_{III} center since for both surfaces this Al center is free. The **s1b2** surface reconstructs after the initial C-O activation step leading to the same structure than the product of the C-O activation on the **s1b** surface.

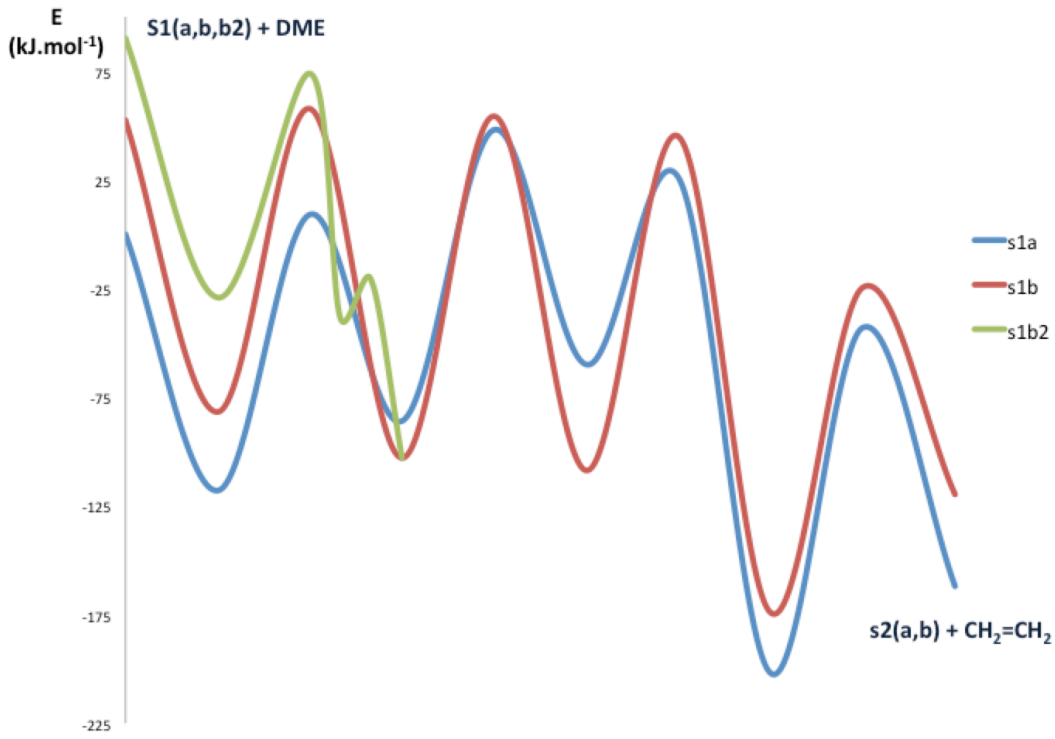

Figure A.2. 8. Comparison between the energy profiles corresponding to the ethylene formation for the **s1a**, **s1b** and **s1b2** surfaces. The energies (in $kJ.mol^{-1}$) are referred to the **s1a** surface and one dimethylether molecule.

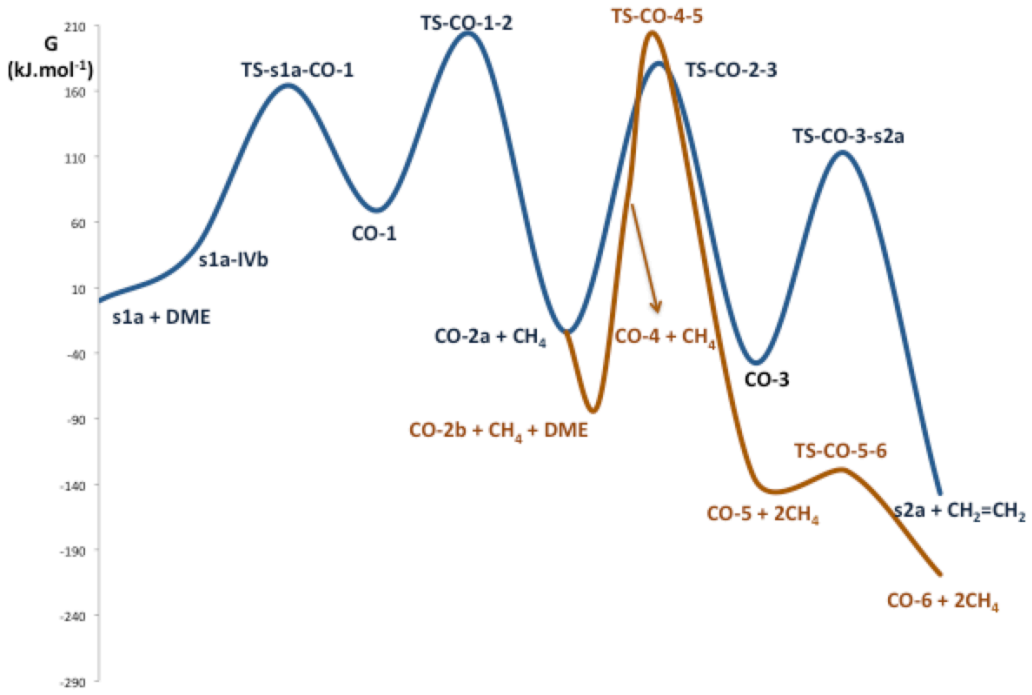

Figure A.2. 9. Gibbs free energy profiles (in kJ.mol^{-1}) on the **s1a** surface for the pathways of ethylene (in dark blue) and formate (in brown) formation, respectively.

A.2. Appendix to Chapter 3.

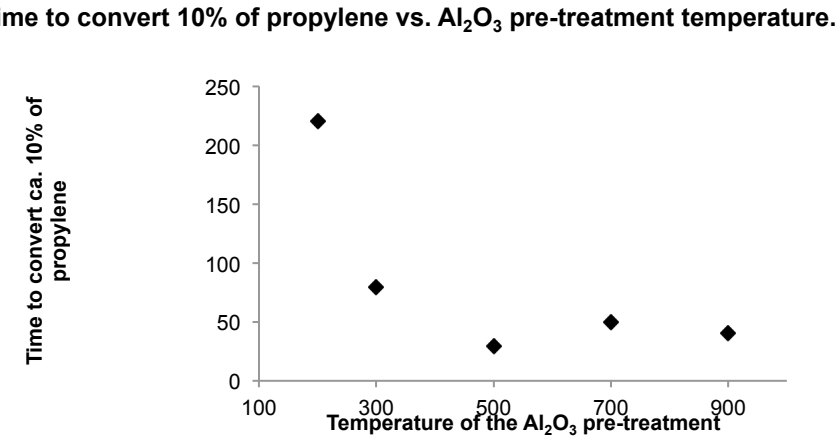

Figure A.3. 1. Time to convert 10% propylene (self-metathesis) with CH_3ReO_3/Al_2O_3 as a function of alumina temperature of pre-treatment. The reaction was conducted in a 300 mL batch reactor with 450 equiv of propylene with respect to the total amount of Re in the catalysts.

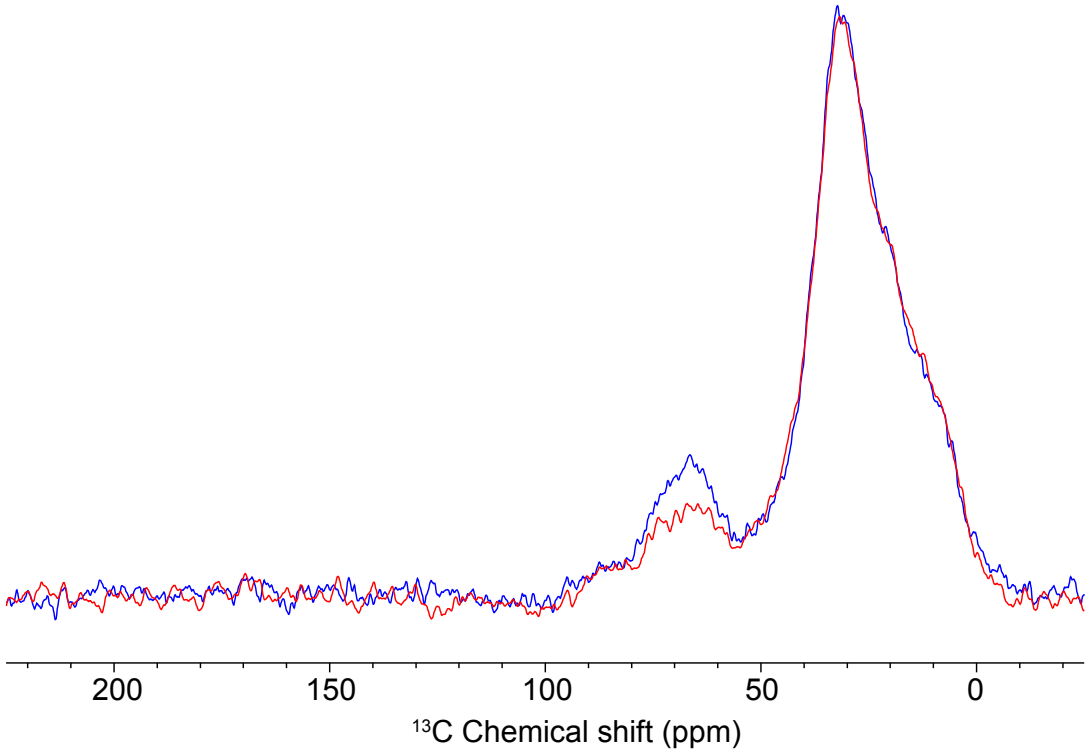

Figure A.3. 2. ^{1}H-^{13}C CPMAS NMR, 700MHz, $*CH_3ReO_3/Al_2O_{3\text{-}(500°C)}$, 5k scans, 10kHz, (blue) and $*CH_3ReO_3/Al_2O_{3\text{-}(500°C)}$ contacted with non-labeled propene (red). The recycling delay was set to 1 sec and the contact time was 600 μsec.

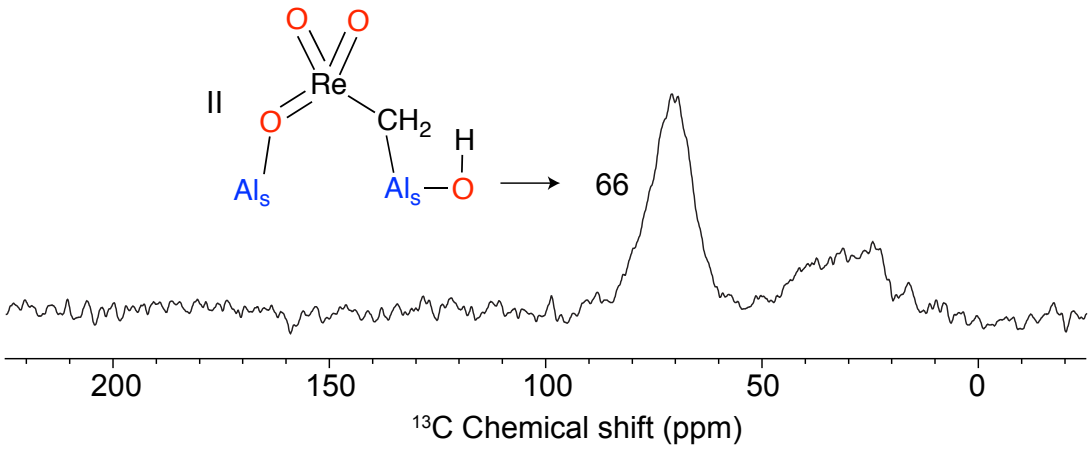

Figure A.3. 3. ^{1}H-^{13}C CPMAS NMR, 700 MHz, $CH_3ReO_3/Al_2O_{3\text{-}(500°C)}$ contacted with ^{13}C di-labeled ethylene, 10 kHz, 70k scans. The recycling delay was set to 1 sec and the contact time was 600 μsec.

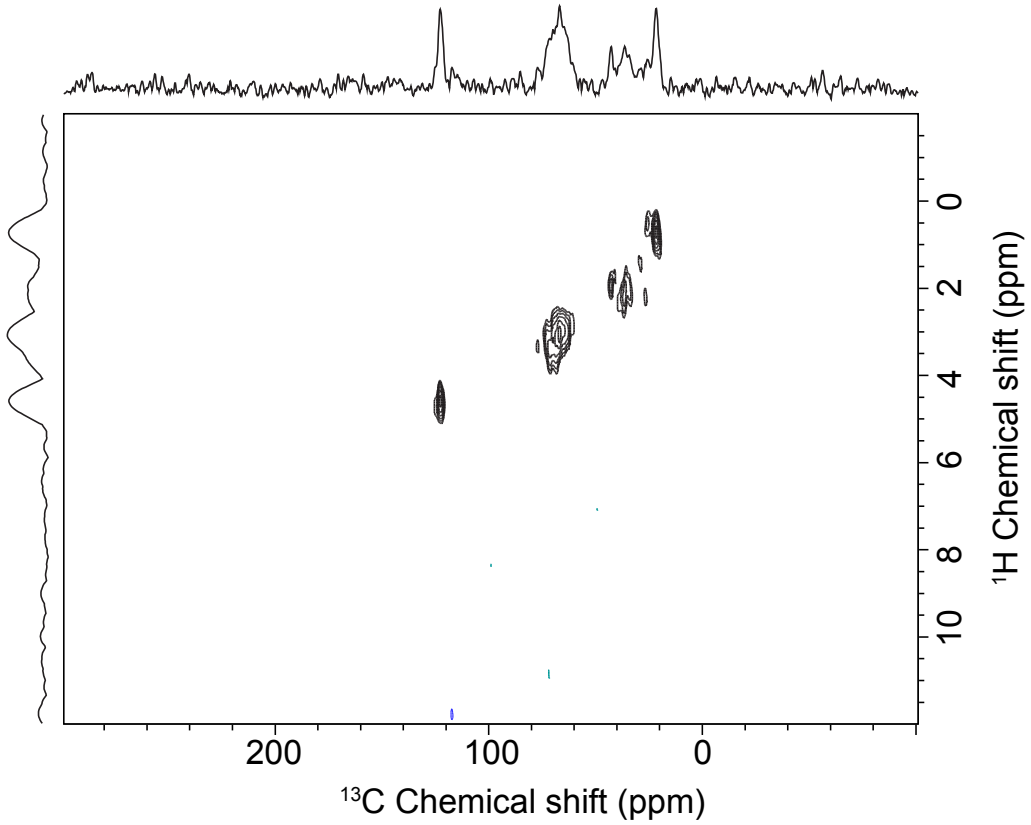

Figure A.3. 4. ^{1}H-^{13}C HETCOR NMR spectrum with DUMBO decoupling at a spinning speed of 9 kHz of a sealed glass insert of 2.5 mBar of ^{13}C di-labeled ethene and 20 mg of non-labeled catalyst ($CH_3ReO_{3\text{-}(500°C)}/Al_2O_3$). The contact time was set at 250 μsec and the recycling delay was set to 1 sec.

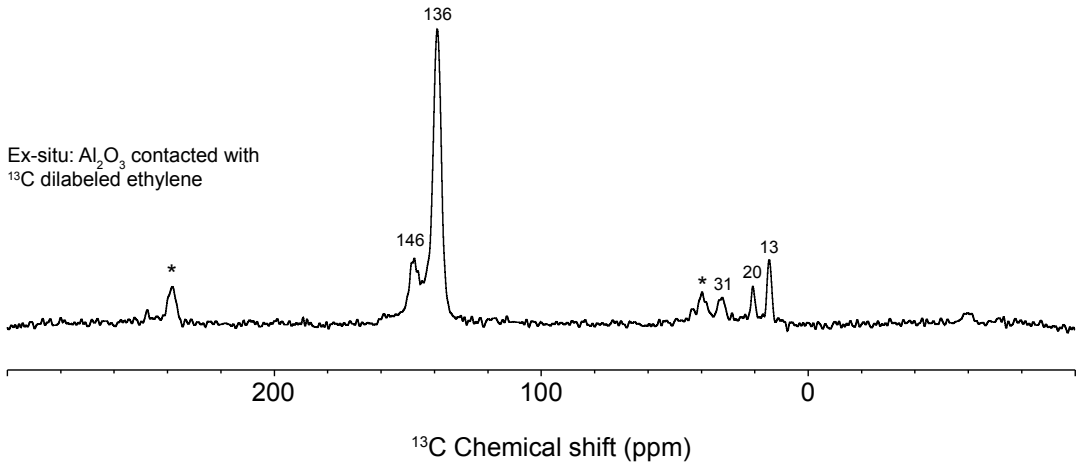

Figure A.3. 5. ^{1}H-^{13}C CPMAS, 400 MHz, 10 kHz, 60k scans, the recycling delay was set to 1 sec and the contact time to 1.5 ms. 100 mg Al_2O_3 dehydroxylated at 700°C contacted with 50 mBar of 13C dilabeled ethylene for 1h following by high vacuum treatment at room temperature for 1 h.

Table A.3. 1 Bond lengths (in Å) of the μ-methylene species (**1-A,B**) attached to different alumina sites as a function of surface hydration (**s0**, **s1** and **s2**).

Structure	d (**Re-C**)	d (**Re=O**)	d (**Re–O**–Al)
1–IVb,III s0	1.99	1.72	1.82
1–IVb,III s1	2.00	1.72	1.83
1–IVb,III s2	2.07	1.72	1.90
1–III,IVb s0	2.00	1.72	1.79
1–III,IVb s1	2.02	1.72	1.79
1–III,IVb s2	2.11	1.72	1.84
1–IVb,IVa s0	2.13	1.72	1.90
1–IVb,IVa s1	2.08	1.71	1.86
1–IVb,IVa s2	2.06	1.73	1.87
1–IVa,IVa s0	2.00	1.72	1.78
1–IVa,IV s1	2.02	1.72	1.78
1–IVa,IV s0	2.14	1.72	1.88
1–IVa,IV s1	2.10	1.72	1.87
1–IVa,IV s2	2.06	1.72	1.87

Table A.3.2. Bond lengths (in Å) of the alkylidene species (**2-A,B**) attached to different alumina sites as a function of surface hydration.

Structure	d (**Re–C**)	d (**Re–O**)	d (**Re–O**–Al)
2– III,IVb s0	1.88	1.71	1.83
2– III,IVb s1	1.88	1.71	1.84/1.82
2– III,IVb s2	1.88	1.72	1.84/1.91
2– IVa,IVa s0	1.88	1.71	1.80
2– IVa,IVa s1	1.88	1.71	1.81/1.83
2– IVb,IVa s0	1.87	1.70	1.92/1.94
2– IVb,IVa s1	1.89	1.70	1.91/1.88
2– IVb,IVa s2	1.90	1.70	1.90

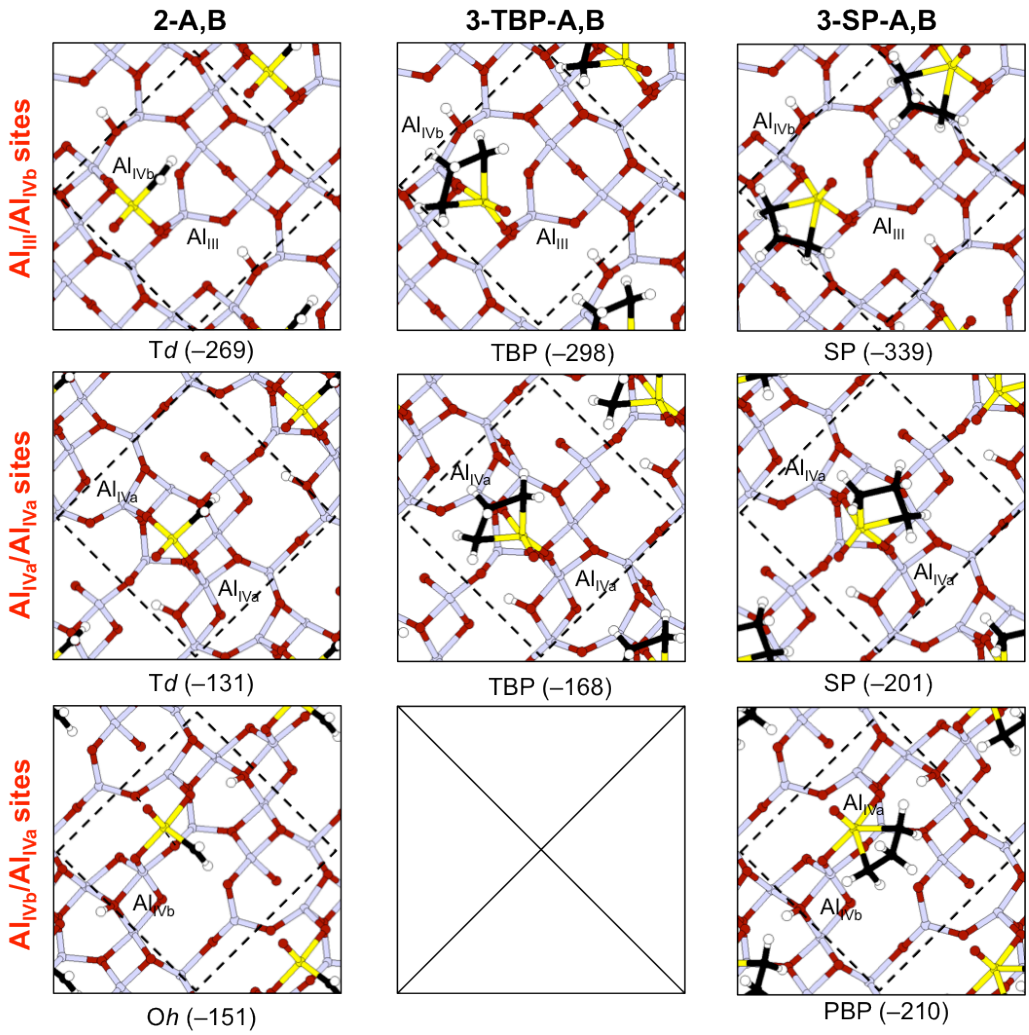

Figure A.3. 6. Structure and stability of the main metathesis intermediate (**2-A,B**, **3-TBP-A,B** and **3-SP-A,B**) on fully dehydroxylated (110) γ-Al_2O_3, type of intermediates according to the Alumina sites. The bottom two layers of the slab have been omitted for clarity. The surface unit cell is indicated by a dashed line. Al (yellow), O (red), Re (grey), C (black), H (white) balls. O-Re and Re-C (italic numbers) distances are indicated (in Å). Adsorption energies (ΔEcoads) are given in parentheses in kJ mol^{-1}.

The following tables (Table A.3.3, 4, 5, 6 and 7) report angles. These angles were calculated as follows:

Trigonal bipyramidal (TBP):

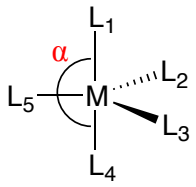

$\alpha = (L_4\text{-M-}L_1)$

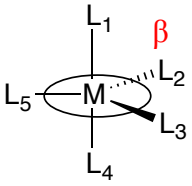

$\beta = \Sigma[(L3\text{-M-}L2) + (L2\text{-M-}L5) + (L5\text{-M-}L3)]$

α = 180° for ideal TBP
β = 360° for ideal TBP

Square based pyramidal (SP):

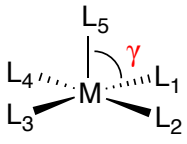

$\gamma = (L_5\text{-M-}L_1) = (L_5\text{-M-}L_2) = (L_5\text{-M-}L_3) = (L_5\text{-M-}L_4)$

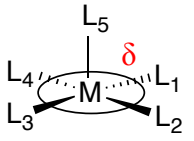

$\delta = \Sigma[(L1\text{-M-}L2) + (L2\text{-M-}L3) + (L3\text{-M-}L4) + (L4\text{-M-}L1)]$

γ= 90° for ideal SBP
δ= 360° for ideal SBP

Octahedral, O*h*:

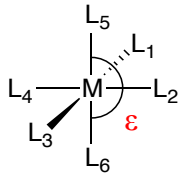

$\varepsilon = (L5\text{-M-}L6)$

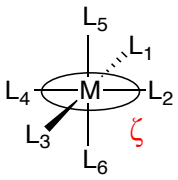

$\zeta = \Sigma[(L1\text{-M-}L2) + (L2\text{-M-}L3) + (L3\text{-M-}L4) + (L4\text{-M-}L1)]$

ε = 180° for ideal O_h
ζ = 360° for pure O_h

Pentagonal BiPyramidal, PBP:

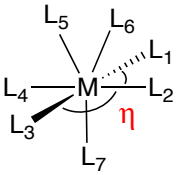

$\eta = (L3\text{-M-}L2) = (L2\text{-M-}L1)$

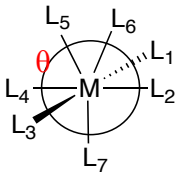

$\theta = \Sigma[(L6\text{-M-}L2) + (L2\text{-M-}L7) + (L7\text{-M-}L4) + (L4\text{-M-}L5) + (L5\text{-M-}L6)]$

η = 90° for ideal PBP
θ = 360° for ideal PBP

NB1: Crucial angles for the determination of 5-, 6-, and 7-coordinate complexes geometries.

Table A.3.3. Important bond lengths (in Å) and angles (in °) of the alkylidene and metathesis intermediates on Al_{III}/Al_{IVb} alumina sites on dehydrated surface (**2-III,IVb**, **3-TBP-IIIb,IVb** and **3-SP-III,IVb**).

s0	**2-III,IVb**	**3-TBP-III,IVb**	**3-SP-III,IVb**
Re=C_{ene}	1.88	-	-
Re-O	1.71	1.75	1.71
Re-OAl_{III}	1.83	1.83	1.84
Re-OAl_{IVb}	1.83	1.85	1.79
Re-Cα	-	2.06	2.20
Re-Cβ	-	2.38	2.80
α (°)[a]	-	165	-
β (°)[a]	-	360	-
γ (°)[a]	-	-	106
δ (°)[a]	-	-	335

[a]: Please refer to *NB1*, for the determination of the angles

Table A.3.4.. Important bond lengths (in Å) and angles (in °) of the alkylidene and metathesis intermediates on Al_{IVa}/Al_{IVa} alumina sites on dehydrated surface (**2-IVa,IVa**, **3-TBP-IVa,IVa** and **3-SP-IVa,IVa**).

s0	**2-IVa,IVa**	**3-TBP-IVa,IVa**	**3-SP-IVa,IVa**
$Re{=}C_{ene}$	1.88	-	-
Re-O	1.71	1.75	1.72
$Re\text{-}OAl_{IVa}$	1.80	1.85	1.79
$ReOAl_{IVa'}$	1.80	1.80	1.82
Re-Cα	-	2.08	2.21
Re-Cβ	-	2.38	2.81
α (°)[a]	-	163	-
β (°)[a]	-	360	-
γ (°)[a]	-	-	104
δ (°)[a]	-	-	339

[a]: Please refer to *NB1*, for the determination of the angles

Table A.3.5. Important bond lengths (in Å) and angles (in °) of the alkylidene and metathesis intermediates on Al_{IVb}/Al_{IVa} alumina sites on dehydrated surface (**2-IVb,IVa** and **3-SP-IVb,IVa**).

s0	**2-IVb,IVa**	**3-SP-IVb,IVa**
$Re{=}C_{ene}$	1.87	-
Re-O	1.70	1.70
$Re\text{-}OAl_{IVb}$	1.92	1.95
$Re\text{-}OAl_{IVa}$	1.94	1.94
$Re\text{-}O_{s1}$	2.20	2.18
$Re\text{-}O_{s2}$	2.45	2.51
Re-Cα	-	2.18
Re-Cβ	-	2.84
ε (°)[a]	163	-
ζ (°)[a]	355	-
η (°)[a]	-	97
θ (°)[a]	-	353

[a]: Please refer to *NB1*, for the determination of the angles

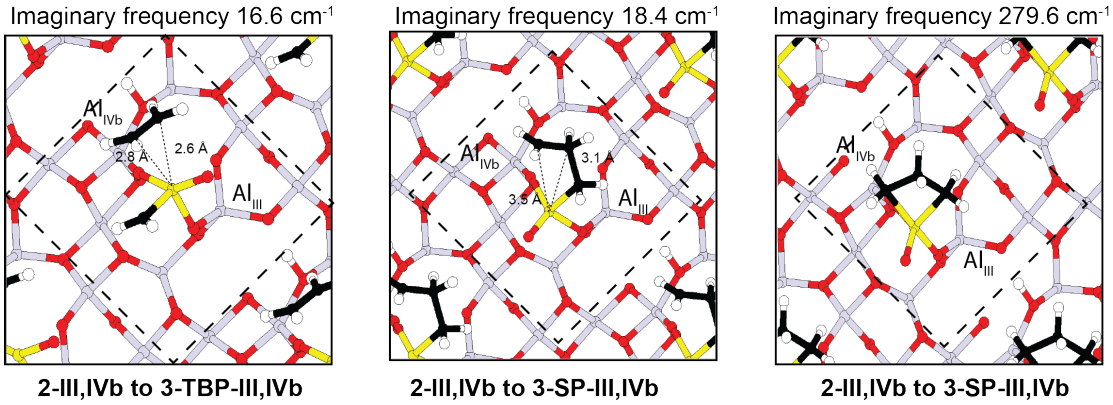

Figure A.3. 7. Structure of the transition state and imaginary frequencies of the [2+2] cycloaddition from **2-III,IVb** to **3-TBP-III,IVb** and **3-SP-III,IVb** and from **3-TBP-III,IVb** to **3-SP-III,IVb** on the dehydrated (110) facet of γ-Al_2O_3. The bottom two layers of the slab have been omitted for clarity. The surface unit cell is indicated by a dashed black line. Al (yellow), O (red), Re (grey), C (black), H (white) balls. Distances are indicated (in Å).

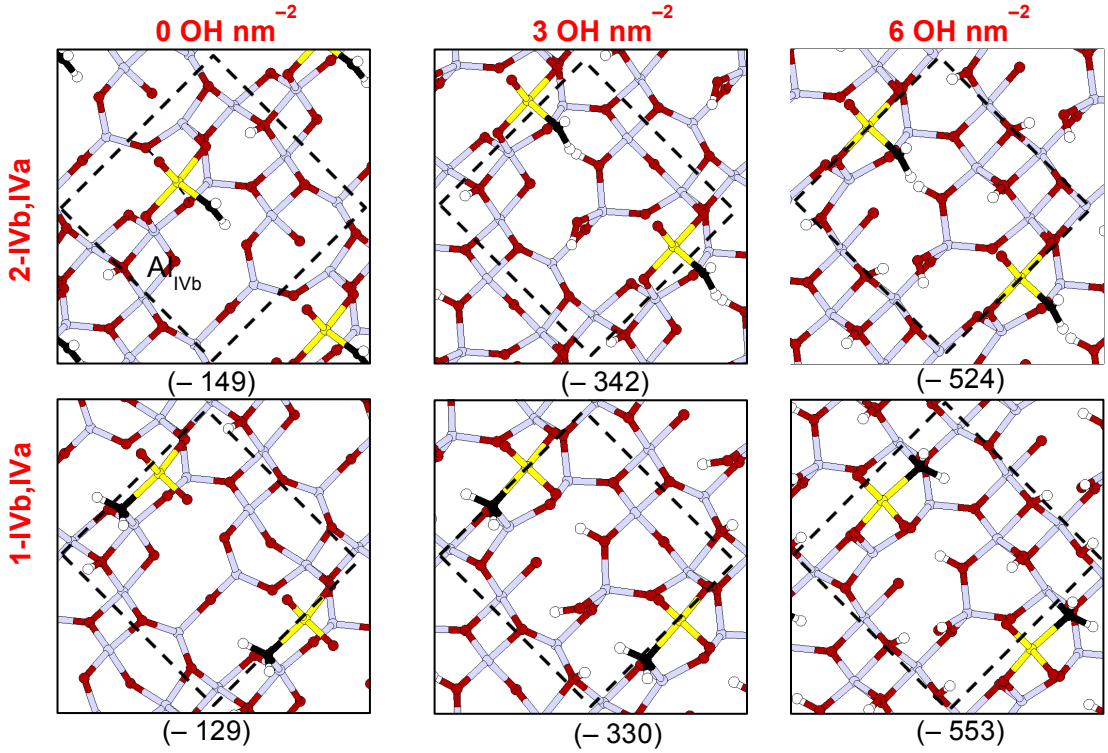

Figure A.3. 8. Structure and stability of the μ-methylene bound to Al_{IVb}/Al_{IVa} (**1-IVb,IVa**) and the alkylidene **2-IVb,IVa** on different state of hydration of (110) facet of γ-Al_2O_3,. The bottom two layers of the slab have been omitted for clarity. The surface unit cell is indicated by a dashed line. Al (yellow), O (red), Re (grey), C (black), H (white) balls. O-Re and Re-C (italic numbers) distances are indicated (in Å). Adsorption energies (ΔEcoads) are given in parentheses in kJ mol-1.

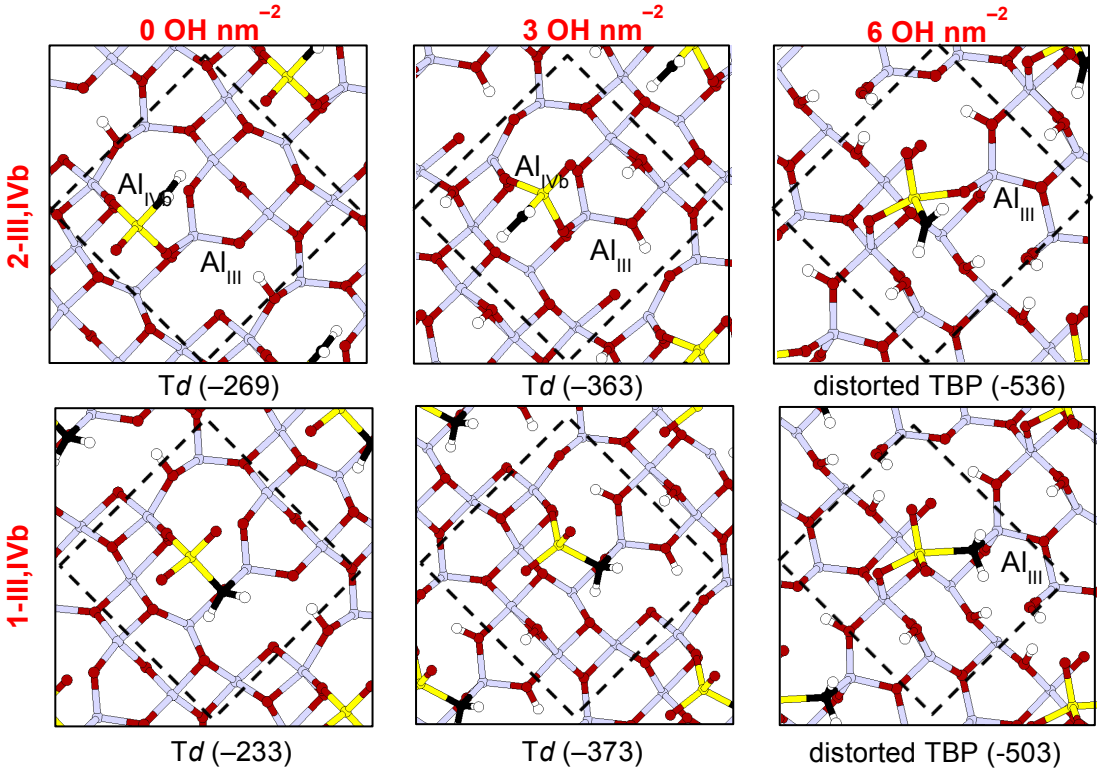

Figure A.3. 9. Structure and stability of the μ-methylene bound to Al_{III}/Al_{IVb} (**1-III,IVb**) and the alkylidene **2-III,IVb** on different state of hydration of (110) facet of γ-Al_2O_3,. The bottom two layers of the slab have been omitted for clarity. The surface unit cell is indicated by a dashed line. Al (yellow), O (red), Re (grey), C (black), H (white) balls. O-Re and Re-C (italic numbers) distances are indicated (in Å). Adsorption energies (ΔEcoads) are given in parentheses in kJ mol^{-1}.

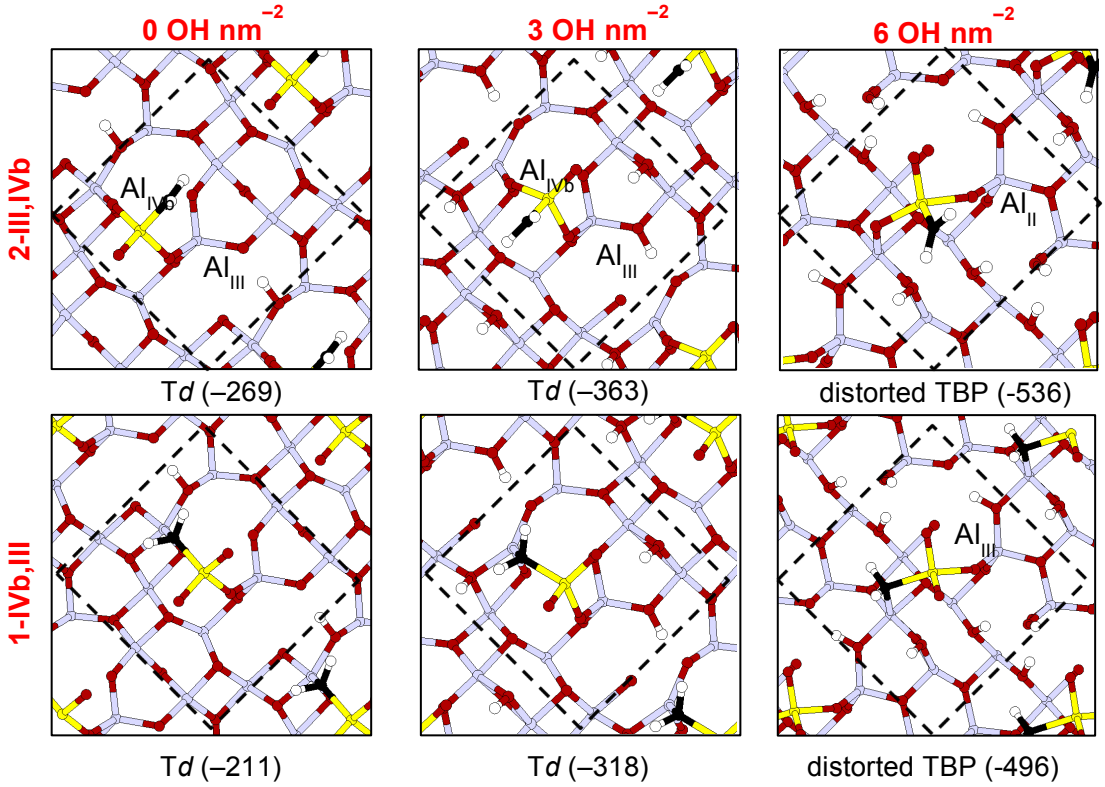

Figure A.3. 10. Structure and stability of the μ-methylene bound to Al_{IVb}/Al_{III} (**1-IVb,III**) and the alkylidene **2-III,IVb** on different state of hydration of (110) facet of γ-Al_2O_3,. The bottom two layers of the slab have been omitted for clarity. The surface unit cell is indicated by a dashed line. Al (yellow), O (red), Re (grey), C (black), H (white) balls. O-Re and Re-C (italic numbers) distances are indicated (in Å). Adsorption energies (ΔEcoads) are given in parentheses in kJ mol^{-1}.

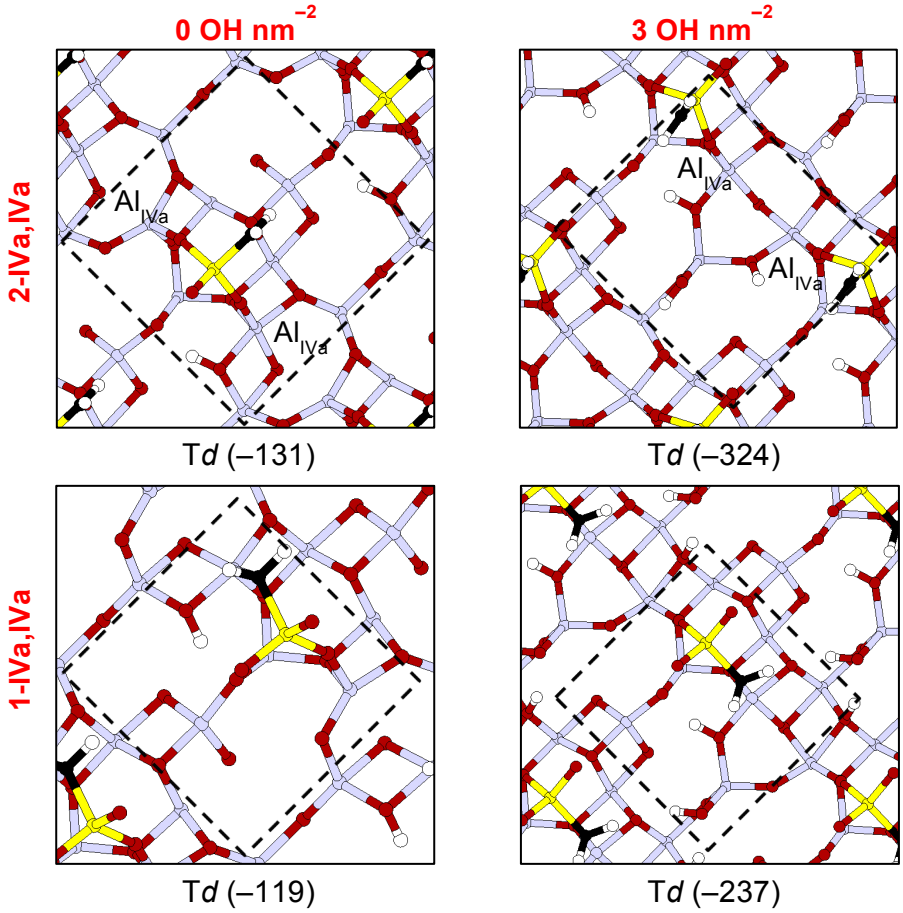

Figure A.3. 11. Structure and stability of the μ-methylene bound to Al_{IVa}/Al_{IVa} (**1-IVa,IVa**) and the alkylidene **2-IVa,IVa** on different state of hydration of (110) facet of γ-Al_2O_3. The bottom two layers of the slab have been omitted for clarity. The surface unit cell is indicated by a dashed line. Al (yellow), O (red), Re (grey), C (black), H (white) balls. O-Re and Re-C (italic numbers) distances are indicated (in Å). Adsorption energies (ΔEcoads) are given in parentheses in kJ mol^{-1}.

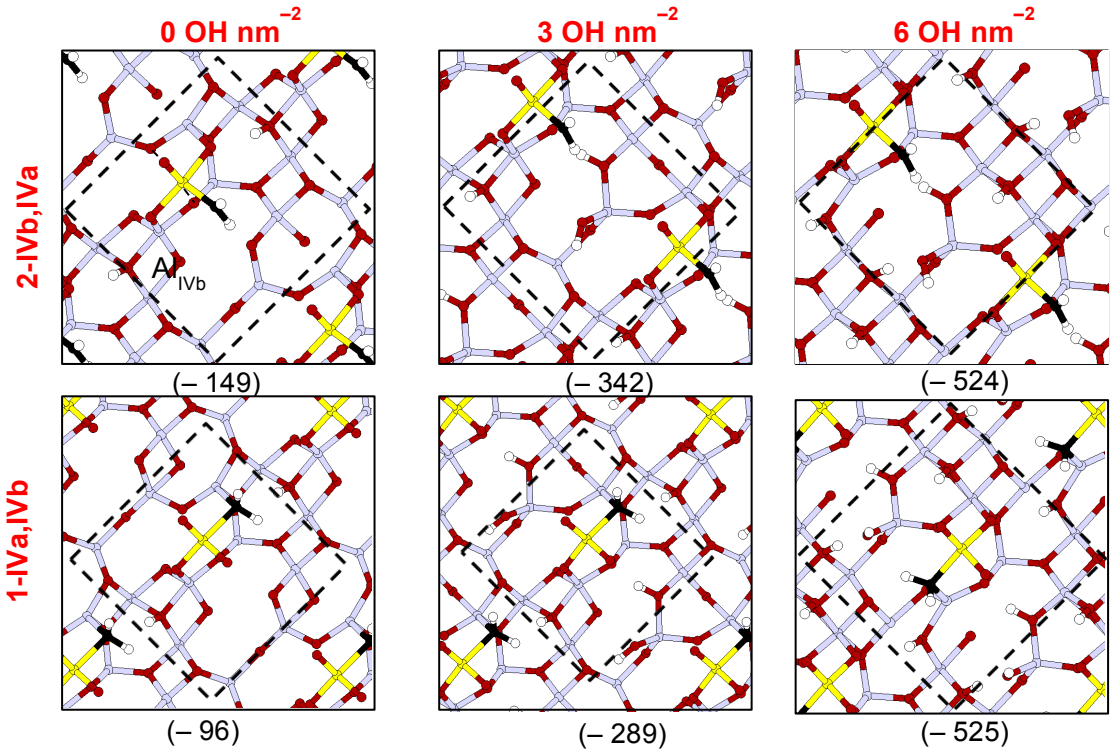

Figure A.3. 12. Structure and stability of the μ-methylene bound to AlIVa/AlIVb (**1-IVa,IVb**) and the alkylidene **2-IVb,IVa** on different state of hydration of (110) facet of γ-Al_2O_3,. The bottom two layers of the slab have been omitted for clarity. The surface unit cell is indicated by a dashed line. Al (yellow), O (red), Re (grey), C (black), H (white) balls. O-Re and Re-C (italic numbers) distances are indicated (in Å). Adsorption energies (ΔEcoads) are given in parentheses in kJ mol^{-1}.

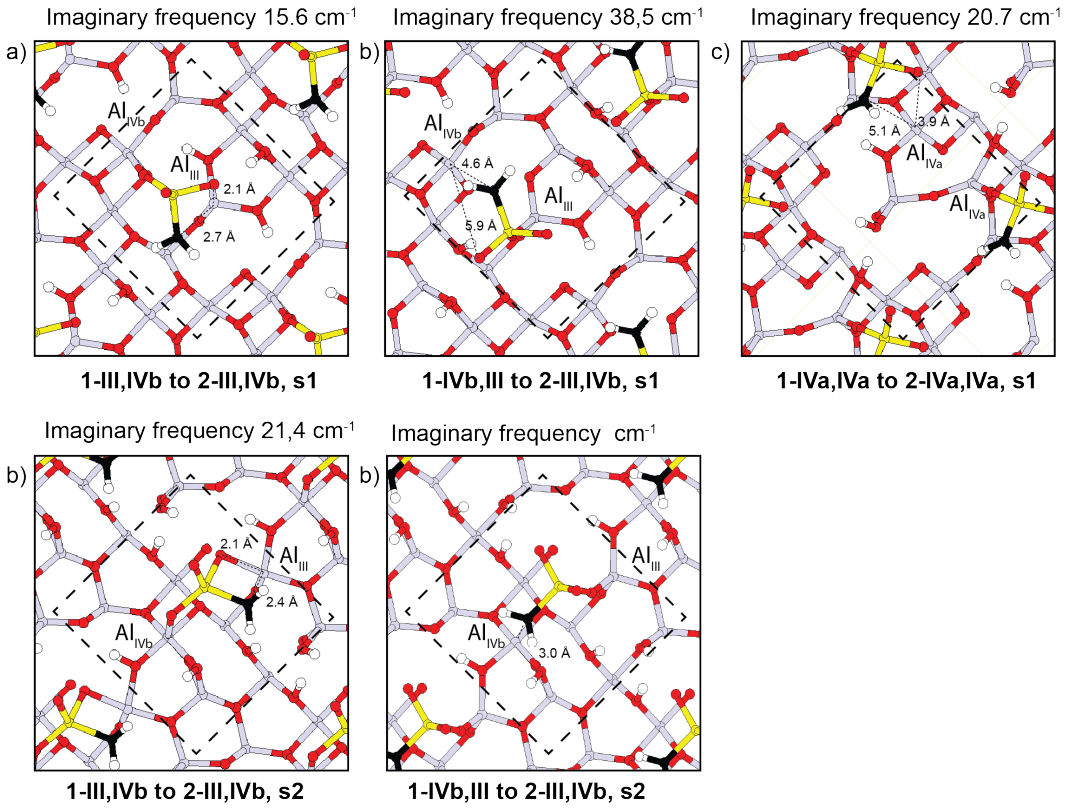

Figure A.3. 13. Structure of the transition state and imaginary frequency of the interconversion reaction from the μ-methylene (**1-A,B**) to the alkylidene (**2-A,B**) on a) s1 and b) s0 (110) facet of γ-Al_2O_3. The bottom two layers of the slab have been omitted for clarity. The surface unit cell is indicated by a dashed black line. Al (yellow), O (red), Re (grey), C (black), H (white) balls. Distances are indicated (in Å).

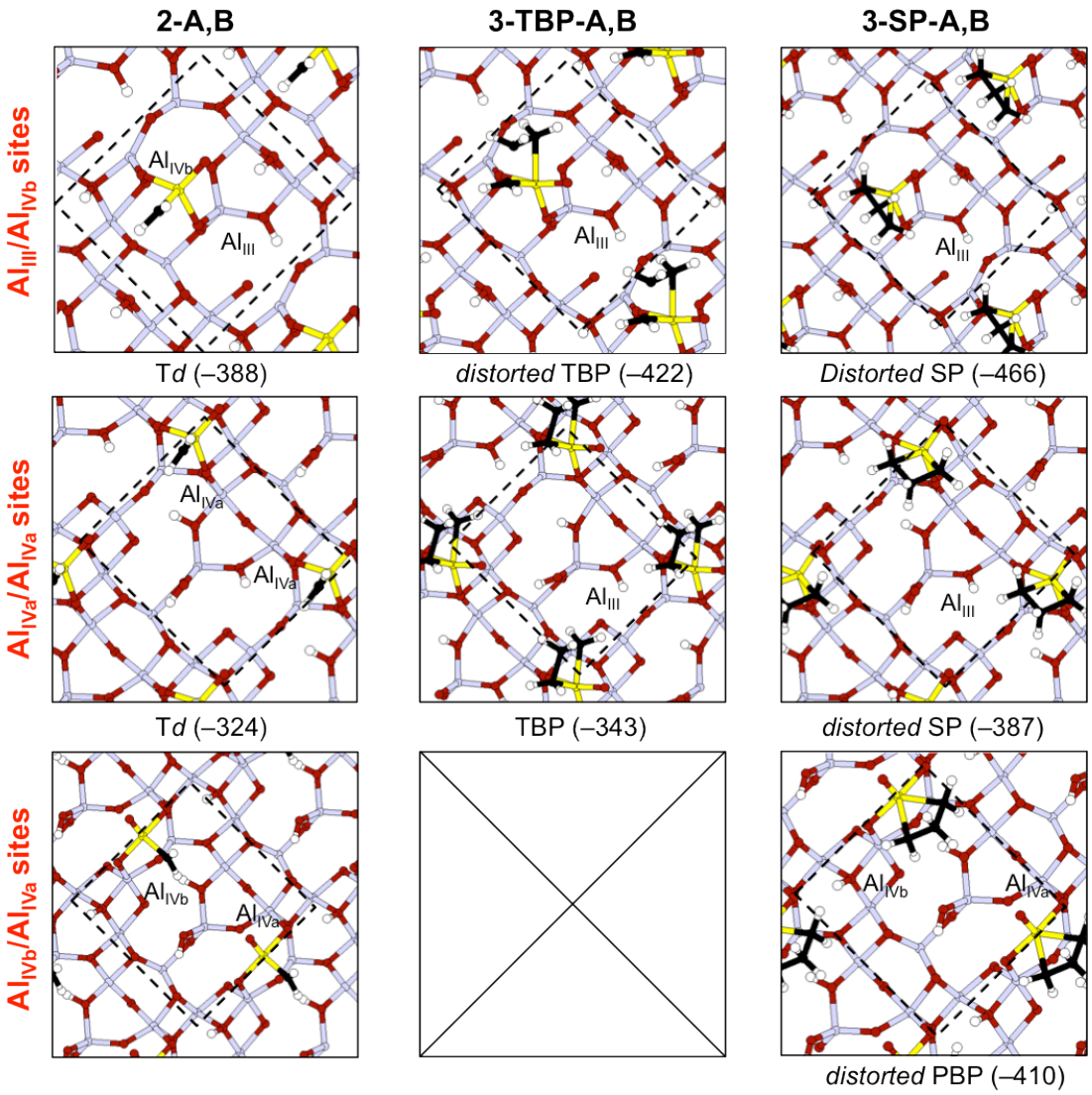

Figure A.3. 14. Structure and stability of the main metathesis intermediate (**2-A,B**, **3-TBP-A,B** and **3-SP-A,B**) on partially hydrated (110) γ-Al_2O_3, type of intermediates according to the Alumina sites. The bottom two layers of the slab have been omitted for clarity. The surface unit cell is indicated by a dashed line. Al (yellow), O (red), Re (grey), C (black), H (white) balls. Adsorption energies (ΔE_{coads}) are given in parentheses in kJ mol-1.

Table A.3.6. Important distance (in Å) and angles (in °) of the alkylidene and metathesis intermediates on Al_{III}/Al_{IVb} alumina sites on s1 hydrated surface (2-III,IVb, 3-TBP-IIIb,IVb and 3-SP-III,IVb).

s1	2-III,IVb	3-TBP-III,IVb	3-SP-III,IVb
$Re=C_{ene}$	1.88	-	-
Re-O	1.71	1.76	1.73
$Re-OAl_{III}$	1.84	1.85	1.87
$Re-OAl_{IVb}$	1.82	1.88	1.83
Re-Cα	-	2.05	2.19
Re-Cβ	-	2.42	2.83
α (°)	-	164	-
β (°)	-	360	-
γ (°)	-	-	98
δ (°)	-	-	326

[a]: Please refer to *NB1* for the determination of the angles

Table A.3.7. Important distance (in Å) and angles (in °) of the alkylidene and metathesis intermediates on Al_{IVa}/Al_{IVa} alumina sites on s1 hydrated surface (2-IVa,IVa, 3-TBP-IVa,IVa and 3-SP-IVa,IVa).

s1	2-IVa,IVa	3-TBP-IVa,IVa	3-SP-IVa,IVa
$Re=C_{ene}$	1.88	-	-
Re-O	1.71	1.76	1.73
$Re-OAl_{IVa}$	1.81	1.83	1.79
$ReOAl_{IVa'}$	1.83	1.87	1.85
Re-Cα	-	2.05	2.16
Re-Cβ	-	2.40	2.82
α (°)	-	163	-
β (°)	-	360	-
γ (°)	-	-	88
δ (°)	-	-	346

[a]: Please refer to *NB1* for the determination of the angles

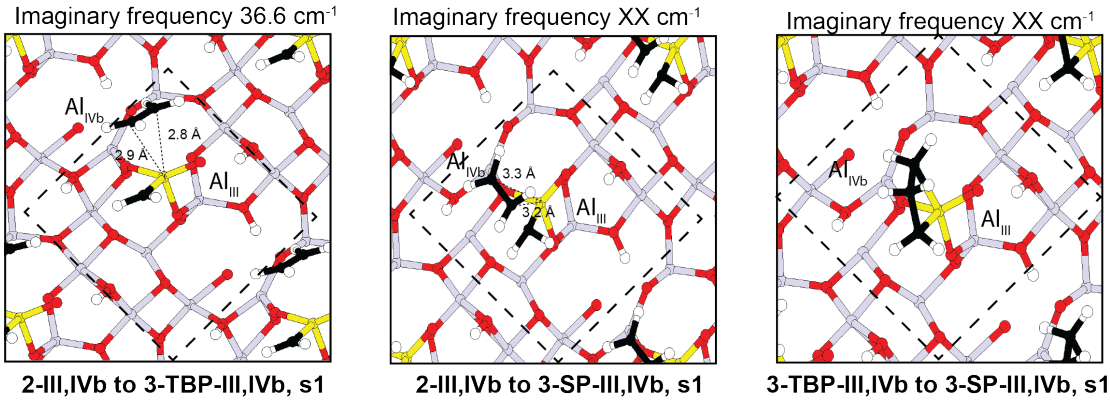

Figure A.3. 15. Structure of the transition state of the [2+2] cycloaddition from **2-III,IVb** to **3-TBP-III,IVb** and **3-SP-III,IVb** and from **3-TBP-III,IVb** to **3-SP-III,IVb** on the s1 (110) facet of γ-Al_2O_3. The bottom two layers of the slab have been omitted for clarity. The surface unit cell is indicated by a dashed black line. Al (yellow), O (red), Re (grey), C (black), H (white) balls. Distances are indicated (in Å).

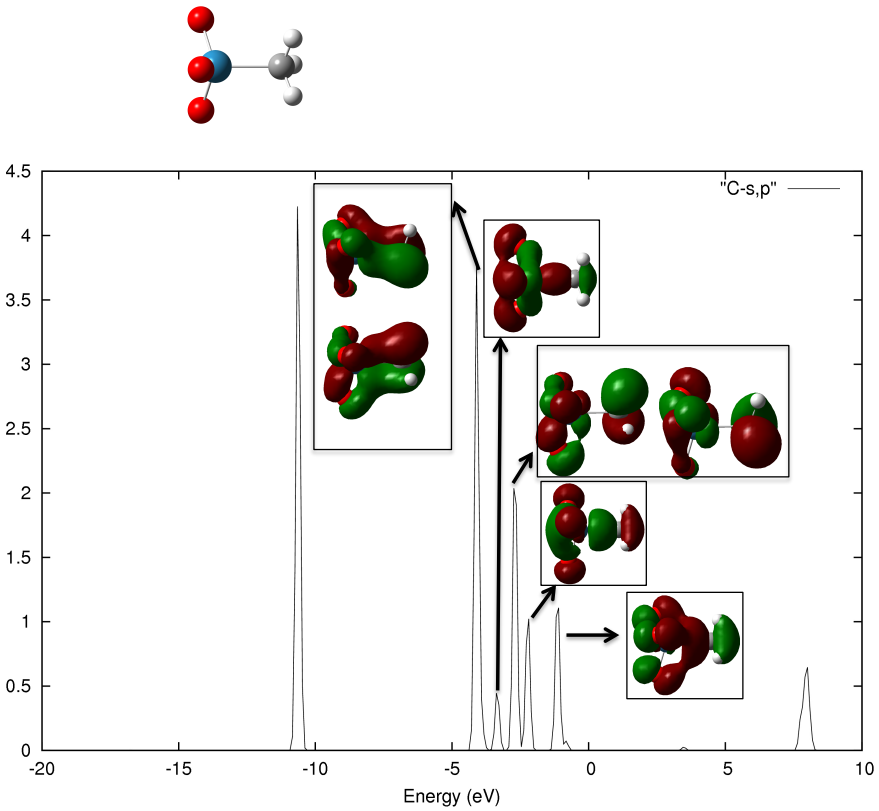

Figure A.3. 16. PDOS of the MTO molecule projected on C s and p orbitals obtained from the plane wave approach (VASP). The occupied molecular orbitals with high p character are shown as insets.

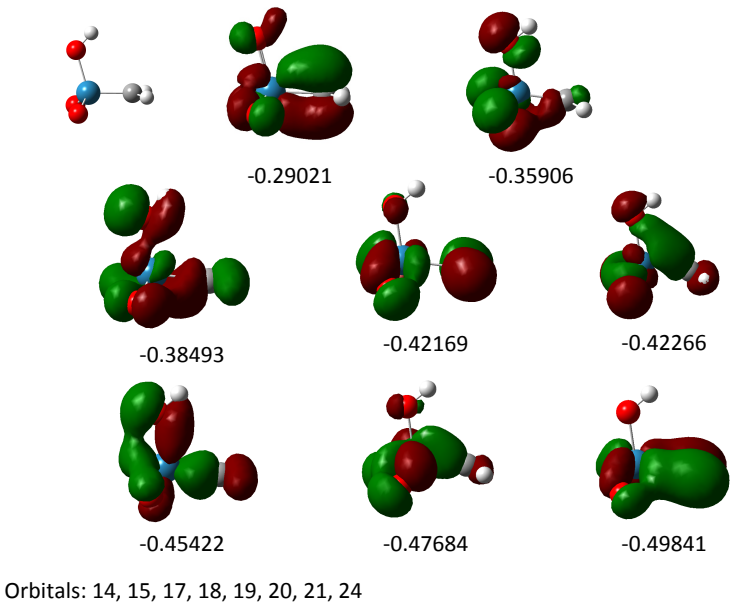

Figure A.3. 17. Occupied molecular orbitals with high p contribution on the C atom for the enolic form of MTO. Energies in hartrees.

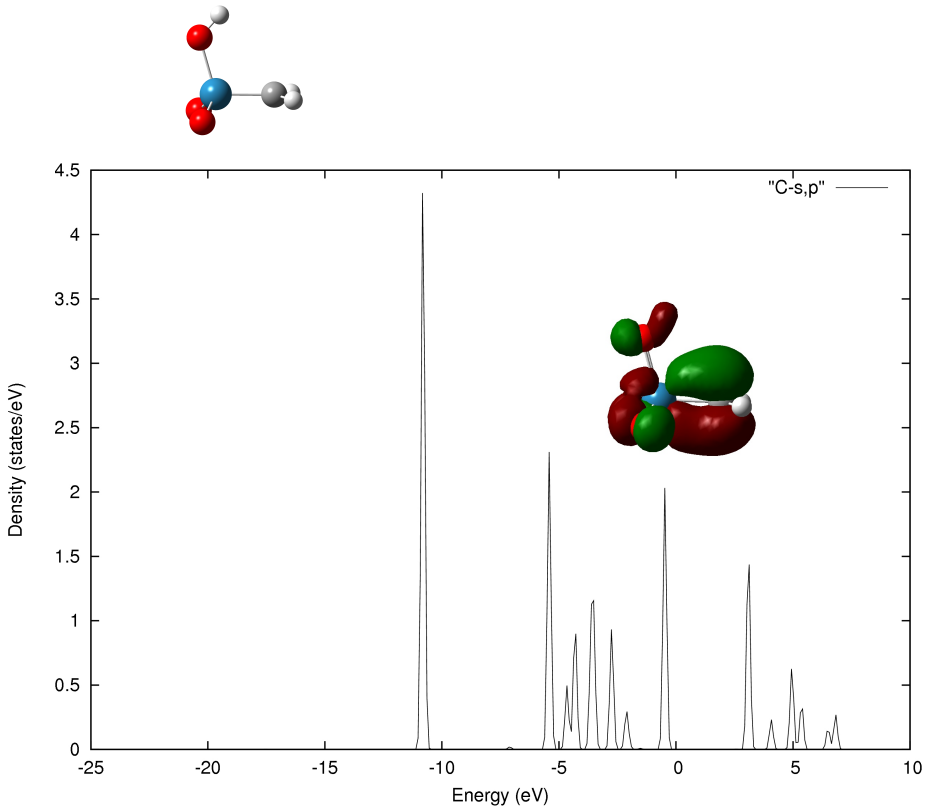

Figure A.3. 18. PDOS of the enolic form of the MTO molecule projected on C s and p orbitals. The highest occupied molecular orbital is shown.

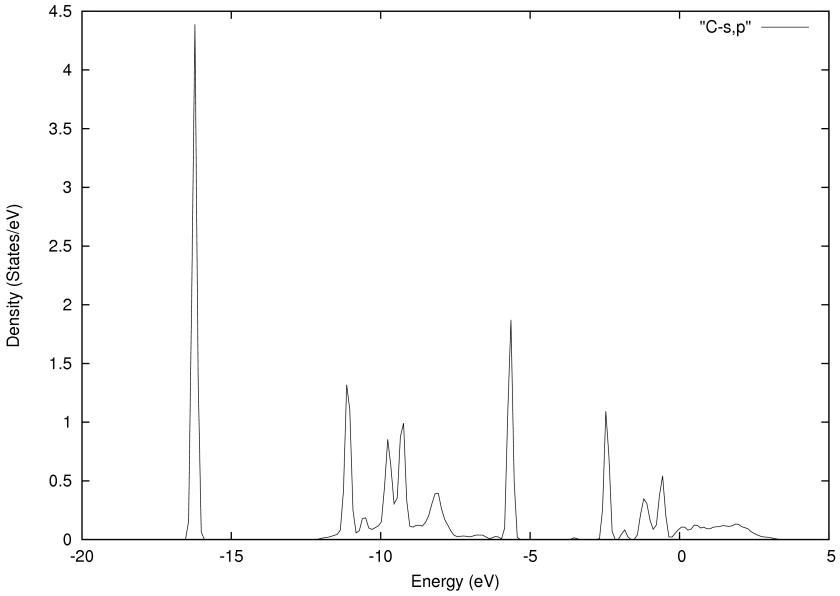

Figure A.3. 19. PDOS projected on C s and p orbitals for methylidene formed on the Al_{III}-Al_{IVb} sites on the **s0** surface

a)

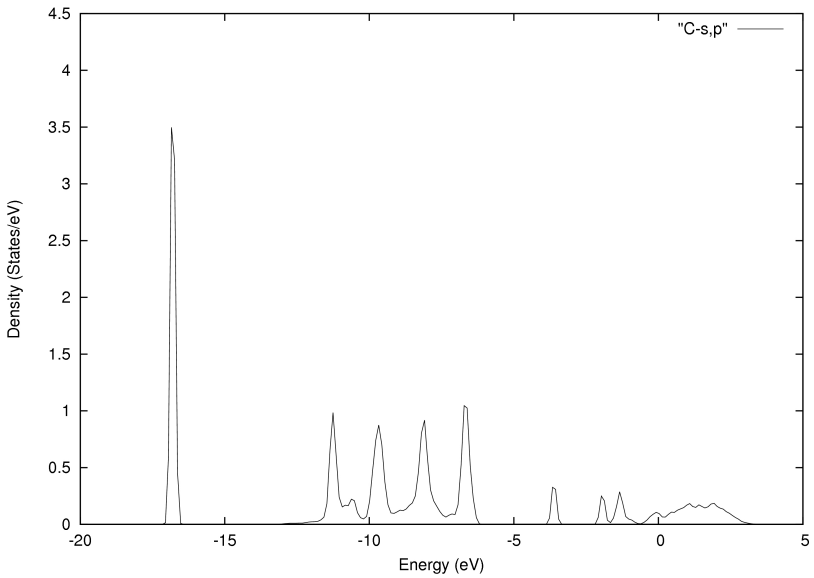

b)

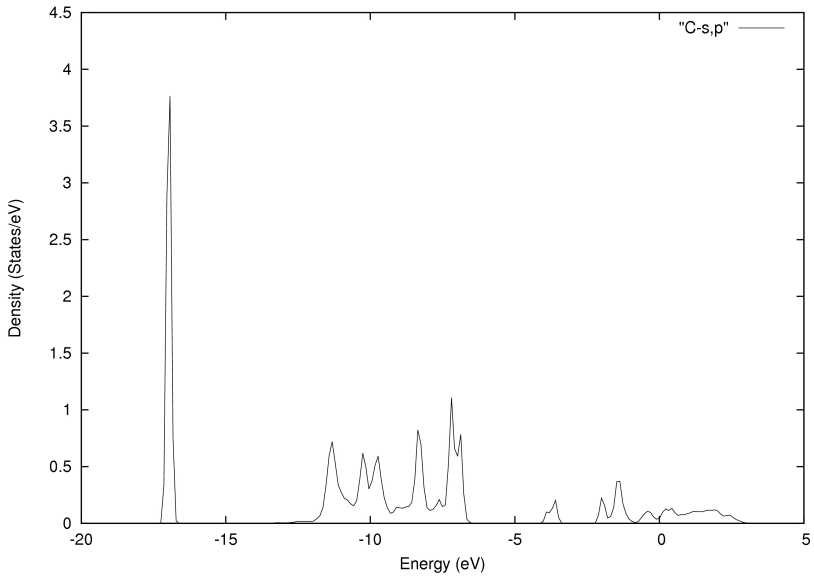

Figure A.3. 20. a) PDOS projected on C s and p orbitals for the **1-IVb,III** structure on the **s0** surface. b) PDOS projected on C s and p orbitals for the **2-III,IVb** structure on the **s1** surface.

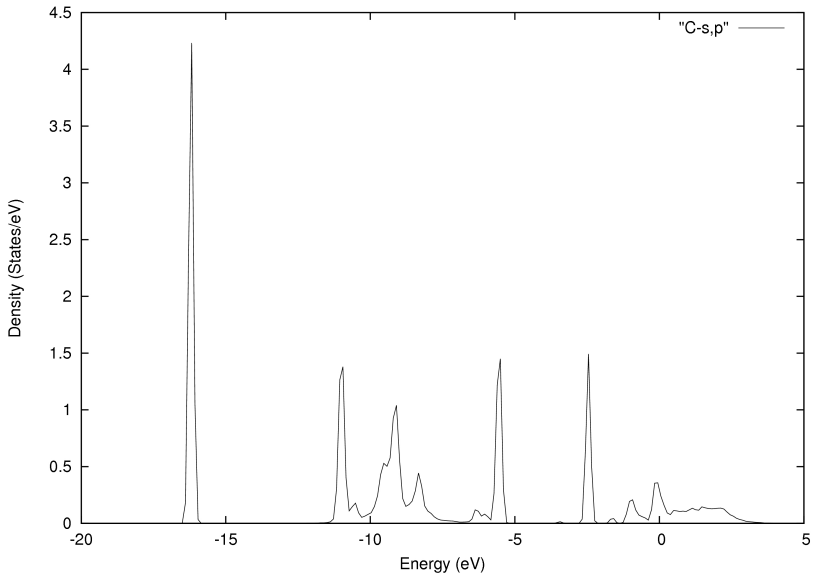

Figure A.3. 21. PDOS projected on C s and p orbitals of **2-III,IVb** on the **s1** surface

a)

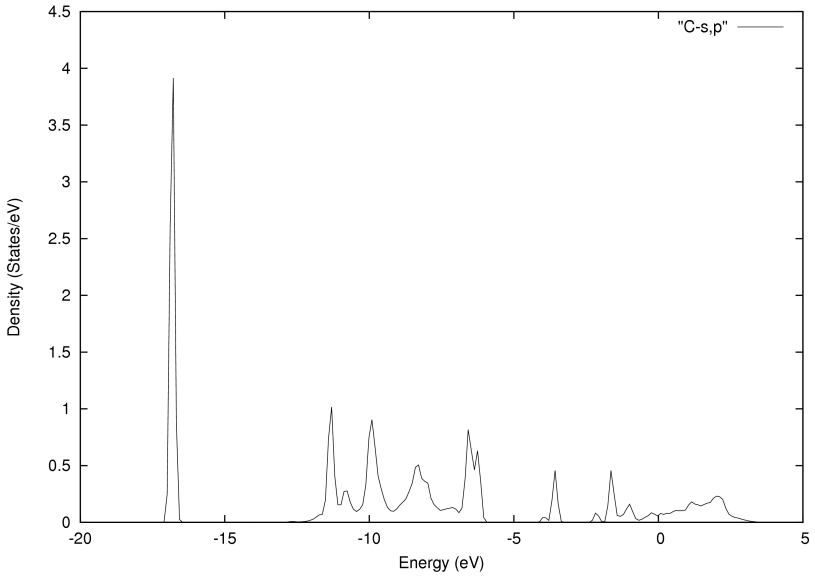

b)

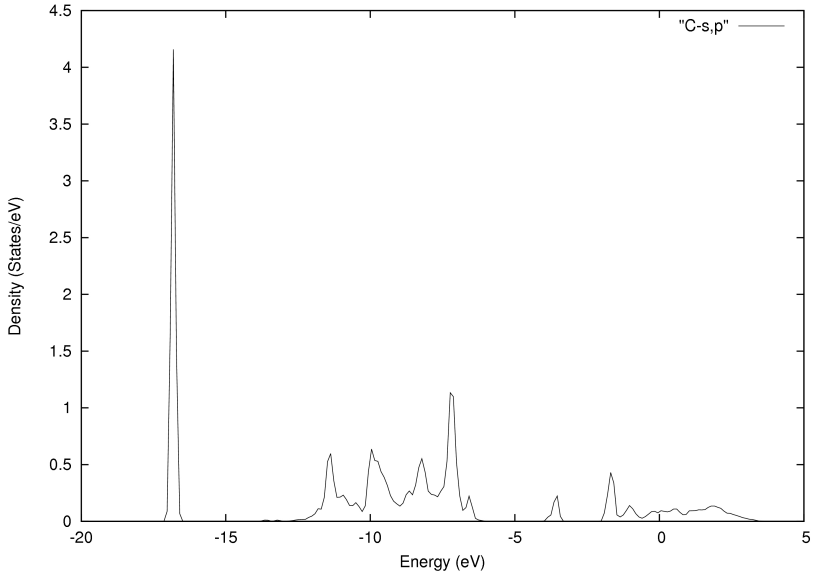

Figure A.3. 22. a) PDOS projected on C s and p orbitals for the **1-IVb,III** structure on the **s1** surface. b) PDOS projected on C s and p orbitals for the **1-III,IVb** structure on the **s1** surface.

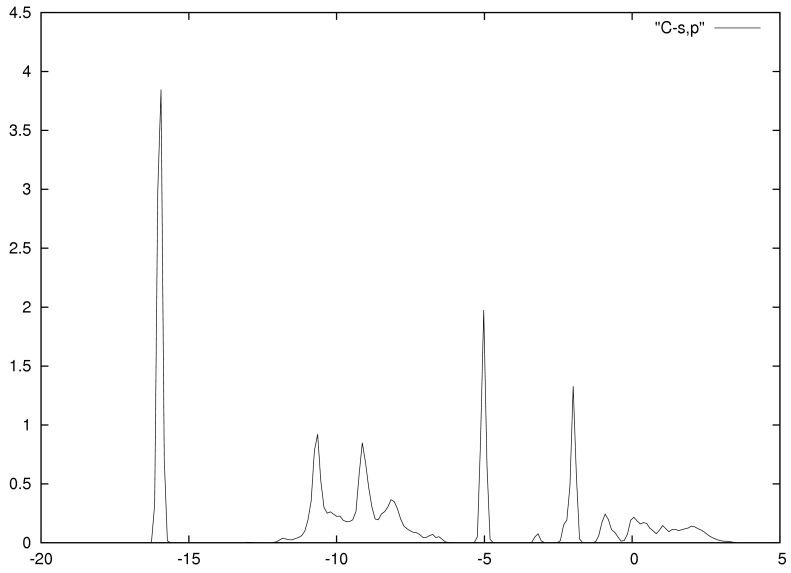

Figure A.3. 23. PDOS projected on C s and p orbitals of **2-III,IVb** sites on the **s2** surface.

a)

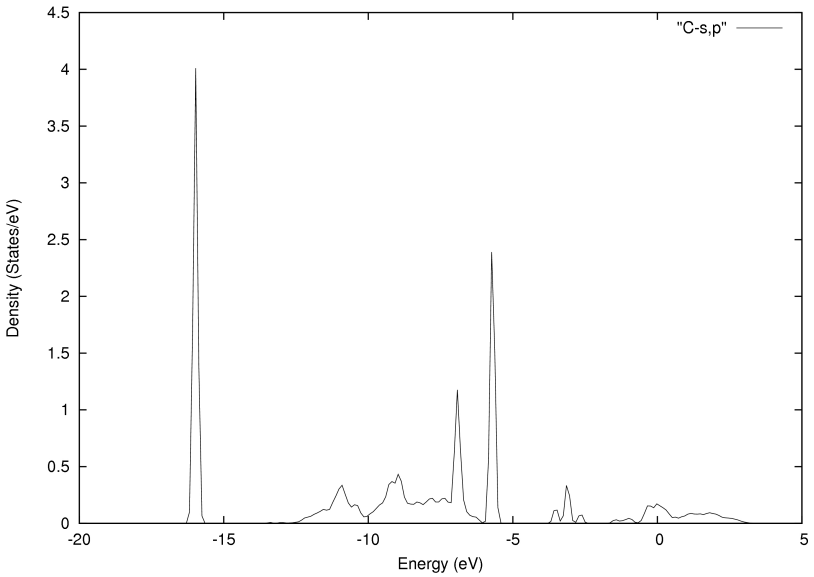

b)

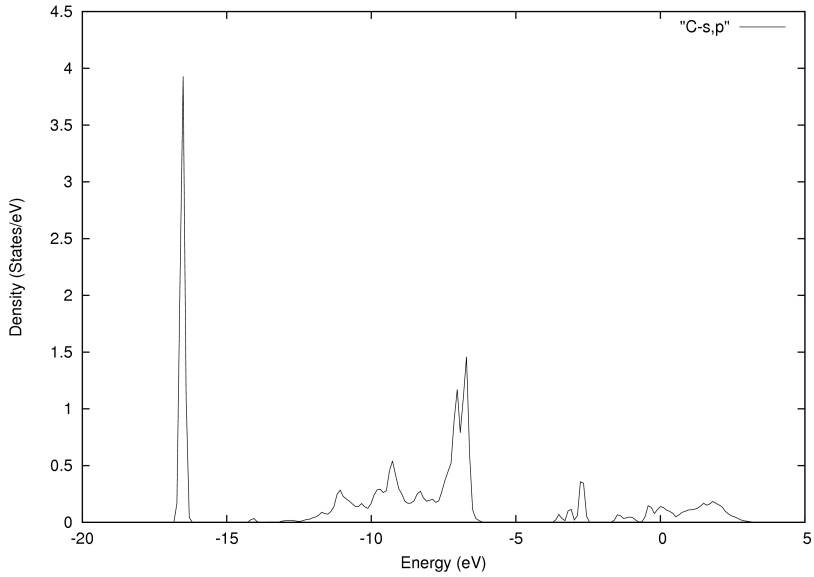

Figure A.3. 24. a) PDOS projected on C s and p orbitals for the **1-IVb,III** structure on the **s2** surface. b) PDOS projected on C s and p orbitals for the **1-III,IVb** structure on the **s2** surface.

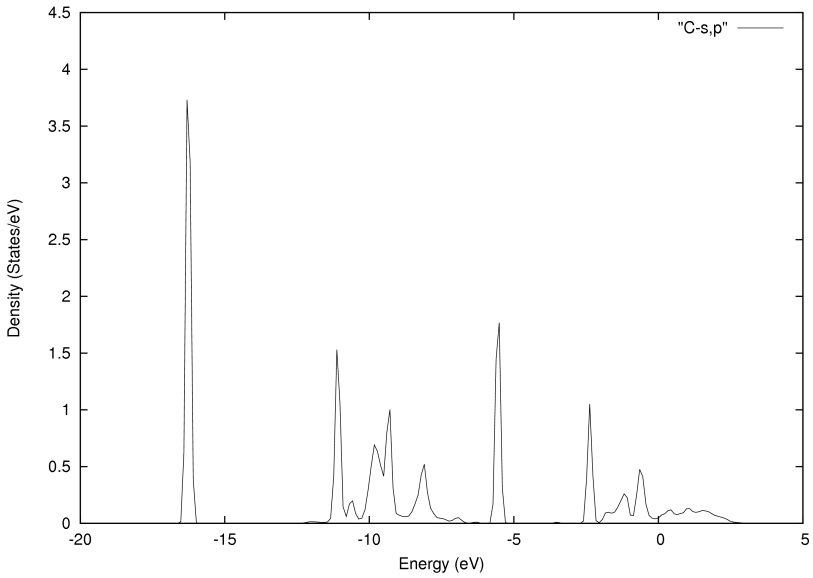

Figure A.3. 25. PDOS projected on C s and p orbitals of **2-IVa,IVa** sites on the **s0** surface

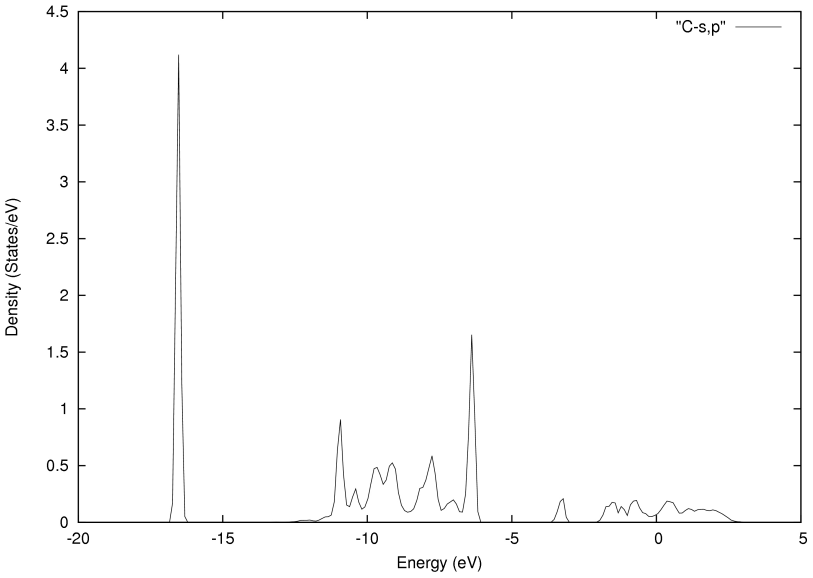

Figure A.3. 26. PDOS projected on C s and p orbitals for the **1-IVa,IVa** structure on the **s0** surface.

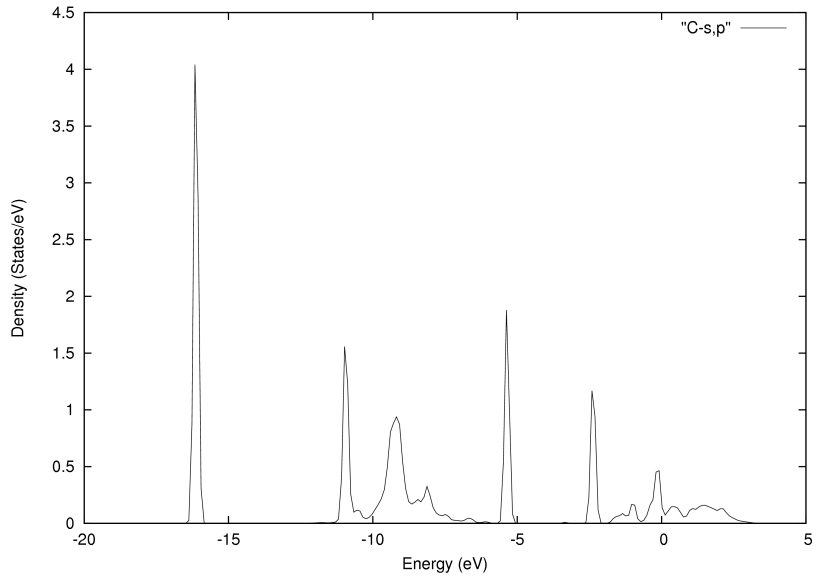

Figure A.3. 27. PDOS projected on C s and p orbitals of **2-IVa,IVa** on **s1** surface.

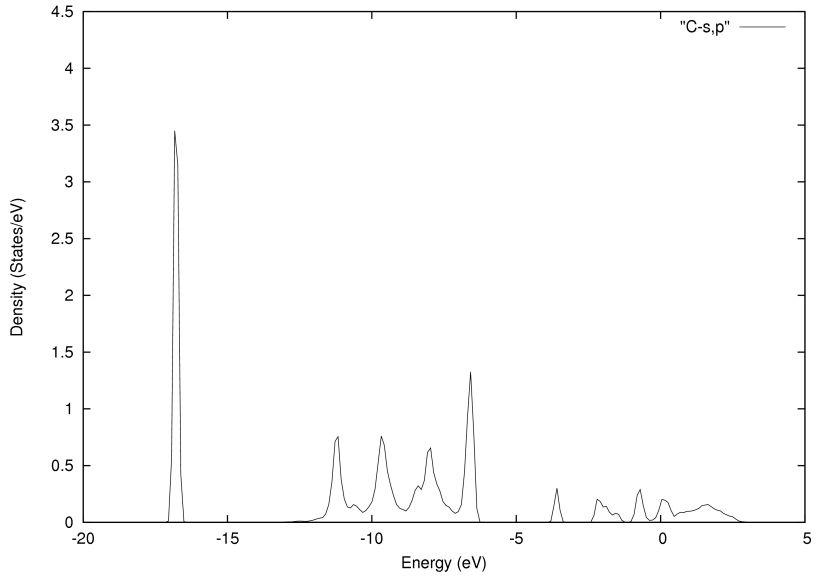

Figure A.3. 28. PDOS projected on C s and p orbitals for the **1-IVa,IVa** structure on the **s1** surface.

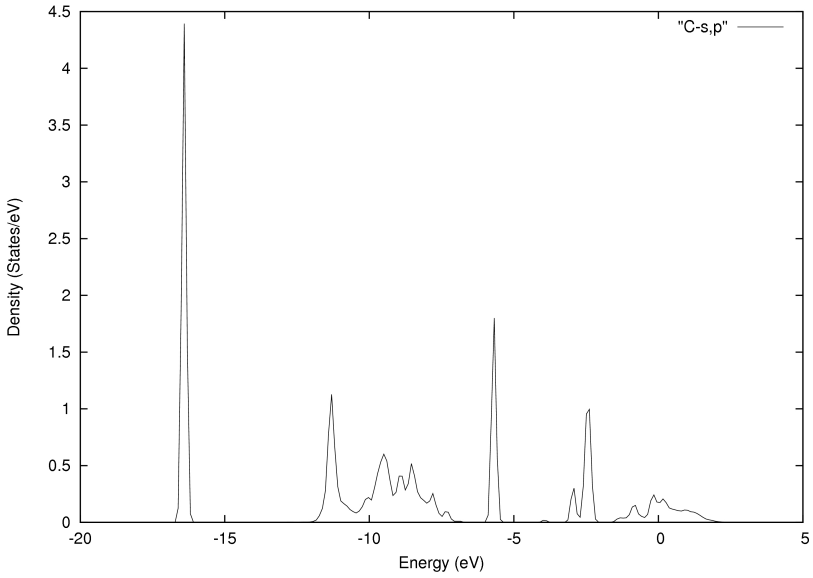

Figure A.3. 29. PDOS projected on C s and p orbitals of **2-IVb,IVa** sites on the **s0** surface.

a)

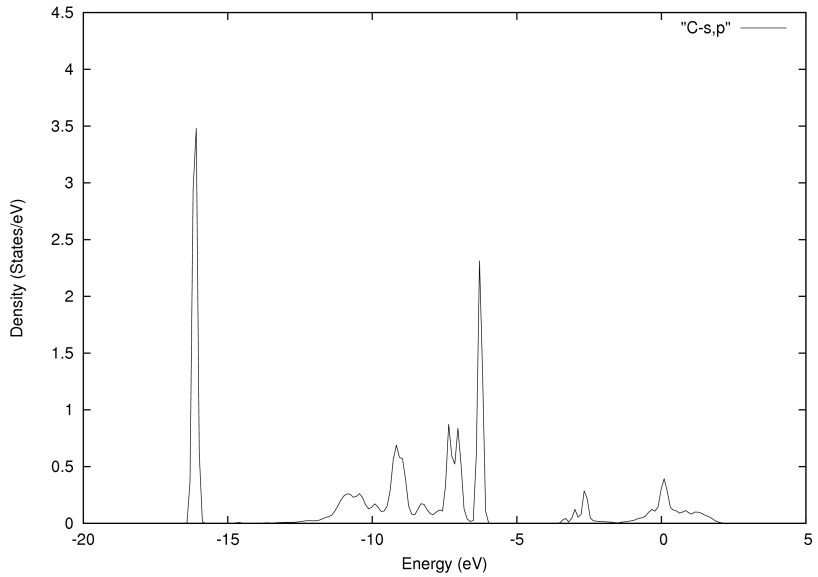

b)

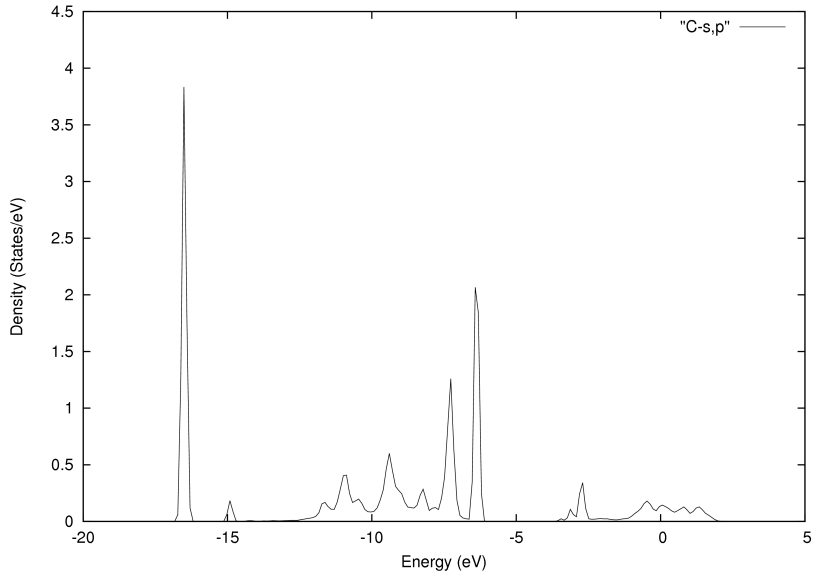

Figure A.3. 30. a) PDOS projected on C s and p orbitals for **1-IVb,IVa** structure on the **s0** surface. b) PDOS projected on C s and p orbitals for the **1-IVa,IVb** structure on the **s0** surface.

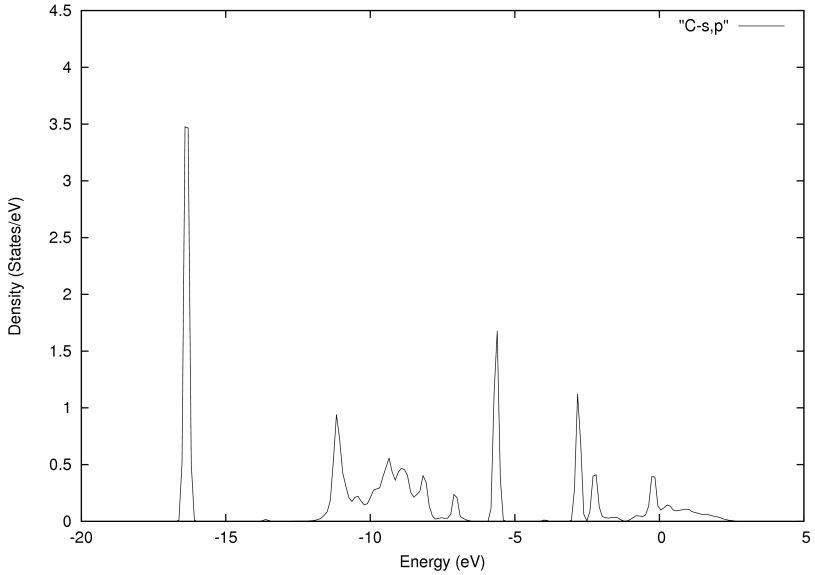

Figure A.3. 31. PDOS projected on C s and p orbitals for the **2-IVb,IVa** on **s1** surface.

a)

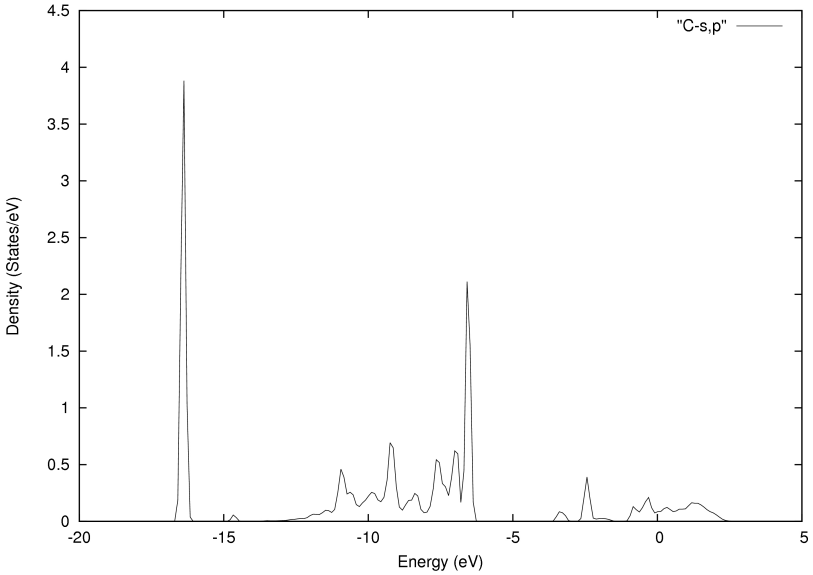

b)

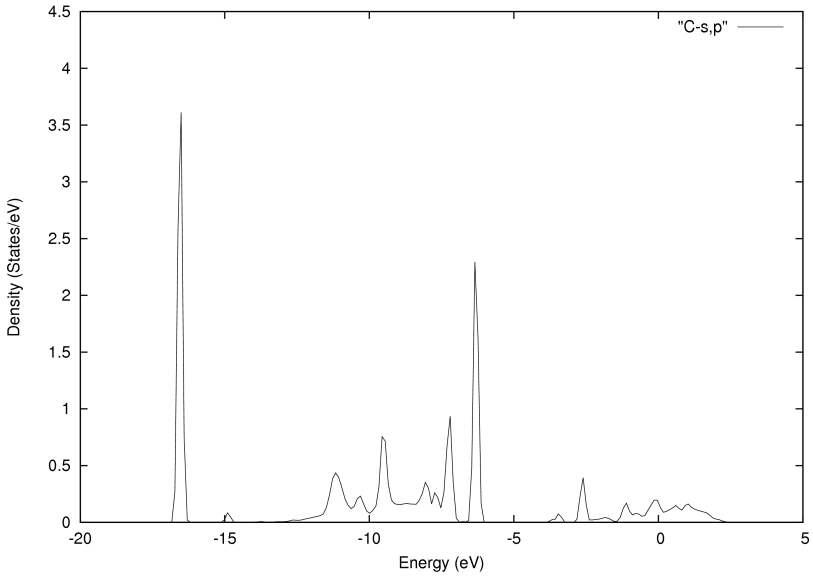

Figure A.3. 32. a) PDOS projected on C s and p orbitals for the **2-IVb,IVa** structure on the **s1** surface. b) PDOS projected on C s and p orbitals for the **2-IVa,IVb** structure on the **s1** surface.

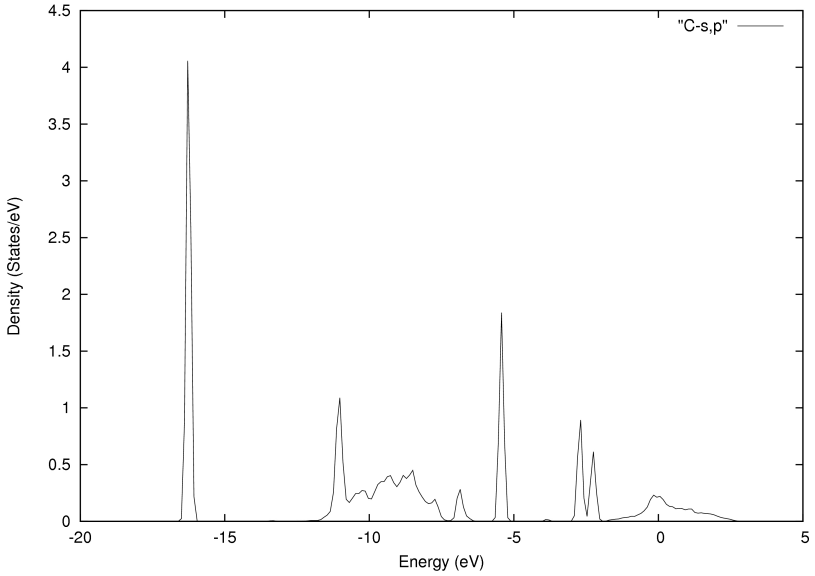

Figure A.3. 33. PDOS projected on C s and p orbitals for the **2-IVb,IVa** on **s2** surface.

a)

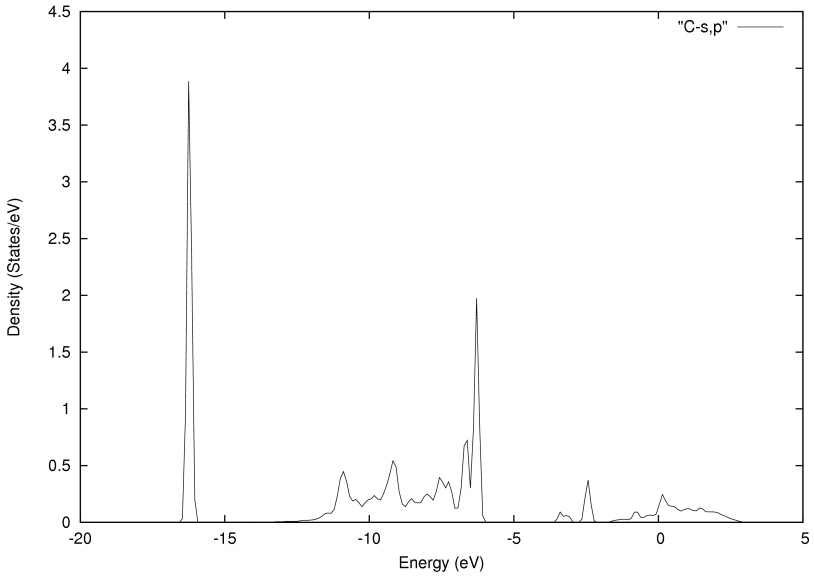

b)

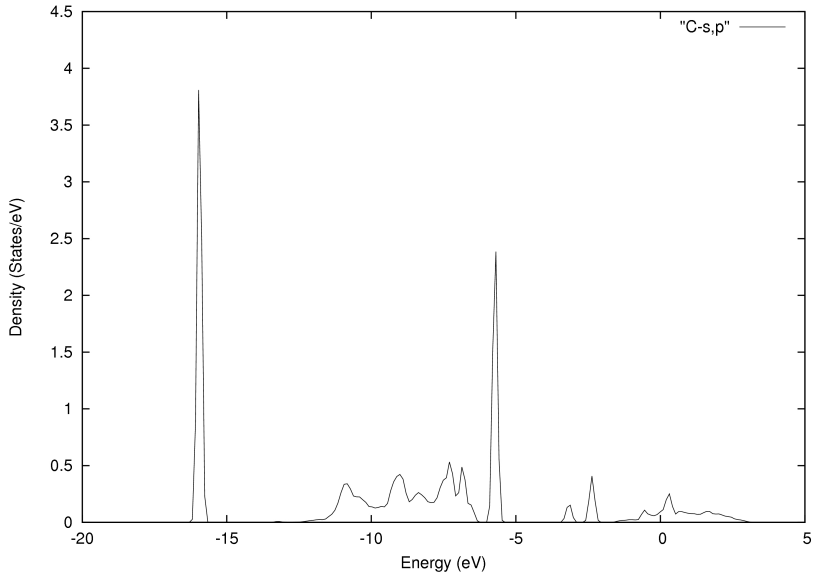

Figure A.3. 34. a) PDOS projected on C s and p orbitals for the **2-IVb,IVa** structure on the **s2** surface. b) PDOS projected on C s and p orbitals for the **2-IVa, IVb** structure on the **s2** surface.

A.3. Appendix to Chapter 5.

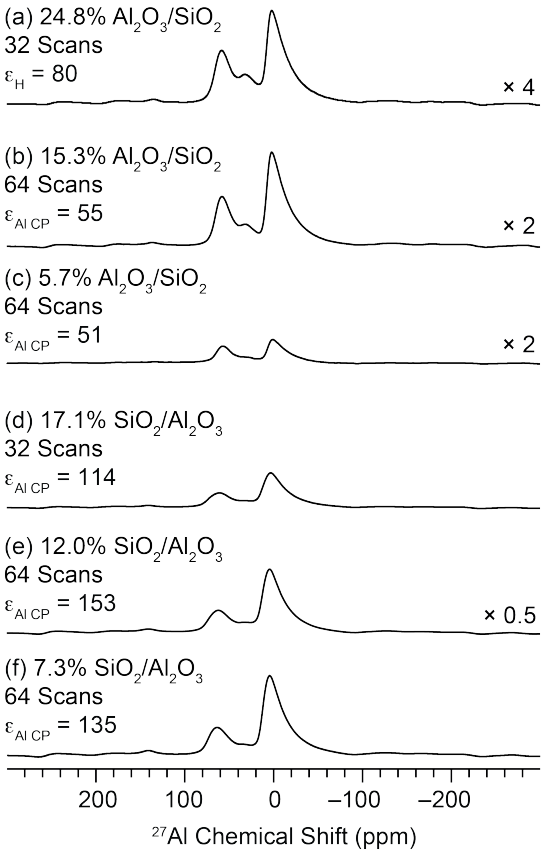

Figure A.5. 1. DNP enhanced ^{1}H-^{27}Al CPMAS solid-state NMR spectra acquired at 400 MHz/263 GHz. All spectra were acquired with a 12.5 kHz sample spinning frequency a) 24.8 w% Al_2O_3 on SiO_2, b) 15.0 w% Al_2O_3 on SiO_2, c) 5.7 w% Al_2O_3 on SiO_2, d) 17.1 w% SiO_2 on Al_2O_3, e) 12.0 w% SiO_2 on Al_2O_3 and f) 7.3 w% SiO_2 on Al_2O_3. The intensity of the spectra was scaled (scaling factors indicated on right) to account for differences in the number of scans used for acquisition to enable a direct comparison of the absolute intensities of the spectra.

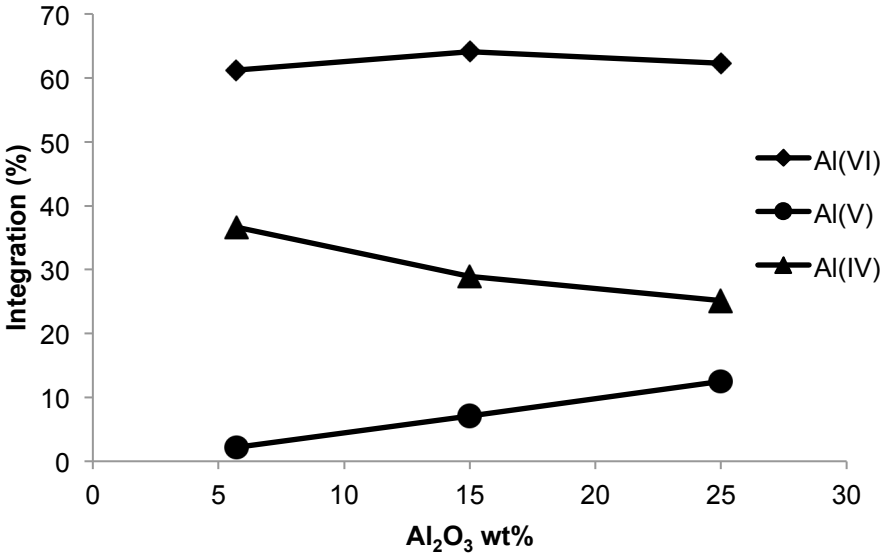

Figure A.5. 2. Relative ratio of Al sites on the Al/SiO_2 surface. The ratio between the aluminum sites were calculated form the decomposed spectra.

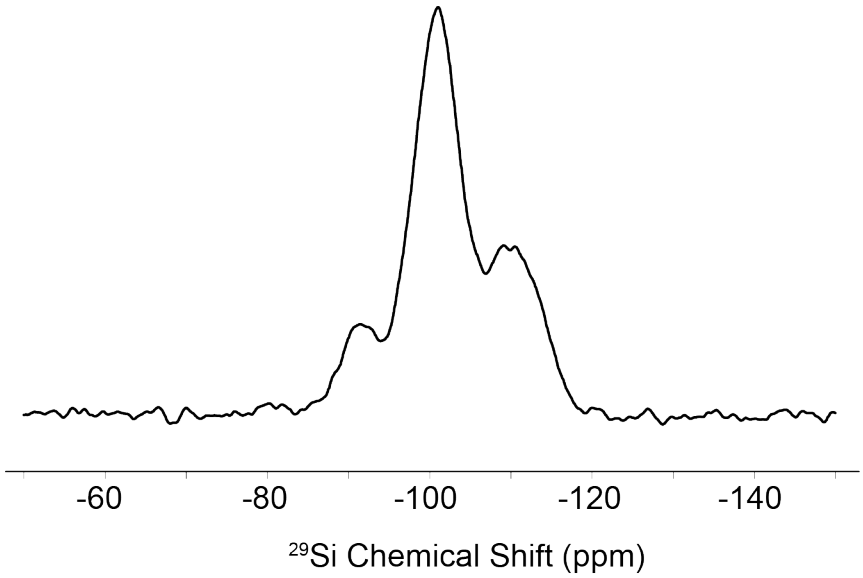

Figure A.5. 3. ^{1}H-^{29}Si CPMAS of the starting silica material, 400 MHz, 10 kHz spinning rate, the contact time was set to 3.

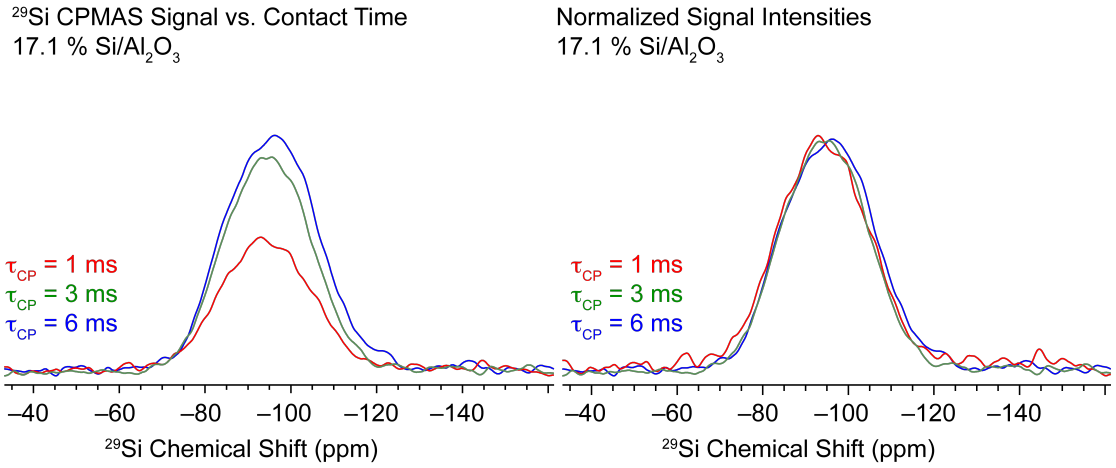

Figure A.5. 4. Comparison of DNP enhanced ^{29}Si CPMAS NMR spectra of 17.1% Si/Al_2O_3 acquired with contact times of 1 ms, 3 ms and 6 ms.

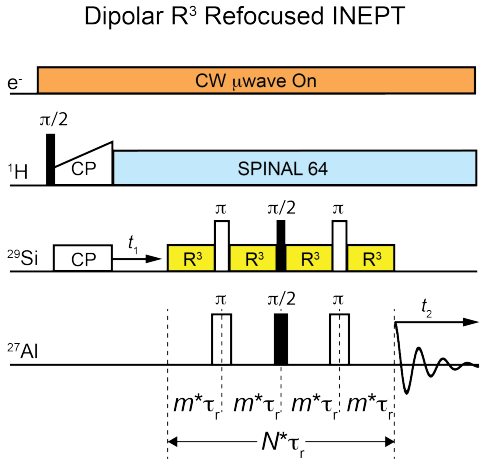

Figure A.5. 5. The refocused INEPT pulse sequence used to obtain two-dimensional ^{29}Si-^{27}Al scalar and dipolar correlation spectra. In order to obtain dipolar correlation spectra first order rotary resonance recoupling (R^3) was employed to recouple ^{29}Si-^{27}Al dipolar couplings.

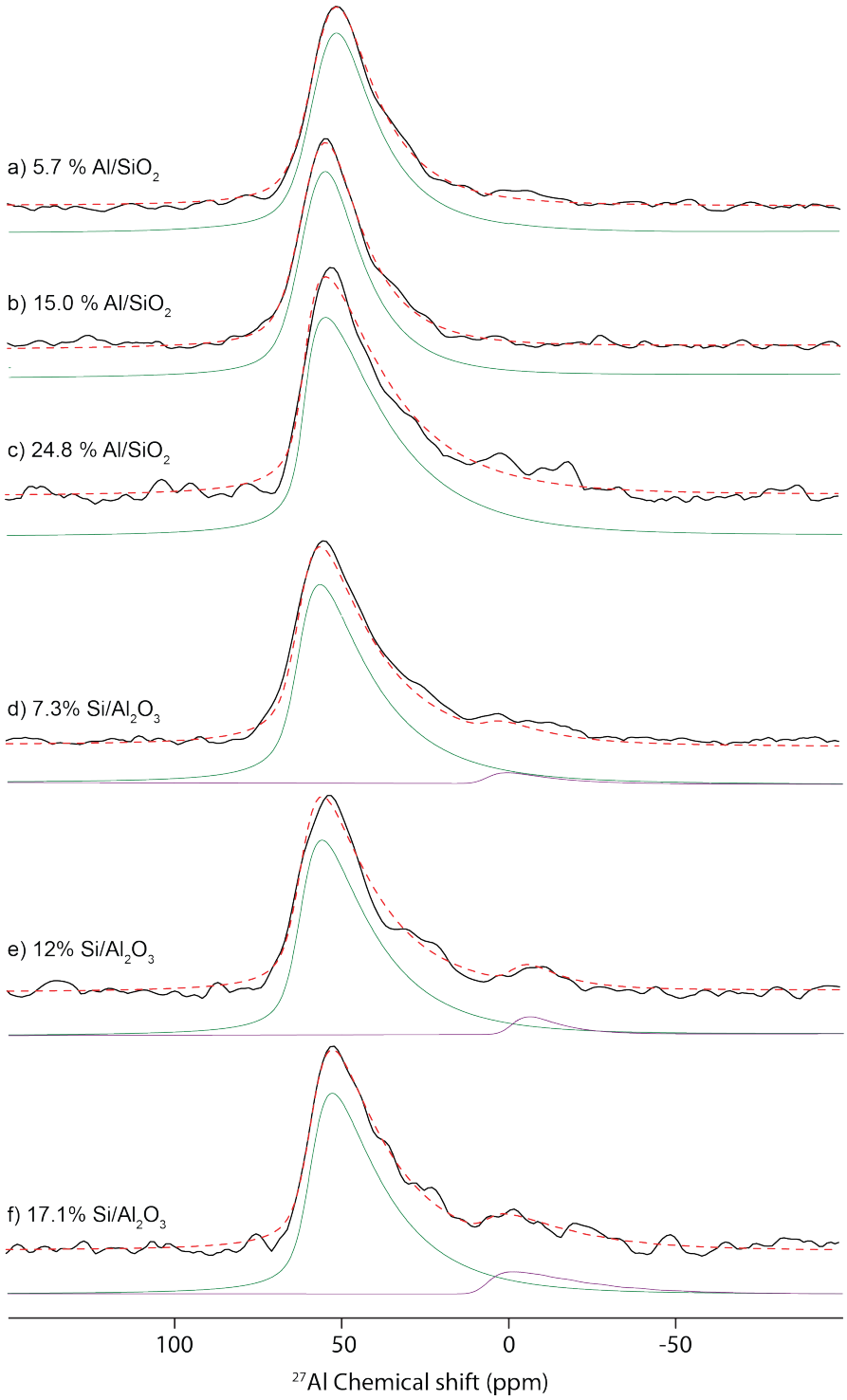

Figure A.5. 6. Projections of the ^{27}Al directly detected dimension of the DNP enhanced scalar refocused INEPT ^{29}Si-^{27}Al HETCOR spectra acquired at 400 MHz/263 GHz for (a) 5.7 w% Al/SiO_2, (b) 15.0 w% Al/SiO_2, (c) 24.8 w% Al/SiO_2, (d) 7.3 w% Si/Al_2O_3, (e) 12.0 w% Si/Al_2O_3 and (f) 17.1 w% Si/Al_2O_3. Experimental spectra (black trace), total fits (red dashed trace) and deconvolutions of individual sites (lower traces) are shown. All spectra were a 12.5 kHz MAS frequency. Decomposition of the spectra was performed using the Gaussian isotropic model (GIM) (Czjzek, d=5) implemented in the DMFit program. The mean isotropic chemical shift (δ_{iso}), the width of the Gaussian distribution of isotropic chemical shifts ($\Delta\delta_{iso}$), the mean quadrupolar coupling constant (C_Q) and the relative integrated intensities were obtained from the fits

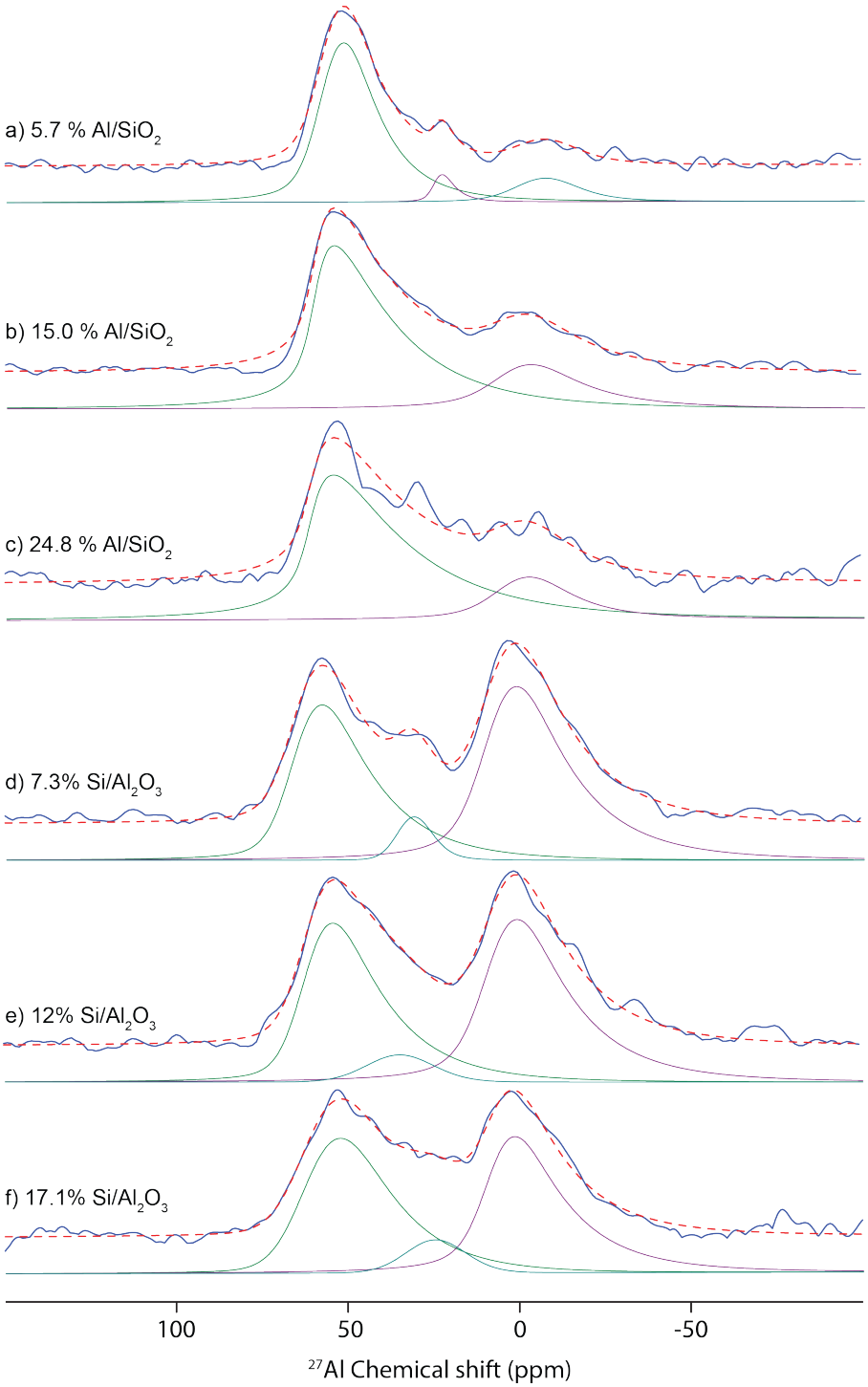

Figure A.5. 7. Projections of the ^{27}Al directly detected dimension of the DNP enhanced dipolar refocused INEPT ^{29}Si-^{27}Al HETCOR spectra acquired at 400 MHz/263 GHz for (a) 5.7 w% Al/SiO_2, (b) 15.0 w% Al/SiO_2, (c) 24.8 w% Al/SiO_2, (d) 7.3 w% Si/Al_2O_3, (e) 12.0 w% Si/Al_2O_3 and (f) 17.1 w% Si/Al_2O_3 Experimental spectra (black trace), total fits (red dashed trace) and deconvolutions of individual sites (lower traces) are shown. All spectra were a 12.5 kHz MAS frequency. Decomposition of the spectra was performed using the Gaussian isotropic model (GIM) (Czjzek, d=5) implemented in the DMFit program. The mean isotropic chemical shift (δ_{iso}), the width of the Gaussian distribution of isotropic chemical shifts ($\Delta\delta_{iso}$), the mean quadrupolar coupling constant (C_Q) and the relative integrated intensities were obtained from the fits.

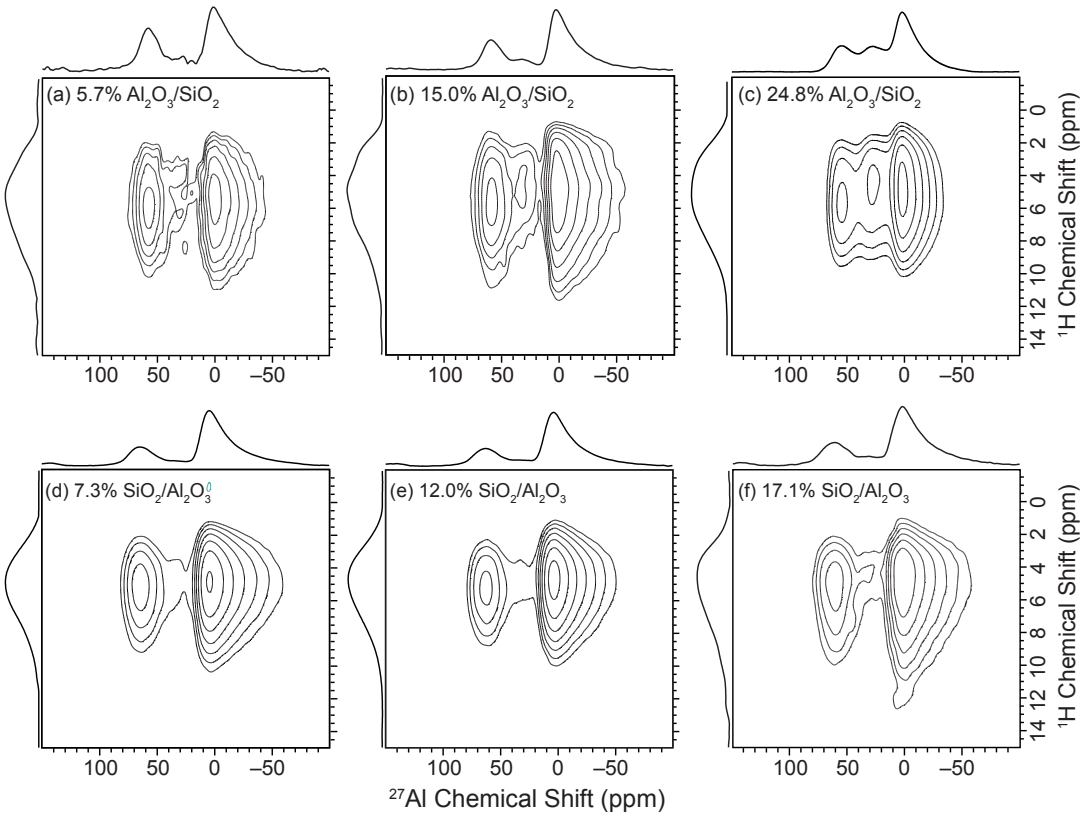

Figure A.5. 8. DNP enhanced 2D ^{1}H-^{27}Al dipolar HETCOR solid-state NMR spectra of (a) 5.7 w% Al/SiO_2, (b) 15.0 w% Al/SiO_2, (c) 24.8 w% Al/SiO_2, (d) 7.3 w% Si/Al_2O_3, (e) 12.0 w% Si/Al_2O_3 and (f) 17.1 w% Si/Al_2O_3. All spectra were acquired with DNP at 400 MHz and a 12.5 kHz MAS frequency. Projections of the 2D spectra are shown along the horizontal and vertical axes. All spectra were acquired with a 500 μs contact time, except for the spectrum of 24.8 w% Al/SiO_2 which was acquired with a 800 μs contact time. Each spectrum was acquired with 2 scans per increment, a 3.8 s polarization delay, 64 t_1 increments and a t_1 increment of 64 μs. ^{1}H chemical shifts were scaled by applying a factor 1.73 to the indirect dimension spectral width.

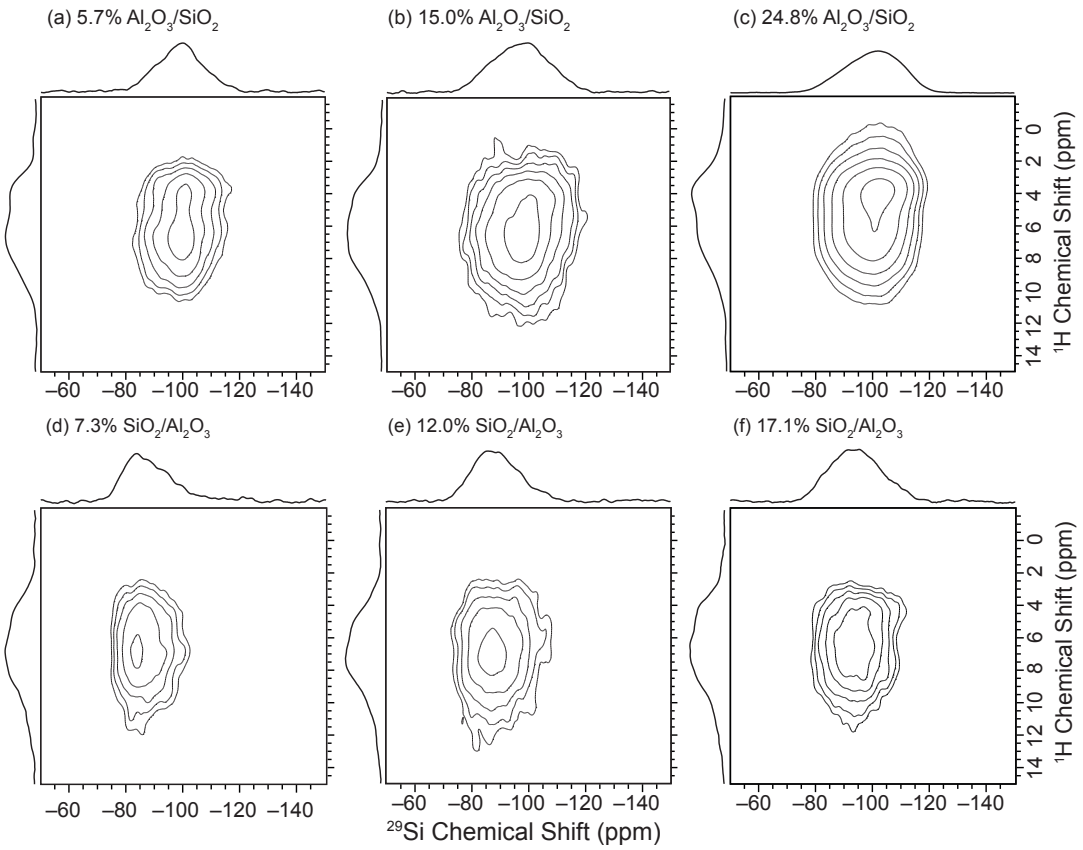

Figure A.5. 9. DNP enhanced 2D ^{1}H-^{29}Si dipolar HETCOR solid-state NMR spectra of (a) 5.7 w% Al/SiO_2, (b) 15.0 w% Al/SiO_2, (c) 24.8 w% Al/SiO_2, (d) 7.3 w% Si/Al_2O_3, (e) 12.0 w% Si/Al_2O_3 and (f) 17.1 w% Si/Al_2O_3. All spectra were acquired with DNP at 400 MHz and a 12.5 kHz MAS frequency. Projections of the 2D spectra are shown along the horizontal and vertical axes. All spectra were acquired with a 500 μs contact time, except for the spectrum of 24.8 w% Al/SiO_2 which was acquired with a 3 ms contact time. Each spectrum was acquired with 2 scans per increment, a 3.5 s polarization delay, 64 t_1 increments and a t_1 increment of 64 μs. ^{1}H chemical shifts were scaled by applying a factor 1.73 to the indirect dimension spectral width.

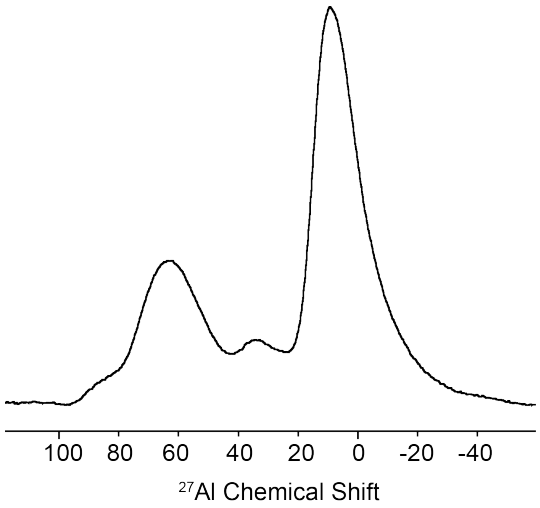

Figure A.5. 10. DNP enhanced ^{1}H-^{27}Al CPMAS solid-state NMR spectra acquired at 600 MHz/395 GHz of the starting alumina material.

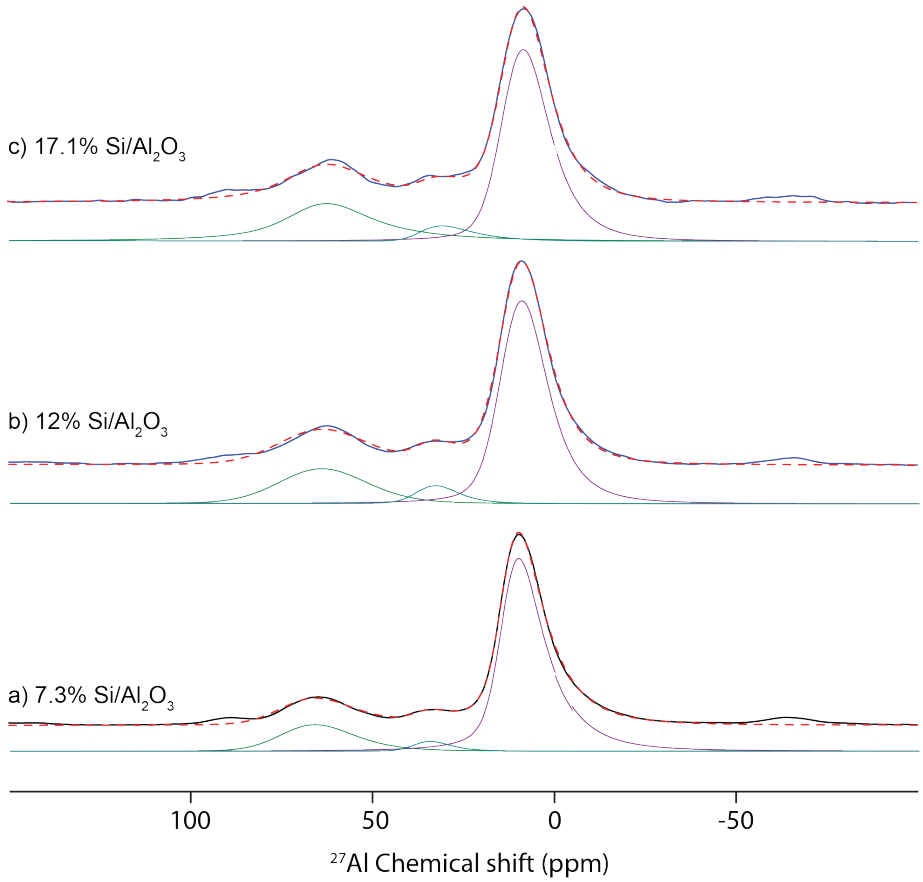

Figure A.5. 11. ^{1}H-^{27}Al CPMAS with saturation recovery cycles, 600 MHz, Micro Wave power at 125 mA, 12.5 kHz spinning rate, the contact time was set to 0.6 ms. 7.3 %, 12% and 17.1% SiO_2 on Al_2O_3. Decomposition of the spectra were done using the Gaussian isotropic model (GIM) (Czjzek, d=5) implemented in the DMFit program. The isotropic chemical shift (δ_{iso}), the Gaussian distribution of the chemical shift ($\Delta\delta_{iso}$), the quadrupolar coupling constant (C_Q) and the relative population values were extracted.

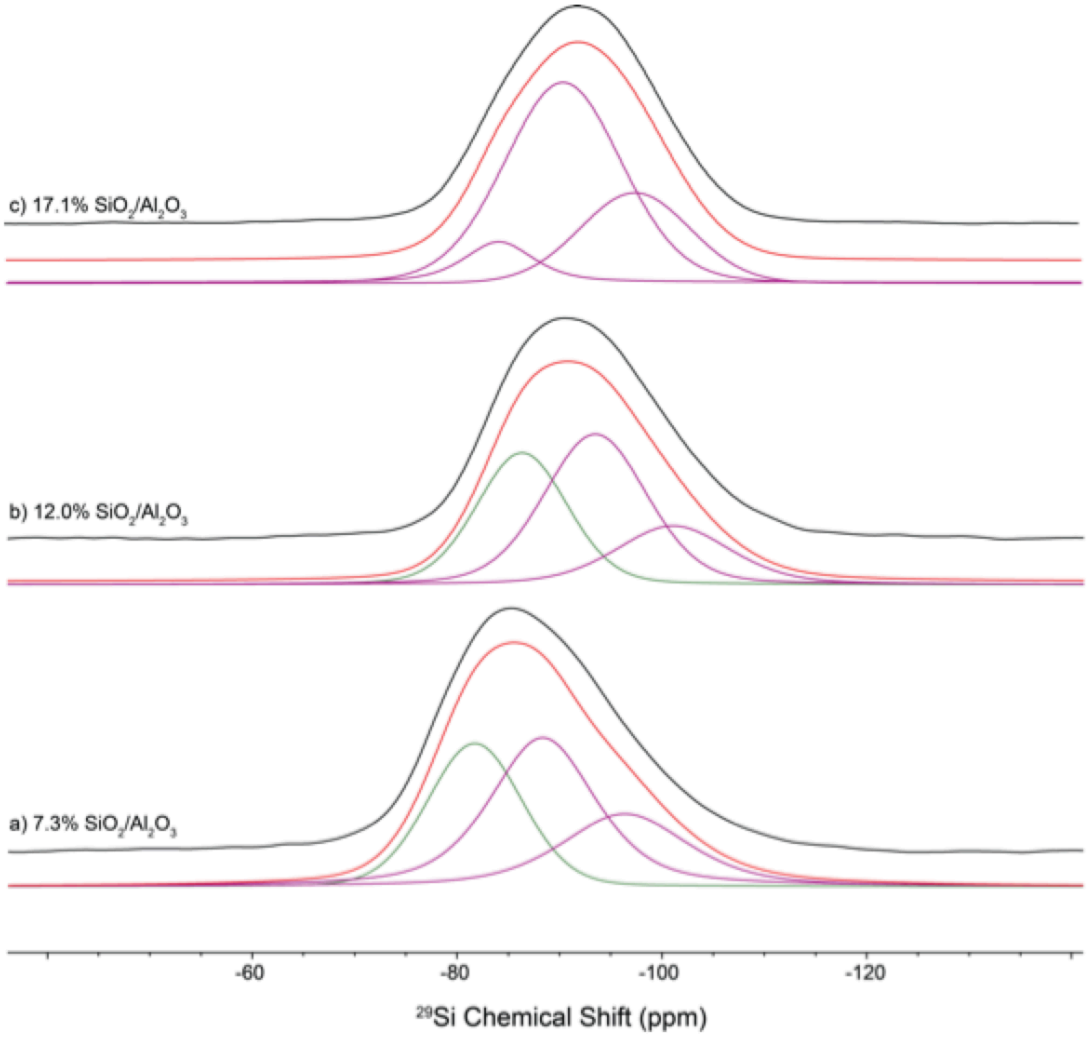

Figure A.5. 12. ^{1}H-^{29}Si CPMAS, 400 MHz, Microwave power at 35 mA, 12.5 kHz spinning rate, the contact time was set to 3 ms and the recycling time was 3.5 sec. a) 7.3 % SiO_2 on Al_2O_3, b) 12 % SiO_2 on Al_2O_3 and c) 17.1 % SiO_2 on Al_2O_3.

Table A.5 1. Results of the simulation (GIM lineshapes) of the 600 MHz ^{1}H-^{27}Al CPMAS with saturation cycle of 7.3 %, 12% and 17.1% SiO_2 on Al_2O_3. The isotropic chemical shift (δ_{iso}), the Gaussian distribution of the chemical shift ($\Delta\delta_{iso}$), the quadrupolar coupling constant (C_Q) and the relative population values are presented.

		7.3% Si/Al_2O_3		
Site	Percent	δ_{iso} (ppm)	$\Delta\delta_{iso}$ (ppm)	C_Q (MHz)
Al^{IV}	16.5	72.3	18.2	5.4
Al^{V}	3.2	37.7	8.4	4.1
Al^{VI}	80.3	13.9	7.5	4.9
		12% Si/Al_2O_3		
Site	Percent	δ_{iso} (ppm)	$\Delta\delta_{iso}$ (ppm)	C_Q (MHz)
Al^{IV}	21.3	69.3	24.3	4.6
Al^{V}	5.6	36.6	9.7	4.3
Al^{VI}	73.2	12.9	10.6	4.4
		17.1% Si/Al_2O_3		
Site	Percent	δ_{iso} (ppm)	$\Delta\delta_{iso}$ (ppm)	C_Q (MHz)
Al^{IV}	26.9	65.8	15.3	4.6
Al^{V}	5.6	36.9	9.7	6
Al^{VI}	67.6	12.7	10.6	4.6

Table A.5. 2. Results of the simulation (GIM lineshapes) of the 400 MHz ^{1}H-^{27}Al-^{29}Si INEPT through scalar coupling. The 1D projection of the ^{27}Al F2 dimension were fitted. The mean isotropic chemical shift (δ_{iso}), the width of the Gaussian distribution of the chemical shift ($\triangle\delta_{iso}$), the mean quadrupolar coupling constant (C_Q) and the relative integrated intensities are presented.

		5.7% Al/SiO_2		
Site	Percent	δ_{iso} (ppm)	$\Delta\delta_{iso}$ (ppm)	C_Q (MHz)
Al^{IV}	100%	58	11.2	4.3
		15.0% Al/SiO_2		
Site	Percent	δ_{iso} (ppm)	$\Delta\delta_{iso}$ (ppm)	C_Q (MHz)
Al^{IV}	100%	61.1	8.9	4.1
		24.8% Al/SiO_2		
Site	Percent	δ_{iso} (ppm)	$\Delta\delta_{iso}$ (ppm)	C_Q (MHz)
Al^{IV}	100%	61.3	4.4	5.5
		7.3% Si/Al_2O_3		
Site	Percent	δ_{iso} (ppm)	$\Delta\delta_{iso}$ (ppm)	C_Q (MHz)
Al^{IV}	96%	62.9	7.1	5.1
Al^{VI}	4%	7.2	6.2	4.8
		12.0% Si/Al_2O_3		
Site	Percent	δ_{iso} (ppm)	$\Delta\delta_{iso}$ (ppm)	C_Q (MHz)
Al^{IV}	94%	70	7.0	5.0
Al^{VI}	6%	5.3	7.2	4.2
		17.1% Si/Al_2O_3		
Site	Percent	δ_{iso} (ppm)	$\Delta\delta_{iso}$ (ppm)	C_Q (MHz)
Al^{IV}	89%	59.38	6.8	5.0
Al^{VI}	11%	7.4	8.3	6.1

Table A.5. 3. Results of the simulation (GIM lineshapes) of the 400 MHz ^{1}H-^{27}Al-^{29}Si INEPT through dipolar coupling. The 1D projection of the ^{27}Al F2 dimension were fitted. The mean isotropic chemical shift (δ_{iso}), the width of the Gaussian distribution of the chemical shift ($\Delta\delta_{iso}$), the mean quadrupolar coupling constant (C_Q) and the relative integrated intensities are presented.

		5.7% Al/SiO_2		
Site	Percent	δ_{iso} (ppm)	$\Delta\delta_{iso}$ (ppm)	C_Q (MHz)
Al^{IV}	82%	57	11	3.8
Al^{V}	5%	24.9	4	2.3
Al^{VI}	13%	-3.4	4	2.9
		15.0% Al/SiO_2		
Site	Percent	δ_{iso} (ppm)	$\Delta\delta_{iso}$ (ppm)	C_Q (MHz)
Al^{IV}	77%	60.6	5	5.2
Al^{VI}	23%	3.6	16	4.3
		24.8% Al/SiO_2		
Site	Percent	δ_{iso} (ppm)	$\Delta\delta_{iso}$ (ppm)	C_Q (MHz)
Al^{IV}	81%	61.7	5	5.8
Al^{VI}	19%	3	16	3.8
		7.3% Si/Al_2O_3		
Site	Percent	δ_{iso} (ppm)	$\Delta\delta_{iso}$ (ppm)	C_Q (MHz)
Al^{IV}	42%	66.2	13	4.9
Al^{V}	5%	33.9	9.9	2.3
Al^{VI}	53%	9	14.2	4.7
		12.0% Si/Al_2O_3		
Site	Percent	δ_{iso} (ppm)	$\Delta\delta_{iso}$ (ppm)	C_Q (MHz)
Al^{IV}	47%	62.7	12.7	4.9
Al^{V}	5%	38.2	21.2	4.3
Al^{VI}	48%	8.4	14	4.5
		17.1% Si/Al_2O_3		
Site	Percent	δ_{iso} (ppm)	$\Delta\delta_{iso}$ (ppm)	C_Q (MHz)
Al^{IV}	48%	62.3	18	5.0
Al^{V}	7%	27.4	19	2.1
Al^{VI}	45%	8.6	12.3	4.6

Table A.5. 4. Results of the simulation (GIM lineshapes) of the 600 MHz ^{1}H-^{27}Al CPMAS with saturation cycle of 7.3 %, 12% and 17.1% SiO_2 on Al_2O_3. The isotropic chemical shift (δ_{iso}), the Gaussian distribution of the chemical shift ($\Delta\delta_{iso}$), the quadrupolar coupling constant (C_Q) and the relative population values are presented.

		7.3% Si/Al_2O_3		
Site	Percent	δ_{iso} (ppm)	$\Delta\delta_{iso}$ (ppm)	C_Q (MHz)
Al^{IV}	16.5	72.3	18.2	5.4
Al^{V}	3.2	37.7	8.4	4.1
Al^{VI}	80.3	13.9	7.5	4.9
		12% Si/Al_2O_3		
Site	Percent	δ_{iso} (ppm)	$\Delta\delta_{iso}$ (ppm)	C_Q (MHz)
Al^{IV}	21.3	69.3	24.3	4.6
Al^{V}	5.6	36.6	9.7	4.3
Al^{VI}	73.2	12.9	10.6	4.4
		17.1% Si/Al_2O_3		
Site	Percent	δ_{iso} (ppm)	$\Delta\delta_{iso}$ (ppm)	C_Q (MHz)
Al^{IV}	26.9	65.8	15.3	4.6
Al^{V}	5.6	36.9	9.7	6
Al^{VI}	67.6	12.7	10.6	4.6

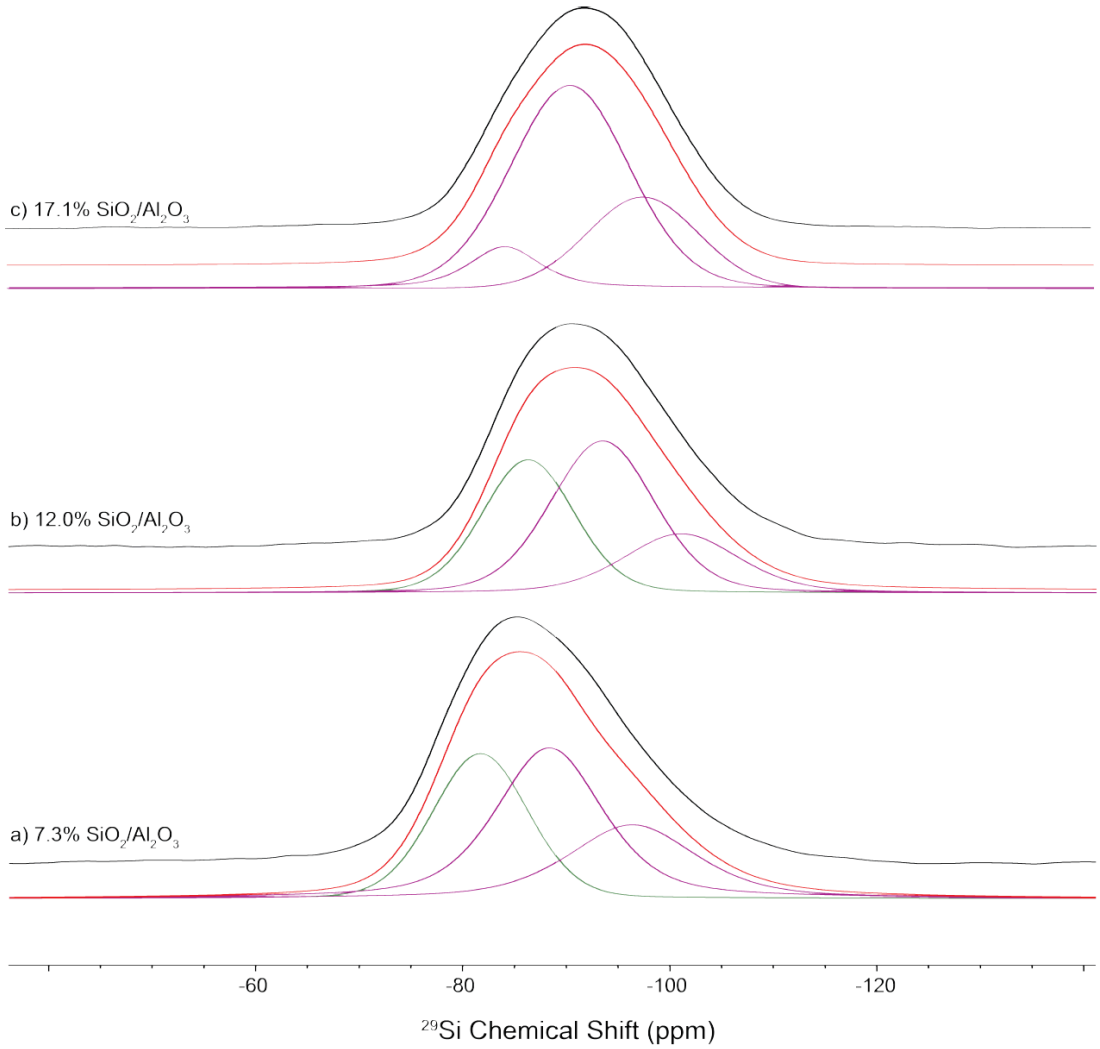

Figure A.5. 13. ^{1}H-^{29}Si CPMAS, 400 MHz, Microwave power at 35 mA, 12.5 kHz spinning rate, the contact time was set to 3 ms and the recycling time was 3.5 sec. a) 7.3 % SiO_2 on Al_2O_3, b) 12 % SiO_2 on Al_2O_3 and c) 17.1 % SiO_2 on Al_2O_3.

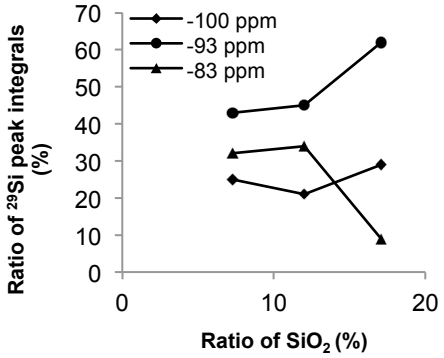

Figure A.5. 14. Evolution of the ratio between the -83, -93 and -100 ppm peaks as a function of silica loading for SiO_2/Al_2O_3 type materials. Calculated from decomposition of CPMAS ^{1}H-^{29}Si spectra recorded on a 400 MHz spectrometer equipped with a DNP.

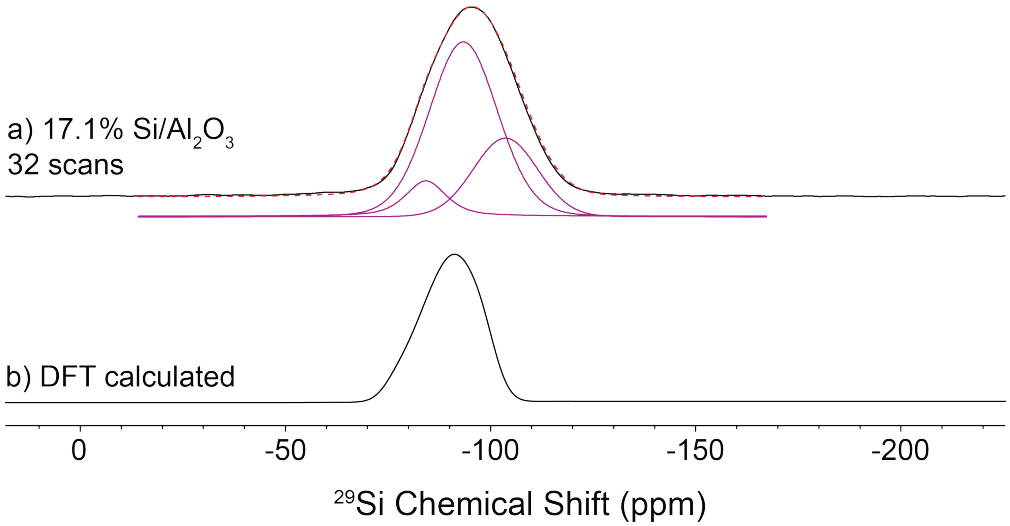

Figure A.5. 15. 400 MHz/263 GHz DNP enhanced ^{1}H-^{29}Si CPMAS solid-state NMR spectra. The spectrum was acquired with a 12.5 kHz spinning frequency and a CP contact time of 3 ms. The recycle delay was 3.5 sec. a) 17.1 w% Si/Al_2O_3, (b) DFT calculated spectrum, for all ^{29}Si nucleus, independently of their proximity to ^{1}H. The model corresponds to a 14% Si/Al_2O_3.

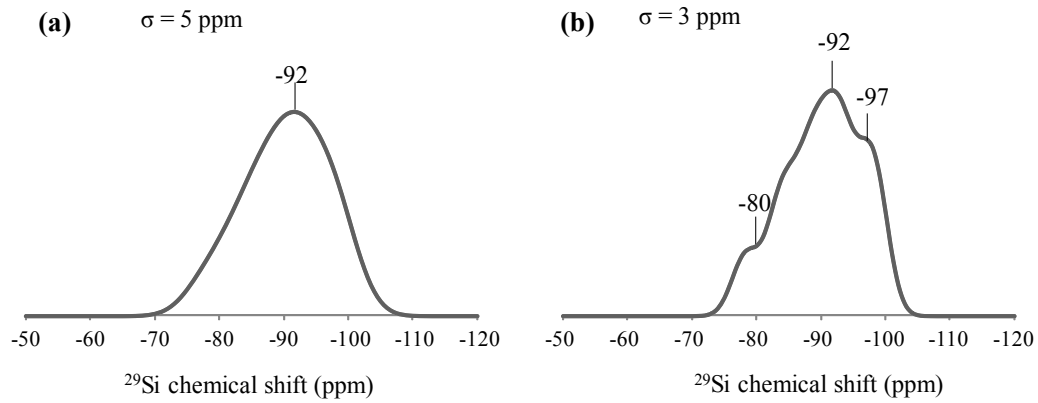

Figure A.5. 16. DFT-computed ^{29}Si NMR spectrum, obtained thanks to the values reported in table 2 (main text) and Gaussian broadening according to the following equation : $y = exp\left\{-\left(\frac{x-x_0}{\sigma}\right)^2\right\}$. (a) σ = 5 ppm, (b) σ = 3 ppm.

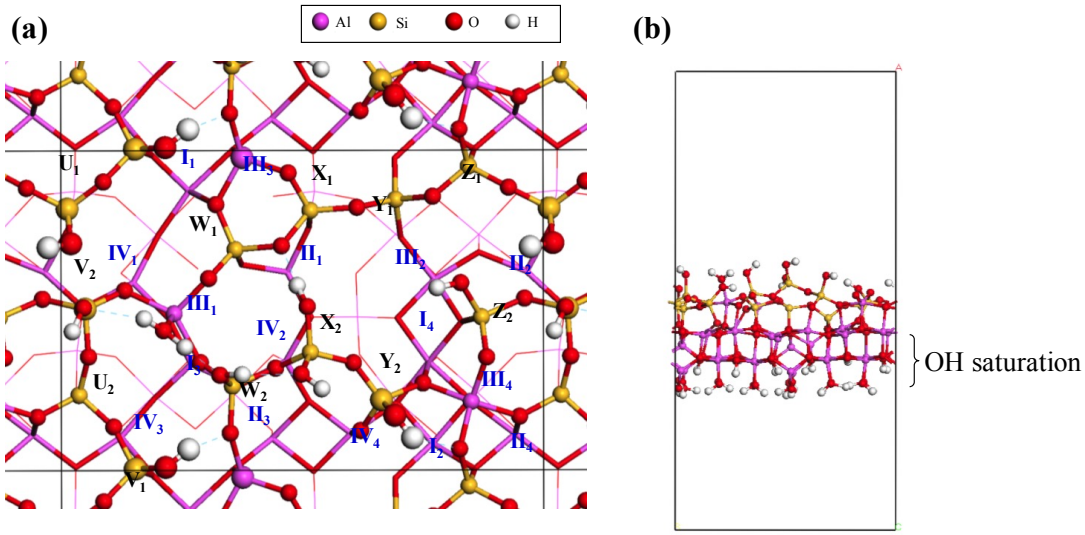

Figure A.5. 17. (a) Top and (b) side views of the models employed for the CASTEP-NMR DFT calculations, at θ_{OH} = 5.4 nm^{-2}. The terminology for Si and outermost Al atoms is given in black and blue respectively. Atoms from the most external surface are shown as balls and sticks in (a), those just below are depicted as sticks.

Table A.5. 5. DFT-computed ^{27}Al NMR isotropic chemical shifts, C_Q (absolute values) and η values, for Al atoms located within and just below the silica layer (see Figure S2 for the terminology).

Al atom	Environment	δ_{iso}(^{27}Al) (ppm)	C_Q(MHz)	η_Q
IV_4	Distorted Al(VI)	9.3	-7.59	0.64
I_4	Al(VI)	10.1	-6.64	0.95
II_4	Al(VI)	17.3	8.973	0.54
IV_3	Distorted Al(VI)	23.2	17.42	0.34
I_1	Al(V)	29.6	4.845	0.83
IV_1	Distorted Al(V)	30.5	12.15	0.56
III_1	BPT Al(V)	31.8	-6.819	0.62
I_3	BPT Al(V)	35.2	9.538	0.55
III_4	Al(V)	38.2	-13.83	0.73
III_2	Al(V)	43.1	-10.32	0.74
I_2	Al(V)	44.2	8.546	0.72
II_2	Distorted Al(IV)	48.6	-16.55	0.79
II_3	Distorted Al(V-IV)	52.5	11.02	0.80
III_3	Al(IV)	62.2	13.48	0.59
II_1	Al(IV)	68.8	-8.01	0.76
IV_2	Distorted Al(IV)	70.18	14.70	0.80

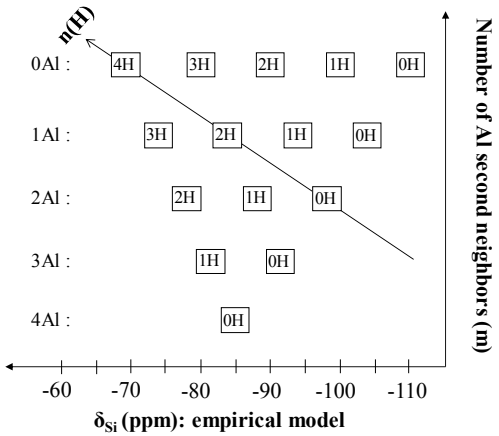

Figure A.5. 18. Empirical assignment of ^{29}Si NMR spectra, according to literature, assuming twofold coordination for all O atoms, and constant chemical shift variation by ^{1}H (+10 ppm) and ^{27}Al (+5 ppm) second neighbours.

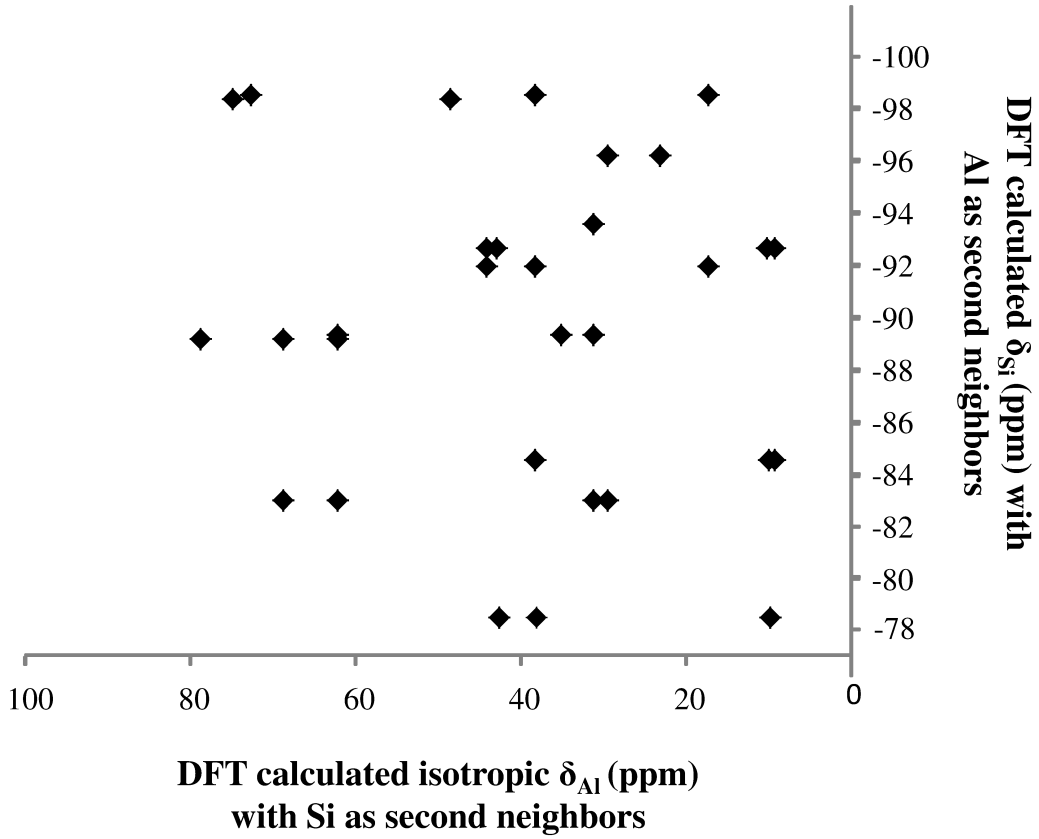

Figure A.5. 19. Connectivity analysis between surface ^{29}Si nuclei (DFT calculated chemical shift is reported on the y-axis) and ^{27}Al second neighbors (DFT calculated isotropic chemical shift is reported on the x-axis).

A.4. Appendix to Chapter 6.

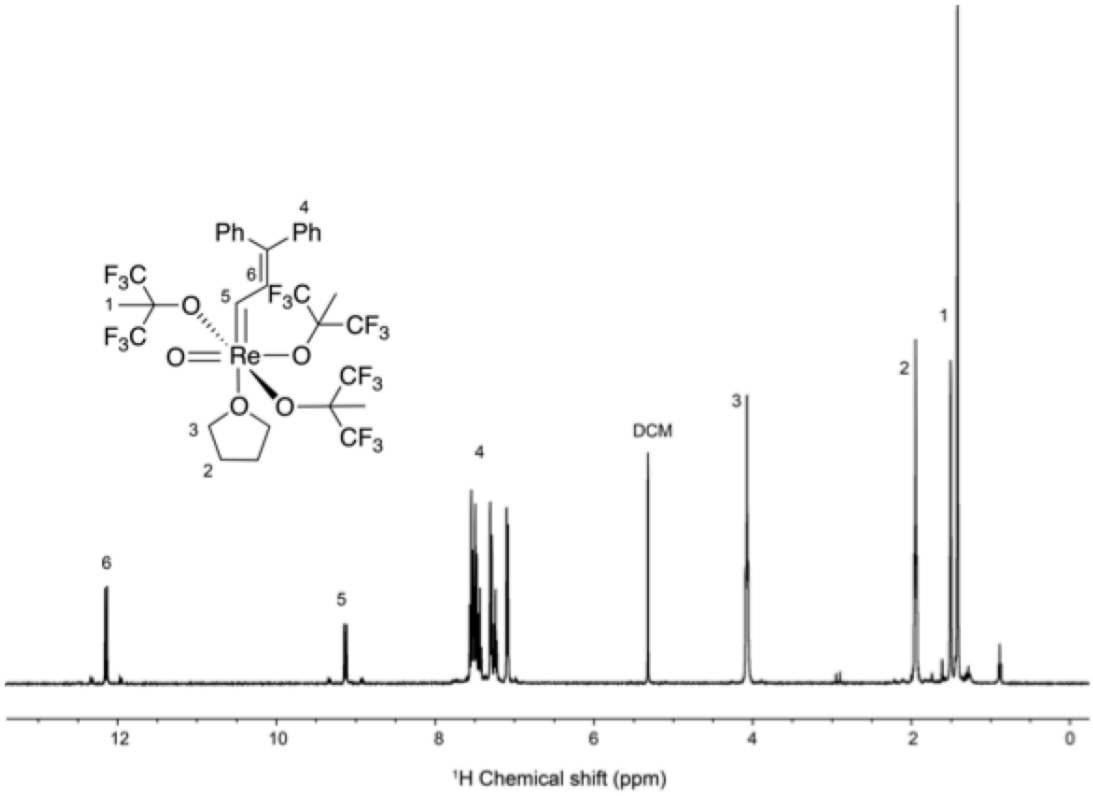

Figure A.6. 1. ^{1}H NMR of 1*, 400 MHz, CD_2Cl_2, 32 scans, recycling delay of 10 sec

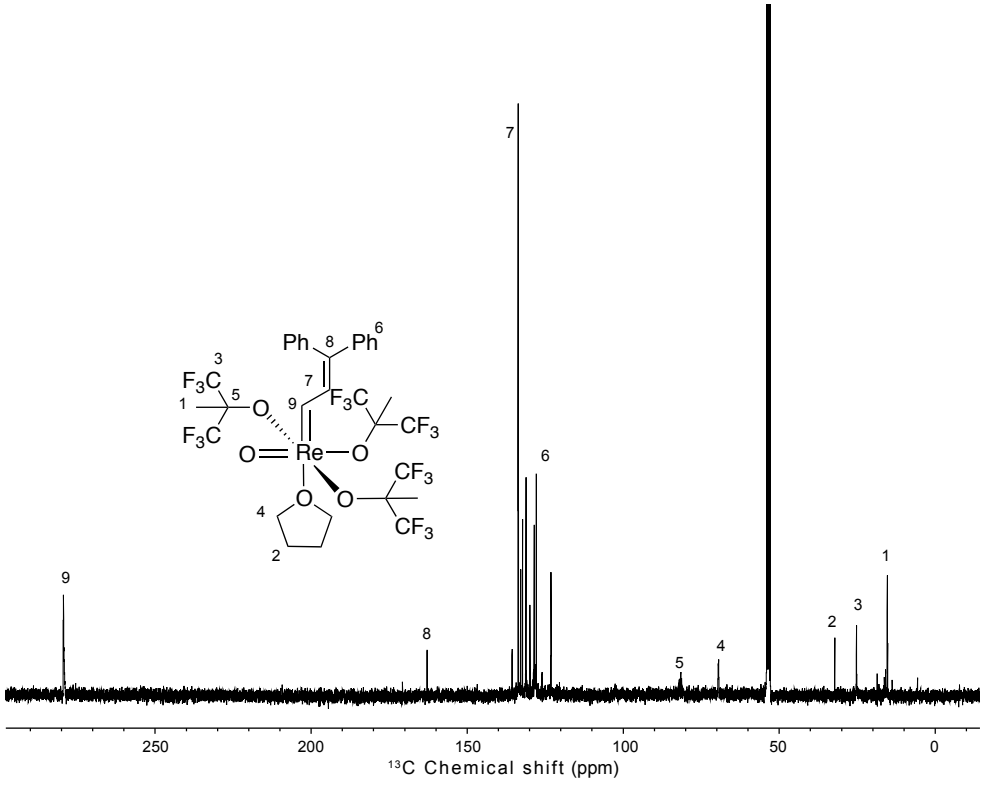

Figure A.6. 2. ^{13}C NMR of 1*, 400 MHz, CD_2Cl_2, 512 scans, recycling delay of 10 sec.

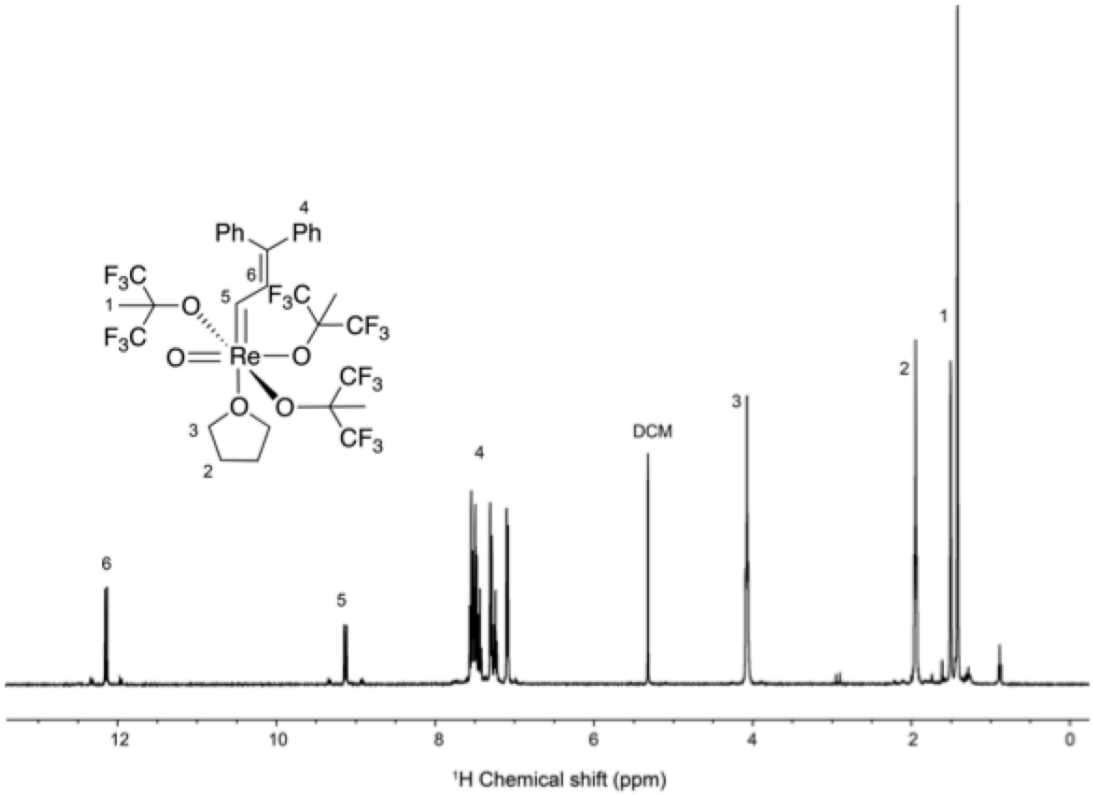

Figure A.6. 3. ^{1}H MAS NMR spectrum of Re(O)(=CH–CH=CPh$_2$)(OtBu$_{F6}$)$_3$(THF) grafted on $SiO_{2-(700)}$ at 400 MHz, d1= 1 sec, 15 KHz spinning speed.

Table A.6. 1. Selected bonds for **Al(OSi(OtBu)$_3$)$_3$** (distances are given in Å)

Structural parameters	**Al(OSi(OtBu)$_3$)$_3$**
Al2 – O1	1.700(7)
Al2 – O2	1.697(7)
Al2 – 03	1.769(6)
Al2 – O4	1.903(6)

Table A.6. 2. Selected angles for **Al(OSi(OtBu)$_3$)$_3$** (given in °)

Structural parameters	**Al(OSi(OtBu)$_3$)$_3$**
O1 – Al2 – O2	115.9(3)
O1 – Al2 – O3	111.3(3)
O3 – Al2 – O4	116.4 (3)
O1 – Al2 – O4	116.8 (3)
O2 – Si3 – O4	114.9 (2)
O3 – Si3 – O4	80.4(3)

Table A.6. 3. Crystallographic data for **$Al(OSi(OtBu)_3)_3$**

	$Al(OSi(OtBu)_3)_3$
Formula	$C_{36}H_{81}AlO_{12}Si_3$
Crystal size (mm)	0.45 x 0.35 x 0.2
cryst syst	Monoclinic
space group	Pn
volume ($Å^3$)	4961.2(6)
a (Å)	15.1419(8)
b (Å)	13.5320(9)
c (Å)	24.294(2)
α (deg)	90
β (deg)	94.687(6)
γ (deg)	90
Z	4
formula weight (g/mol)	817.25
density (g cm^{-3})	1.094
F(000)	1792.0
temp (K)	100(2)
total no. reflections	18849
unique reflections [R(int)]	11977 [0.0462]
Final R indices [$I > 2\sigma(I)$]	R_1 = 0.0.0818, wR_2 = 0.1773
Largest diff. peak and hole ($e.A^{-3}$)	0.53/-0.52
GOF	1.095

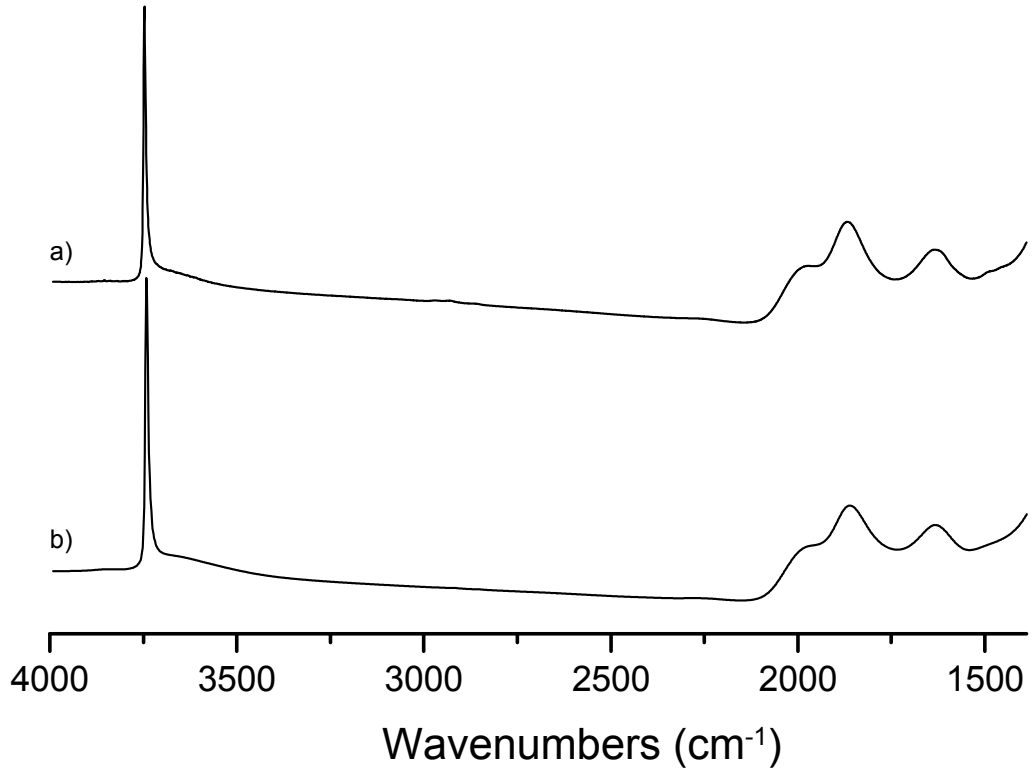

Figure A.6. 4. FT-IR spectra of (a) **Al@SiO$_2$** and (b) $SiO_{2-(700)}$.

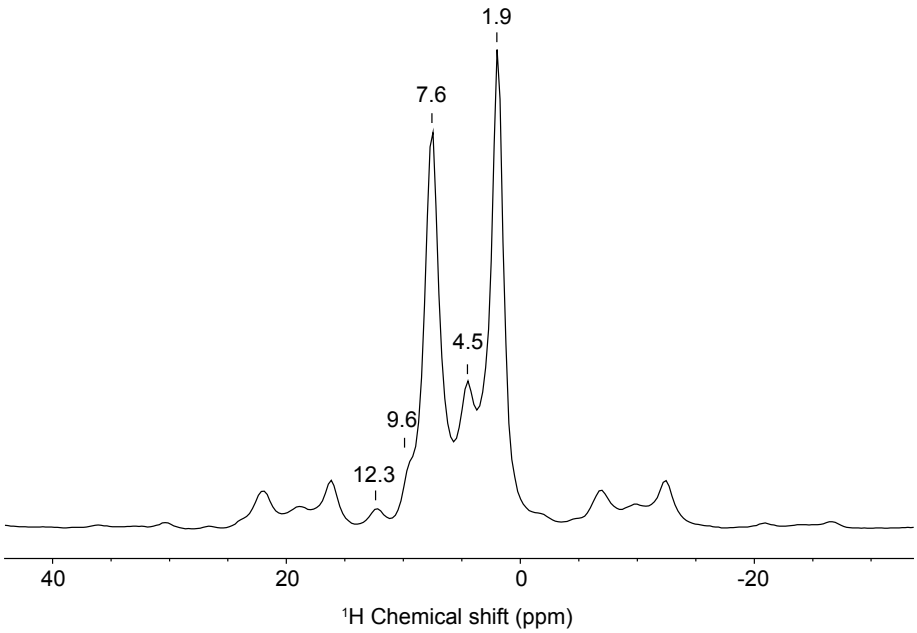

Figure A.6. 5. ^{1}H spin echo NMR of **1@Al@SiO$_2$**, 10 kHz, 700 MHz, 32 scans, recycling delay of 1 sec.

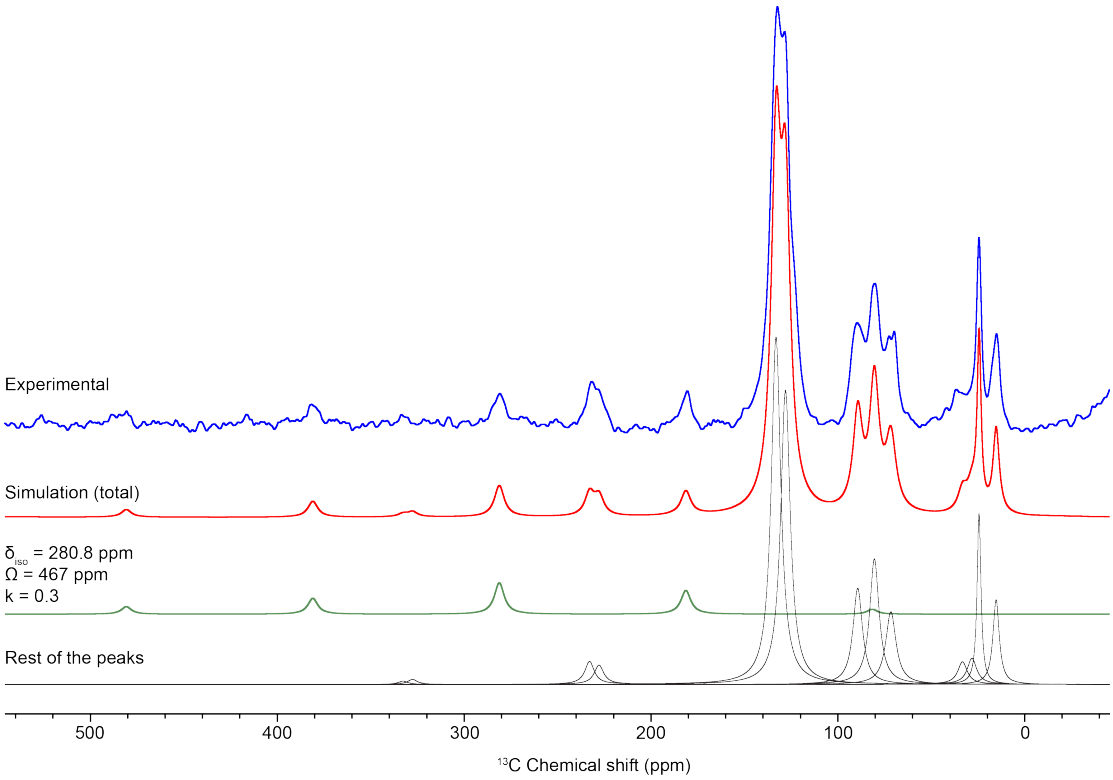

Figure A.6. 6. ^{1}H-^{13}C CPMAS of $Re(O)(=CH–CH=CPh_2)(OtBu_{F6})_3(THF)$ supported on $\mathbf{Al_{IV}@SiO_2}$. 400 MHz, d1= 1 sec, 10 kHz spinning speed. In red, the total simulation of the spectrum. Green line represents the CSA tensor fitting of the alkylidene signal. Black lines represent the other peaks.

A.5. Appendix to Chapter 7.

Re(=O)(OtBuF6)3(THF) was grafted on the tailor made Al@SiO2 surface yielding **7.1** (Scheme A.7.1). This compound was not active in metathesis of propylene at room temperature. Diphenylcyclopropene was therefore contacted to the solid. A change from purple to dark purple was observed. The resulting compound was active in the metathesis of propylene and it was able to reach the thermodynamic equilibrium with 500 equiv. of propylene (with respect to Re) in 2.5 hours. The compounds was characterized using 1H-13C HETCOR, it revealed the presence of the alkylidene species with a carbon peak at 282 ppm assigned to be the alkylidene peak. This is confirmed by the fact that this peak correlates with two proton at 9.8 and 12.6 ppm correpoding to the two protons nearby.

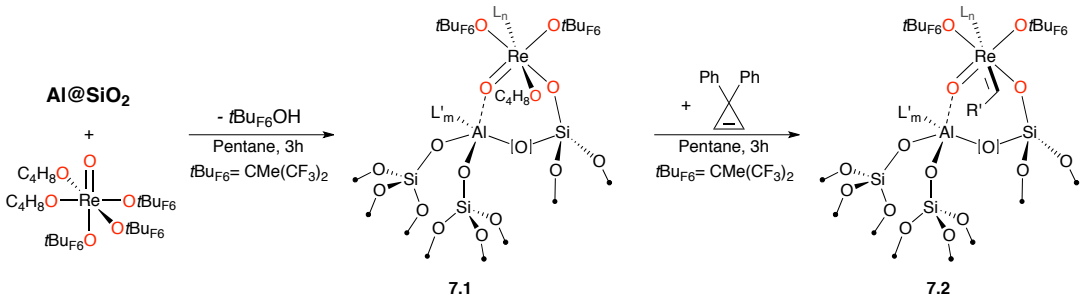

Scheme A.7.1: generation of Re(VII) oxo alkylidene from Re(V) oxo supported on $Al@SiO_2$.

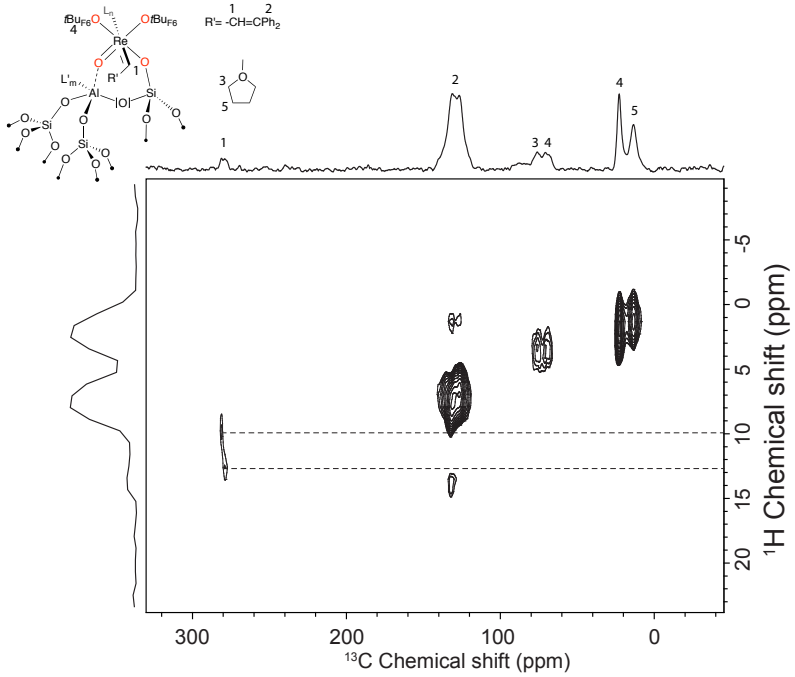

Figure A.7.1 ^{1}H-^{13}C HETCOR of **7.2**. 400 MHz, 2k scans per slices, 96 slices, contact time of 1 ms and recycling delay of 1 sec. The ^{1}H RF field was set to 100 kHz.